IDŐJÁRÁS

QUARTERLY JOURNAL
OF THE HUNGARIAN METEOROLOGICAL SERVICE

CONTENTS

****

http://www.met.hu/firat/ido-e.html

VOL. 104 * NO. 1 * JANUARY–MARCH 2000

IDŐJÁRÁS

Quarterly Journal of the Hungarian Meteorological Service

Editor-in-Chief
T. PRÁGER

Executive Editor
M. ANTAL

EDITORIAL BOARD

AMBRÓZY, P. (Budapest, Hungary)
ANTAL, E. (Budapest, Hungary)
BARTHOLY, J. (Budapest, Hungary)
BOZÓ, L. (Budapest, Hungary)
BRIMBLECOMBE, P. (Norwich, U.K.)
CZELNAI, R. (Budapest, Hungary)
DÉVÉNYI, D. (Budapest, Hungary)
DUNKEL, Z. (Brussels, Belgium)
FISHER, B. (Chatham, U.K.)
GELEYN, J.-Fr. (Toulouse, France)
GERESDI, I. (Pécs, Hungary)
GÖTZ, G. (Budapest, Hungary)
HANTEL, M. (Vienna, Austria)
HASZPRA, L. (Budapest, Hungary)
HORÁNYI, A. (Budapest, Hungary)
HORVÁTH, Á. (Siófok, Hungary)
IVÁNYI, Z. (Budapest, Hungary)
KONDRATYEV, K.Ya. (St. Petersburg, Russia)
MAJOR, G. (Budapest, Hungary)
MÉSZÁROS, E. (Veszprém, Hungary)
MIKA, J. (Budapest, Hungary)
MARACCHI, G. (Firenze, Italy)
MERSICH, I. (Budapest, Hungary)
MÖLLER, D. (Berlin, Germany)
NEUWIRTH, F. (Vienna, Austria)
PINTO, J. (R. Triangle Park, NC, U.S.A)
PROBÁLD, F. (Budapest, Hungary)
RENOUX, A. (Paris-Créteil, France)
ROCHARD, G. (Lannion, France)
S. BURÁNSZKY, M. (Budapest, Hungary)
SPÄNKUCH, D. (Potsdam, Germany)
STAROSOLSZKY, Ö. (Budapest, Hungary)
SZALAI, S. (Budapest, Hungary)
SZEPESI, D. (Budapest, Hungary)
TAR, K. (Debrecen, Hungary)
TÄNCZER, T. (Budapest, Hungary)
VALI, G. (Laramie, WY, U.S.A.)
VARGA-HASZONITS, Z. (Moson-magyaróvár, Hungary)

Editorial Office: P.O. Box 39, H-1675 Budapest, Hungary or
Gilice tér 39, H-1181 Budapest, Hungary
E-mail: prager@met.hu or *antal@met.hu*
Fax: (36-1) 290-7387

Subscription by

mail: IDŐJÁRÁS, P.O. Box 39, H-1675 Budapest, Hungary;
E-mail: prager@met.hu or *antal@met.hu*; *Fax: (36-1) 290-7387*

IDŐJÁRÁS

Quarterly Journal of the Hungarian Meteorological Service
Vol. 104, No. 1, January–March 2000, pp. 1–20

Statistical linkages between ENSO, NAO, and regional climate

Rita Pongrácz and **Judit Bartholy**

Department of Meteorology, Eötvös Loránd University
H-1518 Budapest, P.O. Box 32, Hungary
E-mails: prita@caesar.elte.hu; bari@ludens.elte.hu

(Manuscript received 13 July 1999; in final form 22 February 2000)

Abstract—It has been demonstrated that large scale oscillation phenomena (e.g., ENSO, NAO, PNA,...) have a great importance in influencing many climatic variables at different regions of the Earth. These phenomena do not take place independently, however, the mechanisms and interrelationships are not completely understood so far. The main idea of this paper is to describe statistical linkages between the large scale atmospheric oscillations and regional climate parameters. In order to understand the circulation and temperature structure over the Atlantic European region an analysis of atmospheric macrocirculation patterns (MCPs) is carried out via a conditional probability framework. The frequency distributions of regional MCP classes (constructed by Hess and Brezowsky, and Péczely) under different phases of large-scale oscillations are examined. Focusing on the Carpathian Basin, ENSO related regional climate analysis is carried out. Finally, lag correlation analysis are presented to compare local precipitation, regional temperature anomaly time series and different NAO indices (Jones, Hurrell, spatial SST differences).

Key-words: El Niño-Southern Oscillation, North Atlantic Oscillation, macrocirculation pattern, regional climate, statistical relationship.

1. Introduction

The El Niño phenomenon originally referred to winter-periods when cold upwelling fails to come near the South American shore at Peru and Ecuador, so unusually warm sea surface temperature (SST) occurs in the area. Another phenomenon of the tropical Pacific region is the Southern Oscillation (SO) that refers to the variability of the tropical atmosphere, namely, a large-scale fluctuation of atmospheric air mass between the Eastern and Western parts of the Pacific Ocean. Since these two phenomena have close interrelationship, a common abbreviation, ENSO (El Niño-Southern Oscillation) is widely used to refer to a quasi-periodic redistribution of heat and momentum in the Pacific area. It involves both the atmosphere and the ocean (*Philander*, 1990).

Over much of the middle and lower latitudes of the globe, ENSO events are the most important external sources of year to year variability in climate. The interest shown in ENSO by scientists from different scientific backgrounds has increased since the 1982–83 El Niño, which has been labeled as the strongest one in the last 100 years. There was a good chance that the 1997–98 ENSO event will hit this record, but after a very intense and frightening starting period it did not. Many questions were answered in the last 10–15 years, many potential relationships that might exist between El Niño events and climate anomalies worldwide were examined and some has been proven. Let us mention here just some of them: reduced tropical cyclone activity in the western Pacific, reduced precipitation in Australia (*Nicholls* and *Kariko*, 1993), later onset of the Indian monsoon (*Joseph et al.*, 1994), increased winter rainfall in the southern United States (*Diaz* and *Markgraf*, 1992).

However, many general and specific ENSO related questions could be asked which have not been answered yet: Is it possible to link other oscillations to ENSO? Do ENSO phases have particular circulation features on MCP frequency distributions? Furthermore, the cumulative economic effects of El Niño are substantial, and there is considerable interest in understanding and predicting the occurrence and magnitude of El Niño events (*Glantz et al.*, 1987).

This paper investigates ENSO effects on tropospheric circulation and MCPs; in the following six chapters we will show selected results of our work.

2. Data

Several types of data have been used in the present paper since different kinds of analysis were completed.

Daily circulation and temperature fields from the NMC Grid Point Data Set (version III, 1996) were analyzed. This hemispherical database was composed in 1996 by the *Department of Atmospheric Sciences* at the University of Washington and the *Data Support Section* in NCAR. Height and temperature fields of several geopotential levels are available in NMC octagonal grid form (*Lenne*, 1970). The total 47 × 51 gridpoints are equally spaced when viewed on a polar stereographic grid, centered on the North Pole and rotated such that 10°E is a horizontal line to the right of the Pole. We used the following data sets: sea level pressure, 500 hPa, 700 hPa, 850 hPa geopotential heights and temperature on 500 hPa, 700 hPa and 850 hPa geopotential levels. Most of these time series consist of 33 years (1962–94) daily data fields but some of them are longer and consist of 40 years (1955–94) observations. In the present paper the original grid was converted into a latitude-longitude grid and then the Atlantic European region (30°–70°N latitude, 25°W–40°E longitude) was selected. It is represented by 63 gridpoints using 10° × 10° diamond grid resolution.

Several classifications of macrocirculation patterns (MCP) time series are available; in the present paper we will evaluate only two of them: (1) MCP defined by *Hess* and *Brezowsky* (1952, 1977) for the European continent. This dataset consists of daily HB codes from 1881 to 1997. (2) Another MCP code system was defined by *Péczely* (1961) which considers also the European weather situation particularly in the Carpathian Basin. Time series (*Péczely*, 1983; *Károssy*, 1994, 1997) include daily codes for the period 1881–1996.

Global sea surface temperature (SST) fields were obtained from *NOAA* (1997). This dataset includes daily interpolated fields of 1950–1998 with resolution of $2^{\circ} \times 2^{\circ}$ over the hemispheres. *Reynolds* and *Smith* (1994) describe optimum interpolation technique that has been applied to compose the SST dataset. Several key regions were defined based on the correlation coefficients between SST fields and climate parameters of the Carpathian Basin (*Bartholy* and *Pongrácz*, 1998a). Then, the differences between the spatial average SST values of these key regions were applied as oscillation indices.

Finally, monthly mean temperature and daily precipitation amounts measured at four meteorological stations in Hungary (Debrecen, Keszthely, Pécs, Szeged) were used as a representation of regional meteorological parameters. The precipitation time series consist of daily values from 1901 to 1994, and the temperature dataset includes monthly mean values calculated for 16 Hungarian stations for the period 1881–1994. *Fig. 1* indicates the geographical locations of the meteorological stations in Hungary that have been used in the analysis.

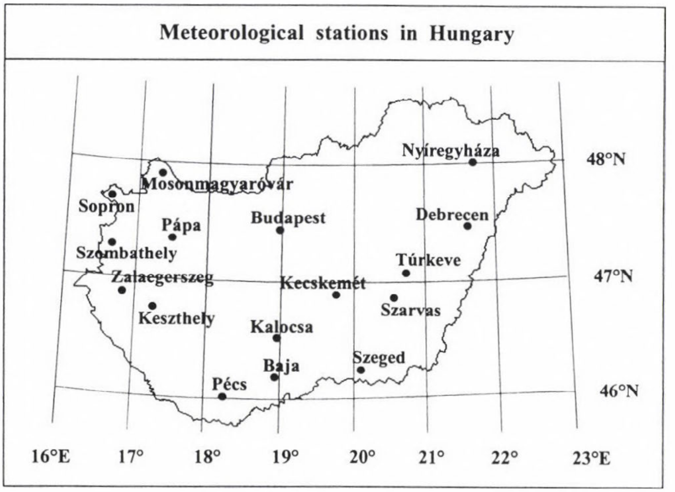

Fig. 1. Locations of the 16 Hungarian meteorological stations used in the analysis.

3. ENSO related circulation and temperature variability

Variabilities of circulation and temperature fields were examined using the available dataset listed in the previous section. EOF-analysis (*von Storch*, 1995) was applied to explore the action centers of the Atlantic European grid during the different ENSO phases (e.g., El Niño, La Niña and neutral periods). During this numerical procedure the eigenvalue equations of correlation matrices of geopotential fields have been solved. Dimension of a matrix equals to the number of gridpoints, that is 63 in this case, representing the Atlantic European region between 30°–70°N latitude and between 25°W–40°E longitude. Eigenvectors provide EOF modes corresponding to the eigenvalues, which indicate percentages of contribution to total variance of geopotential fields.

Thus, the largest positive and negative values demonstrate action centers on maps showing EOF modes. Daily geopotential height and temperature fields of several geopotential levels (AT500, AT700, AT850) were evaluated, as well as daily sea level pressure field. They all were separated into 4 seasonal time series.

First, EOF modes of circulation were calculated in the Atlantic European region during El Niño, La Niña and neutral phases (*Pongrácz et al.*, 1997). These ENSO phases were determined according to *Kiladis* and *Diaz* (1989). Contributions to total variance of the 1st, 2nd, and 3rd EOF modes are 21–26%, 16–23%, and 12–17%, respectively (*Table 1*). In case of neutral, El Niño and La Niña periods slightly larger portion of the total variance are explained by the 1st, the 2nd, and the 3rd EOF-modes, respectively, than in the other phases. The first six EOF modes usually explain the 80% of total variance, while the first nine EOF modes explain the 90%. In this paper EOF modes with the largest variances are shown and discussed.

Table 1. Contribution to total variance of 1st, 2nd and 3rd EOF modes and cumulative contributions to total variance in the case of different time series (%)

	1st EOF modes	2nd EOF modes	3rd EOF modes	The first 6 modes	The first 9 modes
Sea level pressure	23 - 25	18 - 23	13 - 17	78 - 81	87 - 90
850 hPa	22 - 26	18 - 21	12 - 18	79 - 82	89 - 91
700 hPa	21 - 25	17 - 19	12 - 17	78 - 81	89 - 91
500 hPa	21 - 23	16 - 17	12 - 16	75 - 78	87 - 89

In *Fig. 2* the 1st, 2nd and 3rd EOF modes of sea level pressure can be seen for the winter season. This figure and other results suggest that the 1st EOF modes do not significantly differ during the three ENSO phases (*Richman*, 1986). Nevertheless, higher EOF modes show considerable differences comparing El Niño, La Niña and neutral periods; especially, EOFs during La Niña differ from EOFs during El Niño or neutral phase. Positive and negative action centers change their positions during various ENSO phases.

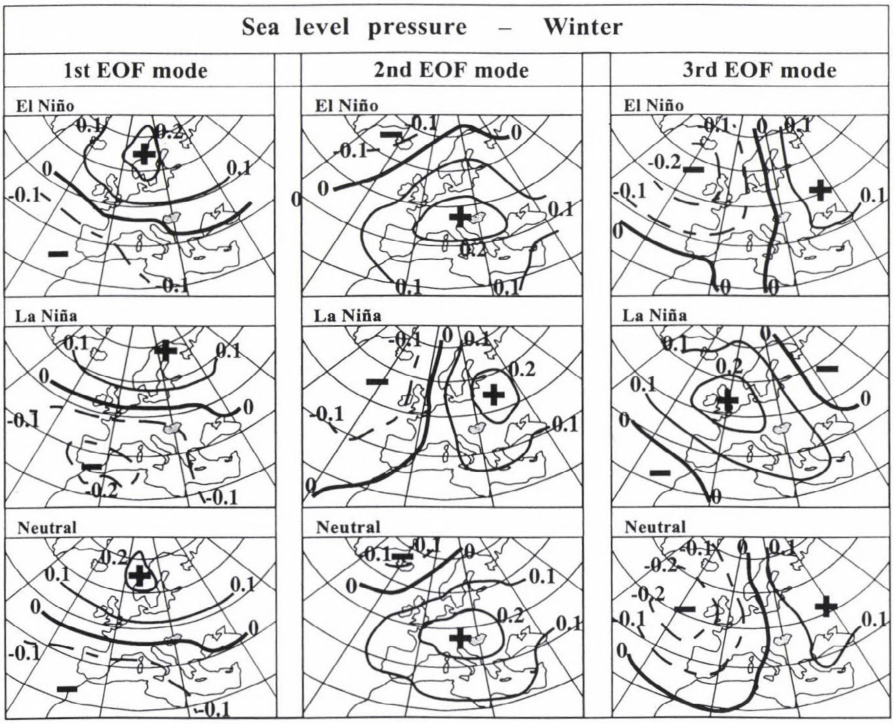

Fig. 2. 1st, 2nd and 3rd EOF modes of sea level pressure field during different ENSO phases (November–December–January, 1962–1994).

Then, EOF modes of temperature field were determined at the three geopotential levels (850 hPa, 700 hPa, 500 hPa). Their contributions to total variance of the fields are slightly smaller (by 3–4%) than in case of circulation. Since, 1st EOFs look similar during the three ENSO phases, only the 2nd EOF modes of temperature fields at 700 hPa and 850 hPa geopotential levels are shown (*Fig. 3* and *4*). The largest differences can be seen between La Niña and other ENSO phases; temperature field at 700 hPa geopotential level provides definitely more diverse structures than that at 850 hPa geopotential level. Differences between El Niño and neutral periods cannot be neglected, either,

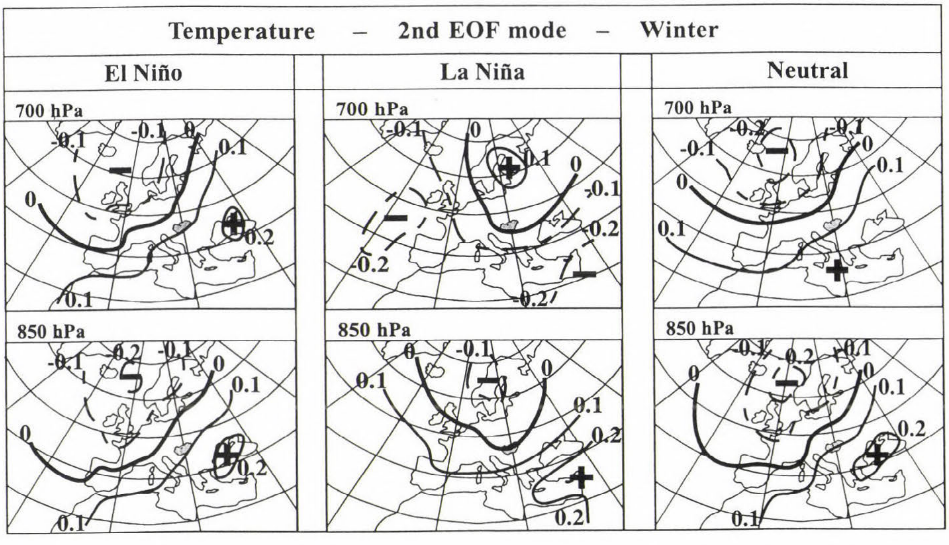

Fig. 3. 2nd EOF modes of temperature field at 700 hPa and 850 hPa geopotential levels during different ENSO phases (November-December-January, 1962–1994).

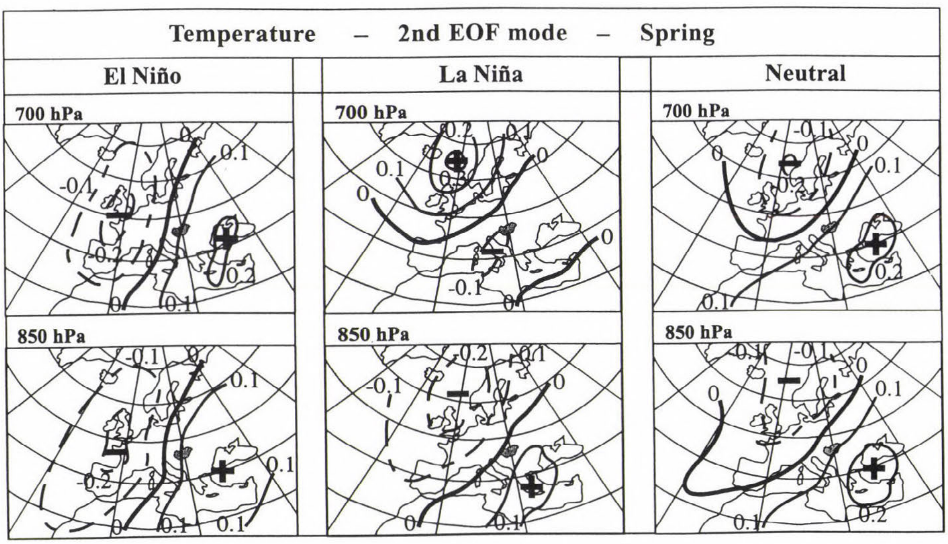

Fig. 4. 2nd EOF modes of temperature field at 700 hPa and 850 hPa geopotential levels during different ENSO phases (February-March-April, 1962–1994).

although they are smaller than in case of La Niña periods. During both season various levels provide similar structures in case of the 2nd and 3rd (not shown in this paper) EOF modes. Nevertheless, it is important to note that during La Niña events this latter statement is not true; more analysis should be made in the future hoping to get more information about the reasons.

The above results of this EOF analysis suggest that ENSO signals have considerable effects on the climate of the Atlantic European region. Further evaluation are planned to compare EOFs on several geopotential levels to the results of singular vector analysis (e.g., *Buizza* and *Palmer*, 1995; *Buizza et al.*, 1997).

Composite temperature and geopotential height anomaly fields were calculated and mapped for the different ENSO phases in the winter key-period, and also with a seasonal lag in spring. For both periods, temperature and circulation patterns present major differences during El Niño and La Niña events. As an illustration temperature anomaly fields are shown at two different geopotential levels during spring (*Fig. 5*). The results suggest that geopotential levels do not affect anomaly fields considerably. However, different ENSO phases provide reverse structures of temperature anomaly.

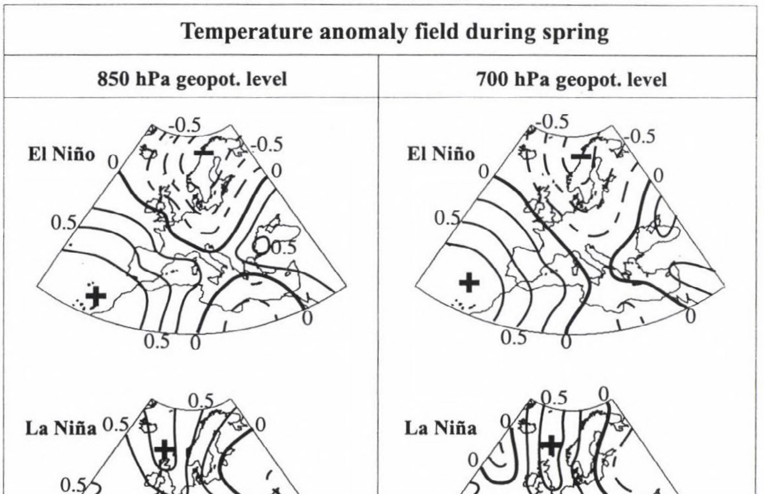

Fig. 5. Anomaly fields of temperature at 700 hPa and 850 hPa geopotential levels during different ENSO phases (February–March–April, 1962–1994).

4. ENSO related changes in regional circulation patterns

As Hungary is located in the Central European region, we focused the ENSO-related investigation to this area.

Effects of different ENSO events on regional circulation structures of the Atlantic European region were examined using the *Hess–Brezowsky* circulation types (1952, 1977). The available dataset consists of daily MCP codes from 1881 to 1997 for Western and Central Europe. To find the major components of ENSO phases on regional features of circulation, it was necessary to aggregate the original 29 HB types into groups. The characteristics of the classification are summarized and described in *Table 2*.

Table 2. Macrocirculation types defined in the Hess-Brezowsky system

Circulation type	Main flow direction	Macrosynoptic type (notation)
Zonal	West (W)	West anticyclonic (Wa) West cyclonic (Wz) Southern West (Ws) Angleformed West (Ww)
Half-meridional	Southwest (SW)	Southwest anticyclonic (SWa) Southwest cyclonic (SWz)
	Northwest (NW)	Northwest anticyclonic (NWa) Northwest cyclonic (NWz)
	Central European high (HM)	Central European high (HM) Central European ridge (BM)
	Central European low (TM)	Central European low (TM)
Meridional	North (N)	North anticyclonic (Na) North cyclonic (Nz) North, Iceland high, anticyclonic (HNa) North, Iceland high, cyclonic (HNz) British Islands high (HB) Central European Trough (TRM)
	Northeast (NE)	Northeast anticyclonic (NEa) Northeast cyclonic (NEz)
	East (E)	Fennoscandian high anticyclonic (HFa) Fennoscandian high cyclonic (HFz) Norwegian Sea – Fennoscandian high anticyclonic (HNFa) Norwegian Sea – Fennoscandian high cyclonic (HNFz)
	Southeast (SE)	Southeast anticyclonic (SEa) Southeast cyclonic (SEz)
	South (S)	South anticyclonic (Sa) South cyclonic (Sz) British Islands low (TB) Western European Trough (TRW)

One aspect for making groups was the dominant direction of air mass movements (*Bartholy* and *Pongrácz*, 1998b). According to the main air flow directions (W, SW, NW, N, NE, E, SE, S), eight different groups and two extra classes where the circulation is controlled by Central European pattern were selected. Furthermore, circulation characteristics could be another factor, thus zonal, half-meridional and meridional MCP classes were defined. Zonal MCP class includes 4 HB types, meridional MCP class consists of 18 different HB types, and the other 7 HB types compose the half-meridional MCP class. Finally, cyclonic and anticyclonic MCP classes were separated. These MCP classes containing several HB types were statistically studied, namely, their empirical relative frequencies were compared and evaluated during El Niño, La Niña and neutral periods.

First, the intensification of ENSO effects on the European macrocirculation was tested. According to our hypothesis, the effects became more intense during the last 40–50 years than they were before. This idea is supported by the comparison of relative frequencies of MCP classes in the entire time series (1881–1997) and the last 43 years (1955–1997). Furthermore, since ENSO seems to have dynamic and global circulation-related reasons (*Cane*, 1992), the macrocirculation of various areas, like the Atlantic European region, must be affected by the intensification. The changes in frequencies of MCP classes characterized by their main direction were compared during the last 117 years (1881–1997) and the last 43 years (1955–1997) during El Niño and La Niña phases in the key ENSO periods, winter and spring (*Fig. 6*). Our results suggest that relative frequencies of MCP classes changed considerably greater (4–5 times in some cases) during the last 43 years than during the longer 117 year long period. Furthermore, in general, both in winter and spring the changes in frequencies of MCP classes occurred with opposite sign during El Niño and La Niña phases. Note that the frequency of MCP classes with eastern flow decreased during La Niña winters (North-Eastern flow: by 78%, Eastern flow: by 42%, South-Eastern flow: by 77%). While La Niña springs can be characterized by enhanced frequency of eastern MCP classes (especially North-Eastern flow), El Niño springs were dominated by diminished frequency of these MCP classes. Finally, the occurrence of the North-Western types increased by 108% during La Niña winters and by only 20% during El Niño winters.

Next, changes in occurrences of the three different circulation characteristics were evaluated during ENSO phases. *Fig. 7* shows how the relative frequency of zonal, half-meridional and meridional MCP classes changed during El Niño and La Niña events comparing the four seasons of the last 43 years. Major changes occurred in winter in case of La Niña phase, namely, meridional circulation decreased while zonal circulation increased by about 21–22%. The greater effect of ENSO phenomema on circulation of the autumn season occurred during El Niño periods: frequency of zonal MCP classes decreased by 22%, and meridional MCP classes increased by 28%. Both El Niño and La

Niña phases affected the circulation of Western and Central Europe in spring: zonal MCP classes increased considerably during El Niño periods, while half-meridional MCP classes decreased and meridional MCP classes increased during La Niña phase.

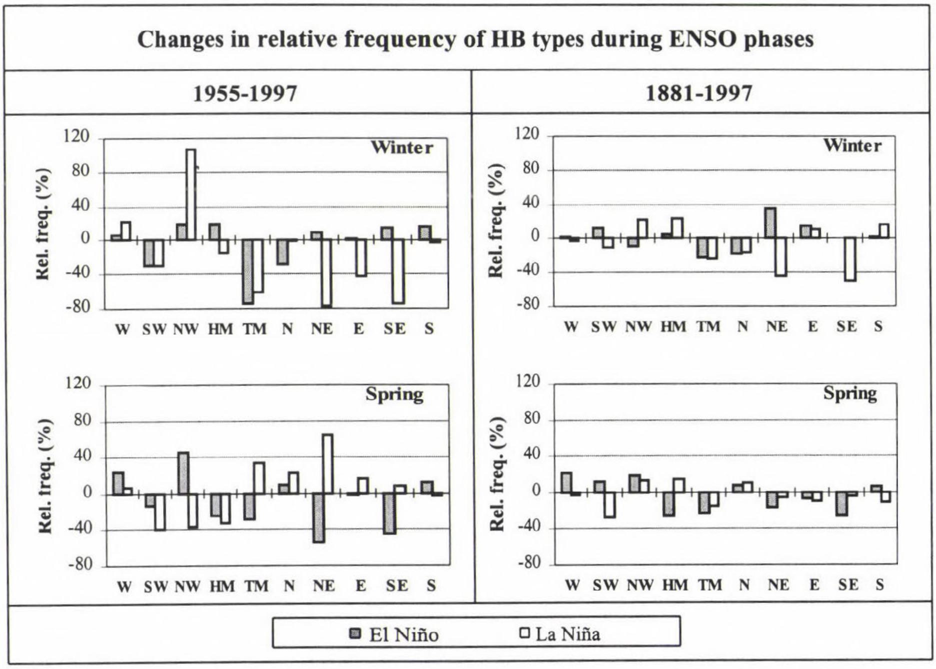

Fig. 6. Changes in relative frequency of MCP classes during ENSO phases in winter and spring in the last 117 years and 43 years.

The major (frequently exceeding 20%) changes in occurrence of MCP classes suggest significant changes in regional temperature and precipitation patterns.

Finally, we studied cyclonic and anticyclonic MCP classes (*Fig. 8*). Effects of ENSO phases on frequencies of cyclonic and anticyclonic circulation patterns in winter and summer were not significant. The largest changes occurred during spring: cyclonic dominance increased and anticyclonic dominance decreased by 28% during El Niño events in the last 43 years. La Niña periods had opposite but slightly smaller effect on the relative frequency of cyclonic and anticyclonic MCP classes. Changes in autumn are still considerable and contrary but weaker than in spring, especially during El Niño years.

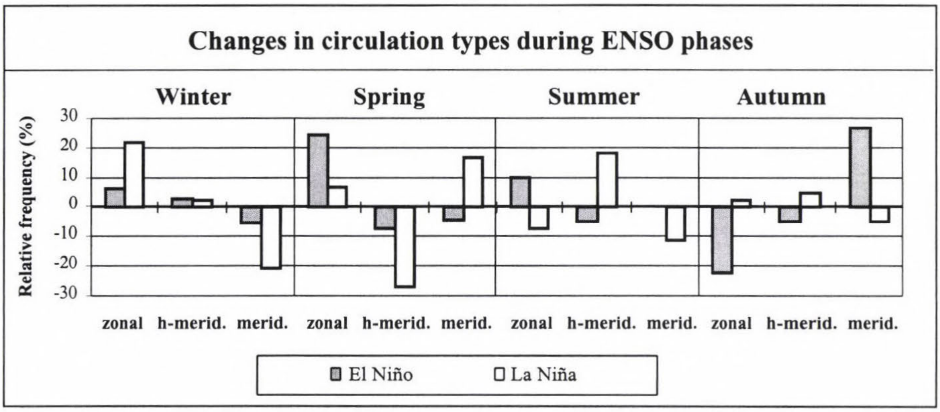

Fig. 7. Changes in circulation types during different ENSO phases (1955–1997).

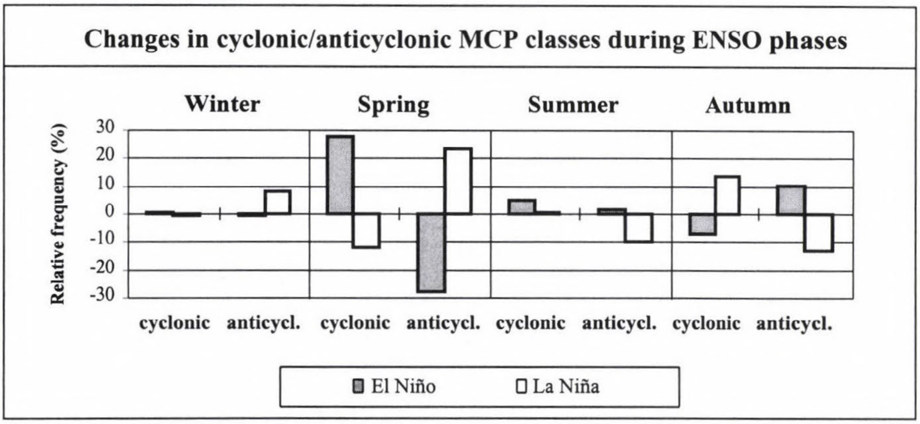

Fig. 8. Changes in frequencies of cyclonic/anticyclonic circulation patterns during different ENSO phases (1955–1997).

Relative frequencies of cyclonic and anticyclonic *Péczely*-MCP classes (1961) which provide circulation features focused mainly on the Carpathian Basin show similar changes during El Niño events: the largest changes occurred in spring (*Fig. 9*). Since HB types consider larger area than Péczely types the changes are greater, as well. During La Niña events both cyclonic and anticyclonic MCP classes (in the Péczely system) possess minor changes in spring and autumn. However, in the winter and the summer months relative frequency changes vary between 10–25% during La Niña events, occurrences of cyclonic MCP classes changed more considerably than those of anticyclonic MCP classes.

Analysis presented in this paper show that macrocirculation patterns significantly differ in the Atlantic European region during El Niño and La Niña periods.

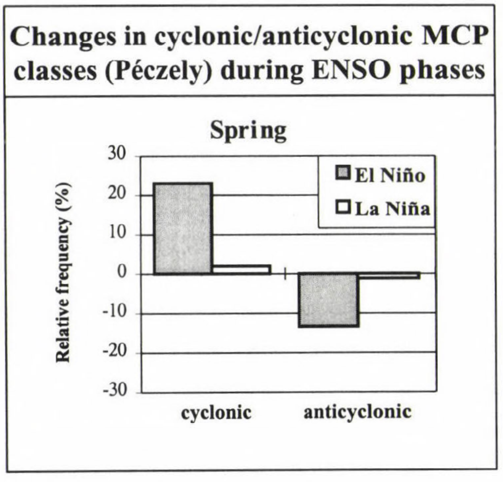

Fig. 9. Changes in frequencies of cyclonic/anticyclonic circulation patterns (defined by Péczely) during different ENSO phases (1955–1996).

5. ENSO related regional climate analysis

In this part of our study the most anomalous periods of the year were selected and investigated for the different ENSO episodes. In order to fulfill this task standard deviations of regional monthly temperature and precipitation values were calculated besides the average anomalies (*Fig. 10*). Large negative temperature anomalies were present during El Niño winters (from December to March), while warmer conditions were more likely to occur in May-June during La Niña phase. La Niña springs (from February to April) are indicated by colder climate conditions. Furthermore, our analysis suggest that La Niña episodes affect the regional monthly precipitation more than El Niño. Large negative precipitation anomalies occurred in October and November, and wetter conditions were likely to be observed in April and August.

These results are mostly supported by our findings when monthly values of standard deviation were taken into consideration. In some cases, for example during El Niño episodes, precipitation anomalies in October are close to 0; on the other hand, the standard deviation is one of the largest during El Niño years. The explanation can be clear, namely, the large anomalies with different signs eliminate one another. Furthermore, average precipitation anomaly is quite large with little deviation during La Niña episodes. The corresponding distributions of anomalies are presented in *Fig. 11* (right panel). Note the different histograms and fitted curves for the different ENSO phases; large positive anomalies (> 40 mm) disappeared during La Niña and increased during El Niño. Chi-square test for homogeneity was carried out pairwise and the results show differing empirical distributions at 0.05 significance level in each pair.

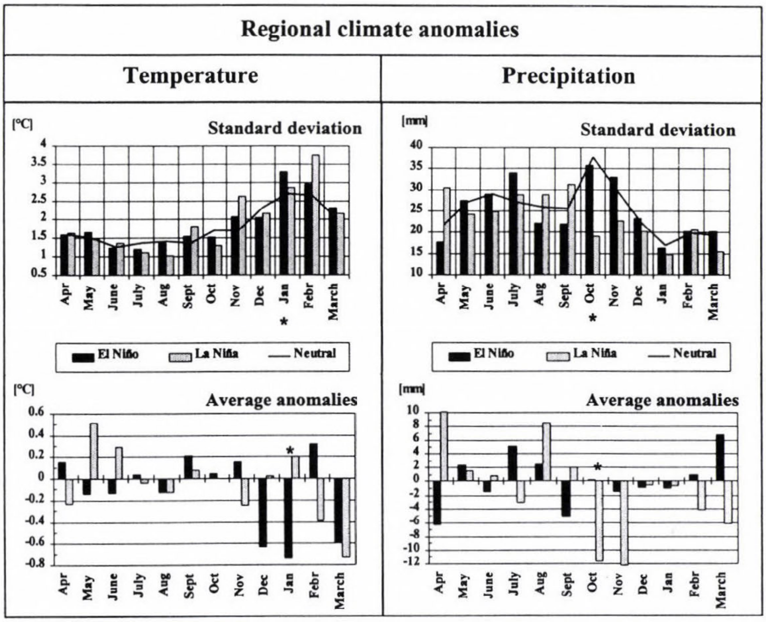

Fig. 10. Standard deviation and average of anomalies of regional climate parameters (temperature and precipitation, based on 16 Hungarian meteorological stations) during different ENSO phases.

Another example can be the temperature anomalies in January: the largest negative anomaly occurred on average during El Niño episodes with high standard deviation, while La Niña can be characterized by slightly less standard deviation, so anomalies eliminate each other (similarly to the precipitation in October during El Niño). Thus, histograms of January temperature anomalies during El Niño, La Niña and neutral phases show significantly different distributions (Fig. 11, left panel): colder than average conditions are more likely to occur during El Niño than during neutral years, while extremely cold and warmer than average conditions occurred during La Niña. Similarly to the precipitation case, chi-square tests for homogeneity show differing empirical distributions at 0.05 significance level pairwise.

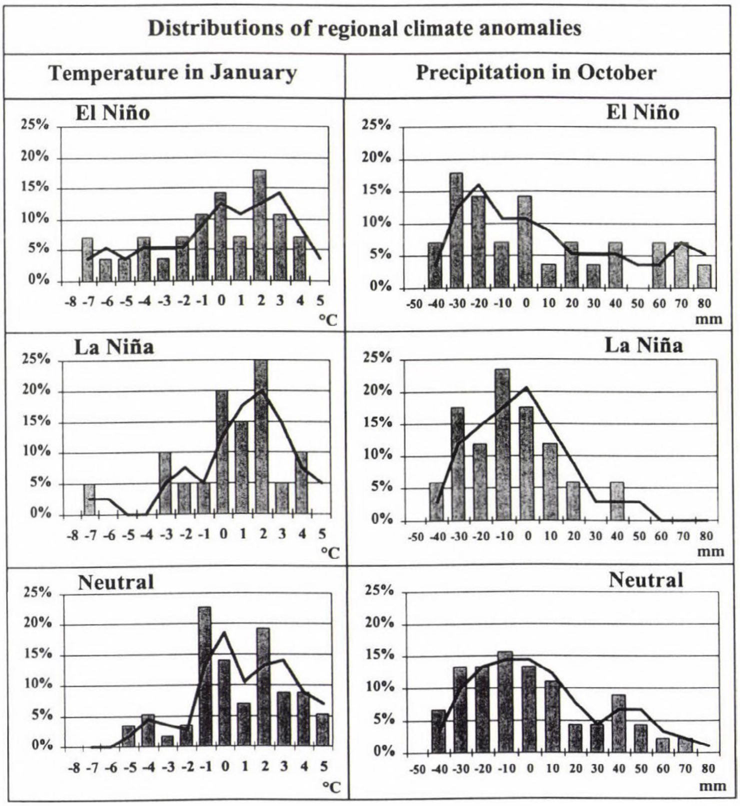

Fig. 11. Empirical distributions of regional temperature (in January) and precipitation anomalies (in October) during ENSO phases.

Relative frequencies of outliers of regional climate parameters were determined during different ENSO phases in each month (*Table 3*). A temperature or precipitation anomaly was considered as an outlier if it is out of the [$-\sigma;\sigma$] or the [$-1.5\sigma;1.5\sigma$] interval. In the case of precipitation the wider interval results less (half-third) negative outlier frequencies than positive ones since the distribution of precipitation cannot be estimated by normal but gamma distribution skewed in positive anomalies (*Wilks*, 1995).

Table 3. ENSO related frequencies (%) of regional temperature and precipitation outliers (considering [-σ;σ] and [-1.5σ;1.5σ] intervals)

Climate variable	ENSO phase	[-σ;σ]		[-1.5σ;1.5σ]	
		+	–	+	–
Temperature	El Niño	15.9	17.7	6.2	9.1
	La Niña	15.9	15.9	6.8	6.8
	Neutral	15.7	14.7	5.8	6.9
Precipitation	El Niño	17.6	14.3	8.9	3.6
	La Niña	14.7	16.2	9.8	3.9
	Neutral	15.5	15.1	8.8	3.4

Although the differences in annual average frequencies are small in general, the monthly values differ considerably (*Fig. 12* and *13*). However, El Niño episodes show the largest differences compared to other ENSO phases, both temperature and precipitation anomalies. Fig. 12 presents outlier occurrences of regional precipitation during ENSO episodes; La Niña years provide more diverse annual frequency distribution than El Niño: the summer half-year (April through September) is dominated by positive outliers, while negative outliers were more likely to occur (18–24%) during the winter half-year (from September to March). Positive outliers were slightly more frequent in El Niño years than negative outliers overall. Large differences occurred between positive and negative outlier frequencies, however, e.g., in August and March.

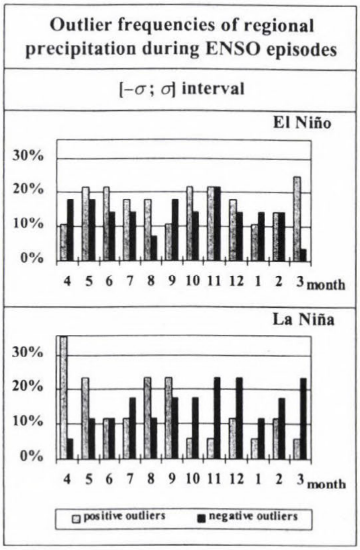

Fig. 12. Outlier frequencies of regional precipitation anomalies during ENSO episodes.

Fig. 13 compares the outlier frequencies of regional temperatures during ENSO phases considering [-σ;σ] and [-1.5σ;1.5σ] intervals. Outliers of the [-σ;σ] interval can be defined as "not average" values, while outliers of [-1.5σ;1.5σ] as "extreme". Some major differences can be noticed in Fig. 13:

1. Neutral phase provides less diverse annual variability than El Niño or La Niña years, in both intervals.
2. While negative outliers were dominant in February-March-April during La Niña episodes in case of [-σ;σ] interval, the entire winter half-year was dominated by extremely cold conditions.
3. Very high and steady frequencies of positive temperature outliers were present for both intervals in May and June during La Niña.
4. In both intervals during El Niño the negative outliers were dominant in the December-March period.

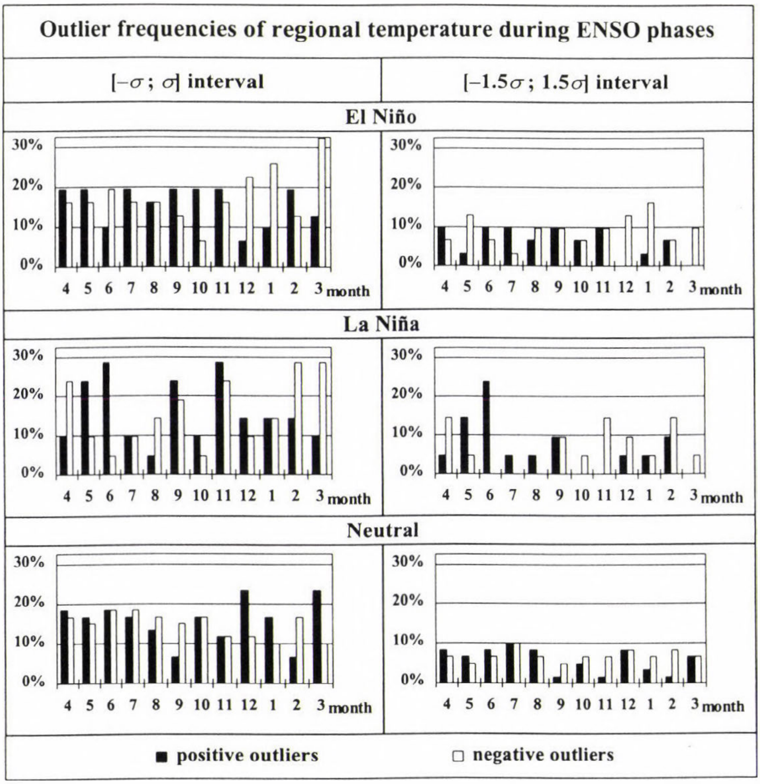

Fig. 13. Comparing outlier frequencies of regional temperature anomalies during ENSO phases.

6. *Joint ENSO and NAO forcing on regional climate*

While ENSO are mostly tropical phenomena, the North Atlantic Oscillation (NAO) is one of the large-scale modes of climate variability on extratropics that is most pronounced during winter (*Wallace* and *Gutzler*, 1981). As the name indicates, the NAO is centered on the North Atlantic Ocean basin. The Icelandic low-pressure center tends to be lower than normal, while the high-pressure center near the Azores tends to be higher than normal and vice versa (*Barnston* and *Livezey*, 1987). Both ENSO and NAO are oscillations with different amplitudes and they have some quasi-periodic features. In this part of our research we examined their interference and their joint regional impact on temperature and precipitation observed in the Carpathian Basin with a teleconnection study.

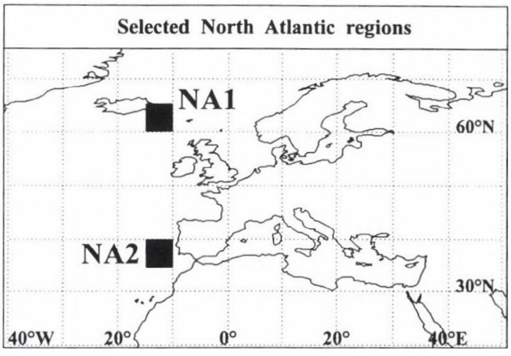

Fig. 14. Key regions for NAO index. NA1: 65°–60°N, 15°–10°W; NA2: 40°–35°N, 15°–10°W.

NAO was represented by the time series of the difference between SST values averaged on two selected regions of the North Atlantic ocean (*Fig. 14*). Locations of sectors NA1 (eastward from Iceland) and NA2 (Azori Islands) are traditionally used for investigating the general characteristics of NAO (e.g., *Hurrell*, 1995). In these sectors spatial average of SST values were calculated for each month, 1950–1998. Annual teleconnection analysis was carried out on this NAO index and on temperature/precipitation time series for the Central European region during different ENSO phases. In order to consider the wave effect of the oscillations, several months pre- and post-lag were included in the study. Although lag correlation coefficients were calculated for the entire [–12 months; +12 months] interval we present 0–9 month pre-lag correlations here since this period can be considered physically reasonable (*Glantz et al.*, 1991). *Fig. 15* presents lag correlation coefficients between NAO index (based on SST) and regional climate parameters observed in December and February during ENSO episodes. These two months are shown here because NAO is the most pronounced during the winter season. Large differences can be seen in correlations between NAO and meteorological characteristics during El Niño and La Niña periods. In general, absolute values of correlation coefficients are higher during La Niña than during El Niño years; it can be partly explained by less La Niña events in the period studied here than El Niño events. However, since other results of our analysis provided similar conclusions, La Niña years undoubtedly tend to affect the regional climate parameters more than El Niño episodes. Furthermore, note the changing signs of strong correlations, especially temperature in December and precipitation in February during La Niña events. Our study suggest that NAO and regional climatology show considerable lag (1–3 months) since simultaneous NAO index and regional temperature/precipitation values do not result in the strongest correlations.

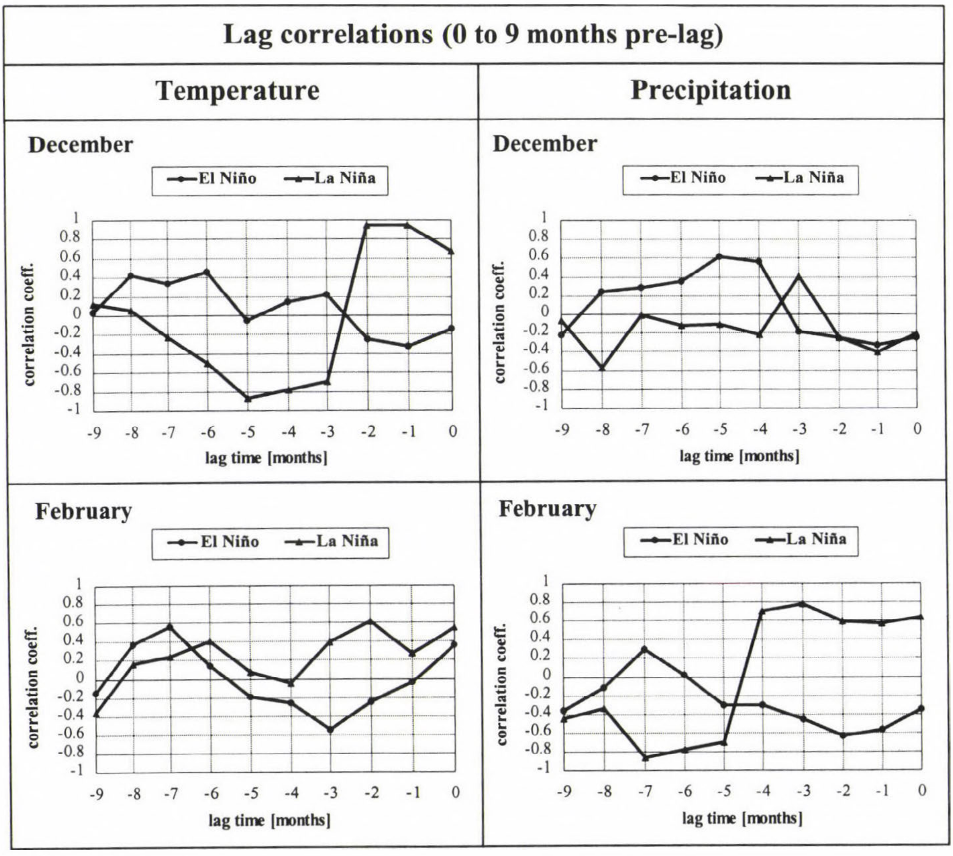

Fig. 15. Lag correlations between NAO index and regional climate parameters during El Niño and La Niña periods.

7. Conclusions

As a summary, it can be concluded that correlation analysis, EOF and other classification techniques seem to be an appropriate methodology for evaluating the impact of interannual oscillations (e.g., ENSO, NAO) on regional climate. Analyzing geopotential height fields, MCPs and global SST fields we did get stronger ENSO signals for the Central European region than in the case of secondary derived quantities (e.g., time series of SOI).

EOF modes of tropospheric circulation and temperature variability differ during the different ENSO episodes: positive and negative action centers change their positions in the case of 2nd and 3rd modes. The largest differences occurred between La Niña and other ENSO phases.

Temperature anomaly fields show reverse structure in the Atlantic European region during El Niño and La Niña episodes.

Considerable changes can be found in MCP empirical frequencies during El Niño and La Niña periods: changes in circulation character, in cyclonic/anti-cyclonic dominancy and in ENSO phase intensity. The largest changes in zonal circulation types occurred during El Niño springs and La Niña winters. Frequency of meridional MCP classes shows large decreases during El Niño autumns and La Niña winters, while half-meridional MCP classes decreased the most during La Niña springs. Changes in empirical frequencies of cyclonic and anticyclonic MCP classes are the most dominant in El Niño springs.

Outlier and anomaly statistics of regional precipitation and temperature differ considerably during El Niño and La Niña episodes. Specifically, La Niña autumns are dominated by large negative anomalies in precipitation, while wet conditions occur in La Niña April. Furthermore, cold conditions are present during El Niño winters and positive temperature anomalies in La Niña May-June.

Joint ENSO and NAO forcing seemed to affect regional climate parameters, especially during La Niña episodes. The 1–3 months lag period resulted in the most dominant relationship.

Acknowledgements—Research leading to this paper has been supported by the *Hungarian National Science Research Foundation* under grants T26629, T25803 and T15707, also, by the *Hungarian Higher Education Support Program* under grant FKFP-0193. Furthermore, the authors thank to the three unknown referees for their useful comments.

References

Barnston, A.G. and *Livezey, R.E.*, 1987: Classification, seasonality and persistence of low-frequency atmospheric circulation patterns. *Mon. Wea. Rev. 115*, 1083–1126.

Bartholy, J. and *Pongrácz, R.*, 1998a: Comparing ENSO related PNA and NAO signals. *Presentation on 7th International Meeting on Statistical Climatology*. Whistler, British Columbia, Canada, May 25-29, 1998.

Bartholy, J. and *Pongrácz, R.*, 1998b: Comparing Signals of ENSO and NAO for Selected Regions of the Northern Hemisphere. *Annales Geophysicae, Suppl. Vol. 16,* C698.

Buizza, R. and *Palmer, T.N.*, 1995: The singular-vector structure of the atmospheric global circulation. *J. Atmos. Sci. 52*, 1434–1472.

Buizza, R., Gelaro, R., Molteni, F. and *Palmer, T.N.*, 1997: The impact of increased resolution on predictability studies with singular vectors. *Quart. J. Roy. Meteorol. Soc. 123*, 1007–1033.

Cane, M.A., 1992: Tropical Pacific ENSO Models: ENSO as a mode of the coupled system. In *Climate System Modeling* (ed.: *K.E. Trenberth*). Academic Press, New York. 583-614.

Dept. of Atmospheric Sciences, Univ. of Washington and *Data Support Section, NCAR,* 1996: *NMC Grid Point Data Set* (version III).

Diaz, H.F. and *Markgraf, V.* (eds.), 1992: *El Niño: Historical and Paleoclimatic Aspects of the Southern Oscillation*. Cambridge University Press, New York.

Glantz, M.H., Katz, R.W. and *Krenz, M.*, 1987: *Climate Crisis: The Societal Impacts Associated with the 1982-83 Worldwide Climate Anomalies*. NCAR, Boulder.

Glantz, M.H., Katz, R.W. and *Nicholls, N.* (eds.), 1991: *Teleconnections Linking Worldwide Climate Anomalies*. Cambridge University Press, New York.

Hess, P. and *Brezowsky, H.*, 1952: Katalog der Grosswetterlagen Europas. *Berichte das Deutschen Wetterdienstes in der US Zone. 33*. Bad Kissingen.

Hess, P. and *Brezowsky, H.*, 1977: Katalog der Grosswetterlagen Europas. *Berichte das Deutschen Wetterdienstes. 113*. Offenbach.

Hurrell, J.W., 1995: Decadal trends in the North Atlantic oscillation regional temperatures and precipitation. *Science 269*, 676–679.

Joseph, P.V., Eischeid, J.K. and *Pyle, R.J.*, 1994: Interannual variability of the onset of the Indian summer monsoon and its assotiation with atmospheric features, El Niño, and sea surfaces temperatures anomalies. *J. of Climate 7*, 81–105.

Károssy, Cs., 1994: Péczely's classification of macrosynoptic types and the catalogue of weather situations (1951-1992). In *Light trapping of insects influenced by abiotic factors. Part I.* (ed.: *L. Nowinsky*). Savaria University Press, Szombathely, 117-130.

Károssy, Cs., 1997: Catalogue of Péczely's macrosynoptic weather situations (1993-1996). In *Light trapping of insects influenced by abiotic factors. Part II.* (ed.: *L. Nowinsky*). Savaria University Press, Szombathely, 159-162.

Kiladis, G.N. and *Diaz, H.F.*, 1989: Global climatic anomalies associated with extremes of the Southern Oscillation. *J. of Climate 2*, 1069–1090.

Lenne, R.L., 1970: *The NMC Octagonal Grid.* NCAR, Boulder, Colorado.

NOAA, 1997: *SST database.* ftp://nic.fb4.noaa.gov/ocean/clim1.

Nicholls, N. and *Kariko, A.*, 1993: East Ausrtralian rainfall events: interannual variations trends and relationships with the Southern Oscillation. *J. of Climate 6*, 1141–1152.

Péczely, Gy., 1961: *Characterising the Meteorological Macrosynoptic Situations in Hungary* (in Hungarian). Orsz. Meteorol. Int. Kisebb Kiadványai 32, Budapest.

Péczely, Gy., 1983: *Catalogue of Macrosynoptic Situations of Hungary in Years 1881–1983* (in Hungarian). Orsz. Meteorol. Szolg. Kisebb Kiadványai 53, Budapest.

Philander, S.G.H., 1990: *El Nino, La Nina, and the Southern Oscillation*. Academic Press, New York.

Pongrácz, R., Bartholy, J., Matyasovszky, I. and *Bogárdi, I.*, 1997: Relations between El Nino/La Nina Events and Large-scale Circulation Variations. *Annales Geophysicae, Suppl. Vol. 15*, C476.

Reynolds, W.M. and *Smith, T.M.*, 1994: Improved global sea surface temperature analyses. *J. of Climate 4, 929–948.*

Richman, M.B., 1986: Rotation of principal components. *J. Climatol. 6, 293–335.*

von Storch, H., 1995: Spatial patterns: EOFs and CCA. In *Analysis of Climate Variability* (eds.: *H. Storch* and *A. Navarra*. Springer-Verlag, Berlin, 227–257.

Wallace, J.M. and *Gutzler, D.S.*, 1981: Teleconnections in the geopotential height field during the Northern Hemisphere. *Mon. Wea. Rev. 109*, 784–812.

Wilks, D.S., 1995: *Spatial Methods in the Atmospheric Sciences*. Academic Press, London.

IDŐJÁRÁS
Quarterly Journal of the Hungarian Meteorological Service
Vol. 104, No. 1, January–March 2000, pp. 21–41

The land-surface model family SURFMOD

Ferenc Ács[1], **Michael Hantel**[2] and **Johann Unegg**[2]

[1]*Department of Meteorology, Eötvös Loránd University, H-1117 Budapest, Pázmány Péter sétány 1/A, Hungary, E-mail: acs@caesar.elte.hu*

[2]*University of Vienna, Hohe Warte 38, A-1190 Vienna, Austria*

(Manuscript received 9 April 1999; in final form 5 January 2000)

Abstract—The land-surface model family SURFMOD (**Sur**face **F**lux **Mod**el), designed jointly at the Universities of Eötvös Loránd and Vienna, is briefly considered. The attention is paid to the comparison of the most complex Psi1-PROGSURF (**Prog**nosis of **Sur**face **F**luxes) and the simpliest Pm-PTSURF (**P**riestley **T**aylor **Sur**face **F**luxes) modes. Pm-PTSURF is not only simple with respect to Psi1-PROGSURF but also it is extremely simple with respect to other biophysical models.

In the preliminary tests on the Cabauw data set it has been shown that

- both modes reproduce satisfactorily the observed annual mean values, seasonal changes and the instantaneous values of turbulent and water fluxes,
- Pm-PTSURF is able to capture—though its extreme simplicity—the governing processes at Cabauw site: the potential evapotranspiration $E(\theta_S)$ governed by atmospheric conditions and
- the simulation results of Psi1-PROGSURF and Pm-PTSURF do not deviate from each other in a great extent since there is no great deviation between their $E(\theta_S)$ parameters.

The results obtained are relevant to the Project for Intercomparison of Land-Surface Parameterization Schemes. SURFMOD is an effective tool in performing comparative studies. Presently it is also used to specify the boundary conditions for the software DIAMOD which is routinely used at the University of Vienna to diagnose the convective fluxes in the free atmosphere.

Key-words: model family, intercomparison of models, complexity versus simplicity.

1. Introduction

The land-surface model family SURFMOD, designed jointly at the Universities of Vienna and Eötvös Loránd, consists of three model family members (see *Table 1*): the PROGSURF (**Prog**nosis of **Sur**face **F**luxes), the PMSURF (**P**enman-**M**onteith **Sur**face **F**luxes) and the PTSURF (**P**riestley **T**aylor **Sur**face

Fluxes). PROGSURF is based on the work of Budapest-Vienna working group (*Ács*, 1995; *Ács et al.*, 1996) and on the previous work of *Ács et al.* (1991) and *Ács* (1994). The most complete description and analysis of PROGSURF is given in *Ács* and *Hantel* (1998a). On the basis of this publication we can qualify PROGSURF as PILPS model[1]. The complete documentation of PROGSURF's source code in a form of a User Manual is also given in *Ács et al.* (1998a). This User Manual enables us to use the PROGSURF not only for scientific but also for educational purposes.

Table 1. SURFMOD family members and modes and their main characteristics

SURFMOD family members and modes			
Family member	Mode	Description	Details
PROGSURF	Psi1	F_{ad} is parameterized fully and F_{ma} by leaf water potential	*Ács* and *Hantel* (1998a)
	Psi2	$F_{ad} \equiv 1$ and F_{ma} is parameterized by leaf water potential	*Ács* and *Hantel* (1998a)
	Theta	F_{ad} is parameterized fully	*Ács* and *Hantel* (1998a) *Ács* and *Hantel* (1998b)
	Combi-nation	*LE* is parameterized by PM combination equation and *H* by aerodynamic formula	*Ács* (2000)
PMSURF	Ps1	F_{ma} is parameterized by leaf water potential	*Ács* and *Hantel* (1999)
	Theta	F_{ma} is parameterized by soil moisture	
PTSURF	Prog	*LE* is parameterized by Priestley-Taylor formula and *H* by aerodynamic formula	
	Pm	*LE* is parameterized by Priestley-Taylor formula and *H* as the residual term from the energy balance equation	

Symbols: F_{ad} – atmospheric demand function in the canopy resistance parameterization, F_{ma} – moisture availability function in the canopy resistance parameterization, *LE* – latent heat flux and *H* – sensible heat flux

To investigate the model optimizing problems in scope of PILPS, we replaced PROGSURF's aerodynamic formulas for turbulent flux parameterization by the Penman-Monteith approach (*Monteith*, 1965; *Dolman*, 1993; *Monteith*, 1995). This reformulation of PROGSURF occured in 1997; the model

[1] Project for Intercomparison of Land-Surface Parameterization Schemes

model obtained (referred to as PMSURF) can be treated either as a new model or as a specific model version of PROGSURF. We chose the latter case. A detailed description of PMSURF in comparison to PROGSURF is presented in *Ács* and *Hantel* (1999). Analogously to PROGSURF, there is also a User Manual for PMSURF (*Ács et al.*, 1998b). PTSURF is constructed at the end of 1998 and at the beginning of 1999. It can be treated as a Priestley-Taylor formula based PROGSURF or PMSURF. The only difference between PROGSURF/PMSURF and PTSURF is in the parameterization of latent heat flux. PROGSURF or PMSURF uses the gradient formula or the Penman-Monteith's formula while PTSURF uses the Priestley-Taylor formula. PTSURF's User Manual is not available, but it can be treated as a documented model since its many parts are very similar to the PROGSURF and/or PMSURF.

Two basic facts are valid concerning PILPS:

- the scatter of results obtained by different land-surface parameterization schemes is enormously great for all tested climate regimes (*Shao* and *Henderson-Sellers*, 1996), and
- the analysis of the causes of deviations are sporadic or completely missing.

In this study, using SURFMOD as an effective tool for performing comparative studies, we try to contribute to PILPS considering following objectives:

1. We describe, validate and compare the most complex (Psi1-PROGSURF) and the simpliest (Pm-PTSURF) modes of SURFMOD. The models are run in off-line mode using Cabauw data set.
2. We show for the Cabauw data set that the very simple Pm-PTSURF mode is capable to capture the governing processes and even it yields the most favorable results with respect to some most complex SURFMOD modes.
3. We show the reasons why the very simple Pm-PTSURF can reproduce the main effects.

2. The SURFMOD model family

SURFMOD's input data are: model constants, initial values of prognostic variables (shortly referred to as initial conditions), variable land-surface parameters and atmospheric forcing data. SURFMOD's outputs are: instantaneous and daily, monthly and yearly averaged energy and water fluxes. SURFMOD's family members and modes can use different initial conditions and atmospheric forcing data. An overview of used initial conditions and atmospheric forcing data is given in *Table 2a* and *2b*, respectively. We see that the modes of family member PROGSURF use all listed initial conditions (altogether 7) and all atmospheric forcing data excepted T_S (altogether 5), whereas the Pm-PTSURF mode needs the smallest number of initial (4 in all) and forcing data (4 in all).

Table 2a. SURFMOD family members and modes and their initial conditions

Initial conditions of SURFMOD								
Family member	Mode	T_{vg}	T_{dg}	M_v	θ_{l1}	θ_{s1}	θ_2	θ_3
PROGSURF	Psi1	used	used	used	used	used	used	used
	Psi2	used	used	used	used	used	used	used
	Theta	used	used	used	used	used	used	used
	Combin.	used	used	used	used	used	used	used
PMSURF	Psi1	not used	not used	used	used	not used	used	used
	Theta	not used	not used	used	used	not used	used	used
PTSURF	Prog	used	used	used	used	used	used	used
	Pm	not used	not used	used	used	not used	used	used

Symbols: T_{vg} – vegetation-ground temperature, T_{dg} – deep-ground temperature, M_v – water stored in the vegetation layer, θ_{l1} – liquid moisture content in the 1st soil layer, θ_{s1} – solid moisture content in the 1st soil layer, θ_2 – moisture content in the 2nd soil layer and θ_3 – moisture content in the 3rd soil layer

Table 2b. SURFMOD family members and modes and their atmospheric forcing data

Atmospheric forcing data of SURFMOD							
Family member	Mode	T_r	e_r	V_r	S	R_a	T_S
PROGSURF	Psi1	used	used	used	used	used	not used
	Psi2	used	used	used	used	used	not used
	Theta	used	used	used	used	used	not used
	Combin.	used	used	used	used	used	not used
PMSURF	Psi1	used	used	used	used	used	used
	Theta	used	used	used	used	used	used
PTSURF	Prog	used	not used	used	used	used	not used
	Pm	used	not used	not used	used	used	used

Symbols: T_r – air temperature, e_r – air humidity, V_r – wind speed, S – solar radiation, R_a – downward atmospheric radiation and T_S – ground surface temperature

SURFMOD's basic features and the main differences between its family members and modes are comparatively presented in the form of tables. The differences are separately presented for prognostic equations, heat fluxes and the relevant parameters in *Table 3, 4* and *5*, respectively. There are no differences in the prediction of soil moisture and vegetation water storage. All modes apply the Richards' equation for soil moisture prediction (*Ács* and

Table 3. SURFMOD family members and modes and their prognostic equations

Prognostic equations of SURFMOD				
Family member	Mode	Water storage on vegetation	Temperature	Soil moisture
PROGSURF	Psi1	budget equation	force-restore method	Richard's equation
	Psi2	budget equation	force-restore method	Richard's equation
	Theta	budget equation	force-restore method	Richard's equation
	Combin.	budget equation	force-restore method	Richard's equation
PMSURF	Ps1	budget equation	–	Richard's equation
	Theta	budget equation	–	Richard's equation
PTSURF	Prog	budget equation	force-restore method	Richard's equation
	Pm	budget equation	–	Richard's equation

Hantel, 1998b) and the mass budget equation for water storage in vegetation layer. Temperature is predicted by the force-restore method or not predicted at all. Then the Penman-Monteith concept is applied where there is no parameterization of soil water freezing or melting.

Table 4. SURFMOD family members and modes and their heat flux parameterizations

SURFMOD heat fluxes				
Family member	Mode	Latent heat flux	Sensible heat flux	Ground heat flux
PROGSURF	Psi1	aerodynamic formula	aerodynamic formula	conduction equation
	Psi2	aerodynamic formula	aerodynamic formula	conduction equation
	Theta	aerodynamic formula	aerodynamic formula	conduction equation
	Combination	Penman-Monteith equation	aerodynamic formula	conduction equation
PMSURF	Ps1	Penman-Monteith equation	residual from energy balance equation	percentage of net radiation
	Theta	Penman-Monteith equation	residual from energy balance equation	percentage of net radiation
PTSURF	Prog	Priestley-Taylor equation	aerodynamic formula	conduction equation
	Pm	Priestley-Taylor equation	residual from energy balance equation	percentage of net radiation

There are also great differences in the heat flux parameterizations (Table 4). Latent heat flux is parameterized either by the aerodynamic formula or by the Penman-Monteith formula or by the Priestley-Taylor formula. Sensible heat flux is calculated either by the aerodynamic formula or as a residiual term from the energy balance equation (*Ács* and *Hantel*, 1999). Ground heat flux is calculated either at 10 cm depth G_1 or at the ground surface G_0. G_1 is parameterized in conjunction with the force-restore method by a heat conduction equation while G_0 is estimated as the percentage of net radiation.

Table 5. SURFMOD family members and modes and their parameters representing soil and atmospheric state

SURFMOD parameters representing soil and atmospheric state				
Family member	Mode	Aerodynamic transfer	Available soil moisture	Atmospheric demand
PROGSURF	Psi1	resistance concept	F_{ma} is parameterized by leaf water potential	$0 < F_{ad} \leq 1$
	Psi2	resistance concept	F_{ma} is parameterized by leaf water potential	$F_{ad} \equiv 1$
	Theta	resistance concept	F_{ma} is parameterized by soil moisture	$0 < F_{ad} \leq 1$
	Combi-nation	resistance concept	F_{ma} is parameterized by leaf water potential	$0 < F_{ad} \leq 1$
PMSURF	Ps1	resistance concept	F_{ma} is parameterized by leaf water potential	$0 < F_{ad} \leq 1$
	Theta	resistance concept	F_{ma} is parameterized by soil moisture	$0 < F_{ad} \leq 1$
PTSURF	Prog	resistance concept	moisture availability function β	$E(\theta_S)$
	Pm	–	moisture availability function β	$E(\theta_S)$

Symbols: F_{ad} – atmospheric demand function in the canopy resistance parameterization, F_{ma} – moisture availability function in the canopy resistance parameterization and $E(\theta)_S$ – potential evapotranspiration

SURFMOD family members and modes differ also in the parameterizations of some relevant parameters. The applied parameterizations for aerodynamic transfer, available soil moisture and atmospheric demand are reviewed in Table 5. The aerodynamic transfer is parameterized using the resistance concept with the Monin-Obukhov similarity theory or not parameterized at all. Then the Penman-Monteith concept with the Priestley-Taylor formula is applied. The effect of available soil moisture upon transpiration is expressed either via stress function F_{ma} or by soil moisture availability function β. F_{ma} can be parameterized by both the soil moisture content and the leaf water potential (*Ács* and *Hantel,* 1998b). The atmospheric demand is parameterized via stress function F_{ad} or via estimation of potential evapotranspiration. F_{ad} can vary between 0 and 1 or it is equal to 1 (*Ács* and *Hantel,* 1998a). In the Priestley-Taylor formula applications the atmospheric demand is parameterized estimating potential evapotranspiration.

Inspecting SURFMOD family members and modes, it is obvious that the most complex SURFMOD mode is the Psi1-PROGSURF while the simpliest mode is the Pm-PTSURF. In the following these two modes will be comparatively presented with more details.

2.1 Prognostic equations

The main difference between Psi1-PROGSURF and Pm-PTSURF is in the application of temperature prediction equations. In the following this aspect will be presented with more attention.

- **Psi1-PROGSURF:** The temperature prediction of vegetation-ground and deep-ground layers is made by using the force restore method (*Bhumralkar,* 1975).

$$C_B \cdot \frac{\partial T_{vg}}{\partial t} = F(T_{vg}, \theta_{l1}, \theta_{s1}), \tag{1}$$

$$\frac{\partial T_{dg}}{\partial t} = \frac{1}{\tau} \cdot (T_{vg} - T_{dg}), \tag{2}$$

where

$$C_B = veg \cdot C_v + (1 - veg) \cdot C_b, \tag{3}$$

$$C_b = 10\,\mathrm{cm} \cdot C + \left(\frac{\lambda \cdot C}{2\,\omega}\right)^{1/2}, \tag{4}$$

$$C = (1 - \theta_{S1}) \cdot C_m + \theta_{l1} \cdot C_l + \theta_{s1} \cdot C_s, \tag{5}$$

$$F(T_{vg}, \theta_{l1}, \theta_{s1}) = (R + H + L \cdot E - G_1) \cdot \delta\,(T_{vg}, \theta_{l1}, \theta_{s1}). \tag{6}$$

The parameter C_B is the bulk heat capacity of the vegetation-ground system (J m^{-2} K^{-1}), C_b is the bulk heat capacity of the upper 10 cm of bare soil (J m^{-2} K^{-1}), C_v is the vegetation heat capacity (J m^{-2} K^{-1}), C is the volumetric heat capacity of the soil surface layer (J m^{-3} K^{-1}), λ is the thermal conductivity of the soil surface layer (W m^{-1} K^{-1}), ω is the angular velocity of the rotation of the earth (s^{-1}), C_m is the volumetric heat capacity of solid soil particles (J m^{-3} K^{-1}), C_l is the volumetric heat capacity of water (J m^{-3} K^{-1}), C_s is the volumetric heat capacity of ice (J m^{-3} K^{-1}) and τ is the length of the day (s). With the step function δ the model switches between unfrozen, partly frozen and totally frozen soil as follows:

$$\delta(T_{vg}, \theta_{l1}, \theta_{s1}) = \begin{cases} 1 & \text{for} \quad T_{vg} > T_{fr}, \quad \theta_{l1} \geq 0, \quad \theta_{s1} = 0 \\ 0 & \text{for} \quad T_{vg} = T_{fr}, \quad \theta_{l1} > 0, \quad \theta_{s1} > 0 \\ 1 & \text{for} \quad T_{vg} < T_{fr}, \quad \theta_{l1} = 0, \quad \theta_{s1} \geq 0. \end{cases} \tag{7}$$

δ regulates the temperature prediction of the vegetation-ground system. During soil freezing/melting processes, T_{vg} is equal to the freezing temperature T_{fr} and temperature prediction is switched off, represented by $F(T_{vg}, \theta_{l1}, \theta_{s1}) \equiv 0$. In the absence of soil freezing/melting processes the temperature prediction of the vegetation-ground system is switched on. The energy budget function $F(T_{vg}, \theta_{l1}, \theta_{s1})$ refers to the vegetation-ground layer. R, H and $L \cdot E$ are net radiation, sensible and latent heat fluxes across the surface (W m^{-2}), G_1 is the soil heat flux across the bottom of the 1st soil layer (W m^{-2}) and L is the latent heat of vaporization (J kg^{-1}).

- **Pm-PTSURF:** Pm-PTSURF does not apply temperature prediction equations at all. Consequently there is no representation of soil water freezing/melting processes.

2.2 Radiation

The are no differences in the parameterization of radiation between the two modes.

2.3 Turbulent heat fluxes

The turbulent heat flux parameterizations are completely different in Psi1-PROGSURF and Pm-PTSURF. They are as follows:

- **Psi1-PROGSURF:** The latent heat flux is parameterized by

$$L \cdot E^j = -\frac{\rho c_p}{\gamma} \frac{f^j \cdot e_s(T_{vg}) - e_r}{r_a^j + r^j}, \tag{8}$$

where ϱ is the air density, c_p is the specific heat of air at constant pressure, γ is the psychrometric constant, $e_S(T_{vg})$ is the saturation vapor pressure at T_{vg}, e_r is the vapor pressure at the reference level and r_a^j is the aerodynamic resistance. The superscript j refers to the domains of vegetation (j=v) with relative coverage *veg*, and of bare soil (j=b) with coverage 1-*veg*. For vegetation we additionally distinguish between wet (j=vw) and dry (j=vd). In both cases we put

$$f^{vw} = f^{vd} = 1. \tag{9}$$

The wet/dry distinction applies only to the surface resistance r^j.

The sensible heat flux is parameterized as

$$H^j = -\rho\, c_p \frac{T_{vg} - T_r}{r_a^j}, \tag{10}$$

where T_r is the reference temperature.

The horizontal mean values of turbulent fluxes are estimated by

$$L \cdot E \quad \text{with} \quad E = veg \cdot E^v + (1 - veg) \cdot E^b \tag{11}$$

and

$$H = veg \cdot H^v + (1 - veg) \cdot H^b. \tag{12}$$

- **Pm-PTSURF:** The latent heat flux is expressed using the soil moisture availability concept, that is

$$L \cdot E^j = \beta^j \cdot L \cdot E_p^j, \tag{13}$$

where E and E_p is the actual and potential evapotranspiration and β is the moisture availability function. As above, the index j represents the surface type. The potential evapotranspiration rate $L \cdot E_p^j$ is parameterized using the Priestley-Taylor formula (*Priestley* and *Taylor*, 1972), that is

$$L \cdot E_p^j = \alpha \cdot \frac{\Delta}{\Delta + \gamma} \cdot A^j, \tag{14}$$

where α =1.26 is the Priestley-Taylor coefficient, Δ is the slope of saturated vapor pressure curve at T_r, A^j is the available energy of surface. For bare soil $A^j = R^j - G^j$ but for vegetation $A^j = R^j$. R^j is the net radiation flux while G^j is the ground surface heat flux.

The sensible heat flux is estimated as residual,

$$H^j = A^j - L \cdot E^j. \tag{15}$$

The horizontal mean values of turbulent fluxes are obtained by Eq. (11) and Eq. (12).

2.4 Ground heat flux

There is a great difference in the ground heat flux parameterization between Psi1-PROGSURF and Pm-PTSURF. The parameterizations used are briefly considered below.

- **Psi1-PROGSURF:** The ground heat flux at 10 cm depth is estimated in conjunction with force-restore method as

$$G_1 = \left(\frac{\omega \cdot C_B \cdot \lambda}{2}\right)^{1/2} \cdot (T_{vg} - T_{dg}). \tag{16}$$

G_1 represents the horizontal mean value.

- **Pm-PTSURF:** The ground heat flux at earth surface is parameterized as the percentage of net radiation.

$$G_0^b = 0.15 \cdot R^b. \tag{17}$$

Under vegetation canopy it can be neglegted, therefore

$$G_0^v = 0. \tag{18}$$

The horizontal mean of G_0 is calculated as in Eq. (11) or Eq. (12).

2.5 Water fluxes

There are no differences in the parameterization of water transfer in the soil and canopy layer between the two modes. The set of equations applied are presented in *Ács* and *Hantel* (1998a). The only difference between the two modes is in the parameterization of evapotranspiration. This is presented in section 2.3.

2.6 Aerodynamic transfer

- **Psi1-PROGSURF:** The aerodynamic transfer is parameterized via the resistance concept using the Monin-Obukhov similarity theory taking into account the atmospheric stability. The aerodynamic resistance is split into laminar and turbulent terms distinguishing transports between momentum and heat/moisture. The resistances are separately calculated above vegetated and bare soil surfaces.

- **Pm-PTSURF:** There is no aerodynamic transfer parameterization since the turbulent fluxes do not depend upon aerodynamic transfer.

2.7 Available soil moisture

There is a great difference in the parameterization of available soil moisture between Psi1-PROGSURF and Pm-PTSURF. The parameterizations are considered separately for vegetation and bare soil surafce.

2.7.1 Vegetation

- **Psi1-PROGSURF:** The soil moisture available for transpiration is parameterized using the resistance concept. The well known *Jarvis* (1976) formula is applied:

$$r^{vd} = \frac{r_{stmin} \cdot F_{ad}}{LAI \cdot GLF \cdot F_{ma}}, \tag{19}$$

  where r^{vd} is the canopy resistance, r_{stmin} is the minimum stomatal resistance at optimum environmental conditions. *LAI* is the leaf area index, *GLF* is the green leaf fraction; it expresses the fraction of live leaves ranging between 0 and 1. F_{ad} and F_{ma} represent the atmospheric demand and moisture availability effect upon stomatal functioning, respectively; they range between 0 and 1.

- **Pm-PTSURF:** The soil moisture/transpiration dependence is parameterized via soil moisture availability function β^v. It is expressed as

$$\beta^v = \begin{cases} 1 & \text{for } \theta_{rz} \geq \theta_c \\ \dfrac{\theta_{rz}}{\theta_c} & \text{for } \theta_{rz} < \theta_c, \end{cases} \tag{20}$$

where θ_{rz} is the soil moisture content in the root zone and θ_c is the critical soil moisture content. It is parameterized by

$$\theta_c = 0.75 \cdot \theta_f, \tag{21}$$

where θ_f is the moisture content at field capacity.

2.7.2 Bare soil

- *Psi1-PROGSURF:* The soil moisture available for evaporation is also parameterized via the resistance concept. The soil surface resistance r^b is estimated by *Sun*'s (1982) empirical formula:

$$r^b = c_1 + c_2 \cdot \left(\frac{\theta_{S1}}{\theta_1} \right)^{c_3}, \tag{22}$$

where θ_1 and θ_{S1} is the actual and saturated soil moisture content in the 1st soil layer. c_1, c_2 and c_3 are empirical constants (for constants see Table 2 in *Ács* and *Hantel*, 1998a).

- *Pm-PTSURF:* The soil moisture availability function for bare soil surface β^b is analogously parameterized to β^v. It is expressed by

$$\beta^b = \begin{cases} 1 & \text{for } \theta_1 \geq \theta_c \\ \dfrac{\theta_1}{\theta_c} & \text{for } \theta_1 < \theta_c. \end{cases} \tag{23}$$

2.8 Soil water freezing or melting

- **Psi1-PROGSURF:** There is soil water freezing or melting in the vegetation-ground layer. The parameterization applied is shortly described in *Ács* and *Hantel* (1998a).

- *Pm-PTSURF:* Soil water freezing or melting processes can not be represented since there is no T_{vg}-temperature prediction.

3. *Validation of the models*

The model family SURFMOD has been extensively tested in off-line mode using the 1987 data from Cabauw, The Netherlands. The Cabauw data set is a PILPS data set. Its complete description is given in Beljaars and Bosveld (1997). In the numerical experiments SURFMOD was always initialized as all PILPS participating models by saturating all liquid water stores. The variable and constant land-surface parameters are specified according to the specifications used in PILPS phase 2a experiment (see Table A2, A3 and A4 in *Chen et al.*, 1997 or Table 1 and 2 in *Ács* and *Hantel*, 1998a).

The model validation is performed by comparing simulated and observed surface fluxes. In the following the annual mean characteristics, the seasonal changes and the instantaneous values obtained in the IOP (intensive observation period) of the most important turbulent heat and water balance components are shortly described. At the end we are going to try to explain the results, that is the behaviour of SURFMOD modes.

3.1 Annual mean characteristics

The spinup time of both SURFMOD modes is 2 years. The annual mean sensible and latent heat fluxes of Psi1-PROGSURF and Pm-PTSURF together with other PILPS results are presented in *Fig. 1*. The sensible heat flux of Pm-PTSURF is -7.4 W m^{-2}, the latent heat flux is -34.7 W m^{-2}. The point is exactly located on the net radiation line since the measured net radiation is used as input. The corresponding point for Psi1-PROGSURF is not closer to the observation but the somewhat under net radiation line. This deviation from net radiation line is caused by application of force-restore method (*Ács* and *Hantel*, 1999).

The annual runoff versus evapotranspiration is given in *Fig. 2*. There is only a minor difference between the results obtained by Psi1-PROGSURF (E = -435 mm yr^{-1} and R = 337 mm yr^{-1}) and Pm-PTSURF (E = -440 mm yr^{-1} and R = 332 mm yr^{-1}). Pm-PTSURF's result is slightly closer to the observation than the Psi1-PROGSURF's result.

3.2 Seasonal variations

The seasonal change of sensible heat flux and evapotranspiration is presented in *Figs. 3* and *4*, respectively. According to the convention applied all vertical fluxes are positive if directed downwards. Inspecting Fig. 3 we see that the difference between the simulation results is small in summer but large in October, November and December. The results obtained by Psi1-PROGSURF are closer to the observations with respect to Pm-PTSURF's results. This is especially obvious in autumn.

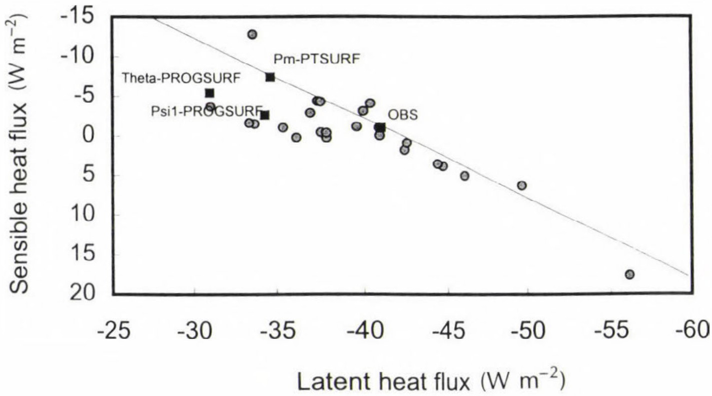

Fig. 1. Annually averaged sensible versus latent heat fluxes estimated by modes Pm-PTSURF, Psi1-PROGSURF and Theta-PROGSURF (thick symbols) along with the equivalent PILPS phase 2a results (thin dots; for details see Fig. 5 in *Chen et al.*, 1997). The SURFMOD modes are characterised in Table 1; OBS = observed value.

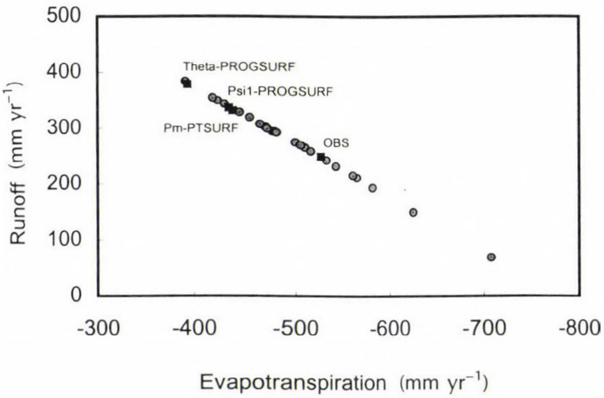

Fig. 2. As Fig. 1 but for runoff versus evapotranspiration (compare with Fig. 10 in *Chen et al.*, 1997).

Fig. 4 presents the simulated and observed evapotranspiration. The main characteristics can be summarized as follows: Pm-PTSURF yields better results than Psi1-PROGSURF in February, March, April and May but Psi1-PROGSURF is more superior with respect to Pm-PTSURF in October, November and December. In summer months the simulation results do not show any observable tendency.

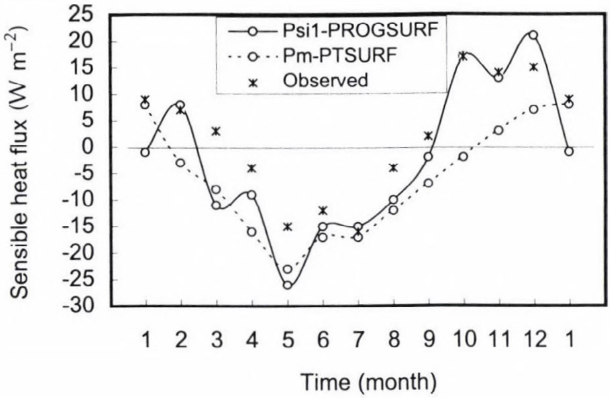

Fig. 3. Annual course of sensible heat flux simulated by Psi1-PROGSURF and Pm-PTSURF.

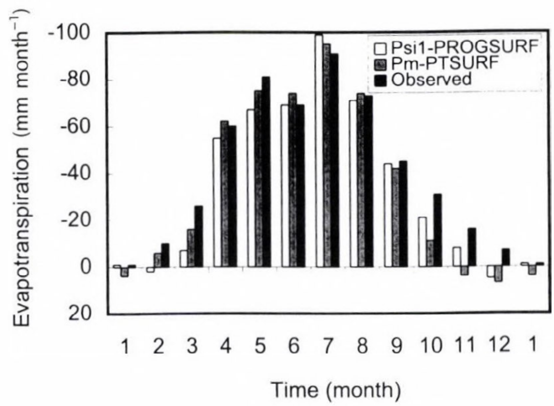

Fig. 4. Annual course of evapotranspiration simulated by Psi1-PROGSURF and Pm-PTSURF.

3.3 Turbulent fluxes in the intensive observation period

Instantaneous values of turbulent heat fluxes have been measured in the intensive observation period between September 10–19, 1987. The comparison of simulated and observed latent heat fluxes for Psi1-PROGSURF and Pm-PTSURF is presented in *Figs. 5* and *6*, respectively. The results obtained are suitable: The correlation coefficients obtained are between 0.8 and 0.9; the slope of regression lines obtained by Psi1-PROGSURF and Pm-PTSURF are 0.97 and 1.55, respectively. The comparison of simulated and observed sensible

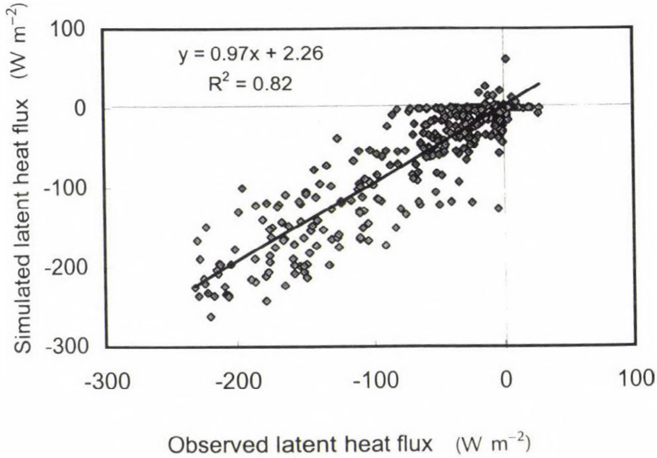

Fig. 5. Psi1-PROGSURF-simulated versus observed latent heat flux in the IOP (from day 253 to day 262). Thick line: regression.

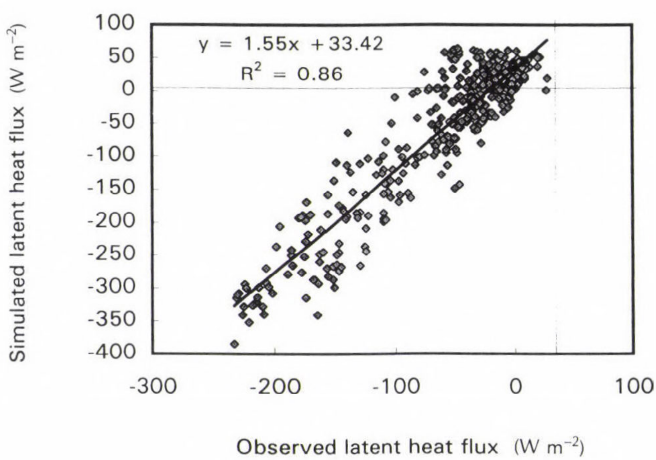

Fig. 6. Pm-PTSURF-simulated versus observed latent heat flux in the IOP (from day 253 to day 262). Thick line: regression.

heat fluxes for Psi1-PROGSURF and Pm-PTSURF is presented in *Figs. 7* and *8*, respectively. The correlation coefficients obtained are less than for the latent heat flux but still above 0.69. The slope of the regression lines deviates from 1; it amounts 0.78 for Psi1-PROGSURF and 0.47 for Pm-PTSURF.

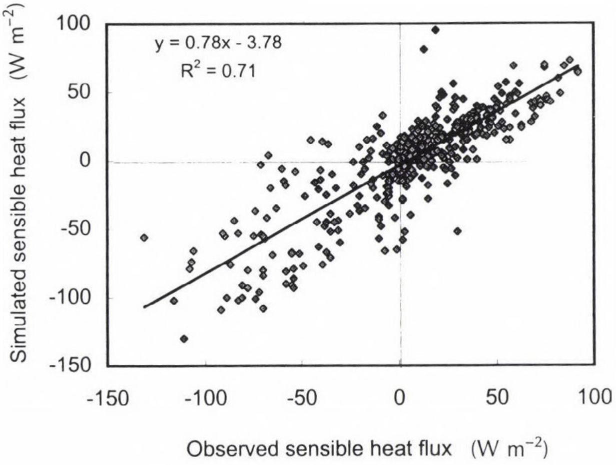

Fig. 7. Psi1-PROGSURF-simulated versus observed sensible heat flux in the IOP (from day 253 to day 262). Thick line: regression.

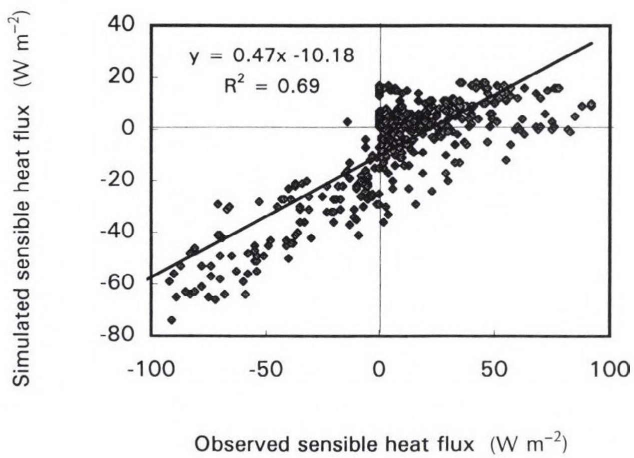

Fig. 8. Pm-PTSURF-simulated versus observed sensible heat flux in the IOP (from day 253 to day 262). Thick line: regression.

3.3.1 Analyses of the results

The results obtained by Psi1-PROGSURF and Pm-PTSURF can be explained by analysing simultaneously both the seasonal change of root-zone soil water

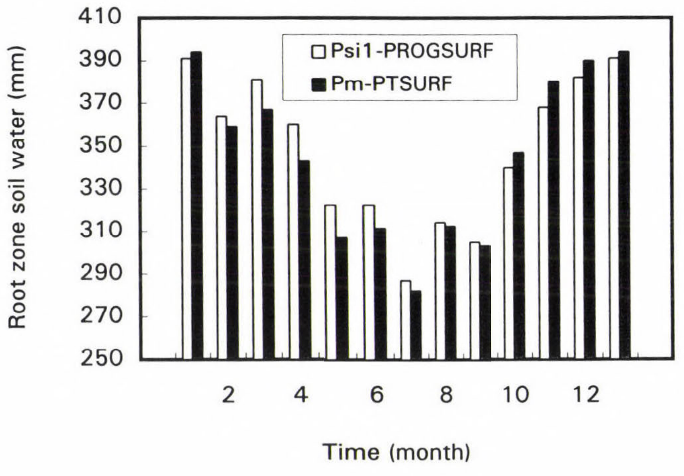

Fig. 9. Annual course of root-zone soil water simulated by Psi1-PROGSURF and Pm-PTSURF.

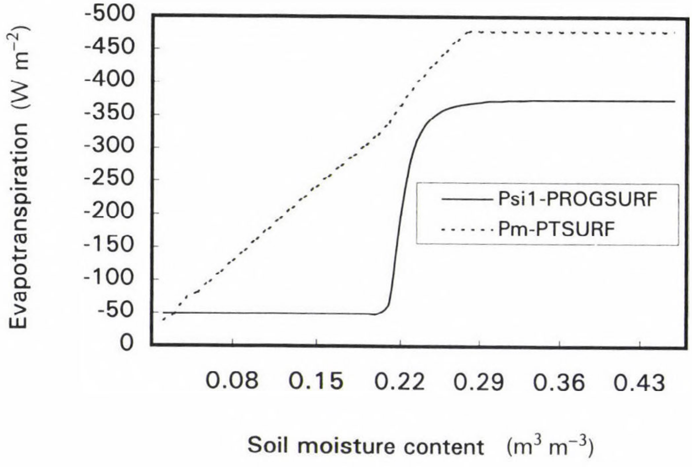

Fig. 10. Evapotranspiration versus root-zone soil moisture simulated by Psi1-PROGSURF and Pm-PTSURF. The soil/vegetation parameter refers to the Cabauw site. The atmospheric boundary conditions used are as follows: the global radiation is 800 W m^{-2}, air temperature, vapor pressure and wind velocity at the reference level is 25.8°C, 18 hPa and 6.0 m s^{-1}, respectively, and there is no precipitation.

and the evapotranspiration/soil moisture content relationship $E(\theta)$. The annual course of root-zone soil water for both SURFMOD modes is presented in Fig. 9, while the $E(\theta)$ relationships are drawn in *Fig. 10*. $E(\theta)$ curves need special attention. Both $E(\theta)$ curves are determined by the slope $S = \partial E(\theta)/\partial\theta$ in the transition region and the saturation value $E(\theta_S)$. Note that for Pm-PTSURF $E(\theta_S) = E_p$. Evidently, for low values of θ (dry surface), the evapotranspiration $E(\theta)$ is independent of both S and $E(\theta_S)$. For extremely high values of θ (well-watered surface) it is only dependent upon $E(\theta_S)$. In the transition zone both parameters $E(\theta_S)$ and S become active.

Inspecting Fig. 10 we see that there is a drastic deviation between the $E(\theta)$ curves obtained by Psi1-PROGSURF and Pm-PTSURF. The deviations are enormously great for low θ values up to about $\theta = 0.22$ m^3 m^{-3}. The deviations are constant and considerably less for high θ values that is in the saturation zone of $E(\theta)$ curves. At the same time Fig. 9 shows that the soil moisture in summer for the Cabauw data is between about 0.28 and 0.34 m^3 m^{-3}; i.e., it is located even in the saturation zone of $E(\theta)$ curves. Note the difference between root zone soil *moisture* (abscissa of Fig. 10) and root zone soil *water* (ordinate of Fig. 9) although both quantities are proportional. Thus, the evapotranspiration for the Cabauw site is controlled by the parameter $E(\theta_S)$; the parameter S is of no importance. Since there is an acceptable deviation between the parameter $E(\theta_S)$ obtained by Psi1-PROGSURF and Pm-PTSURF, the deviations between their simulation results are also not great.

4. Conclusion

An overview of the land-surface model family SURFMOD is given. We paid more attention to the comparison of the most complex Psi1-PROGSURF and the simpliest Pm-PTSURF modes. Pm-PTSURF deviates from the Psi1-PROGSURF as follows:

- air humidity is not used but net radiation or surface temperature is used as input (see Table 2b),
- ground heat flux at surface is calculated via net radiation (see Table 4),
- latent heat flux is parameterized via the Priestley-Taylor formula which implies no leaf water potential calculation (see Table 4),
- sensible heat flux is estimated as the residiual from the energy balance equation (see Table 4) and
- the applied method for latent and sensible heat flux parameterization implies that there is no need for aerodynamic resistance calculation (see Table 5) as well as that in winter no snow and/or soil freezing/melting processes can be represented (see Table 2a).

Summarizing the deviations we can say that Pm-PTSURF is not only simple with respect to Psi1-PROGSURF but also it is extremely simple with respect to other biophysical models (*Shao* and *Henderson-Sellers*, 1996).

Psi1-PROGSURF and Pm-PTSURF has been compared in off-line mode for the Cabauw data set, using the same specifications that have been applied in the PILPS campaign (*Chen et al.*, 1997). The models reproduces satisfactorily the observed annual mean values, the seasonal changes and the instantaneous values of turbulent and water fluxes. For example, the annual mean values of evapotranspiration and runoff obtained by Pm-PTSURF are ~440 and 332 mm, respectively. This result proves that Pm-PTSURF can capture—in spite of its extreme simplicity—those relevant phenomenons which determine the Cabauw site: the potential evapotranspiration governed by atmospheric conditions during almost the full year. Moreover it yields better results in terms of turbulent and water fluxes with respect to some much more complex SURFMOD modes as for example Theta-PROGSURF (see Fig. 1 and 2). This numerical experiment proves that the extremely simple models as Pm-PTSURF can also remarkably reproduce the observations. At the end, we have shown the main reason why the simulation results of Psi1-PROGSURF and Pm-PTSURF do not enormously deviate.

Further developments of the model family SURFMOD are in preparation. SURFMOD presently serves as a substitute for observed fluxes of latent and sensible heat for the software DIAMOD (*Hantel et al.*, 1993; *Haimberger et al.*, 1995) and also as an effective tool in performing comparative studies.

Acknowledgements—The authors wish to thank the *Österreichische Akademie der Wissenschaften* within the National Austrian Committee for the IGBP. We thank *Dr. L. Haimberger* for the helpful discussions and help in data transfer processing. The technical help provided by *Mr. Z. Barcza* has been very constructive and it is highly appreciated.

References

Ács, F., Mihailovic, D.T. and *Rajkovic, B.*, 1991: A coupled soil moisture and surface temperature prediction model. *J. Appl. Meteor. 30*, 812-822.

Ács, F., 1994: A coupled soil-vegetation scheme: Description, parameters, validation, and sensitivity studies. *J. Appl. Meteor. 33*, 268-284.

Ács, F., 1995: Simple surface flux model for use within diagnostic atmospheric models. *Proc. of the EGS XX General Assembly* (Supplements Issue of Annales Geophysicae, Part II., Supplement II to Volume 13), C470, Hamburg, 3-7 April.

Ács, F., Dorninger, M. and *Hantel, M.*, 1996: The Surface Flux Model SURFMOD. User Manual. *Internal Report of the Institute for Meteorology and Geophysics, University of Vienna.*

Ács, F. and *Hantel, M.*, 1998a: The Land-Surface Flux Model PROGSURF. *Global Planet. Change 19*, 19-34.

Ács, F. and *Hantel, M.*, 1998b: The Land-Surface Hydrology Parameterization in PROGSURF: Formulation and Test Results with Cabauw Data Set. *Időjárás 102*, 109-127.

Ács, F., Dorninger, M. and *Hantel, M.*, 1998a: The Land-Surface Model PROGSURF. User Manual. *Internal Report of the Institute for Meteorology and Geophysics, University of Vienna.*

Ács, F., Dorninger, M. and *Hantel, M.*, 1998b: The Land-Surface Model PMSURF. User Manual. *Internal Report of the Institute for Meteorology and Geophysics, University of Vienna.*

Ács, F. and *Hantel, M.*, 1999: The Penman-Monteith concept based land-surface model PMSURF. *Időjárás 103*, 19-36.

Ács, F., Hantel, M. and *Unegg, J.*, 2000: The Budapest-Vienna Land-Surface Model Family SURFMOD. *Internal Report of the Institute for Meteorology and Geophysics, University of Vienna.*

Bhumralkar, C.M., 1975: Numerical experiments on the computation of ground surface temperature in an atmospheric general circulation model. *J. Appl. Meteor. 14,* 1246-1258.

Beljaars, A.C.M. and *Bosveld, F.C.*, 1997: Cabauw data for the validation of land surface parameterization schemes. *J. Climate 10*, 1172-1194.

Chen, T.H., Henderson-Sellers, A., Milly, P.C.D., Pitman, A.J., Beljaars, A.C.M., Polcher, J., Abramopoulos, F., Boone, A., Chang, S., Chen, F., Dai, Y., Desborough, C.E., Dickinson, R.E., Dumenil, L., Ek, M., Garratt, J.R., Gedney, N., Gusev, Y.M., Kim, J., Koster, R., Kowalczyk, E.A., Laval, K., Lean, J., Lettenmaier, D., Liang, X., Mahfouf, J.-F., Mengelkamp, H.-T., Mitchell, K., Nasonova, O.N., Noilhan, J., Robock, A., Rosenzweig, C., Schaake, J., Schlosser, C.A., Schulz, J.-P., Shao, Y., Shmakin, A.B., Verseghy, D.L., Wetzel, P., Wood, E.F., Xue, Y., Yang, Z.-L. and *Zeng, Q.*, 1997: Cabauw experimental results from the project for intercomparison of land-surface parameterization schemes. *J. Climate 10,* 1194-1216.

Dolman, A.J., 1993: A multiple-source land surface energy balance model for use in general circulation models. *Agric. Forest Meteorol. 65,* 21-45.

Haimberger, L., Hantel, M. and *Dorninger, M.*, 1995: A thermodynamic model for the atmosphere. Part III: DIAMOD with orography and improved error model. *Meteorol. Zeitschrift., N.F. 4,* 162-182.

Hantel, M., Ehrendorfer, M. and *Haimberger, L.*, 1993: A thermodynamic diagnostic model for the atmosphere. Part II: The general theory and its consequences. *Meteorol. Zeitschrift, N.F. 1,* 87-121.

Jarvis, P.G., 1976: The interpretation of the variations in leaf water potential and stomatal conductance found in canopies in the field. *Philos. Trans. Roy. Soc. London*, Ser. B., 273, 593-610.

Monteith, J.L., 1965: Evaporation and Environment. In *The State and Movement of Water in Living Organisms* (ed.: *G. Fogg*). *Proc. 19th Symp. Soc. Exp. Biol.*, Cambridge, Cambridge University Press, 205-236.

Monteith, J., 1995: Accomodation between transpiring vegetation and the convective boundary layer. *J. Hydrol. 166*, 536-550.

Priestley, C.H.B. and *Taylor, R.J.*, 1972: On the assessment of surface heat flux and evaporation using large-scale parameters. *Mon. Wea. Rev. 100*, 81-92.

Shao, Y. and *Henderson-Sellers, A.*, 1996: Validation of soil moisture simulation in landsurface parameterization schemes with HAPEX data. *Global Planet. Change 13,* 11-46.

Sun, S.F., 1982: Moisture and heat transport in a soil layer forced by atmospheric conditions. *M.S. Thesis, Dept. of Civil Engineering, University of Connecticut.*

IDŐJÁRÁS
Quarterly Journal of the Hungarian Meteorological Service
Vol. 104, No. 1, January–March 2000, pp. 43–51

A method to estimate temporal behavior of extreme quantiles

István Matyasovszky

Department of Meteorology, Eötvös Loránd University,
H-1117 Budapest, Pázmány Péter sétány 1/A; E-mail: matya@ludens.elte.hu

(Manuscript received 3 December 1999; in final form 8 January 2000)

Abstract—Quantiles at tails of a density function with infinite support are defined as extremes, and a method is presented to estimate their temporal variations. The procedure does not need any specifications on the probability distribution, the unique assumption is its smooth variation in time. As an illustration, the methodology is applied to daily maximum and minimum temperature time series in Hungary. The example demonstrates that extremes may exhibit considerably variations when conventional trend estimates do not show statistically significant changes.

Key-words: extremes, quantile, time dependent distribution, maximum and minimum temperatures.

1. Introduction

Detection and estimation of climatic changes in observed data series have a broad literature. Examinations are principally based on variations of mean, i.e., much of these works uses particular versions of trend models (*Zheng* and *Basher*, 1999). However, several other statistical properties may vary during a changing climate. For instance, long-term change of extremes is an especially important issue for its socio-economic impacts.

The term "extremes" can be defined by several ways. These include such as the average returning period of an occurrence arising with small probabilities, probability distribution of maximum or minimum of a variable during a specific period, number of exceedances of high or low thresholds, duration below or above these thresholds, and many other choices.

Theory of extremes is well-developed when data set in question consists of a sequence of identically and independently distributed variables (*Gumbel*, 1958; *Leadbetter et al.*, 1983; *Tiago de Oliveira*, 1986). Although asymptotic properties of extremes are valid for quite broad classes of dependent sequences, the practical modeling encloses serious difficulties under temporal dependency. The most significant problem emerges when the underlying sequence does not consist of identically distributed variables, which is the case, for instance, in a changing climate. Therefore, our idea is to define the term "extreme" so simply that it can be handled for dependent and non-homogeneous time series.

Extreme event is now defined as an occurrence arising with small probabilities at tail(s) of a density function with infinite support of a given variable. Such an event can be specified with a high or low (or both) quantile(s), and the task is then to estimate its (their) temporal variation. This can be done when the probability distribution is smoothly varying in time.

Rest of the paper presents a methodology estimating time dependent quantiles. Then the procedure is applied to daily maximum and minimum temperature time series of four locations in Hungary. Finally, a section for discussion and conclusions is provided.

2. *Methodology*

Let $Y(t)$ be a continuous parameter stochastic process and denote the α quantile of the probability distribution of $Y(t)$ at time t as $q_\alpha(t)$, i.e., $q_\alpha(t)$ satisfies the equation

$$F_t(q_\alpha(t)) = \alpha\,, \tag{1}$$

where $F_t(y)$ is the probability distribution function of $Y(t)$ evaluated at $Y(t)=y$. An estimate $\hat{q}_\alpha(t)$ can be obtained from the observed pairs $(t_i, Y(t_i))$, $i=1,\dots,n$ by solving Eq. (1) after replacing F_t with an estimate $\hat{F}_t$. Here $Y(t_i)$ for any t_i is supposed to be independent from $Y(t_j)$, $t_j \neq t_i$. A choice of $\hat{F}_t$, which smooths over t, is

$$\hat{F}_t(y) = \sum_i K[(t_i - t)/b)\, I[Y(t_i) \le y] / \sum_i K[(t_i - t)/b)\,, \tag{2}$$

where K is a kernel function and I is the indicator function: $I[A]=1$ if A is true, $I[A]=0$ otherwise (*Magee et al.*, 1991). Eq. (2) is an extension for conditional distribution functions of the Parzen-Rosenblatt kernel density estimator (*Parzen*, 1962; *Rosenblatt*, 1956), or it can be considered as a specific case of the Nadaraya-Watson estimator (*Nadaraya*, 1964; *Watson*, 1964) when indicator series in Eq. (2) is regressed on t. The kernel function determines how to decrease the influence of an observation at t_i when moving off t, and the bandwidth b determines the rate of this decrease. In order to have a "good" estimate Eq. (2), $F_t(y)$ is assumed to be slowly varying in time, which is now defined as $q_\alpha(t)$ has finite derivatives up to an order of $k>0$ for any $0<\alpha<1$.

K is generally defined on the interval [-1,1] and is called of order k if

$$\int_{-1}^{1} K(z) z^j dz = \begin{cases} 0, & 0<j<k, \\ 1, & j=0 \end{cases} \tag{3}$$

is satisfied. The parameter k coincides with the order of biasedness, i.e., using a kernel of order k, Eq. (2) delivers an estimate with an asymptotic bias proportional to kth derivative of F with respect to t. Since the probability distribution function is supposed to be smoothly varying in time, a small value for k can be chosen in Eq. (3). Supposing that F can be taken as a local linear function of time (k = 2), the optimal K in a sense defined in *Fan* (1992) is

$$K(z) = \frac{3}{4}(1 - z^2), \quad z \in [-1,1], \tag{4}$$

the so-called Epanechnikov kernel.

The bandwidth can be estimated by minimizing the cross-validated quantity

$$CV(b) = \sum_i L_\alpha(Y_i - \hat{q}_\alpha^{(i)}(t_i)), \tag{5}$$

where $L_\alpha(z) = |\alpha - I[z<0]| \cdot |z|$ is the loss function employed (*Koenker* and *Bassett*, 1978) and $\hat{q}_\alpha^{(i)}$ denotes the estimate of $q_\alpha(t_i)$ using bandwidth b with observation i omitted in Eq. (2).

3. Application

Daily maximum and minimum temperatures for four stations (Pécs, Szeged, Miskolc, Budapest KMI) for the period from 1901 to 1990 are examined with respect to their low and high time dependent quantiles. An analysis is performed with quantiles α = 0.01, 0.05, 0.10, and with $1-\alpha$, respectively. Only the winter (December, January, February) and summer (June, July, August) seasons are analyzed since the probability distribution function F changes considerably within the other two seasons.

As a first step the optimal bandwidth has to be estimated for both the maximum and minimum temperatures for every quantile and for both seasons. It is known that crossvalidated estimation of the bandwidth results in a degenerate choice of b = 0 when data series are autocorrelated (*Duin*, 1976) as it is the case for maximum or minimum temperatures. Therefore, quantity (5) has been modified such that $\hat{q}_{\alpha}^{(i)}$ denotes the estimate of $q_{\alpha}(t_i)$ using bandwidth b with observations omitted of a neighborhood of observation i. This neighborhood has been chosen 5 days since autocorrelations for lags larger than this value are quite small. An interesting experience of bandwidth estimation is that variability of optimal bandwidths corresponding to the two elements, seasons and quantiles, is surprisingly small. Therefore, in order to decrease the relatively large variance of bandwidth estimates, the mean of bandwidths has been calculated and used in Eq. (2). It is obtained to be 22 years. This simple operation results in a slightly biased estimation but with considerably smaller variance. Therefore, it can be expected that this unique value provides even better bandwidth estimates than the originally obtained particular ones.

Major results which are illustrated by quantiles 0.05 and 0.95 in *Figs. 1* and *2* can be summarized as follows. Generally, there are three phases of temperature changes. Considerably increasing or nearly constant values can be observed in the first part of the period, then a cooling starts from twenties-forties. Finally, a warming emerges again after fifties-seventies except for minimum temperature in summer. In winter, variation of low quantiles is remarkably larger than variation corresponding to high quantiles, which results in changes of variance, too. Summer has approximately same magnitudes of quantile variations. Direction of changes of low and high values is not strongly parallel producing further changes of variance. Behavior of Miskolc somewhat differs from other locations due to local climate effects.

An interesting question can be how these tendencies relate to changes in means. Therefore, a commonly used linear trend analysis was carried out for seasonal means of temperature data. *Tables 1* and *2* show the slope of trends indicating significant ones at a 5% probability level. To accept the hypothesis of no trend, the test statistic in absolute value should be smaller than 1.99. In spite of a general warming found in many time series (*Molnár* and *Mika*, 1997), there are fewer positive slopes than negative ones. Minimum temperatures do not exhibit any significant trends in winter, while the summer has strongly significant negative trends except for Budapest KMI where an almost significant (at a 5% level) increasing trend is detected. The individual behavior of Budapest KMI is probably due to a powerful urban effect. Maximum temperatures have no significant trends in both seasons with an exception of Miskolc in summer.

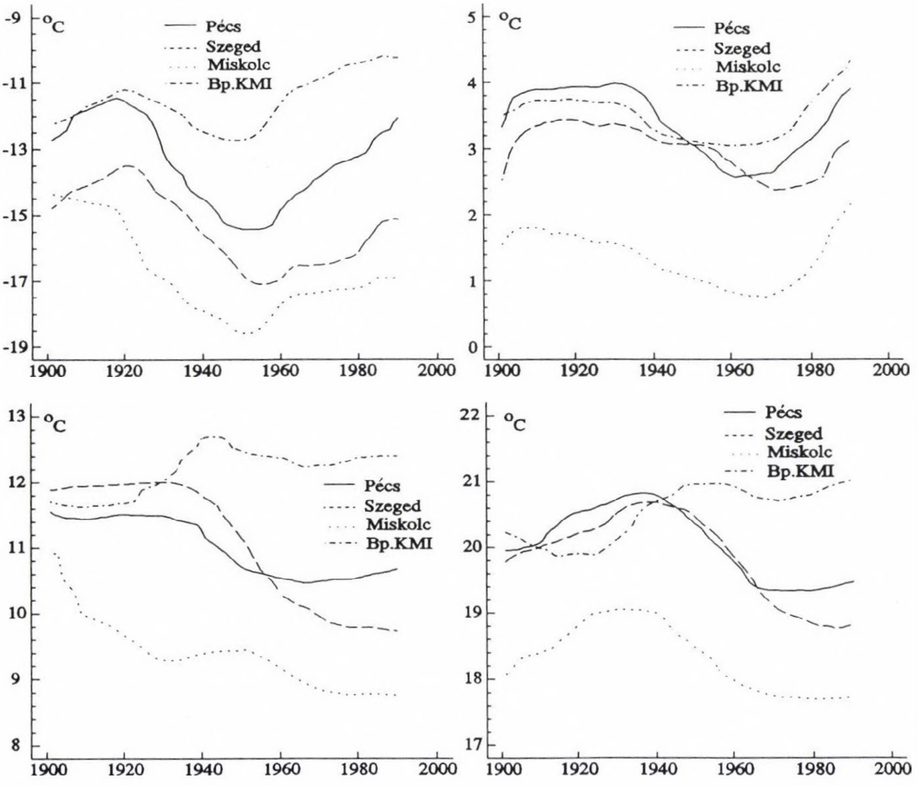

Fig. 1. Time dependent quantiles of daily minimum temperatures for $q = 0.05$ (left) and $q = 0.95$ (right) in winter (top) and summer (bottom).

There could be two reasons of these surprising findings. First, data series probably have considerable inhomogeneities, which, however, is beyond the scope of this study. Second reason is that the real trends are far from linearity; there can be warming and cooling phases during the entire period. In order to illustrate this fact *Fig. 3* shows seasonal mean temperature data and their corresponding linear trends for the following three cases: trend can be accepted as linear; trend is not linear; there is no trend. Seasonal mean of daily minimum temperature for Szeged in summer can be considered as an example for the first case. Fig. 1 and Fig. 3 show an intensive cooling from forties. However, behavior of both the 0.05 and 0.95 quantiles (Fig. 1) strengthens the visual observation for seasonal means that first part of the period does not suffer this cooling. Seasonal mean of daily maximum temperature for Pécs in summer, the second case mentioned above, makes the complex behavior of data more clearer. No linear trend can be detected (Fig. 3), while the corresponding quantiles (Fig. 2) exhibit remarkable temporal changes. Looking at observed data in Fig. 3 at least one cooling interval in the middle of the period and two warming phases at boundaries can be recognized. This is clearly reproduced by time dependent quantiles (Fig. 2). Our last case is represented by seasonal mean of daily maximum temperature for Miskolc in winter. Here, seasonal means are scattered purely randomly around a line parallel with the axis of years (Fig. 3). Thus, the mean is certainly unchanged, but not so the quantiles. This can easily be understood because extremes are depend on the probability distribution and not on mean. For instance, supposing that daily maximum and minimum temperatures are distributed normally, the variance also has a key role in controlling extremes quantiles.

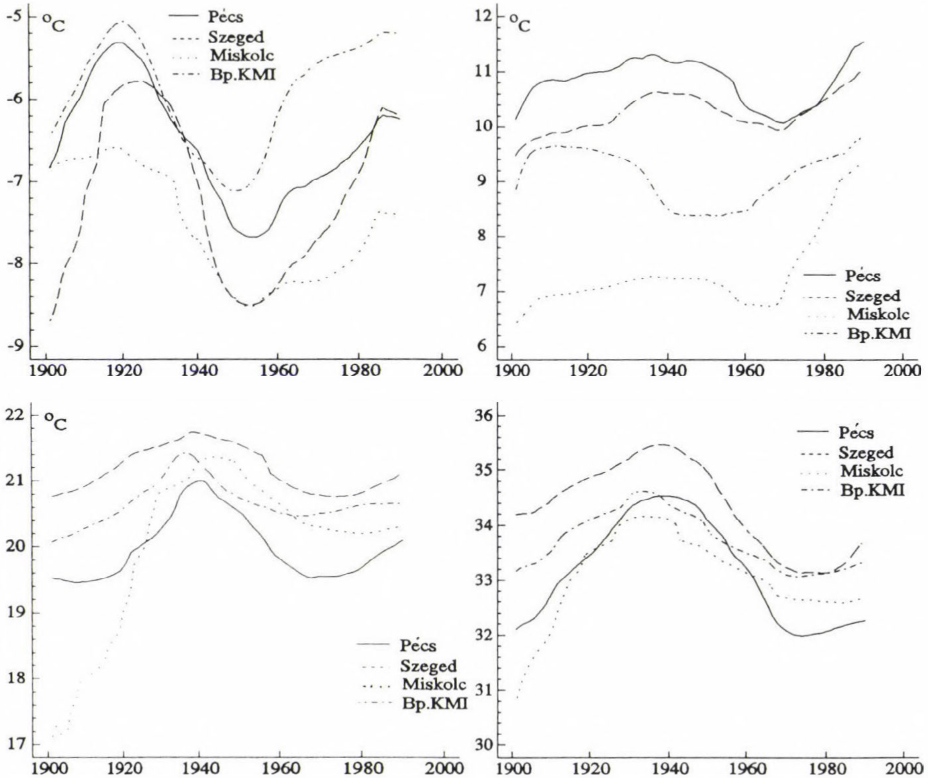

Fig. 2. Time dependent quantiles of daily maximum temperatures for $q = 0.05$ (left) and $q = 0.95$ (right) in winter (top) and summer (bottom).

Table 1. Slopes and test statistics for a linear trend analysis in winter

Station	Slope	Test statistic
Seasonal mean of daily minimum temperature		
Pécs	-0.0127	-1.05
Szeged	-0.0084	-0.62
Miskolc	-0.0126	-0.91
Budapest KMI	+0.0063	+0.56
Seasonal mean of daily maximum temperature		
Pécs	-0.0142	-1.17
Szeged	+0.0022	+0.18
Miskolc	-0.0003	-0.03
Budapest KMI	+0.0018	+0.17

Table 2. Slopes and test statistics for a linear trend analysis in summer

Station	Slope	Test statistic
Seasonal mean of daily minimum temperature		
Pécs	-0.0143	-2.88*
Szeged	-0.0277	-5.15*
Miskolc	-0.0133	-3.10*
Budapest KMI	+0.0082	+1.86
Seasonal mean of daily maximum temperature		
Pécs	-0.0017	-0.23
Szeged	-0.0032	-0.49
Miskolc	+0.0251	+2.81*
Budapest KMI	-0.0052	-0.81

Asterisk shows significant linear trend at a 5% level

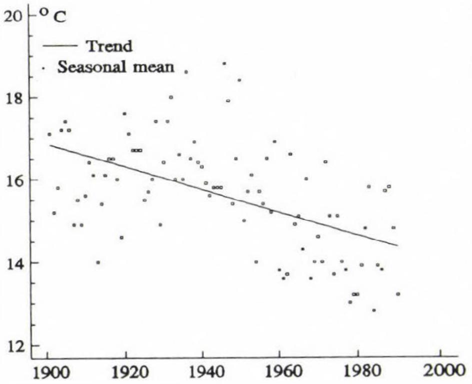

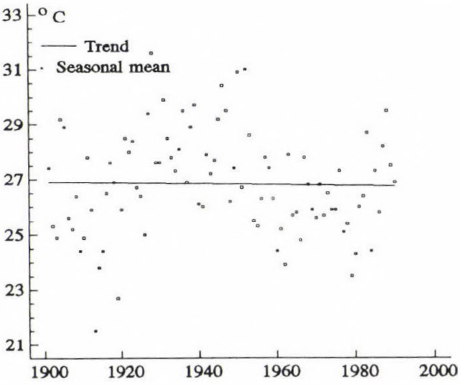

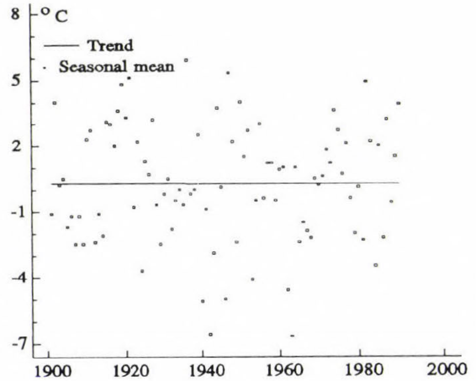

Fig. 3. Linear trends for seasonal mean of daily minimum temperature for Szeged in summer (left); for seasonal mean of daily maximum temperature for Pécs in summer (right); for seasonal mean of daily maximum temperature for Miskolc in winter (bottom).

4. Summary

A method to estimate time dependent quantiles of a variable has been presented. The procedure does not need any specifications on the probability distribution, the unique assumption is its smooth variation in time, which seems certainly reasonable on a climatic scale. An important aspect of the procedure is that bandwidth, a key element of the method, is optimized directly for quantiles and not for distribution functions.

An application for daily maximum and minimum temperatures in Hungary illustrates that high and/or low quantiles characterizing extremes may present considerably variations when conventional trend estimates do not show statistically significant changes.

Acknowledgement—Research leading to this paper has been supported by grant from Hungarian Science Foundation OTKA T025803.

References

Duin, R.P.W., 1976: On the choice of smoothing parameters for Parzen estimators of probability density functions. *IEEE Trans. Comput. C-25*, 1175-1179.

Fan, J., 1992: Design-adaptive nonparametric regression. *J. Am. Statist. Ass. 87*, 998-1004.

Gumbel, E.J., 1958: *Statistics of Extremes*. Columbia Univ. Press, New York.

Koenker, R. and *Bassett, G.S.*, 1978: Regression quantiles. *Econometrica 46*, 107-112.

Leadbetter, M.R., Lindgre, G. and *Rootzen, H.*, 1983: *Extremes and Related Properties of Random Sequences and Processes*. Springer-Verlag, New York.

Magee, L., Burbidge, J.B. and *Robb, L.*, 1991: Computing kernel-smoothed conditional quantiles from many observations. *J. Amer. Stat. Assoc. 86*, 673-677.

Molnár, K. and *Mika, J.*, 1997: Climate as a changing component of landscape: recent evidence and projections for Hungary. *Z. Geomorph. N.F. Suppl.-Bd. 110*, 185-195.

Nadaraya, E.A., 1964: On estimating regression. *Theory Probab. Applic. 15*, 134-137.

Parzen, E., 1962: On the estimation of probability density functions and mode. *Ann. Math. Statist. 33*, 1065-1076.

Rosenblatt, M., 1956: On some nonparametric estimates of a density function. *Ann. Math. Statist. 27*, 832-837.

Tiago de Oliveira, J., 1986: Extreme values and meteorology. *Theor. Appl. Climatol. 37*, 184-193.

Watson, G.S., 1964: Smooth regression analysis. *Sankhya Ser A 26*, 359-372.

Zheng, X. and *Basher, R.E.*, 1999: Structural time series models and trend detection in global and regional time series. *J. Climate 12*, 2347-2358.

IDŐJÁRÁS

Quarterly Journal of the Hungarian Meteorological Service
Vol. 104, No. 1, January–March 2000, pp. 53–59

On the diurnal variation of noctilucent clouds

Wilfried Schröder

Geophysical Station, Hechelstrasse 8, D-28777 Bremen, Germany

(Manuscript received 15 January 1999; in final form 16 September 1999)

Abstract—In a review (Meteorologische Rundschau, 1966, p. 26-27) the author suggested to make more accurate distinctions between "appearance" (in German Häufigkeit) and "brightness" (in German Helligkeit). The author analyses some arguments which were in favor of the daily variation of noctilucent clouds (NLC). It can be shown that there is no remarkable diurnal variation of noctilucent clouds. Earlier observations (1885–1897) make no difference between brightness and appearance, therefore it seems that noctilucent clouds have been detected more after midnight. Recent observations for the total noctilucent cloud period (May–August) do not support this earlier result in general. On the other hand recent data (1985–1997) show a little preference of the clouds after midnight. More studies are necessary for this complex.

Key-words: noctilucent clouds, diurnal variation, mesospheric circulation.

1. Introduction

In the last part of *Jensen et al.* (1989) describe and discuss the diurnal variation of noctilucent clouds as recorded by visual observations. It seems to be useful to make a more careful overview of the ground based data which have been sampled during the last 100 years. Furthermore, an insight into the general problems associated with visual data may be useful for further interpretations (see *Fig. 1* as an example of a noctilucent cloud).

Noctilucent clouds were first observed in Germany in 1885, two years after the great Krakatoa volcanic event of August 1883. Around this event anomalous twilight phenomena were observed and the attention was drawn to these atmospheric processes (see *Gadsden* and *Schröder*, 1989). Originally, people spoke of "glowing clouds" or "silvery clouds". It was probably *O. Jesse* who introduced the term "noctilucent clouds" (Leuchtende Nachtwolken). *Jesse*, who was then active at the Berlin Observatory, also performed the first photographic measurements of the clouds (*Archenhold*, 1928).

With the "Vereinigung der Freunde der Astronomie und kosmischen Physik", a German society of friends of astronomy, a working group was formed under the leadership of Archenhold, Foerster and Jesse with the goal of observing noctilucent clouds. They worked mostly during 1889–1899. More or less sporadic observations were made in Europe and USSR up to the end of the Second World War. More systematic surveillance of these phenomena has been made only since the International Geophysical Year (IGY, 1957) in different parts of the world.

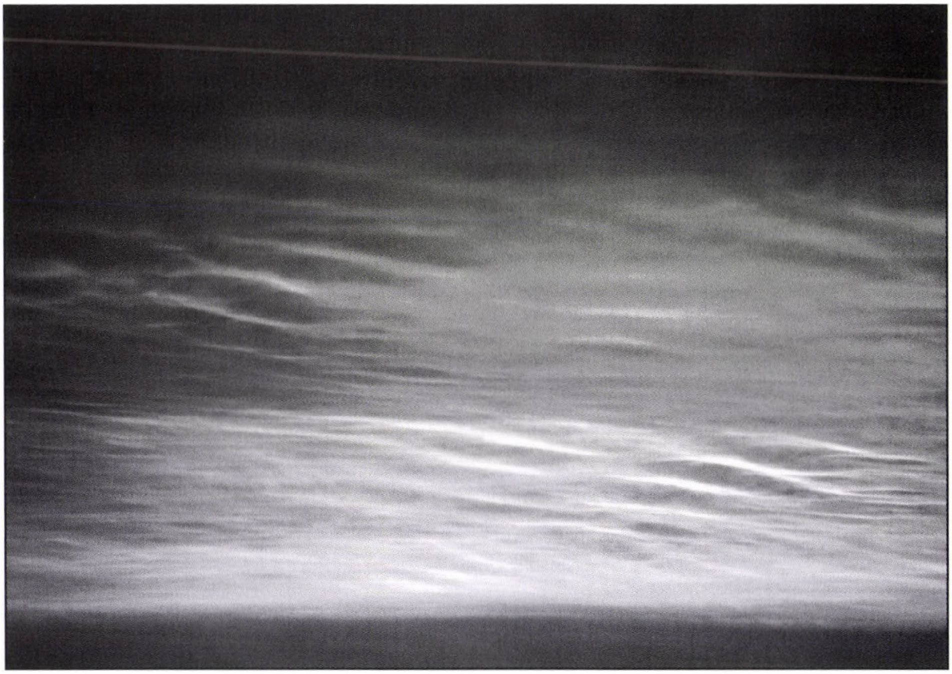

Fig. 1. Noctilucent clouds.

The observations are predominantly visual but there are many photographs and other special measurements too. Taken as a whole, these data have allowed no clear understanding of the complex problem of noctilucent clouds, mainly because of their sporadic nature. This includes the various climatological aspects, i.e., the diurnal and seasonal variation.

2. Observations of diurnal variation of NLC

In their last section *Jensen et al.* (1989) discuss the diurnal variation of noctilucent clouds. It seems to be necessary to make a more accurate distinction between the terms "brightness" and "appearance". For visual observations, a scale of noctilucent cloud intensity exists; it has the following five points:

(1) very weak NLC, barely visible against the background of the twilight sky, detected only through very careful examination of the sky;

(2) NLC easily detected, but having low brightness;

(3) NLC clearly visible, standing out sharply against the twilight sky;

(4) very bright;

(5) NLC extremely bright and noticeably illuminate objective facing them.

In many papers diurnal variation was reported in terms of "first sightings" at night and this may possibly have led to the conclusion that the clouds are more frequent after midnight than before. For instance, *Archenhold* (1928) reported: "In 1889–1894, the clouds were observed only 6 times before, but 33 times after midnight". At first *Vestine* (1934) accepted this result, and some decades later *Ludlam* (1957) wrote: "Except in very intense displays, the clouds have been seen more frequently after than before midnight...". A more careful examination of the various data was made later by *Fogle et al.* (1965) and by *Schröder* (1968a,b). It was found that 83% of the North American displays and 60% of the displays over the USSR during the IGY (1957–1958) were first seen before midnight. Furthermore, *Pavlova* (1962) reported that the total number of occasions of the observations of noctilucent clouds was 1.56 time greater in the morning than in the evening twilight. These data relate to the times of first "sighting" (detection by visual observations on each night).

If we look at the "brightness" of the noctilucent clouds, a difference can be pointed out. In one of his first analyses *Jesse* (1890) reported on the variation of brightness of the clouds that "we found an increased brightness of all noctilucent clouds in the morning hours". This was the first report of increasing brightness of noctilucent clouds during the morning hours and this effect has been confirmed in many notes after 1889. The fact that noctilucent clouds are generally brighter and most widespread after midnight may account for the differences found between the earlier and more recent studies on the daily variation of noctilucent cloud frequency (*Fogle* and *Haurwitz*, 1966; *Schröder*, 1968a).

Using the visual estimation of noctilucent cloud brightness, it should be noted that the clouds are usually very patchy, and observers often note the intensity of the bright patches in the display. For visual observation the structure in noctilucent clouds has been classified into four different types (*Gadsden* and *Schröder*, 1989):

I. Veils; II. Bands; III. Billows (or waves); IV. Whirls.

It is possible that in complex displays all four forms are observed simultaneously. The genesis of these formations shows remarkable differences in brightness and lifetime, therefore, visual observations very often report the "brightness" of the clouds as a general term, rather than referring to the different structures. Generally it has been reported by observers that noctilucent cloud brightness (and their different morphological forms I–IV) change considerably during the time of observation.

Table 1 and *2* (cf. also *Fig. 2* for the data of 1991–1995) present a summary of visual estimations of noctilucent clouds based on reports received from regular meteorological stations and individual observers. In general the brightness is reported in the 1–5 scale of intensity described above. It must be considered that the notification of brightness is related to different parts of a display; the clouds are mostly patchy, therefore, general brightness estimation is impossible by visual observations (cf. *Kosibowa* and *Pyka*, 1973, 1979; *Schröder*, 1968b).

Table 1. Variation of brightness of noctilucent cloud displays (1-5 scale classification)

	Time of observations (local time)									
Intensity	22:00 22:30	22:30 23:00	23:00 23:30	23:30 24:00	00:00 00:30	00:30 01:00	01:00 01:30	01:30 02:00	02:00 02:30	02:30 03:00
1	9	6	4	9	6	4	2	4	7	3
2	12	14	12	9	12	13	12	13	13	8
3	3	5	5	9	7	3	9	10	9	1
4	2	2	2	2	4	4	1	8	3	2

The conclusions of Table 1 and 2 are the same as have been reported by earlier observers: (a) in general the noctilucent cloud displays show a variation of brightness; (b) most of the clouds are noted after midnight with the intensity 3–5; (c) maximum before local midnight is not found. Intensity 1–4 have been observed for all different forms of the clouds. Intensities 4 and 5 were very often associated with the forms IIa (bands with diffuse edges), IIIa (billows/waves consisting of straight and narrow, sharply outlined parallel short bands), IIIb (wave-like structure with undulations in the short-bands) and IVb (whirls having the form of a simple band of one, or several bands with a radius of curvature of 3–5°).

Table 2. Brightness of noctilucent clouds detected by visual observations (German and Polish data)

Date of display	Intensity		Date of display	Intensity		Date of display	Intensity		Date of display	Intensity	
	before midnight	after midnight		before midnight	after midnight		before midnight	after midnight		before midnight	after midnight
21.07.1960	I, II		03.07.1966		I/II	12.07.1968	I^{+}	II, III, I^{+}	24.06.1972	I	
07.06.1962	II	III, IV	04.07.1966		IV	14.07.1968	I, III	II, IV	28.06.1972		II, III
09.06.1962	II, III	I-IV	05.07.1966		I, IV	21.07.1968		IV	02.07.1972	IV, II	
27.07.1963	II		07.07.1966		II	22.07.1968	I, II (III-V^{+})	III-V^{+}	06.07.1972	II, III	II, I
29.07.1963	II, I		08.07.1966		II	24.07.1968	II, III (III)$^{+}$	III	22.07.1972	II	II
09.06.1964	II	II-IV	15.07.1966	II		27.07.1968	I, II, III	III^{+}	04.08.1972	I	II
16.07.1964	I, II		17.07.1966	I, II		28.07.1968	II, III	V^{+}	07.06.1976	I	III/IV
20.07.1964	II, I		01.06.1067	II	IV/III/II	30.07.1968		III-I	09.06.1976		I
04.05.1965	I, II		16.06.1967	I	I^{+}	04.08.1968	I, (IV)$^{+}$	IV^{+}	17.06.1976		I/II
07.07.1965	II	IV-I	04.07.1967	II	II-IV, I	05.08.1968		IV	21.06.1976	I, IV	III/IV
24.07.1965	II	III-IV-I	16.07.1967		IV, III (V^{+})	14.05.1971	II	I, II-III	23.06.1976	III	I, II
20.05.1966	II - I		18.07.1967	II	III, II^{+}	19.05.1971	I-II		01.07.1976	I, II, II	II, III, IV
22.05.1966	I-II		07.05.1968		I-II	23.05.1971	II-III-VI		05.07.1976	I	I
02.06.1966	II	III-IV	26.05.1968		II	25.06.1971		II	10.07.1976	II, III	III
09.06.1966	II/I	I, II, IV	22.06.1968	I, II, III		26.06.1971		I	02.07.1977		I, II, III
10.06.1966	III/I	II-IV	23.06.1968	III, IV	III	27.06.1971		IV-II-I	07.06.1977	II, IV	IV, III, I
15.06.1966	I, III	I-IV	25.06.1968	I	II	02.07.1971	II	III-I	13.06.1977	I, II, III	III, II, I
18.06.1966		III	27.06.1968		I/II, II^{+}	04.07.1971	I-II	III-II-I	19.06.1977	I-II	II-I
23.06.1966		II/IV	29.06.1968		I, II, II, III^{+}	08.07.1971	I-II	II-I	23.06.1977	II, I, IV	III-II-I
26.06.1966	I	I	30.06.1968	I, II		16.07.1971		I-II, II-III	28.06.1977	III-II-	
27.06.1966		III	01.07.1968	I, II	IV^{+}	17.07.1971	I-II-III		30.06.1977	I, II, III, IV	
30.06.1966	II, I	IV	05.07.1968	I-IV		21.06.1972	II-IV	IV/I	04.07.1977	II, III	
02.07.1966	III	III	09.07.1968			23.06.1972	I-II	II, III, I	10.07.1977	I-II	III-II-I

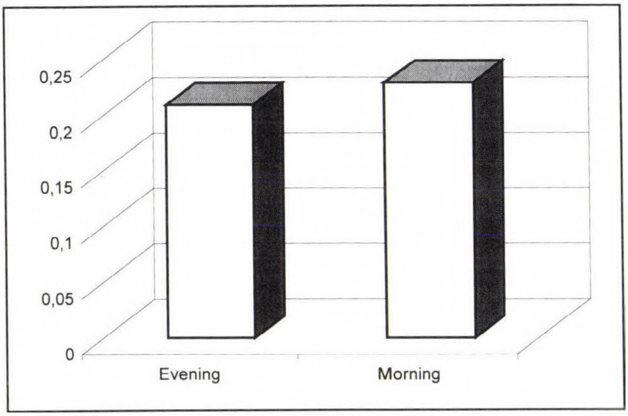

Fig. 2. Relative rate of noctilucent clouds for the periods before and after local midnight for the observations gathered in the years 1991 to 1995 (German data).

It seems to be useful to comment further on the visual data. Most of the displays showed a variation of brightness during the observation epoch, i.e., no display showed "constant" brightness. Because of the variation during the night and/or in twilight, we must consider some subjective aspects and the adaptability of vision of the observer during darkness. During the evening (and morning) twilight the human eye cannot adjust fully to lower illuminations and
It seems to be useful to comment further on the visual data. Most of the displays showed a variation of brightness during the observation epoch, i.e., no display showed "constant" brightness. Because of the variation during the night and/or in twilight, we must consider some subjective aspects and the adaptability of vision of the observer during darkness. During the evening (and morning) twilight the human eye cannot adjust fully to lower illuminations and
is less capable of detecting low contrast forms of noctlilucent clouds against the sky background. It would be useful to continue the visual observations of noctilucent clouds, including ground-based data and measurements, paying more attention to the variability of the different forms.

During recent decades the relationship between increased airglow, noctilucent clouds and the influx of cosmic dust has been discussed (*Gadsden* and *Schröder*, 1989). Noctilucent clouds appear at nearly the same time as the May and June increase of meteor streams (e.g., Aquarids, Arietids and Zeta Perseids). The cloud period diminishes shortly after the great injection of August Perseids. In general, the meteor flux is only one possible factor in the development of noctilucent clouds; the other is the condensation of ice particles in the NLC-Zone or at ions detected in the height. But, indeed, the observed diurnal variation in brightness of increased airglow is of interest.

Considering the conclusions of *Jensen et al.* (1989) and the noctilucent cloud and increased airglow data, it would be valuable to continue this research in the future.

The diurnal variation of noctilucent clouds has been noted in general terms. Further research should aim to present more details on the dependence of brightness of noctilucent clouds on oservational (local) time and to make some possible refinements, including the assumptions of *Jensen et al.* (1989).

3. Conclusion

From the available data no clear conclusions are possible. Some of the observations indicated an increased brightness of the NLC-display after midnight but it seems to be useful to get more data for analyses. In general, the old data of *Jesse* (1890) showed an increase after midnight, but they are different from the "frequency of appearance". Therefore, presently we would say that the brightness of NLC showed a variation during the observation time, although the question of frequency of occurrence at night is now an unsolved problem.

Acknowledgement—I am grateful to *U. Freitag* and the referees for their helpful comments.

References

Archenhold, F. S., 1928: Die leuchtenden Nachtwolken und bisher unveröffentlichte Messungen ihrer Geschwindigkeit. *Weltall 27*, 137-144.

Fogle, B., Capman, S. and *Echols, C.*, 1965: Noctilucent clouds—a survey with special reference to recent observations. *Univ. of Alaska, UAG-R,* 162.

Fogle, B. and *Haurwitz, B.*, 1966: Noctilucent clouds. *Space Sci. Rev. 6*, 279-340.

Gadsden, M. and *Schröder, W.*, 1989: *Noctilucent Clouds.* Springer-Verlag, New York.

Jensen, E., Thomas, G.E., and *Toon, O.B.*, 1989: On the diurnal variation of noctilucent clouds. *J. Geophys. Res. 94,* 14.693-14.699.

Jesse, O., 1890: *Untersuchungen über die sogenannten leuchtenden Nachtwolken.* Sitz-Ber. Preuß. Akad. Wiss. Berlin, 1031-1044.

Kosibowa, S. and *Pyka, J.L.*, 1973: Mesospheric clouds visible in Poland during 1971. *Acta Geophys. Pol. XXI*, 168-178.

Kosibowa, S. and *Pyka, J.L.*, 1979: Mesospheric clouds observed in Poland during 1977. *Acta Geophys. Pol. XXVII*, 187-193.

Ludlam, F.H., 1957: Noctilucent clouds. *Tellus 9,* 341-364.

Pavlova, T.D., 1962: *Preliminary Statistical Data on the Frequency of the Appearance of Noctilucent Clouds in the Year 1959* (in Russian). Trudy covescan. po. serebristym oblakam, Tallinn.

Schröder, W., 1968a: Zur Charakteristik der Leuchtenden Nachtwolken während der Jahre 1963-1967. *Gerlands Beitr. Geophys. 77*, 441-448.

Schröder, W., 1968b: Analyse der täglichen Häufigkeit der Leuchtenden Nachtwolken. *Meteorol. Rdsch. 21*, 28-30.

Vestine, E.H., 1934: Noctilucent clouds. *J. Roy. Astron. Soc. Can. 28,* 249-272 and 303-317.

BOOK REVIEWS

Ernő Mészáros: **Fundamentals of Atmospheric Aerosol Chemistry**. Akadémiai Kiadó, Budapest, 1999. 308 pages, 11 chapters, several figures and tables, more than 600 references.

Aerosol particles are important constituents of the atmosphere. Although, they were already known by the scientists of the last century, their intensive study was started in the 1950s. These particles play determining role in cloud and precipitation formation, solar radiation transfer, and visibility. Nowadays, the questions of global warming give a special emphasis on aerosol research as the aerosol particles may cause negative radiative forcing, partly compensating the effect of greenhouse gases. They are also involved in chemical transformations like the ozone removal in the stratosphere. All these effects depend on the physical and chemical properties of the particles.

Professor Mészáros' book introduces the reader into the science of atmospheric aerosol step by step, overviewing the origin of the particles, their types and atmospheric roles. The book consists of 11 chapters. The first chapter is an introductory one where the reader may get acquainted with the basic terms of aerosol science and with the basic physical properties and processes related to the particles. The second chapter covers the chemical properties. It also describes the most widespread sampling and analytical techniques. A short subchapter is devoted to a quickly developing field, to the ground-, aircraft- and satellite-based remote sensing of atmospheric aerosol.

The next three chapters present the different ways of aerosol formation: chemical reactions, burning processes, disintegration of the surface, and release from the biosphere. Having the particles in the atmosphere, they can be classified according to their chemical composition. One of the groups is that of the water soluble inorganic particles which, among others, includes the sea salt particles and the different sulfate and nitrate containing ones. Chapter 6 discusses their size distribution, as well as their spatial and temporal distributions over the globe.

Metal containing aerosol particles form the next group which is introduced in Chapter 7. They, as catalysts, play an important regulatory role in the chemical transformations in the atmosphere. A part of them, the so-called heavy metals are also known by their adverse effects on the living environment. Lead, a high amount of which is emitted by the gasoline driven vehicles, has got a special public attention during the last decades because of its harmful health effect. However, the lead pollution is not only the problem of our era, it was also high during the Greek and Roman cultures, as we can learn from a short subchapter.

Carbonaceous particles have got into the focus of aerosol science only recently. Due to their optical properties they play an important role in the radiation balance of the Earth, but they are also involved in the cloud and precipitation formation. Chapter 8 presents their size distribution as well as their spatial and temporal distributions. In the case of organic aerosol, the chapter also discusses its certain subclasses (aliphatic and aromatic compounds, organic acids, etc.).

Cloud droplets form on certain type of aerosol particles (condensation nuclei). Thus, the physical and chemical nature of aerosol play a significant role in the cloud/precipitation formation. In the cloud and precipitation droplets chemical transformations may occur. Evaporation of the droplets may release particles again, while the precipitation may wash them out to the surface. This sort of deposition may contribute to serious environmental problems like acidification. All these processes are overviewed in Chapter 9.

The next chapter discusses the effect of atmospheric aerosol on visibility and climate. The cooling effect of the aerosol particles is still one of the most uncertain questions of the global climate change research.

In the previous chapters the emphasis was on the tropospheric aerosol. The stratosphere differs from the troposphere in several aspects. In the stratosphere the residence time of the particles is much longer and thus they are able to cause global effects. This last chapter of the book reviews the origins and effects of the stratospheric aerosol, also mentioning the effect of the huge volcanic eruptions and the heterogeneous chemical reactions causing ozone loss in the stratosphere (formation of the "ozone hole").

The book is rich in measurement data which are presented in well designed figures and tables (more than 70 figures and almost 50 tables). In the enormous reference list (around 600 items) the reader can find the sources of the data, and further readings if he/she is interested in more details. The well-structured volume, considered as an introduction to the subject, can be recommended for both graduate students and research workers in earth and environmental science. The author is a skilled writer of scientific books, and his style also makes the subject understandable for all educated persons interested in atmospheric environment.

László Haszpra

N. Rescher: **Predicting the Future. An Introduction to the Theory of Forecasting.** State University of New York Press, Albany, 1998. 315 pages, five parts, 14 chapters, 4 tables.

W. A. Sherden: **The Fortune Sellers. The Big Business of Buying and Selling Predictions.** John Wiley & Sons, New York, 1998. 308 pages, 9 chapters, 54 figures.

Not only weather but almost everything that touches our life is filled with a kind of uncertainty that grows as we try to look weeks, months and years into the future. On a daily basis, we are showered with all types of predictions. Meteorological predictions (weather forecasts and climatological predictions) represent only a very small part of the multibillion-dollar and day-by-day growing industry of selling and buying predictions.

History is full of all sorts of wild schemes aimed at figuring out the future. Marcus Tullius Cicero (106-43 BC), statesman and poet, ancient Rome's greatest orator stated that the Roman government relies on two basic principles: ritualism and divination. In his work from 44 BC, "De Divinatione" (On Divination, i.e., supernatural insight into the future) Cicero presents an extended discussion of pluses and minuses of divination, eventually declaring that liabilities far outweight the benefits.

Predicting the Future by philosopher of science *Nicholas Rescher*, as he states "is the first book on the theory of prediction-in-general since Ciceros's De Divinatione". The author presents a general theory of prediction: its basic principles, methodology, promises and problems. Rescher also sorts out the difference between prediction (falsifiable or verifiable statements) and forecasts (unfalsifiable or unverifiable statements). He discusses the relationship between prediction and probability, as well as the theory of knowledge and the nature of reality. Rescher presents different sorts of methodology ranging from completely unformalised judgements (essentially personal options) to very formal schemes based on the laws of natural sciences and mathematical modeling.

As Rescher says, the mere correctness of a prediction is neither necessary nor sufficient to label either the prediction or the predictor "good". Equally, failure of the prediction does not necessarily mean that it or the method was bad. Discussing barriers of predictability ranging from instability and chaos to free will, innovation and quantum indeterminancy, Rescher provides reasons why we will never attain the nirvana of perfect foreknowledge.

While Nicholas Rescher focuses in his book on the ontology and epistemology of scientifically based prediction methods, *William Sherden*, financial and strategic planning consultant of multinational coorporations, casts a critical eye on seven areas in wich forecasts of the future have become big business: meteorology, macroeconomics, finance, demography, technology, organizational planning and futurology—the future of the future itself. With a combination of anecdotes, examples, historical and statistical facts the book attempts to separate predictions one can count on from vague, personal opinions and guesswork. Sherden demonstrates the reasons why reliable forecasts of the weather more than about 10 days ahead will remain in the realm of fantasy, regardless of whatever advances technology may bring. The book also traces the fascinating tale of how profits can actually be made from stock-market predictions—but not by investing. Based upon observations made as business consultant, Sherden presents a compelling argument for the case that "there is just no future in the past". To sum it up, Sherden offers an informal, almost journalistic tour through the minefields of the predictive enterprise as it is practised today.

Taken together, these two books constitute a very good introduction of the state of the predictive arts. The *Fortune Sellers* tells it like it is about the way prediction is practised in the worlds of commerce and industry, while *Predicting the Future* lays down a solid philosophical and logical foundations of making predictions. Bad news is that both authors conclude that perfect prediction is impossible. According to Sherden's estimations, we annually get at least $200 billion of mostly erroneous future predictions from professional prognosticators. Both authors give us the clearest possible explanation why it happens.

Good news for meteorologists is formulated by William Sherden as follows: "Weather forecasting is the most successful of all the future-predicting professions. ... In fact, meteorology is the only forecasting profession that employs proved laws of nature to make predictions. ... Meteorology is also the only forecasting profession among the fortune sellers that has shown clear signs of improvement."

György Gyuró

ATMOSPHERIC ENVIRONMENT

an international journal

To promote the distribution of Atmospheric Environment *Időjárás* publishes regularly the contents of this important journal. For further information the interested reader is asked to contact *Prof. P. Brimblecombe*, School for Environmental Sciences, University of East Anglia, Norwich NR4 7TJ, U.K.; e-mail: atmos_env@uea.ac.uk

Volume 34 Number 1 2000

NOTES TO CONTRIBUTORS OF *IDŐJÁRÁS*

The purpose of the journal is to publish papers in any field of meteorology and atmosphere related scientific areas. These may be

- reports on new results of scientific investigations,
- critical review articles summarizing current state of art of a certain topic,
- shorter contributions dealing with a particular question.

Each issue contains "News" and "Book review" sections.

Authors may be of any nationality, but the official language of the journal is English. Papers will be reviewed by unidentified referees.

Manuscripts should be sent to
Editor-in-Chief of IDŐJÁRÁS
P.O. Box 39
H-1675 Budapest, Hungary

in three copies including all illustrations. One set of illustrations has to be of camera ready quality, the other two might be lower quality.

Title part of the paper should contain the concise title, the name(s) of the author(s), the affiliation(s) including postal and E-mail address(es). In case of multiple authors, the cover letter should indicate the corresponding author.

Abstract should follow the title, it contains the purpose, the data and methods as well as the basic conclusion.

Key-words are necessary to help to classify the topic.

The text has to be typed in double spacing with wide margins. Word-processor printing is preferred. The use of SI units are expected. The negative exponent is preferred to solidus. Figures and tables should be consecutively numbered and referred to in the text.

Mathematical formulas are expected to be as simple as possible and numbered in parentheses at the right margin. Non-Latin letters and hand-written symbols should be indicated and explained by making marginal notes in pencil.

Tables should be marked by Arabic numbers and printed in separate sheets together with their captions. Avoid too lengthy or complicated tables.

Figures should be drawn or printed in black and white, without legends, on separate sheets. The legends of figures should be printed as separate list. Good quality laser printings are preferred as master copies.

References: The text citation should contain the name(s) of the author(s) in Italic letter and the year of publication. In case of one author: *Miller* (1989), or if the name of the author cannot be fitted into the text: *(Miller,* 1989); in the case of two authors: *Gamov* and *Cleveland* (1973); if there are more than two authors: *Smith et al.* (1990). When referring to several papers published in the same year by the same author, the year of publication should be followed by letters a,b etc. At the end of the paper the list of references should be arranged alphabetically. For an article: the name(s) of author(s) in Italics, year, title of article, name of journal, volume number (the latter two in Italics) and pages. E.g. *Nathan, K.K.,* 1986: A note on the relationship between photosynthetically active radiation and cloud amount. *Időjárás 90,* 10-13. For a book: the name(s) of author(s), year, title of the book (all in Italics except the year), publisher and place of publication. E.g. *Junge, C. E.,* 1963: *Air Chemistry and Radioactivity*. Academic Press, New York and London.

The final version should be submitted on diskette altogether with one hard copy. Use standard 3.5" or 5.25" DOS formatted diskettes. The preferred word-processors are WordPerfect 5.1 and MS Word 6.0.

Reprints: authors receive 30 reprints free of charge. Additional reprints may be ordered at the authors' expense when sending back the proofs to the Editorial Office.

More information: gmajor@met.hu
Information on the last issues:
http://www.met.hu/firat/ido-e.html

Published by the Hungarian Meteorological Service

Budapest, Hungary

INDEX: 26 361

HU ISSN 0324-6329

IDŐJÁRÁS

QUARTERLY JOURNAL
OF THE HUNGARIAN METEOROLOGICAL SERVICE

CONTENTS

****

http://www.met.hu/firat/ido-e.html

VOL. 104 * NO. 2 * APRIL–JUNE 2000

IDŐJÁRÁS

Quarterly Journal of the Hungarian Meteorological Service

Editor-in-Chief
T. PRÁGER

Executive Editor
M. ANTAL

EDITORIAL BOARD

AMBRÓZY, P. (Budapest, Hungary)
ANTAL, E. (Budapest, Hungary)
BARTHOLY, J. (Budapest, Hungary)
BOZÓ, L. (Budapest, Hungary)
BRIMBLECOMBE, P. (Norwich, U.K.)
CZELNAI, R. (Budapest, Hungary)
DÉVÉNYI, D. (Budapest, Hungary)
DUNKEL, Z. (Brussels, Belgium)
FISHER, B. (Chatham, U.K.)
GELEYN, J.-Fr. (Toulouse, France)
GERESDI, I. (Pécs, Hungary)
GÖTZ, G. (Budapest, Hungary)
HANTEL, M. (Vienna, Austria)
HASZPRA, L. (Budapest, Hungary)
HORÁNYI, A. (Budapest, Hungary)
HORVÁTH, Á. (Siófok, Hungary)
IVÁNYI, Z. (Budapest, Hungary)
KONDRATYEV, K.Ya. (St. Petersburg, Russia)
MAJOR, G. (Budapest, Hungary)
MÉSZÁROS, E. (Veszprém, Hungary)
MIKA, J. (Budapest, Hungary)
MARACCHI, G. (Firenze, Italy)
MERSICH, I. (Budapest, Hungary)
MÖLLER, D. (Berlin, Germany)
NEUWIRTH, F. (Vienna, Austria)
PINTO, J. (R. Triangle Park, NC, U.S.A)
PROBÁLD, F. (Budapest, Hungary)
RENOUX, A. (Paris-Créteil, France)
ROCHARD, G. (Lannion, France)
S. BURÁNSZKY, M. (Budapest, Hungary)
SPÄNKUCH, D. (Potsdam, Germany)
STAROSOLSZKY, Ö. (Budapest, Hungary)
SZALAI, S. (Budapest, Hungary)
SZEPESI, D. (Budapest, Hungary)
TAR, K. (Debrecen, Hungary)
TÄNCZER, T. (Budapest, Hungary)
VALI, G. (Laramie, WY, U.S.A.)
VARGA-HASZONITS, Z. (Mosonmagyaróvár, Hungary)

Editorial Office: P.O. Box 39, H-1675 Budapest, Hungary or
Gilice tér 39, H-1181 Budapest, Hungary
E-mail: prager@met.hu or *antal@met.hu*
Fax: (36-1) 290-7387

Subscription by

mail: IDŐJÁRÁS, P.O. Box 39, H-1675 Budapest, Hungary;
E-mail: prager@met.hu or *antal@met.hu*; *Fax: (36-1) 290-7387*

IDŐJÁRÁS
Quarterly Journal of the Hungarian Meteorological Service
Vol. 104, No. 2, April–June 2000, pp. 67–89

New methods for severe precipitation warning for Hungary

Ágnes Takács[1], **Cecilia Girz**[2], **Edward Tollerud**[2] and **Sándor Kertész**[1]

[1]*Hungarian Meteorological Service, H-1525 Budapest, P.O. Box 38, Hungary;*
E-mail: takacs@fsl.noaa.gov, kertesz.s@met.hu
[2]*NOAA/OAR Forecast Systems Laboratory, 325 Broadway, Mail Code: R/FS1,*
80303 Boulder, Colorado, United States of America
E-mail: girz@fsl.noaa.gov, tollerud@fsl.noaa.gov

(Manuscript submitted for publication 5 November 1999; in final form 17 April 2000)

Abstract—Under a project funded by the United States–Hungarian Science and Technology Joint Fund, research has been conducted to improve the forecasting of extreme rainfall events (often accompanied by flash flooding) in Hungary. Many of these events appear to result from mesoscale circulations, possibly small mesoscale convective systems (MCSs), thus presenting a very challenging forecast problem. Two keys to improving these forecasts are (1) a better physical understanding of the mesoscale circulations that produce severe rainfall, and (2) improved methods to identify and monitor the evolution of potentially dangerous systems as early in their development as possible. Three areas of research have been pursued. First, a variant of the Probable Maximum Precipitation (PMP), the *Possible* Maximum Precipitation (PoMP), has been derived and then employed retrospectively in the diagnosis of several incidents of extreme precipitation that occurred in Hungary during the summer of 1998. One of the events studied, a case of very heavy rainfall in Mosonmagyaróvár on 27 July, is described in detail. In this event as well as the others, PoMP results showed promise as a way to estimate potential severe rainfall. A second area of research involved the implementation and testing of an automated satellite rain estimation technique. Observations from the European Meteorological Satellite (METEOSAT) were used daily to provide precipitation fields over Hungary and neighboring countries. Detailed analyses were made of the extreme precipitation events. Precipitation patterns were generally very widespread and satellite estimates compared poorly with gauge data. Possible reasons for these discrepancies included errors arising from the quality and frequency of the satellite data, questionable applicability of rain-estimation parameters in the mountainous regions surrounding the Carpathian Basin, and the frequent occurrence of embedded convection in these cases. A third area of research involved attempts to qualitatively assess the frequency of occurrence of large MCSs. Although some statistical evidence (primarily the existence of nocturnal maxima of heavy precipitation rates in some regions of Hungary) suggested the existence of MCSs, a qualitative examination of satellite and radar observations during two summers (1997 and 1998) did not uncover the characteristic signatures of Mesoscale Convective Complexes (MCCs), the largest MCSs.

Key-words: flood warning, hydrometeorological techniques, satellite rain estimates, possible maximum precipitation, heavy precipitation, diurnal variation of precipitation.

1. Introduction

Severe weather causes substantial loss of life and much material damage in Hungary. One of the most damaging severe-weather-caused events is extreme rainfall which can produce flash floods, or overflow storm sewers in urban areas. These types of heavy precipitation events are often mesoscale in nature, and therefore present an important challenge to forecasters. Two keys to improving these difficult forecasts are (1) better physical understanding, and (2) improved methods to identify and monitor the evolution and precipitation of potentially dangerous systems as early as possible. This paper describes research intended to advance both these areas.

In Section 2 we present statistical results that address (1) by describing diurnal and other aspects of heavy precipitation events in Hungary. In particular, we discuss the possible contribution of mesoscale convective complexes (MCCs) to dangerous precipitation in Hungary. To address (2), we have developed a forecasting method involving two components: Possible Maximum Precipitation (PoMP) computations and satellite rainfall estimates. Section 3 includes a discussion of the PoMP and the PMP, from which it was derived, and the operational measurements it requires. An earlier application of the method is presented in *Takács et al.* (1998). In Section 4 we describe how we adapted the Griffith-Woodley satellite rainfall estimation technique to make it applicable to conditions in Hungary. Use of pseudo-soundings from runs of the Aladin NWP model (*Horányi et al.*, 1996) is a novel feature of this application. A case study of a heavy precipitation event on 27 and 28 July 1998 in northeast Hungary illustrating this procedure is presented in Section 5.

This paper documents results of a three-year project sponsored by the United States-Hungarian Science and Technology Joint Fund. The reader will find that despite the demonstration of promise of new forecasting techniques, several substantive questions could not be answered by the end of the three years. For these aspects of unfinished research, we have indicated the path that we think is the most fruitful for resolving the issues.

2. Characteristics of heavy precipitation events in Hungary

During background research for this study, we performed statistical analyses of precipitation events in Hungary[1]. To study precipitation intensity and duration,

[1] Results of this research are described in the unpublished manuscript *Development of a warning system for quantitative prediction of heavy rainfall*, the Final Report for the research project entitled "Improvement of meteorological forecasts for hydrological purposes", sponsored by the Ministry of Environment Protection and Water Management, Budapest, 1989, Á. Takács, Project Leader.

we examined several years of short-term precipitation data extracted from paper charts at Hungarian recording stations, concentrating on locally heavy precipitation during a five-year period between 1985 and 1989. Because it was fundamentally important to consider the temporal distribution of precipitation, we only included events during which the core of the precipitation system could be shown to be located over recording stations. This reduced the total possible number of events that we could investigate to 93.

We derived the following information from the precipitation chart recordings:

- start time of heavy precipitation,
- system duration (in tenths of hours),
- total amount of precipitation produced by the system (in mm),
- average intensity of the entire system (in mm h^{-1}),
- duration of the most intense period within the system (in minutes),
- amount of precipitation during the most intense period (in mm),
- intensity of precipitation during the most intense period (in mm h^{-1}).

The average duration of these precipitation systems (*Table 1*) was 6.2 h. In addition to overall statistics, we also investigated mesoscale precipitation systems with an average lifetime of 1 to 6 h. However, due to limitations of the recordings available to us, we were not able to delineate the precipitation cores embedded in synoptic-scale systems in every case. The primary reason for this was the complicated nature of the precipitation fields during many frontal passages. Consequently, we had to reduce the number of cases further by excluding precipitation events that lasted more than 6 h and thus were likely produced by processes operating at scales larger than the convective or meso scales.

Table 1. Heavy rainfall characteristics for Hungary based on 93 cases, 1985-89

Cases	All (n=93)	Duration <6 h (n=58)
Entire system		
Lifetime (h)	6.2	2.5
Precipitation amount (mm)	24.9	20.0
Lifetime average precipitation intensity (mm h^{-1})	8.6	12.0
Most intense period		
Lifetime (min)	7.4	6.7
(h)	0.12	0.11
Precipitation amount (mm)	4.8	5.8
Maximum precipitation intensity (mm h^{-1})	48.0	61.0

It is apparent from Table 1 that shorter system lifetimes result in reduced amounts of total precipitation over the lifetime of the entire system; however, the corresponding precipitation intensity increases significantly. This is also true for the most intense precipitation period within the system. For mesoscale systems lasting less than 6 h, ~30% of the total amount of precipitation comes from the most intense period of the event, in spite of the fact that this period is only about one-twentieth of the entire system lifetime.

An examination of the frequency of precipitation system start times (*Table 2*) reveals that 41% of the events lasting under 6 h begin during the afternoon convective time period between 3 and 5 PM LST, while 19% begin sometime in the 8-h time period between 4 AM and noon LST. If we select cases with core precipitation amounts in excess of 50 mm, the most dangerous 18 events, instead of the 60% during these two time periods for the full set, 72% of the events now develop during these two periods of the day. (Note that this latter percentage is in fact understated given that the morning period for the latter events is two hours shorter.)

Table 2. Diurnal variation of heavy rainfall in Hungary based on 58 cases during 1985–89 with duration <6 h

Cases	All (n=58)	Precipitation amount >50 mm (n=18)
Time of day (LST)		
04:00–12:00	19%	
05:00–11:00		22%
15:00–17:00	41%	50%
Total	60%	72%

The rain events described in this paper are each part of larger synoptic weather patterns. Might they also be part of an MCC, as defined for the largest organized mesoscale convective systems (*Maddox*, 1980)? The occasional occurrence of MCCs or the more generic MCS in the Carpathian Basin is suggested by *Bodolai-Jakus et al.* (1987), who describe heavy rainfall events in Hungary and the Carpathian Basin with features that resemble those in MCCs.

MCCs are defined by the size, shape and duration of the cloud as seen in a thermal infrared satellite image. These large organized convective clouds must attain the criteria outlined in *Table 3*. Consequently, these systems are more than two orders of magnitude larger than individual thunderstorms. Their cousins, the MCSs, have similar characteristcs, but are smaller and last for shorter times.

Table 3. Definition of mesoscale convective complexes (MCC) based on analyses of enhanced IR satellite imagery*

Size†	A. Cloud shield with contiguously low IR temperature ≤-32°C must have an area 100,000 km^2 B. Interior cold cloud region with temperatures ≤-52°C must have an area ≥50,000 km^2
Duration	Size definitions A and B must be met for a period of ≥6h
Maximum extent	Contiguous cold cloud shield (IR temperature ≥-32°C) reaches maximum size
Shape	Eccentricity (minor axis/major axis) must be ≥0.7 at the time of maximum extent

* After *Maddox*(1980)

† Initiation occurs when size definitions A and B are first satisfied. Termination occurs when size definitions A and B are no longer satisfied.

The results of Tables 1 and 2 are in a similar vein. Since one characteristic of MCC precipitation is a tendency for maxima in the few hours after local midnight, the tendency shown in the tables toward increasing rainfall during the early morning hours for the most intense events is at least indicative of mesoscale development. To further address this possibility, we have computed regional statistics for precipitation totals for 6 h diurnal periods during the summer of 1997 using rainfall reports from reporting stations in four regions of Hungary (*Fig. 1*). In all regions (with the exception of the mountainous region of northeast Hungary, where orographic processes tend to dominate), there are maximum precipitation rates in the early morning hours between 00:00 and 06:00 UTC. Diurnal differences are strongest in southeast Hungary. Precipitation frequencies, on the other hand, have the familiar afternoon thunderstorm maxima in all regions (not shown).

Although these overall statistics are consistent with MCC development, the case presented here provided no clear evidence of MCCs in the satellite imagery or other observations. Furthermore, examination of satellite and radar observations in the region of several other severe precipitation events during the summers of 1997 and 1998 did not definitively identify MCC development, although smaller mesoscale systems did undoubtedly occur.

Development of very large MCSs or MCCs in the Carpathian Basin may be limited by several factors. Probably the most compelling is the lack of a continuous low-level moisture supply. A related factor involves the existence of raised terrain on all sides of the Basin, which does not lend itself to the development of a strong low-level jet of the kind that appears to be a critical component of United States MCCs. The only exception is the Southwest, where the warm moist air from the Mediterranean can more easily reach the Basin. Thus, although MCSs and possibly MCCs may form in the Basin, they are likely to be less frequent and usually smaller and shorter lived than the MCCs in the United States, where the terrain is ideal for their development.

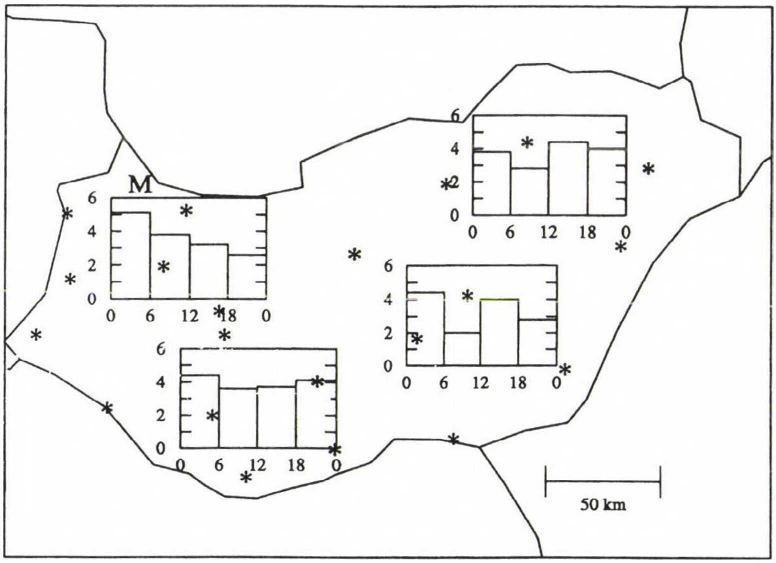

Fig. 1. Diurnal variation of precipitation in four regions of Hungary observed at gauge sites (denoted by asterisk) measuring 6 h precipitation totals. Times along the x-axes are in UTC. Precipitation values (mm) along the y-axes are averaged over all available nonzero observations during June–August 1997. The location of Mosonmagyaróvár is indicated by "M".

3. Possible maximum precipitation method

3.1 General description of precipitation systems

Systems that produce very heavy precipitation in a short period of time are among the most dangerous mesoscale weather phenomena. Although system lifetimes typically vary between 1 and 6 h, they are occasionally as short as 10 to 30 min. Their areal extent is on the order of 10 to 100 km. Frequently these systems cannot be observed with conventional meteorological instruments, making their prediction impossible. Because remote sensors like radar and satellites provide quasi-continuous measurements in space and time, they allow the identification and tracking of these systems during development and later in their lifecycle. These platforms thus provide a basis for prediction, but only for a relatively short lead-time ranging from 0 to 2 h (*Browning*, 1982). Consequently, this type of prediction serves mainly as a means for issuing watches and warnings.

If we wish to study precipitation systems that produce heavy rainfall in a short period of time over a small area, we need to examine all physical processes that play a significant role in producing precipitation. The basic conditions for creating precipitation in the atmosphere (*Harvey*, 1976) are:

- sufficient moisture content,
- cooling of air to its dewpoint (saturation),
- condensation,
- growth of raindrops.

Because in most cases air cools as a result of upward motion, it is very important to examine vertical motion processes. Heavy rainfall develops under conditions of upward vertical motions that exceed those for other precipitation systems by an order of magnitude. Therefore, for the development of intense precipitation systems we need to consider convective ascent, and because this ascent results from the instability of the air column, we need to assess atmospheric instability also.

In almost every case where the above conditions are satisfied, precipitation occurs; however, the precipitation magnitude will not always be large. Consequently, beyond satisfying these conditions, it is important to examine how physical processes change during severe precipitation systems (*Takács*, 1989).

We can examine the physical processes involved in precipitation formation through the parameters describing them. The precipitable water (W_p) is the most appropriate parameter for calculating the moisture content of the atmosphere. This represents the liquid water content that would result from condensation of all water vapor in the atmosphere. It can be calculated for the layer between any two pressure surfaces by using the computational algorithm of *Schlatter* and *Baker* (1981).

The extent of saturation can be expressed by the dynamical saturation deficit (RT–RT_t), given here as the difference between the actual thickness (RT) and the saturation thickness (RT_t) between any two pressure surfaces. The calculation is again performed by using the computational algorithm of *Schlatter* and *Baker* (1981).

In quantitative precipitation forecasts the precipitable water and the saturation deficit are generally determined for the layer between the 1000 and 500 hPa pressure surfaces. For our study, it turned out to be very helpful to calculate these parameters for several layers, including those between 1000 and 925, 925 and 850, 850 and 700, and 700 and 500 hPa. Multiple layers were useful because during periods of intense precipitation moisture parameters like those studied here behave in a dissimilar fashion within the different layers.

We estimated the extent of lifting by using the vertical velocity at the 850 hPa, a level near the middle of the lowest 3 km of the troposphere (*Bodolainé*, 1983). To determine the total lifting during 12 hour periods, we used a regression relation between the isallohyptic field and the vertical velocity calculated from the wind field by the kinematic method.

To approximate atmospheric stability we first applied the well-known Showalter (*SSI*), *K* and *NI* indices in the manner described by *Makainé* and *Tóth* (1978). Because these indices were not sufficient to delineate heavy rainfall situations, we added the Total Totals (*TT*), Vertical Totals (*VT*), and Cross Totals (*CT*) instability indices used by forecasters in the U.S. (*Maddox*, 1979). Definitions of these indices are listed in *Table 4*.

Table 4. Stability indices

Showalter index (SSI)	$SSI = T_{500} - T_{500Parcel}$
K index (K)	$K = (T_{850} - T_{500}) + (T_{d850}) - (T_{700} - T_{d700})$
NI index (NI)	$NI = (T_{850} - T_{d850}) + (T_{700} - T_{d700}) + (T_{500} - T_{d500})$
Total Totals (TT)	$TT = (T_{850} + T_{d850}) - 2T_{500}$
Vertical Totals (VT)	$VT = T_{850} - T_{500}$
Cross Totals (CT)	$CT = T_{d850} - T_{500}$

where T_{850} is 850 hPa temperature
T_{700} is 700 hPa temperature
T_{500} is 500 hPa temperature
$T_{500Parcel}$ is lifted parcel temperature at 500 hPa
T_{d850} is 850 hPa dewpoint temperature
T_{d700} is 700 hPa dewpoint temperature
T_{d500} is 500 hPa dewpoint temperature

The condensation level and the expected height of the cloud tops were used to estimate the size of the cumulonimbus storm clouds. We used hand analysis methods to deal with phenomena that cannot be easily parameterized. These included specific configurations of pressure and temperature, high- or low-level jets, and areas with wind speeds exceeding the surrounding environment.

3.2 Estimating the location of heavy convective rainfall

To correctly estimate and apply the parameters that describe precipitation-producing physical processes for heavy rainfall forecasting or warning, we need to understand their behavior when such precipitation systems occur. For this part of the study, we used the same 93 cases for which heavy precipitation statistics were described in Section 2. We determined the average value of all parameters in our set of heavy precipitation cases and used these averages as first approximations to parameter thresholds.

With these thresholds in mind, it is possible to determine regions with the highest likelihood of heavy rainfall by overlaying analyzed parameter fields on a composite chart and locating common areas where the individual parameters exceeded or closely approached their thresholds. Analyses were performed using sounding data at times closest to the time of interest. *Fig. 2* shows a composite chart where this common area is clearly indicated and where heavy precipitation did in fact occur. (We have plotted only three parameters in the figure for ease of visualization.)

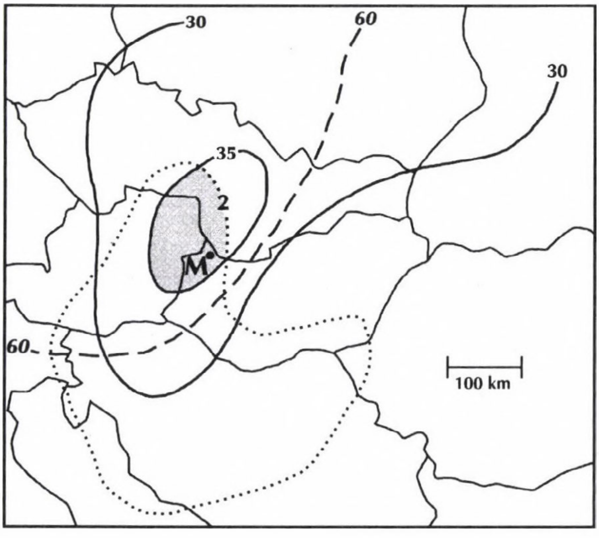

Fig. 2. Composite chart produced from observations at 00:00 UTC on 28 July 1998. The dotted contour encloses SSI values smaller than 2, solid contours are W_p in units of mm, and the dashed contour encloses RT–RT_t values smaller than 60 gpm. Within the shaded area all parameters exceed threshold values. "M" denotes the location of measured rainfall of 132 mm at Mosonmagyaróvár.

Conventional meteorological observing systems do not lend themselves to the determination of the time of initiation of precipitation. To do this, we need meteorological radar and satellite measurements, preferably in digital form. Because the main objective of our paper is to improve our ability to estimate and forecast the amount of heavy rainfall, we do not directly consider the issue of convective initiation.

3.3 Estimating the magnitude of heavy rainfall with the PoMP method

In our experience, numerical forecast models generally underestimate the magnitude of extreme precipitation events. Therefore, our main goal is to demonstrate a method suitable for estimating the actual amount of precipitation for situations in which very large amounts can be expected.

Our method is based on the Probable Maximum Precipitation (PMP) estimation technique. Conceptually, the PMP is the greatest depth of precipitation that is physically possible for a given storm area and duration (*Hansen et al.*, 1982). This value will vary with geographical location and time of year.

In actual atmospheric situations, the PMP will be impossible to achieve because of atmospheric constraints on the production of rainfall. Thus, the PMP will be an unrealistically large estimate. We hypothesize, however, that if the PMP exists and can be accurately determined, then it can also be used to provide an upper limit of precipitation potential for actual atmospheric situations. For the sake of distinguishing it from the Probable Maximum Precipitation, we designated this more restricted estimate the *Possible* Maximum Precipitation, or PoMP.

One method to estimate the PoMP is to maximize the individual components of the formula used to calculate the precipitation amount P (mm/12 h):

$$P = \frac{W_p w}{RT - RT_t}, \tag{1}$$

where

W_p = potential precipitable water (mm) between 1000 and 500 hPa levels;
w = vertical velocity (gpm/12 h) at the 850 hPa level; and
$RT - RT_t$ = dynamical saturation deficit (gpm) between 1000 and 500 hPa levels. (This formula is part of the Meeting Model which is used operationally for quantitative precipitation forecasts at the HMS; see *Bodolainé*, 1983).

Similar to our earlier studies (Section 3.2), we use average component values computed from case studies as thresholds when the computed components are less than these averages. However, when the actual computed values are larger than their thresholds, we use those instead. We remark here that in the case of W_p, the value computed for the layer between 1000 and 500 hPa levels results in good estimates for P. By the same token, the dynamical saturation deficit in either of the two lower layers (between 1000 and 925, or 925 and 850 hPa) provides a better estimate of heavy rainfall amount. This suggests that for the occurrence of extreme precipitation it is necessary to have high moisture content throughout the entire air column, while saturation in lower layers is sufficient to satisfy the condition of heavy rainfall.

By performing the estimation for all radiosonde stations, we obtain a precipitation field which shows the possible maximum values at all points. In reality, of course, these values will never occur simultaneously over the entire field. However, we hope that at any given point the PoMP will provide forecasters with a satisfactory first-guess estimate of precipitation amount in case extreme rainfall does in fact occur. The estimation can be performed after each radiosonde measurement, so that in practice we can have a newly estimated field every 12 h.

We performed an experiment on an independent sample of rainfall events (not shown), which indicated 67% agreement between the PoMP prediction of heavy rainfall and actual events. We consider this good result to be a partial confirmation of this method. We believe that the results can be further improved if we consider hourly surface measurements and, in particular, radar and meteorological satellite measurements to periodically correct the first-guess field.

4. Satellite rainfall estimates

4.1 The Griffith-Woodley technique

The Griffith-Woodley satellite rain estimation technique is an empirical scheme originally developed for estimating convective rainfall in the subtropics (*Griffith et al.*, 1978) and the tropics (*Woodley et al.*, 1980; *Augustine et al.*, 1981). The technique involves several assumptions. First is that convective clouds, whether they are observed on satellite images or as radar echoes, follow a life cycle during which rain amount increases to some peak amount, then drops off as the cloud rains out and the visual cloud dissipates. The technique also assumes that the amount of rain produced varies with the size of the cloud—bigger clouds, as well as clouds with colder tops, produce more rain than their smaller, warmer cousins.

The technique uses a sequence of digital, thermal infrared satellite images to compute rainfall automatically. In deriving the technique, convective clouds were identified on the Synchronous Meteorological and Geostationary Operational Environmental Satellite (SMS/GOES) thermal infrared images, and were calibrated with a combined system of WSR-57 (10-cm S-band) weather radar data and hourly rain gauge data from a dense network (1 gauge per square mile) in south Florida, USA. Since not all clouds produce rain, a study was performed to determine the temperature that identifies raining clouds with the result that raining clouds are defined to be those clouds that are –20°C or colder, and it is this temperature that determines the area of the cloud. Rain volume (R_v) is estimated for each cloud as a function of the size of the cloud, the cloud-top temperature, and whether the cloud is increasing or decreasing in size:

$$R_v = I \cdot < A_e/A_m > \cdot A_m \cdot \Delta t \cdot \sum [a(i) \cdot b(i)] \cdot 10, \tag{2}$$

where

R_v is rain volume for a single cloud (m^3),

I is rain rate (mm h^{-1}) derived from radar echo data,

A_e is radar echo area (km^2),

A_m is maximum area during a cloud's lifetime (km^2),

$<A_e/A_m>$ is an inferred coverage of the radar echo area for the cloud,

Δt is the time interval between successive satellite images (h),

the *summation* produces more rain for clouds with tops colder than -20°C,

a is the fractional coverage of the cloud for temperatures colder than -20°C,

b is an empirical weighting coefficient that increases rainfall for clouds colder than -20°C,

and the *factor* of 10 accounts for conversion among units.

The period of the rain is the time of the image forward to the time of the next image. Thus, if satellite images are at 30-min intervals, the calculated rain represents rain ending 30 min after the image time. The value of the coefficient b is computed from

$$b = \exp(0.02667 + 0.01547D)/11.1249 \qquad 154 \leq D < 176, \tag{3a}$$

$$b = \exp(0.11537 + 0.01494D)/11.1249 \qquad 176 \leq D \leq 255, \tag{3b}$$

where

D is digital count from the GOES IR image.

Rain volume is not the usual variable; rainfall amounts are typically reported and displayed. Consequently, a scheme to derive isohyets, referred to as the "10/50–40/50" apportionment scheme, has been devised. The scheme is named the "10/50–40/50" apportionment because it apportions half of the total rain volume to the coldest 10% of the cloud ("10/50"). The remaining 50% of the rain volume is apportioned to the other half of the cloud, that is, to the second coldest 40% of the cloud ("40/50"). The motivation for this is the following. The -20°C temperature contour is used to identify raining clouds, to calculate cloud area, and to compute the volume estimate, but we know from studies performed during the technique's calibration that rain does not fall under the entire -20°C area. In growing and mature systems, the overshooting tops are the coldest part of the cloud, and represent its most active part. Thus, we attribute the active rainfall area to only the coldest half of the cloud, and make rain amount a function of cloud-top temperature as well. To compute rain amount, cloud-top temperatures are ranked coldest to warmest, and pixels in the coldest 50% have the following amount of rain:

$$D_{i,j} = \{[(R_v/2) \cdot b_{ij}]/(g_{ij} \cdot \sum b)\} \cdot 10^{-3}, \tag{4}$$

where

$D_{i,j}$ is rain amount (mm) in the satellite *i,j* pixel,
$R_v/2$ is one-half of the cloud's rain volume (m^3) on a particular image,
b_{ij} is the empirical weighting coefficient for the *i,j* pixel,
g_{ij} is the area (km^2) of the *i,j* pixel,
the sum is over the coldest 10% (or second coldest 40%) of the pixels, and the factor of 10^{-3} converts among units.

Although the Griffith-Woodley rain estimate technique was derived for tropical and semi-tropical situations, the technique was modified to work in the midlatitudes by accounting for environmental differences between Florida and the location of interest. The underlying assumption is that the dynamical processes of convective clouds are similar no matter where they occur, but that it is differences in moisture in lower levels, entrainment at midlevel, and cloud height and horizontal extent that produce differences in rainfall amount. *Griffith et al.* (1981) used a one-dimensional cumulus cloud model (*Simpson* and *Wiggert*, 1969; 1971) to correct for these differences. Mandatory- and significant-level data from an atmospheric sounding are input for the 1-D model. The model performs a single-sounding analysis, computing cloud base, cloud top, and precipitation production, using Kessler's cloud physics scheme for 8 thermal bubble sizes, ranging from 500 to 3,000 m. Model output consists of cloud-top height (m), and cloud water (g kg^{-1}).

Because the appropriate bubble radius is not known *a priori*, the average *(Rbar)* and standard deviation *(σ)* of the model-predicted cloud water of the 8 bubbles are computed each time a sounding (or pseudo-sounding) is run. An environmental correction factor, the model adjustment factor *(MAF)* is computed from the average and standard deviation:

$$MAF = (Rbar \cdot \sigma) / (Rbar_F \cdot \sigma_F), \tag{5}$$

where $Rbar_F$ and σ_F are the mean and standard deviation based on an average Florida sounding. The values of $Rbar_F$ and σ_F are 10.210 g kg^{-1} and 4.195 g kg^{-1}, respectively. A sample output from the 1-D cloud model and *MAF* computation is shown in *Table 5* for an Aladin pseudo-sounding from Budapest. Since this sounding produces cloud water values that are smaller than the average values for Florida, the estimated satellite rainfall for this region is reduced by a factor of 0.51.

Model adjustment factors are computed at every sounding location available at a given time. The *MAFs* are interpolated to the satellite grid using a Barnes interpolation scheme (*Barnes*, 1964) to produce a field of model adjustment factors. The gridded satellite estimates are multiplied by this 2-D field of *MAF*s to produce an environmentally corrected rain estimate.

Table 5. 1-D cloud model output for the 21:00 UTC Aladin pseudo-sounding for Budapest, Hungary on 27 July 1998

Radius (m)	Cloud water ($g\ kg^{-1}$)
500	1.133
750	3.711
1000	5.818
1250	8.004
1500	8.539
2000	9.177
2500	9.584
3000	9.865
Average	6.979
σ	3.154
MAF	0.51

4.2 Modifications for operational use at HMS

The FORTRAN code for the Griffith-Woodley technique with several modifications was transferred for use in Hungary. The first modification was to translate between METEOSAT and GOES digital counts. For both GOES and METEOSAT, counts range from 0 to 256. However, GOES counts are inverted (cold tops have high counts, warm tops have low counts) compared to METEOSAT data. A relationship between METEOSAT counts and brightness temperature was provided by the Satellite Laboratory of the HMS for 6 and 7 July 1997, and from this relationship a second-order polynomial was fit to the GOES and METEOSAT data. METEOSAT counts are converted to equivalent GOES counts before the rain computation is done.

A second modification was to use the so-called streamlined version of the technique. Eq. (2) describes the life history technique, which is a diagnostic technique. Before a calculation of a cloud's rainfall can be computed, a sequence of images showing a relative maximum in cloud area must be in hand. The life history technique clearly cannot make estimates in real time. The streamlined version remedies this by assuming a fixed value of 16.7×10^2 mm h^{-1} for the rainfall rate, I. The echo coverage ratio ($<A_e/A_m>$) also assumes a fixed value which varies with the size of the cloud—0.067 for clouds larger than 10,000 km^2, 0.047 for clouds between 2,000 and 10,000 km^2, and 0.016 for clouds smaller than 2,000 km^2. Eq. (2) then becomes

$$R_v = C \cdot A_m \cdot \Delta t \cdot \Sigma[a(i) \cdot b(i)] \cdot 10, \tag{6}$$

where C is 26.72, 78.49, or 111.89 depending on cloud size as noted above, and, unlike Eq. (2), A_m is cloud *area* measured on the picture of interest, not maximum area. The other terms are as defined before.

Third, twice daily operational sounding data are usually used to calculate the model adjustment factor. At the HMS, we tested the suitability of pseudo-soundings available every three h from the Aladin model (*Horányi et al.*, 1996). This meant that model adjustment factors were updated every 3 h using the model data, rather than every 12 h from the temperature (i.e., sounding) data. Also, pseudo-soundings can be generated from the model for any location where extreme rains are possible. Thus PoMP no longer has to be dependent on the operational soundings in a small number of locations.

Last, at the time of the study operationally available satellite data at the HMS consisted of two types: digital data that are transmitted every three hours, and digitalized METEOSAT images at 30-min intervals filling the gap between the digital images. We decided to use both the digital and digitalized images in the rain computation in order to have a more complete record of the temporal evolution of the clouds. The implications of this are discussed below.

5. Case study

5.1 Synoptic situation

On 27 and 28 July, 1998, a relatively slow-moving, active cold front passed over the Carpathian Basin (*Fig. 3*). Ahead of the front on the 27th, a warm, very moist air mass moved into the warm sector, raising maximum temperatures over most of Hungary above 30°C. On that day, severe thunderstorms initially developed in the warm sector over the Kisalföld region of Hungary, later spreading into the eastern half of the country. Substantial precipitation (20–30 mm) fell in the northwest; in Mosonmagyaróvár an impressive 132 mm was measured during a 1.5 h period between 2300 UTC on 27 July and 0100 on 28 July (*Fig. 4*). Hail was also observed here.

The following contributed to the heavy precipitation:

- the large amount of precipitable water (32–35 mm);
- near-saturation atmospheric conditions (<60 gpm);
- surface wind convergence;
- the development of significant temperature contrast and wind convergence at the 850 hPa level; and
- an area of higher windspeed at 500 hPa (>25 m s^{-1}).

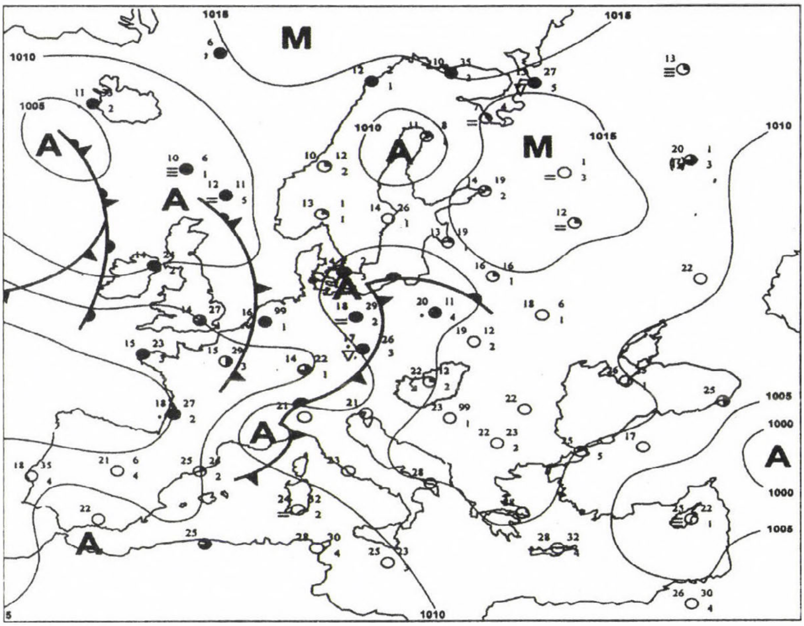

Fig. 3. Synoptic map for 00:00 UTC 28 July 1998 provided courtesy of the Hungarian Meteorological Service.

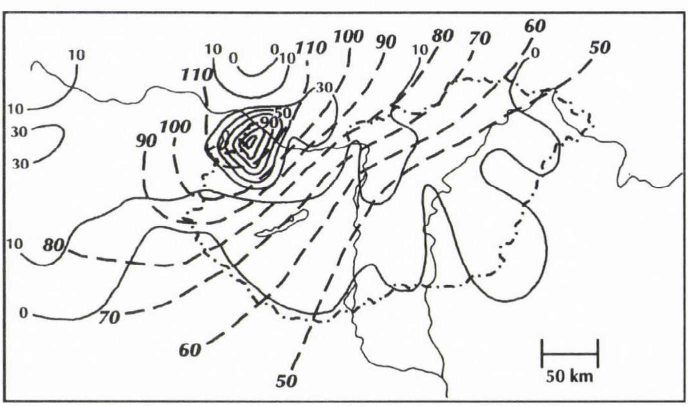

Fig. 4. PoMP (mm) for 00:00 UTC 28 July 1998 (dashed contours) and precipitation (mm) observed between 06:00 UTC 27 July and 06:00 UTC 28 July (solid contours).

5.2 PoMP results

Using parameters that describe the above-mentioned phenomena, a composite chart (Fig. 2) was created from 00:00 UTC 28 July radiosonde observations. From the chart, it is possible to delineate a high-risk area within which severe local precipitation may occur. Estimates of this area given by the PoMP computed by the previously described method are shown on Fig. 4. In this case, the method worked quite well; it is apparent that both the location of the precipitation maximum and its magnitude were accurately estimated.

5.3 Satellite rainfall estimates

Satellite estimates for each day during summer 1998 were computed in near real time using the digital plus the digitalized METEOSAT imagery. These results will be referred to as the D+D set. In general, the satellite estimated rainfalls were too large compared to the gauge amounts, and the areal extent of the satellite rains seemed to be greater than indicated by the gauge data. A statistical comparison of satellite and gauge amounts for the 24-h period ending at 06:00 UTC 28 July 1998 bears this out. For this comparison, the half-hourly satellite estimates were bilinearly interpolated to gauge locations, and then summed. Point comparisons are made for the operational gauge data from the Carpathian Basin. Gauge data have been provided by the Meteorological Service of the Hungarian Republic, and the national weather services of neighboring countries.

The average D+D satellite estimates are much larger than their gauge counterparts (31.4 vs. 7.9 mm) and have greater standard deviations (52.8 vs. 15.2 mm) (see *Table 6*). Median values for the gauge and satellite data sets are very small (0.8 and 0.0 mm, respectively) because of the large number of reports of no rainfall for this day. Approximately one-third of the gauges and about half the satellite estimates are zero. When the zero values are removed (see the lower half of Table 6), the satellite average and median values (65.0 and 51.3 mm, respectively) are five to six times larger than the gauge average and median values (12.2 and 8.8 mm, respectively). The bias (defined as the satellite estimate less the gauge amount) and root mean square error (defined as the square root of the average of the squared bias) are also very large, being 23.5 and 53.7 mm, respectively.

A plot of these 112 points (*Fig. 5*) shows that the data are widely scattered with low correlation (0.41). Satellite rainfalls are more likely to overestimate the gauge rainfalls than to underestimate them. For the two satellite outliers at small gauge rainfalls, the satellite estimates (which are on the order of 250 mm) are a factor of 10 greater than the gauge amounts (which are on the order of 20 mm). The heaviest rainfall of 132.1 mm occurred at Mosonmagyaróvár. Storm total rainfall from the satellite estimate in the four pixels surrounding this gauge have values of 60.8, 72.6, 104.4, and 130.2 mm. The interpolated satellite amount is 85.7 mm, about one-third smaller than the actual amount.

Table 6. Sample statistics for 24 h accumulated rainfalls ending 06:00 UTC 28 July 1998

	D + D	Gauge	DO
Number	112	112	112
Average (mm)	31.4	7.9	25.7
Standard deviation (mm)	52.8	15.2	52.0
Median (mm)	0.0	0.8	0.0
Bias (mm)	23.5	-	33.6
RMS error (mm)	53.7	-	51.2
No. non-zeros	54	72	45
Average (mm)	65.0	12.2	63.9
Standard deviation (mm)	76.4	19.0	82.6
Median (mm)	51.3	8.8	36.3
Bias (mm)	36.0	-	54.5
RMS error (mm)	66.5	-	63.5

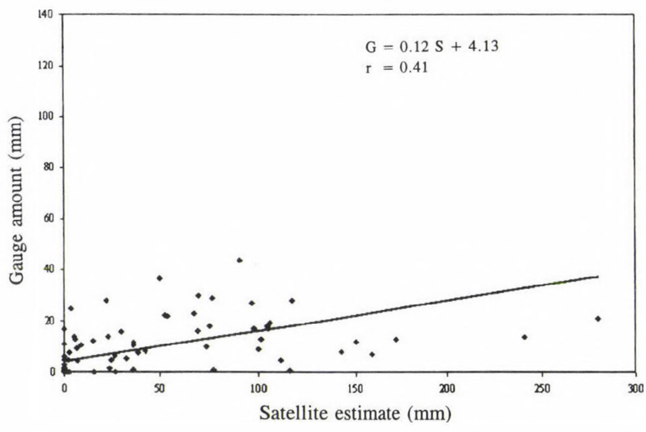

Fig. 5. Scatterplot of the satellite estimates from the digital plus digitalized data set for the images between 09:00 UTC 27 July 1998 and 06:00 UTC 28 July 1998, and their corresponding gauge amounts for the 24 h period ending 06:00 UTC 28 July 1998. The regression fit and correlation coefficient are also shown.

There are several reasons why satellite estimates and gauge observations should differ. The most obvious is that satellite estimates represent rain amounts averaged over much larger regions than the gauge rainfalls. A satellite pixel nominally represents $\sim 50\ km^2$. In convective rains, gauge amounts may be representative of only $10\ km^2$ or less. Consequently, satellite amounts should be expected to underestimate peak rainfalls for convective systems. This has been found in previous verification studies (*Griffith et al.*, 1978; *Augustine et al.*, 1981; *Griffith et al.*, 1981; *Griffith*, 1987). However, in this study overestimation by the satellite was more likely to occur.

RMS errors between satellite and gauge amounts of 50 to 70 mm are much larger than those seen in a previous summertime application of the technique (*Griffith*, 1987), where rms errors for daily point rainfalls were about 15 mm. (Correlations were comparable.) It was suspected that the digitalized imagery was a source of error in the rain estimates. There are large differences between the appearance of clouds in the digital and digitalized images. The digitalized images appear to have a smaller range of brightness, and the clouds look fuzzier. The rainfall patterns (*Fig. 6*) are dramatically different. Thirty-minute rainfalls computed from a digital image (*Fig. 6a*) are fairly smooth, whereas those computed from the digitalized image (*Fig. 6b*) have many centers of rain maxima. It is unlikely that the cloud has changed this drastically in 30 minutes. In fact, there is always a similar looking discontinuity in the isohyets between every pair of digital and digitalized images. These localized bright spots in the digitalized data produce overestimates in the satellite rains.

The drawback of the digital data set is that these images are available only every 3 hours. The effect of infrequent images is also toward overestimation. In the technique, cloud top temperatures are assumed to be static between images. This assumption is obviously not true, but it's not too bad an assumption for time periods short compared to the life time of the cloud. However, when there are no more frequent images then every three hours, and the growth or decay of the cloud is not updated, the computed rain that is extrapolated from this single image is generally too great compared to the actual rain falling in the subsequent three hours.

Nevertheless, to test the effect of the digitalized data, satellite rainfalls were estimated using only the digital images (DO). *Fig. 7* is a scatterplot of estimated rain amounts from the DO imagery versus gauge amounts. Average values and standard deviations of the satellite estimates (Table 6) are still much larger than the gauge values, but less than the estimates for the D+D data. The satellite-estimated rainfall at Mosonmagyaróvár has increased significantly (to 112 mm, interpolated from 17.3, 67.2, 68.7, and 194.3 mm), but so have the estimated rains for the two outliers in the upper right-hand corner of Fig. 6. These now exceed 270 mm.

One last meteorological factor needs to be addressed. While there is convection on this day, it is embedded in the front. The Griffith-Woodley rain estimation technique was derived for free convection, and its most successful applications are for isolated convective systems. In an unpublished study of the application of this technique to embedded convection ahead of fronts in the United States during the winter, we found poor comparisons between the satellite and gauge results.

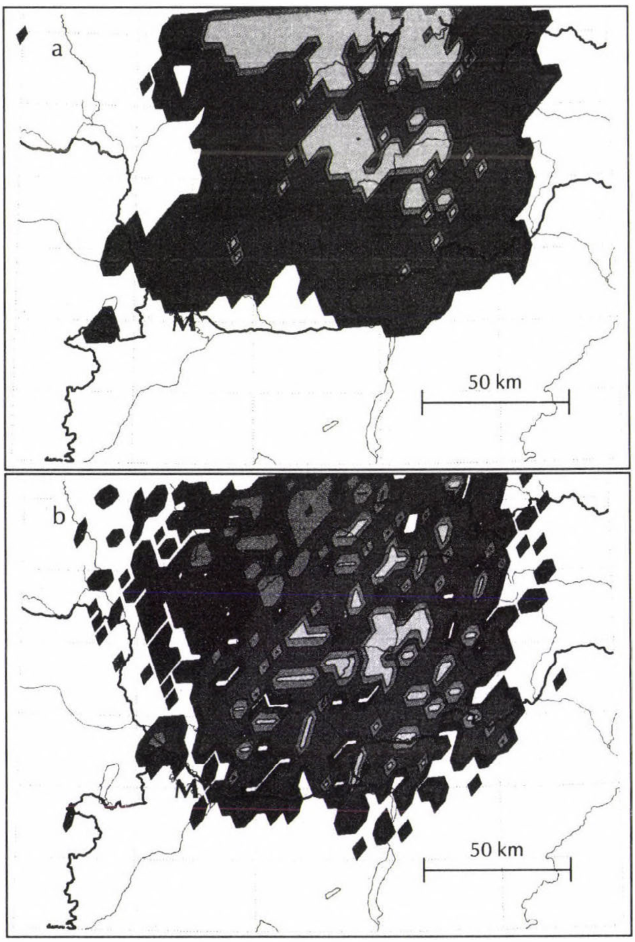

Fig. 6. Satellite estimates of 30-min rainfall on 27 July 1998 (*a*) at 21:00 UTC for a digital and (*b*) at 21:30 UTC for a digitalized image. Rainfall contours are 0–5 mm (dark grey), 5–10 mm (medium dark grey), 10–20 mm (medium light grey), and >20 mm (light grey). The heavy solid line running horizontally across each panel is the border between Hungary and the Slovak Republic. The location of Mosonmagyaróvár is indicated in each panel by "M".

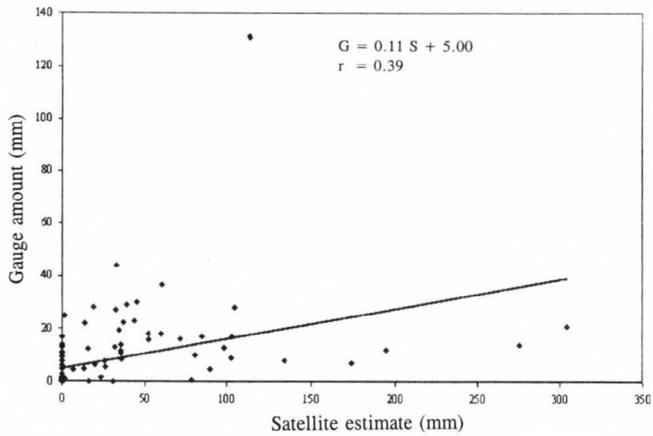

Fig. 7. Same as *Fig. 5*, but for the digital only (DO) images between 09:00 UTC 27 July 1998 and 06:00 UTC 28 July 1998.

6. Conclusions

The success of the PoMP method in delineating regions of heavy precipitation in the case study presented here suggests that it can be used to provide a first-guess estimate for the amount of heavy rainfall during episodes of large precipitation. These estimates are likely to be more realistic than precipitation output from numerical weather prediction (NWP) models, which tend to underestimate rainfall in these situations. Operational runs of the satellite rain estimation technique timed to update the PoMP fields during potentially serious rainfall episodes could add critical lead time to heavy rainfall warnings. This would be particularly true if soundings from NWP models like Aladin were used to produce the necessary map adjustment factors at times that are several hours removed from synoptic radiosonde observations. Ultimately, the hope is to provide warnings that are more timely and more accurate, and thus more likely to save lives and property.

For the Mosonmagyaróvár case and two others not shown, satellite rain estimates from the D+D imagery overestimated the rain measured by the gauges in the mean, and underestimated the maximum rainfall at the location of the event. The overestimation appears to be caused in part by use of the digitalized imagery. For the maximum gauge amounts, the satellite appears to have underestimated rain because of the relatively coarser resolution of the satellite pixels and the bilinear interpolation of the satellite data to gauge location. In fact, individual pixel rainfalls in the vicinity of the gauge locations could be quite close to the gauge value. Differences between gauge and satellite values did not seem to be related to the model adjustment factor. Use of pseudo soundings from Aladin produced reasonable results for the model adjustment factors, despite the limitation that only the mandatory levels are generated.

Two questions about the rainfall estimates remain unanswered. The error in the DO results arising from the 3-h temporal resolution of the digitized imagery is unknown. Similarly, we also could not adequately assess effects arising from the fact that these systems predominantly consist of embedded convection ahead of fronts, for which the Griffith-Woodley technique is known to perform poorly in the winter.

At the Hungarian Meteorological Service, satellite rain estimates are now computed operationally in near real time, are available to forecasters, and are shown at the daily weather briefing. Since the availability of the digital EUMETSAT imagery every 30 min, the satellite estimates appear to cover smaller areas, and to compare better with the gauge data. Analysis of these newer results awaits further study.

Finally, during the course of our study we have learned more about the nature of heavy rainfall-producing systems from the statistical evaluations of parameter thresholds applied in the PoMP computations and from studies of the nocturnal pattern of Hungarian rainfall. More complete studies of heavy rainfall events would undoubtedly help to make these methods more reliable.

Acknowledgments—We thank *Márta S. Buránszki* and *András Horányi* of the Hungarian Meteorological Service for their help during the course of this project. *Imre Bonta* (also of the HMS) provided important analyses of the synoptic conditions for several of the events studied during 1998. We thank *Woody Roberts* of the Forecast Systems Laboratory and *Dongsoo Kim* of the Forecast Systems Laboratory and the Cooperative Institute for Research on the Atmosphere (CIRA) for their useful comments on an early version of this paper, and *Nita Fullerton* of the Forecast Systems Laboratory for a thorough technical review. *John Osborn* of the Forecast Systems Laboratory prepared figures used in this paper. This project is sponsored by the U.S.–Hungarian Science and Technology Joint Fund in cooperation with the Forecast Systems Laboratory and the Hungarian Meteorological Service under Project 523.

References

Augustine, J.A., Griffith, C.G., Woodley, W.L. and *Meitin, J.G.*, 1981: Insights into errors of SMS-inferred GATE convective rainfall. *J. Appl. Meteor. 20*, 509-520.

Barnes, S.L., 1964: A technique for maximizing details in numerical weather map analysis. *J. Appl. Meteor. 3*, 396-409.

Bodolai-Jakus, E., Kapovits, A., Tänczer, T. and *Pintér, F.*, 1987: Detailed Analysis of a meso- scale convective complex situation in the Carpathian Basin. *Proc. Symp. Mesoscale Analysis & Forecasting*, Vancouver, Canada, ESA SP-282, 345-350.

Bodolainé, J.E., 1983: Synoptic conditions of floods over the Danube and the Tisza River Basins (in Hungarian). Országos Meteorológiai Szolgálat Hivatalos Kiadványai XVI, Budapest.

Bodolainé, J.E., 1997: Conceptual models of mesoscale convective systems in Middle Europe (in Hungarian). *Légkör*, Vol. XLII., No. 4., 10-16.

Browning, K.A. (ed.), 1982: *Nowcasting*. Academic Press, London.

Griffith, C.G., 1987: Comparisons of gauge and satellite rain estimates for the central United States during August 1979. *J. Geophys. Res.-Atmospheres 92*, 9551-9566.
Griffith, C.G., Woodley, W.L., Grube, P.G., Martin, D.W., Stout, J. and *Sikdar, D.N.*, 1978: Rain estimation from geosynchronous satellite imagery — visible and infrared studies. *Mon. Wea. Rev. 106*, 1153-1171.
Griffith, C.G., Augustine, J.A. and *Woodley, W.L.*, 1981: Satellite rain estimation in the U.S. High Plains. *J. Appl. Meteor. 20*, 53-66.
Hansen, E.M., Schreiner, L.C. and *Miller, J.F.*, 1982: Application of probable maximum precipitation estimates - United States East of the 105th meridian. *Hydrometeorological Report*, No. 52. National Weather Service, NOAA, US Department of Commerce, Washington, DC. 168 pp.
Harvey, J.G., 1976: *Atmosphere and Ocean. Our Fluid Environments*. The Artemis Press, Sussex.
Horányi, A., Ihász, I. and *Radnóti, G.*,1996: ARPEGE/ALADIN: A numerical weather prediction model for Central-Europe with the participation of the Hungarian Meteorological Service. *Időjárás 100*, 277-301.
Maddox, R.A., 1979: A methodology for forecasting heavy convective precipitation and flash flooding. *National Weather Digest: Flood 4.*
Maddox, R.A., 1980: Mesoscale Convective Complexes. *Bull. Amer Meteor. Soc. 61*, 1374-1387.
Makainé, Cs.M. and *Tóth, P.*, 1978: *Synoptic meteorology*. Tankönyvkiadó, Budapest.
Schlatter, T.W. and *Baker, D.V.*, 1981: Algorithms for thermodynamic calculations. PROFS Program Office, NOAA ERL. Boulder, CO. (Copy is available from the Forecast Systems Laboratory, R/FS1, 325 Broadway, Boulder, CO 80304-3328.)
Simpson, J. and *Wiggert, V.*, 1969: Models of precipitating cumulus towers. *Mon. Wea. Rev. 97*, 471-489.
Simpson, J. and *Wiggert, V.*, 1971: 1968 Florida cumulus seeding experiment: numerical model results. *Mon. Wea. Rev. 99*, 87-118.
Takács, Á., 1989: Monitoring of weather conditions on mesoscale to improve a precipitation warning system for hydrological purposes. IAHS Third Int. Assembly, Baltimore, MD. *IAHS Publ.* No. 186, 117-123.
Takács, Á., Tollerud, E.I. and *Girz, C.M.I.R.*, 1998: Improving convective forecasts in Hungary. Preprints, *16th Conference on Weather Analysis and Forecasting*, Phoenix, AZ, USA. Amer. Meteor. Soc., 118-120.
Woodley, W.L., Griffith, C.G., Griffin, J.S. and *Stromatt, S.C.*, 1980: The inference of GATE convective rainfall from SMS-1 imagery. *J. Appl. Meteor. 19*, 388-408.

IDŐJÁRÁS

Quarterly Journal of the Hungarian Meteorological Service
Vol. 104, No. 2, April–June 2000, pp. 91–107

Sensitivity of forecast trajectories to wind data inputs during strong local wind conditions

Lazar Lazić[1] and **Ivana Tošić**

Department of Meteorology, University of Belgrade, P.O. Box 368
YU-11001 Belgrade, Yugoslavia; E-mail: lazar@afrodita.rcub.bg.ac.yu

(Manuscript submitted for publication 3 November 1999; in final form 25 February 2000)

Abstract—Forecast reference trajectories and forecast trajectories with different wind data frequencies were computed for two local winds, Bora and Koshawa, at eight vertical levels using Eta Model. 48 h real data simulations of local wind cases were achieved with a 28 km horizontal resolution and 16 layers in the vertical. Numerical experiments with different frequencies of wind data in trajectory calculations (90 s – control case, 15 min, 30 min, 1 h, 3 h, 6 h and 12 h) over the Bora and Koshawa wind regions were performed. These are motivated by theoretically based expectations that a certain intermediate wind data frequency is required for accurate forecast trajectory of downslope and windstorms with Bora and Koshawa wind properties. Three-dimensional forecast trajectories over real mountains with various wind data frequencies were calculated and analysed. The total number of trajectories is 280 in each data set.

Mean absolute error (distance between reference and forecast trajectory), mean relative error (mean absolute error divided by mean reference trajectory for the total transport distance) in both horizontal and vertical directions are computed. The 4515 locations are compared with the control case. The mean relative error for all forecast trajectories is about 30% in Bora case and 20% in Koshawa case. Trajectories with wind data frequency of 15 min, 30 min and 1 h are accurate enough, the mean relative error is less than 10% in Bora case and less than 5% in Koshawa case. The mean relative error of parcel positions along trajectories shows large values in case of 3 h, 6 h and 12 h wind data frequencies, especially in vertical direction. In general, Koshawa case was less sensitive to the temporal frequency of wind data than Bora case.

The maximum of the mean relative error (about 200%) is associated with forecast trajectories in vertical direction in case of 12 h wind data frequency of Bora wind. This result suggests that trajectories calculated from the analysed wind data (12 h data frequency) are not accurate when they are used. This result also indicates the importance of using vertical velocity for calculating trajectories.

Key-words: Eta Model, forecast trajectories, wind data frequency, strong local winds, Bora, Koshawa, mean absolute error, mean relative error.

---

[1] Corresponding author

1. Introduction

Air parcel trajectories have been extensively used over the past decade to study the atmospheric transport because they are relatively simple to compute. An individual trajectory gives only a general description of the flow field. Trajectories can be calculated from observed wind data or wind fields simulated by a numerical model.

The construction of three-dimensional atmospheric trajectories provides a valuable diagnostic tool for illustrating and studying the three-dimensional flow fields, their structure and associated transports, exchange processes associated with extratropical weather disturbances, stratospheric and tropospheric air mass exchanges associated with a jet stream, dispersal of upper atmospheric pollutants and possible nuclear contamination (*Petersen* and *Uccellini*, 1979).

Doty and *Perkey* (1993) examined trajectories in the vicinity of an intense extratropical cyclone using data of various temporal resolutions from 15 min to 12 h. They found small errors (75 km or less) at high-resolution data (15 min to 1 h) and much higher errors (100–500 km) with 3 h data. Regarding the spatial density of data, *McQueen* and *Draxler* (1994) found less error with a higher data density.

Trajectory error may be related to synoptic conditions as well. *Rolph* and *Draxler* (1990) found nearly constant relative error (absolute error divided by forecast trajectory total transport distance), but larger absolute error during cyclonic conditions with strong winds as compared to anticyclonic conditions. *Maryon* and *Buckland* (1995) examined dispersion from a puff released in the atmospheric boundary layer during cyclonic and anticyclonic conditions over ten days with a Lagrangian global multiple-particle model using analysed three-dimensional wind fields. *McQueen* and *Draxler* (1994) found low relative error (15%) with persistently strong flow. *Heffter et al.* (1990) and *Haagenston et al.* (1990) also suggest that relative error is inversely proportional to wind speed.

Local winds Bora and Koshawa are persistently strong flows caused by local orography and specific synoptic conditions. Bora and Koshawa are similar winds (e.g., they are downslope), but there is a difference also. Koshawa is more channelized wind than Bora at larger scales.

The Eta Model (*Mesinger et al.*, 1988; *Janjić*, 1990, 1994) has shown excellent capabilities for simulation of mountain-induced phenomena (e.g., lee cyclogenesis, local winds). Therefore it is expected that the model will also yield realistic trajectories. The trajectory method is a useful tool in displaying and analysing features of the mountain-induced phenomena (*Lazić* and *Tošić*, 1998). This method has previously been used for studying blocking effect of mountains on the atmosphere (*Chen* and *Smith*, 1987).

The purpose of this study is to estimate the forecast trajectory error, using two data sets with strong wind, by comparing calculated trajectories with the control case, which used wind data at the highest available temporal frequency, that is 90 s in this study. Six experiments used the simulated wind field at smaller temporal frequencies. The first used the wind every 15 min, the second every 30 min, the third every 1 h, the fourth every 3 h, the fifth every 6 h and the sixth every 12 h. Comparisons were made for all trajectories in given horizontal positions (five in this study), all trajectories at given vertical levels (eight in this study), and all trajectories in each data set of Bora and Koshawa.

After presenting general characteristics of the local winds Bora and Koshawa in Section 2, the model summary is given in Section 3, and the scheme for trajectory calculations is presented in Section 4. The error statistics are defined in Section 5. Forecast trajectories with various wind data frequencies are examined in Section 6. The sensitivity of trajectories to the variations of wind data frequencies, using calculated error statistics, are discussed in Section 7. Conclusions are summarized in Section 8.

2. *Characteristics of Bora and Koshawa winds*

2.1 Characteristics of Bora wind

Bora is a katabatic wind. The kinetic energy of gusts is derived entirely from the potential energy of cold air that spills over the coastal mountain ranges of Dinaric Alps and falls down their steep slopes to the Adriatic Sea (*Fig. 1*).

The Bora occurs when cold air accumulates over the north side of Dinaric Alps. The depth of the cold air reservoir has to reach at least up to the mountain passes for the Bora to commence. Not much movement needs to be present from inland across the coastal mountain ranges, or even at the crest of these mountain ranges, during Bora conditions. The relatively short way of the cold air masses along the mountain slopes is not suffice to warm the descending air to the normal temperatures of the coastal plains. Therefore, Bora is a cold wind.

There are two types of weather patterns which produce the Bora (*Yoshino*, 1976):

- A cyclonic weather pattern (cyclonic Bora) characterized by a depression over the southern Adriatic Sea or the Ionian Sea. Along its southeastern side, warm air is flowing aloft in a southerly to southwesterly air current. Thus the Bora in the lowest layers of the troposphere is overrun by warm, moist air masses.
- An anticyclonic weather pattern (anticyclonic Bora) characterized by strong high pressure over Central Europe, and a not well-developed low to the south.

In each case, the pressure is higher on the continental side of the mountains and lower over the Mediterranean. Therefore, a large horizontal pressure gradient builds up across the mountain barrier of Dinaric Alps.

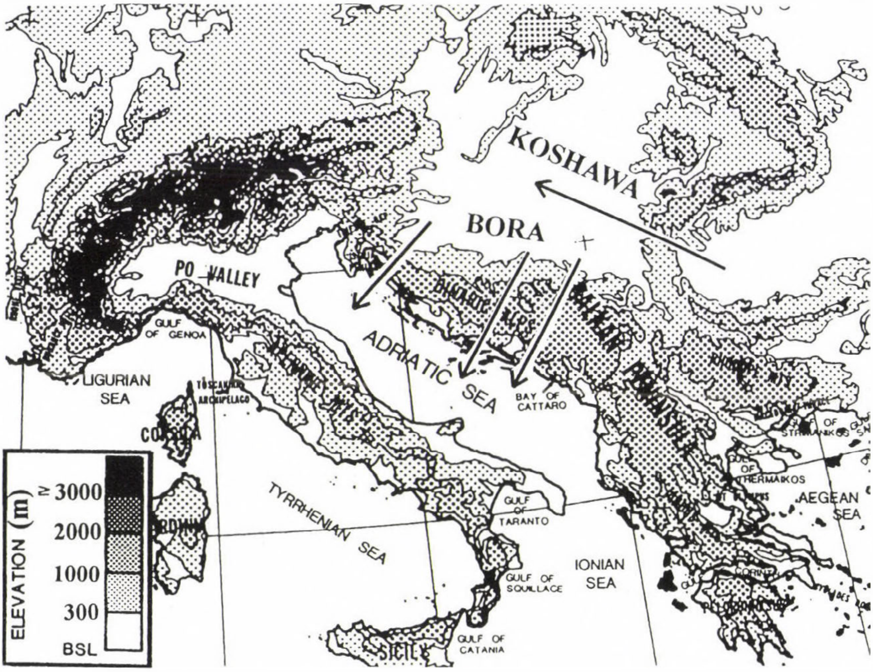

Fig. 1. Bora and Koshawa wind regions with real orography.

Bora is the most common wind in the Adriatic Sea area, where it flows mainly from the northeast through gaps in the Dinaric Alps (Fig. 1). The direction of the wind along the Croatian and Yugoslavian coast depends on the orientation of adjacent mountains, gaps and valleys. Over the open sea, the direction of the Bora is usually northerly to northeasterly, while on the Italian coast the wind almost always backs to a northwesterly direction. Bora is most common during the cold season of the year (November through March).

2.2 Characteristics of Koshawa wind

Koshawa is usually a cold, very squally wind, descending from east or south-east in the region of the Danube "Iron Gate" through the Carpathians (Fig. 1), continuing westward over Belgrade, thence spreading northward to the Rumanian and Hungarian borderlands and southward as far as Nish. In winter it makes the temperature turn as cold as –30°C and it is cool and dusty even in summer. It usually occurs with a depression over the Adriatic and high pressure over southern Russia, which is a frequent situation in winter.

Koshawa is usually explained as a "jet-effect wind" through Iron Gate, giving speeds much above the gradient (*Küttner*, 1940; *Unkašević et al.*, 1999), regarded a katabatic wind, intermediate between foehn and Bora. If the wind is sometimes warm, like a foehn, it is called "warm Koshawa"; if cold like the Bora, it is called "cold Koshawa". The low level jet-effect wind, or low level jet, is a wind which is increased in speed by channeling of the air by some orographic configuration such as a narrow mountain pass or canyon. When air stratification is stable, as it usually is in summer, the air tends to flow through the gap from high to low pressure, emerging as a "jet" with large standing eddies. The excess of pressure on the upwind side is attributed to a pool of cold air held up by the mountains.

The Koshawa has annual variation with a maximum in November and a minimum in July, and it has a marked diurnal variation with a maximum occurring between 05:00 and 10:00 local time.

3. Model summary

The model used for simulation of this study is a limited area primitive equation model with step-mountain coordinate (*Mesinger*, 1984), the so-called Eta Model. The model uses the semi-staggered E grid. The technique preventing grid separation is combined with split explicit time differencing. The horizontal advection has a built-in nonlinear energy cascade control. The internal boundary conditions at the sides of the step-mountains preserve all major properties of horizontal advection. A more detailed description of the dynamical part of the model can be found in *Mesinger et al.* (1988).

The physics package of the model includes the Mellor-Yamada level 2.5 planetary boundary layer and Mellor-Yamada level 2 surface layer, large scale precipitation, convective parametrization based on the Betts, Miller and Janjić scheme, surface flux of sensible and latent heat, and radiative processes. The model physics package has been described in more detail by *Janjić* (1990, 1994).

The horizontal resolution used for the experiments was $0.25° \times 0.25°$ (28 km $\times$ 28 km) with 16 layers in the vertical. Elementary time step is 90 s. The model horizontal domain was defined between 0° to 30°E and from 40°N to 50°N.

Time-dependent lateral boundary values are taken from the ECMWF (European Centre for Medium-Range Weather Forecasts) analyses, linearly interpolated between analysed fields available at 6 h intervals. The boundary grid points of the outermost row affected by this forcing extend inwards to affect the next row. The integration domain of the model excludes these two outermost rows. The second row within the outer boundary is a blend (four-point space interpolation) of the outer row and the third row inside which is included in the integration.

4. *Trajectory calculations*

Trajectories can be calculated forward and backward in time. Forward trajectories are calculated within the Eta Model itself. Backward trajectories are calculated in a separate program using wind data saved from a model simulation.

The horizontal wind components (u, v) from the Eta Model are defined on a latitude-longitude (λ, φ) grid, and vertical component of motion is $\dot{\eta} = \frac{d\eta}{dt}$, defined on each eta surface of the model. For a given position and time, the new location for an integration of one trajectory time step (temporal in this study) was accomplished by a two-step approach. To derive the needed wind components at a given position, bilinear horizontal and linear vertical interpolation are performed. First, bilinear interpolation is performed horizontally on the two model η levels which are above and below the trajectory position in the vertical. Then, linear vertical interpolation is done of two horizontally interpolated values to obtain the wind component at the parcel position. This interpolation is done for all three wind components. Using these interpolated wind components (u_1, v_1, $\dot{\eta}_1$), a first guess of the new position (λ_1, φ_1, η_1) for the parcel was obtained by

$$\lambda_1^{\tau+1} = \lambda^\tau + u_1 \Delta t \frac{180/\pi}{R \cos\varphi^\tau}, \tag{1}$$

$$\varphi_1^{\tau+1} = \varphi^\tau + v_1 \Delta t \frac{180/\pi}{R}, \tag{2}$$

$$\eta_1^{\tau+1} = \eta^\tau + \dot{\eta}_1 \Delta t, \tag{3}$$

where

$$u_1 = u_1(\lambda^\tau, \varphi^\tau); \qquad v_1 = v_1(\lambda^\tau, \varphi^\tau); \qquad \dot{\eta}_1 = \dot{\eta}_1(\lambda^\tau, \varphi^\tau). \tag{4}$$

A new set of wind components was then calculated in the same manner for this new location, i.e.,

$$u_2 = u_2(\lambda^{\tau+1}, \varphi^{\tau+1}); \qquad v_2 = v_2(\lambda^{\tau+1}, \varphi^{\tau+1}); \qquad \dot{\eta}_2 = \dot{\eta}_2(\lambda^{\tau+1}, \varphi^{\tau+1}). \tag{5}$$

The final displacement was calculated using the average of the two sets of wind components:

$$\lambda_2^{\tau+1} = \lambda^\tau + \frac{1}{2}(u_1 + u_2)\Delta t \frac{180/\pi}{R \cos \frac{1}{2}(\varphi_1^{\tau+1} + \varphi_1^\tau)}, \tag{6}$$

$$\varphi_2^{\tau+1} = \varphi^\tau + \frac{1}{2}(v_1 + v_2)\Delta t \frac{180/\pi}{R}, \tag{7}$$

$$\eta_2^{\tau+1} = \eta^\tau + \frac{1}{2}(\dot{\eta}_1 + \dot{\eta}_2)\Delta t. \tag{8}$$

This procedure is repeated until the desired final time is reached. Backward trajectories are calculated in the same way except for using a negative time step Δt.

5. *Error statistics*

In order to assess quantitatively the deviation of air parcel trajectories due to various wind data frequency, mean absolute errors (*MAE*) and mean relative errors (*MRE*) are calculated. The longitude-latitude positions of each trajectory positions were transformed to x-y positions using a map projection transformation in order to calculate the error statistics described in the following.

The *MAE* are separated into horizontal (*MAEH*) (in kilometers) and vertical (*MAEV*) (non-dimensional value of eta coordinate between 0 and 1) directions. They may be written as

$$MAEH(t) = \frac{1}{N}\sum_{n=1}^{N} \left\{ \left[x_c^n(t) - x_e^n(t)\right]^2 + \left[y_c^n(t) - y_e^n(t)\right]^2 \right\}^{1/2}, \tag{9}$$

$$MAEV(t) = \frac{1}{N}\sum_{n=1}^{N} \left| \eta_c^n(t) - \eta_e^n(t) \right|, \tag{10}$$

where x, y and η show the location of an air parcel, the superscripts denote the trajectory number, and the subscripts denote the control (c) or experimental (e) case. During the 48-hour integration, some trajectories move out of the model domain (especially where the transport speed is high). The *MAEH* and *MAEV* are therefore computed only with the parcels, N, available within the domain.

Although the *MAEH* and *MAEV* show the absolute transport errors, it is also important to look at the mean relative errors (*MRE*), i.e., the mean absolute errors relative to the mean total transport distance. Here, we define the parameters, *MREH* and *MREV* as

$$MREH(t) = \frac{MAEH(t)}{THT(t)}, \tag{11}$$

$$MREV(t) = \frac{MAEV(t)}{TVT(t)}, \tag{12}$$

where *THT* and *TVT* are the mean total absolute horizontal and vertical transport distance of a control case. They are defined as

$$THT(t) = \frac{1}{N}\sum_{n=1}^{N} \left\{\left[x_c^n(t) - x_c^n(t_0)\right]^2 + \left[y_c^n(t) - y_c^n(t_0)\right]^2\right\}^{1/2}, \tag{13}$$

$$TVT(t) = \frac{1}{N}\sum_{n=1}^{N} \left|\eta_c^n(t) - \eta_c^n(t_0)\right|, \tag{14}$$

where $x_c^n(t_0)$, $y_c^n(t_0)$, $\eta_c^n(t_0)$ are the initial location of an air parcel n, and $x_c^n(t)$, $y_c^n(t)$, $\eta_c^n(t)$ are its location at time t. Use of *THT* and *TVT* definitions is limited to strong straight flow fields, such as Bora and Koshawa winds. These definitions need some modifications in the case of circular flow fields (cyclone, trough, anticyclone, etc.).

6. Forecast trajectories

From December 1, 00:00 UTC to December 3, 1990, 00:00 UTC, a typical cyclonic Bora case occurred, and a typical Koshawa case was from December 5, 00:00 UTC to December 7, 1995, 00:00 UTC. The numerical simulations were initialized at December 1, 1990, 00:00 UTC and at December 5, 1995, 00:00 UTC using ECMWF analysis. The time-dependent boundary values of the prognostic variables were updated by the linear time interpolation of the ECMWF analyses taken at 6 h intervals.

Using simulated wind, forward trajectories were calculated starting from the lowest eight model levels (LT=1 with approximate height of z=3820 m; LT=2, z=3057 m; LT=3, z=2380 m; LT=4, z=1784 m; LT=5, z=1264 m; LT=6, z=818 m; LT=7, z=442 m; and LT=8, z=136 m). Cluster analysis of trajectories in both cases were made with 5 initial points in horizontal, central point plus 4 points with $\pm 1°$ relative to the central in both λ and φ directions. Total number of trajectories were 280 in each case.

Sensitivity to the wind data frequency is studied by varying the time step of model trajectory in the experiments, and comparing calculated trajectories with the control case, which used wind data at the highest temporal frequency available, that is, 90 s. Six experiments used the simulated wind field at smaller temporal frequencies. The first used the winds every 15 min, the second every 30 min, the third every 1 h, the fourth every 3 h, the fifth every 6 h and the sixth every 12 h.

6.1 Bora case

The control 48 h three-dimensional trajectories have been calculated forward at seven levels for the selected initial central position $\lambda=20°$, $\varphi=47°$ and are shown in *Fig. 2*. Trajectory departing from the lowest model level (LT=8 at z=136 m or $\eta=0.98$) was largely blocked by the mountains early in the integration and is not shown in the plots. Accumulation of air associated with small wind speed and moderate lifting of incoming air in front of mountains can be observed. This is evidenced by small distances between one-hour positions on the trajectories. A stronger Bora wind speed and its acceleration during descent can be seen just over and in the lee of mountains. The trajectories originating at levels 1 and 2 (LT=1 and LT=2) are outside the Bora layer. The trajectory departing from the level 7 was strongly affected by mountains so that it was rising continuously changing direction after 16 h and forming an S-like shape.

The trajectory originating from level 3 (LT=3, z=2380 m) ascends until 20 h of integration (*Fig. 2b*). Between 20 and 31 h the trajectory descends down the slope of the Dinaric Alps (*Fig. 2a*). After that, this trajectory ascends again until 33 h, then descends once more over Italian coast until 39 h. After that the air particle rises inside a low pressure system. There are two local wind speed maxima along this trajectory. One is at 31 h with speed of 19 m s^{-1} in accelerate falling over Dinaric Alps. The second one is over Italy at 35 h, with speed of 21 m s^{-1}.

The trajectory departing from level 4 (LT=4, z=1784 m) rises until 14 h of integration (Fig. 2b). It then descends until 19 h, down the slope of the Dinaric Alps (Fig. 2a). After ascending briefly it descends again, eventually leaving the model domain at 29 h. A maximum wind speed is attained at 17 h of 21 m s^{-1}. Another maximum wind speed along this trajectory occurs at 21 h over the lee sides of the Apennine Alps with the value of 26 m s^{-1}.

The trajectory originating from level 5 (LT=5, z=1264 m) ascends until 18 h and then descends until 23 h. Along this trajectory segment a maximum wind speed is achieved at 19 h of 17.5 m s^{-1}. After that the parcel rises again until 27 h over Italy, and then descends until 29 h over the lee side of the Apennine Alps, attaining a maximum wind speed of 17 m s^{-1}.

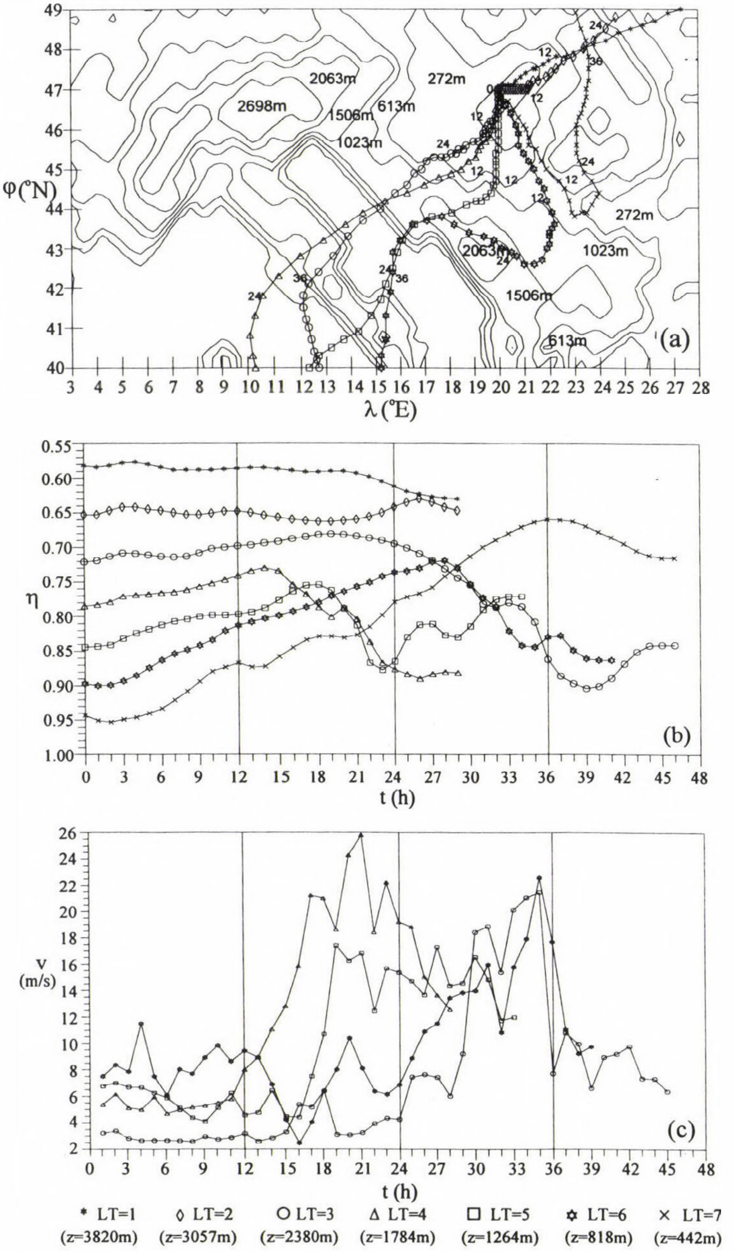

Fig. 2. Trajectories in Bora control case: (*a*) horizontal positions (numbers along trajectories indicate the time of integration in hours) and model orography; (*b*) vertical positions; (*c*) wind speed along trajectories.

The trajectory departing from level 6 (LT=6, z=818 m) ascends until 28 h. It then descends until 35 h over the lee side of the Dinaric Alps, achieving a maximum wind speed of 22 m s^{-1}. After that it rises again until 37 h, over Italy, and then descends once more. It leaves the integration domain at 41 h.

The trajectories based on the 15 min, 30 min and 1 h data are very similar to the control case, while the trajectories based on the 3 h, 6 h and 12 h data show considerable differences. Differences are larger in cases with larger time step. Increasing time step of wind data in the experiments, we notice a decrease in the maximum wind speed.

6.2 Koshawa case

The control 48 h three-dimensional trajectories have been calculated forward at seven levels for the selected initial central position $\lambda=24°$, $\varphi=44°$ and are shown in *Fig. 3*. Trajectory departing from the lowest model level (LT=8 at z=136 m or $\eta=0.98$) was blocked by the mountains (step eta orography of 272 m) in the initial position and is not shown in the plots.

In contrary to Bora case, in this case all trajectories increased speed early in the integration. A maximum speed was around at 3 h of integration, placed in the channel type of orography in Iron Gate through the Carpathians. All trajectories ascend in the beginning over orography steps of 613 m, 1023 m and some of them over 1506 m, and then descend over the lee side of the Carpathians. The low level jet is simulated at 1200 m with wind speed of 25 m s^{-1}. At the same time a maximum speed was 21 m s^{-1} at level of 800 m, and a maximum speed was 22 m s^{-1} at level of 1800 m.

The trajectories originating at levels 1 and 2 (LT=1, z=3820 m and LT=2, z=3057 m) have the near southerly direction increasing the height over the orography model step of 1506 m of the Carpathians (*Fig. 3a, b*). The trajectory originating from level 3 (LT=3, z=2380 m) has a maximum horizontal wind speed of 18 m s^{-1} at 3 h of integration, above orography step of 1506 m (*Fig. 3a, c*). The trajectory departing from level 4 (LT=4, z=1784 m) has a maximum wind speed at 3 h of 22 m s^{-1}, just over orography step of 1506 m.

The trajectory originating from level 5 (LT=5, z=1264 m) has a maximum wind speed at 3 h of 25 m s^{-1}. That is a low level jet of Koshawa wind, located at around 1200 m in vertical direction, with southeasterly direction, in the channel type of orography through the Carpathians. The trajectory departing from level 6 (LT=6, z=818 m) achieves a maximum wind speed of 21 m s^{-1} at 3 h. The trajectory originating from level 7 (LT=7, z=442 m) has a maximum wind speed at 4 h of 12 m s^{-1}. Typical distribution of wind speed along trajectories coincides with observations of Koshawa. Wind speed decreases in all trajectories after passing the Koshawa region.

The trajectories based on the 15 min, 30 min and 1 h data are very similar to the control case, while the trajectories based on the 3 h, 6 h and 12 h data show considerable differences. Differences are larger in cases with larger time step. Increasing time step of wind data in the experiments, we notice a decrease in the maximum wind speed.

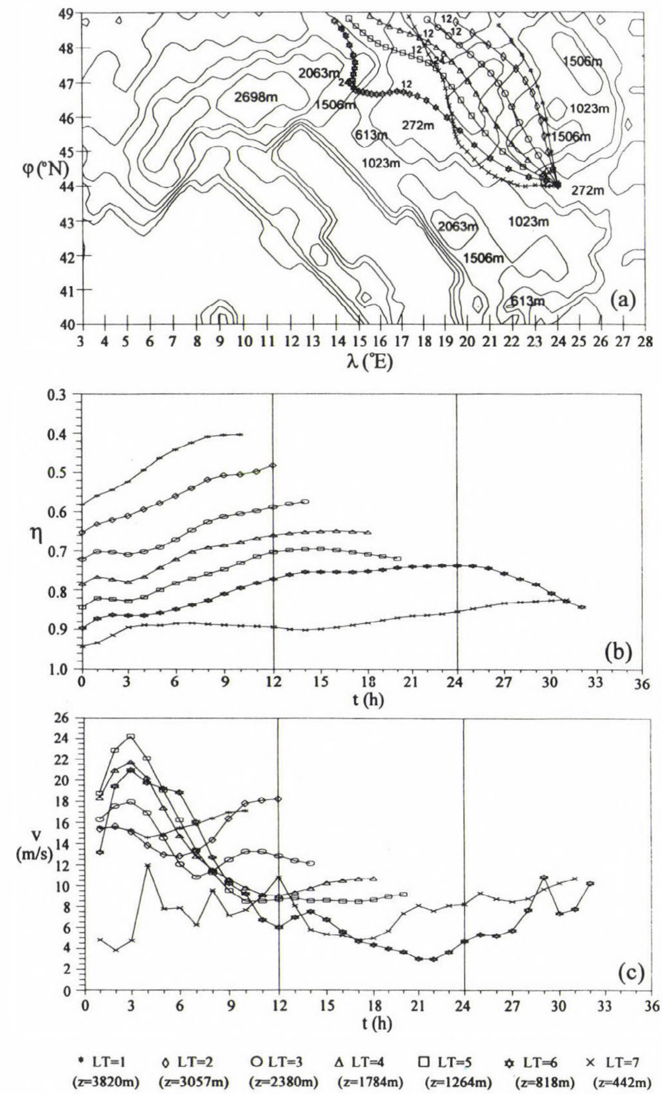

Fig. 3. Trajectories in Koshawa control case: (*a*) horizontal positions (numbers along trajectories indicate the time of integration in hours) and model orography; (*b*) vertical positions; (*c*) wind speed along trajectories.

7. Overall results

Mean absolute error in horizontal direction (*MAEH*), mean relative error in horizontal direction (*MREH*), mean absolute error in vertical direction (*MAEV*) and mean relative error in vertical direction (*MREV*) have been calculated from 280 trajectories in each data set. During the 48-hour integration, some trajectories moved out of the model domain (especially where the transport speed was high). The error statistics were computed only with the parcels, available within the domain and presented up to 36 h. Therefore in each data set in all experiments, 4515 locations were compared with the control case.

7.1 Bora case

During 24 h of integration in cases of 15 min, 30 min and 1 h wind data time step the *MAEH* remains below or at 50 km, and the *MAEH* is less than 150 km at the end of 36 h interval (*Fig. 4a*). The *MAEH* in cases of 3, 6 and 12 h wind data time steps continuously increases during the whole period, with values between 100 and 250 km at 24 h and between 250 and 400 km at 36 h of integration (Fig. 4a).

The *MREH* is less than 10% up to 24 h, and remains below 25% between 24 and 36 h of integration in cases of 15 min, 30 min and 1 h wind data time steps (*Fig. 4b*). The *MREH* in cases of 3, 6 and 12 h wind data time steps is between 15 and 80%. The *MREH* is between 40 and 60% in case of 12 h wind data time step.

The *MREH* of all trajectories is initially quite high when the absolute errors are typically comparable to or larger than the transport distance. The error stabilizes near 8% after about 3 h in cases of 15 min, 30 min and 1 h wind data time steps.

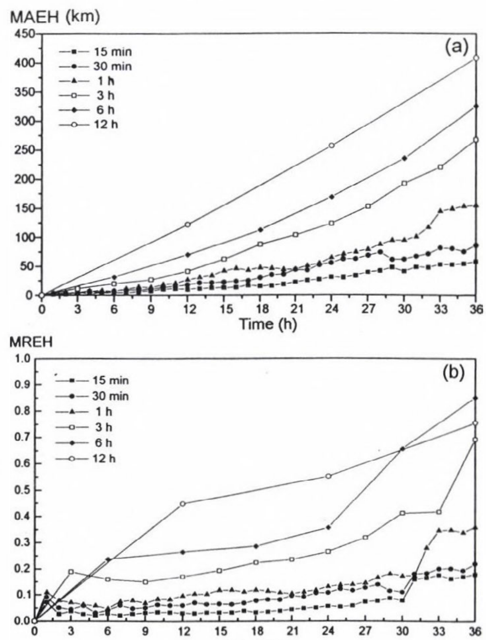

Fig. 4. The mean errors in horizontal direction in Bora case: (*a*) the mean absolute error (*MAEH*) and (*b*) the mean relative error (*MREH*).

The errors increase significantly in some cases from 30 to 33 h of integration as a result of trajectories living the domain and thus suddenly decreasing the number of trajectories available for the mean absolute error calculations.

The *MAEV* is less than 0.01 (approximately 65 m) up to 24 h, and remains under 0.04 (approximately 250 m) between 24 and 36 h of integration in cases of 15 min, 30 min and 1 h wind data time steps (*Fig. 5a*). The *MAEV* is between 0.01 and 0.05 (65–300 m) up to 24 h in cases of 3, 6 and 12 h wind data time steps. Between 24 and 36 h of integration this error varies between 0.03 and 0.14. Maximum value of the *MAEV* reaches near 0.14 at 36 h in case of 12 h wind data time step.

The *MREV* remains below 25% up to 24 h, and is less than 50% between 30 and 36 h of integration in cases of 15 min, 30 min and 1 h wind data time steps (*Fig. 5b*). The *MREV* in cases of 3, 6 and 12 h wind data time steps is between 25 and 100%. Between 24 and 36 h of integration this error varies between 50 and 200%. The *MREV* has a maximum by 36 h of about 200% in case of 12 h wind data time step.

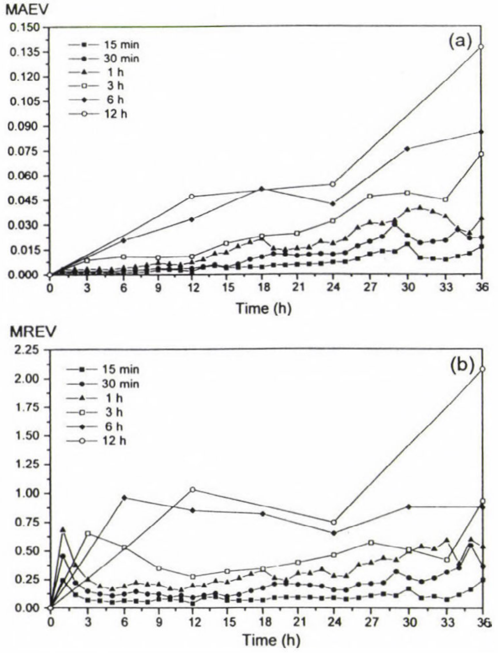

Fig. 5. The mean errors in vertical direction in Bora case: (*a*) the mean absolute error (*MAEV*) and (*b*) the mean relative error (*MREV*).

The *MREV* of all trajectories is initially quite high when the absolute errors are typically comparable to or larger than the transport distance. The error stabilizes near 20% after about 4 h in cases of 15 min, 30 min and 1 h wind data time steps.

7.2 Koshawa case

The *MAEH* increases during integration remaining below 50 km in cases of 15 min, 30 min and 1 h wind data time steps (*Fig. 6a*). Error variations in these cases are very similar to each other, with smaller values in cases with 15 and 30 min. In cases of 3, 6 and 12 h wind data time steps the *MAEH* increases during the whole period, with values between 150 and 450 km at 36 h of integration (Fig. 6a).

The *MREH* remains under 5% in cases of 15 min, 30 min and

1 h wind data time steps during the whole period of integration (*Fig. 6b*). The *MREH* is between 10 and 35% in cases of 3, 6 and 12 h wind data time steps.

The *MREH* of all trajectories is initially quite high when the absolute errors are typically comparable to or larger than the transport distance. After about 10 h the error stabilizes near 2% in cases of 15 min, 30 min and near 4% in case of 1 h wind data time step.

The *MAEV* remains below 0.01 (approximately 65 m) in cases of 15 min, 30 min and 1 h wind data time steps (*Fig. 7a*). The *MAEV* is between 0.025 and 0.105 (160–600 m) in cases of 3, 6 and 12 h wind data time steps.

The *MREV* is about 10% in cases of 15 min, 30 min and 1 h wind data time steps (*Fig. 7b*). In cases of 3, 6 and 12 h wind data time steps the *MREV* is between 40% (for 3 h time step case) and 80% (for 12 h time step case).

The *MREV* of all the trajectories is initially quite high when the absolute errors are typically comparable to or larger than the transport distance. After about 9 h the error stabilizes near 5% in cases of 15 min, 30 min and near 10% in case of 1 h wind data time step.

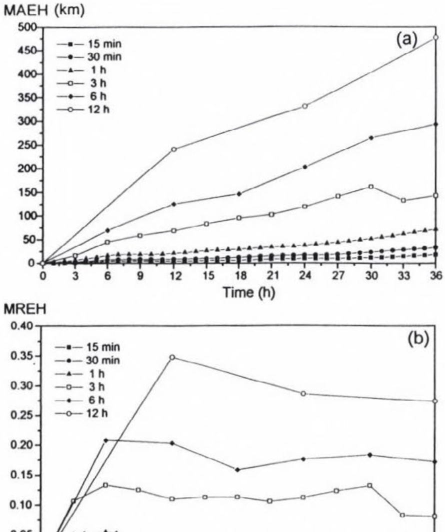

Fig. 6. The mean errors in horizontal direction in Koshawa case: (*a*) the mean absolute error (*MAEH*) and (*b*) the mean relative error (*MREH*).

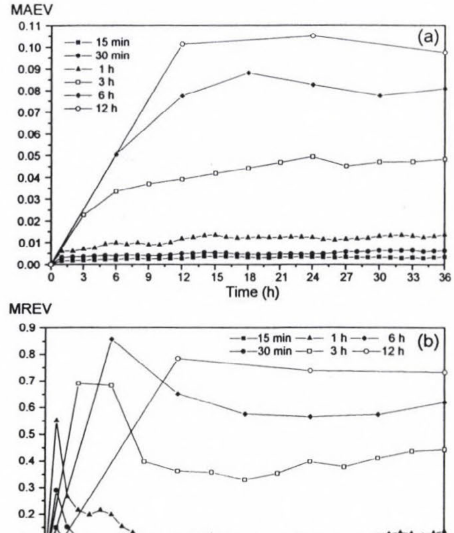

Fig. 7. The mean errors in vertical direction in Koshawa case: (*a*) the mean absolute error (*MAEV*) and (*b*) the mean relative error (*MREV*).

8. Conclusions

Numerical experiments with different frequencies of wind data in trajectory calculations of the Bora and Koshawa local winds were performed. Three-dimensional trajectories in these experiments were calculated and inspected. Forward trajectories, calculated using the Eta Model, showed changes in their behavior when comparing calculations in control case with cases of 15 min, 30 min, 1 h, 3 h, 6 h and 12 h wind data frequencies. Increasing time step of wind data in the experiments, the maximum wind speed decreased along the trajectories.

In order to assess quantitatively the deviation of air parcel trajectories due to various wind data frequencies, mean absolute error (distance between reference and forecast trajectory), mean relative error (mean absolute error divided by mean reference trajectory total transport distance) were calculated. The mean absolute error and the mean relative error were separated into horizontal and vertical directions. In each data set, calculation was done for the clusters of 280 trajectories, and 4515 locations were compared with the control case.

The mean relative error for all forecast trajectories was about 30% in Bora case and about 20% in Koshawa case. Trajectories with wind data frequency of 15 min, 30 min and 1 h were accurate enough, with mean relative error less than 10% in Bora case and less than 5% in Koshawa case. These statistics indicate that wind data frequency of 1 h, which is usually used in calculation of backward trajectories has small errors. This denotes that it is not necessary to memorize wind data in every time step of the model integration for calculating of backward trajectories.

The mean relative error of parcel positions along trajectories showed large values in case of 3 h, 6 h and 12 h wind data frequencies, especially in vertical direction. A maximum of the mean relative error (about 200%) was associated with forecast trajectories in vertical direction in case of 12 h wind data of Bora wind. This result suggests that trajectories calculated from the analysed wind data (12 h data frequency) are not accurate when they are used. This means that the current synoptic observational frequency is inadequate for accurate calculations of long-range transport or episodic events. This result also indicates the importance of using the vertical velocity for calculating the trajectories.

In general, Koshawa case was less sensitive to the temporal frequency of wind data than Bora case. Trajectories in Koshawa case were more precise than in Bora case because Koshawa wind is a low level jet-effect wind and more channelized by the orography at larger scales than Bora wind. The low level jet-effect wind is increased in speed through the channeling of air by some orographic configuration.

Construction of accurate three-dimensional atmospheric trajectories provides a valuable diagnostic tool for illustrating and understudying the three-dimensional flow fields and associated transports, as well as the dispersal of upper atmospheric pollutants and possible nuclear contamination. Koshawa wind is sometimes dusty or contains air pollutants (*Vukmirović et al.*, 2000), so this investigation is also important for accurate long-range air pollution transports and environmental studies.

Acknowledgments—This study was partly supported by the Serbian Academy of Science and Art under Grant F-147 and partly by the Association for Science of Serbia under Grant 0704.

References

Chen, W.D. and *Smith, R.B.*, 1987: Blocking and deflection of airflow by the Alps. *Mon. Wea. Rev. 115*, 2578-2597.

Doty, K.G. and *Perkey, D.J.*, 1993: Sensitivity of trajectory calculations to the temporal frequency of wind data. *Mon. Wea. Rev. 121*, 387-401.

Haagenston, P.L., Gao, K. and *Kuo, Y.H.*, 1990: Evaluation of meteorological analyses, simulations, and long-range transport calculations using ANATEX surface tracer data. *J. Appl. Meteor. 29*, 1268-1283.

Heffter, J.L., Stunder, B.J.B. and *Rolph, G.D.*, 1990: Long-range forecast trajectories of volcanic ash from Redoubt volcano eruption. *Bull. Amer. Meteor. Soc. 71*, 1731-1738.

Janjić, Z.I., 1990: Physical package for the step-mountain, eta coordinate model. *Mon. Wea. Rev. 118*, 1429-1443.

Janjić, Z.I., 1994: The step-mountain eta coordinate model: Further developments of the convection, viscous sublayer and turbulence closure schemes. *Mon. Wea. Rev. 122*, 927-945.

Küttner, J., 1940: Der Koshawa in Serbien. *Meteor. Z. 57*, 120-123.

Lazić, L. and *Tošić, I.*, 1998: A real data simulation of the Adriatic Bora and the impact of mountain height on Bora trajectories. *Meteorol. Atmos. Phys. 66*, No. 3-4, 143-155.

Maryon, R.H. and *Buckland, A.T.*, 1995: Tropospheric dispersion: the first ten days after a puff release. *Quart. J. Roy. Meteorol. Soc. 121*, 1799-1833.

McQueen, J.T. and *Draxler, R.R.*, 1994: Evaluation of model back trajectories of the Kuwait oil fires smoke plume using digital satellite data. *Atmos. Environ. 28*, 2159-2174.

Mesinger, F., 1984: A blocking technique for the representation of mountains in atmospheric model. *Riv. Met. Aeronautica 44*, 195-202.

Mesinger, F., Janjić, Z.I., Ničković, S., Gavrilov, D. and *Deaven, D.G.*, 1988: The step-mountain coordinate: model description and performance for cases of Alpine lee cyclogenesis and for a case of an Appalachian redevelopment. *Mon. Wea. Rev. 116*, 1493-1518.

Petersen, R.A. and *Uccellini, L.W.*, 1979: The computation of isentropic atmospheric trajectories using a Discrete Model formulation. *Mon. Wea. Rev. 107*, 566-574.

Rolph, G.D. and *Draxler, R.R.*, 1990: Sensitivity of three-dimenzional trajectories to the spatial and temporal densities of the wind field. *J. Appl. Meteor. 29*, 1044-1054.

Unkašević, M., Mališić, I. and *Tošić, I.*, 1999: Some aspects of the wind "Koshava" in the lower troposphere over Belgrade. *Meteorol. Appl. 6*, 69–80.

Vukmirović, Z., Unkašević, M., Lazić, L., Tošić, I., Rajšić, S. and *Tasić, M.*, 2000: Analysis of an exceptional Saharan dust event in Serbia using the Eta Model. Submitted to *Atmos. Res.*

Yoshino, M., 1976: *Local wind Bora*. University of Tokyo Press, Tokyo. 289 pp.

IDŐJÁRÁS
Quarterly Journal of the Hungarian Meteorological Service
Vol. 104, No. 2, April–June 2000, pp. 109–122

Numerical study of heat and moisture exchange in the morning boundary layer

Rumjana Mitzeva and **Gergana Gerova**

Department of Meteorology, Faculty of Physics, University of Sofia
5, J. Bourchier, Sofia–1126, Bulgaria
E-mail: rumypm@phys.uni-sofia.bg

(Manuscript submitted for publication 3 November 1999; in final form 25 February 2000)

Abstract—One-dimensional numerical model of the evolution of the morning convective boundary layer (CBL) for strong insolation, light wind and absence of clouds being previously developed is here completed with a study of moisture transport. The basic assumption is that heat and moisture transport in the CBL is due to discrete convective elements, i.e., thermals. Governing equations for the vertical profile of horizontal-mean virtual potential temperature and specific humidity are derived partitioning the CBL each level and each moment into two domains, one covered by thermals and another occupied by downdrafts.

The impact of the magnitude of radiation heating and moisture as well as the impact of the distribution of thermals at the earth surface on the CBL characteristics are studied and discussed. The results from the calculations with simulated and observed initial temperature and humidity profiles show that the model reasonably well simulates the heat and humidity exchange in the morning boundary layer in fair weather conditions.

Key-words: convective boundary layer, thermals, numerical model.

1. Introduction

Atmospheric movements in the convective boundary layer are of a great interest for science because of their essential impact upon nature, people and economy. There are a variety of models describing the evolution of the mixing layer (ML) which differ in their main assumptions or in the approach to the "closure" problem. The choice of a model depends on the aim of investigation and on the authors' conception.

The model developed and tested in this paper is fitted to clear-sky days with light mean winds when the dominant mechanism driving the turbulence is buoyancy, and the mechanically generated mixing by shear can be neglected.

It is based on the well-known fact that during daytime when the sun heats the ground, the air near the ground warms and rises as convective thermals. Plenty of numerical models incorporate that idea (*Telford,* 1966; *Manton*, 1975; *Andreev* and *Ganev,* 1981; *Cushman-Roisin,* 1982; *Chatfield* and *Brost,* 1987).

The model in this paper is an extension of the model presented in *Mitzeva et al.* (1997) and in addition includes the study of moisture transport.

In Section 2 one can find the model description. The numerical scheme, initial and boundary conditions are given in Section 3. The results of the numerical simulations and comparison with observations are presented in Section 4. The summary and discussion are given in the final section of the paper.

2. *Model description*

The main assumptions and governing equations for the calculation of virtual potential temperature (VPT) and specific humidity (SH) in the convective boundary layer (CBL) are given in this section. The argumentation of this parameterization and more details can be found in *Mitzeva et al.* (1997).

The basic idea in the model is that heat and moisture in the CBL are transported by discrete convective elements, i.e., thermals and compensating downdrafts. For the parameterization of the CBL in *Mitzeva et al.* (1997), a horizontal area of CBL, $S(z,t)$, at a given level z and given moment t is partitioned into two domains: one part of the area is covered with rising thermals (updrafts), $S_T(z,t)$, and the rest of the area is occupied by compensating downdrafts, $S_E(z,t)$, (*Fig. 1*). Thus, the vertical velocity field is used as indicator for thermals in this particular parameterization. This separation is also valid for the other CBL characteristics, because the velocity controls their spatial and temporal distribution. Following the same procedure of averaging over a horizontal area as in *Mitzeva et al.* (1997), the final set of the equations for the horizontal mean VPT, $\overline{\theta_V}$ and SH, $\overline{q}$ evolution is as follows:

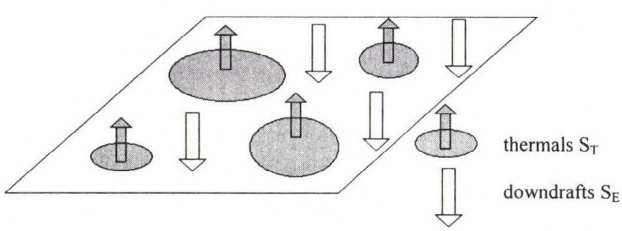

Fig. 1. Schematic illustration of the partition of CBL at a given level and given time into thermal and downdraft domains.

$$\frac{\partial\overline{\theta_V}}{\partial t} + \frac{\partial}{\partial z}\left[B(z,t)\overline{\theta_V}\right] = C(z,t), \tag{1}$$

$$\frac{\partial\overline{q}}{\partial t} + \frac{\partial}{\partial z}\left[B(z,t)\overline{q}\right] = D(z,t), \tag{2}$$

where $B(z,t)$, $C(z,t)$ and $D(z,t)$ are given by:

$$B(z,t) = \frac{1}{1 - S_T/S}\overline{W_T}, \tag{3}$$

$$C(z,t) = -\frac{\partial}{\partial z}\left[\frac{1}{1 - S_T/S}\overline{W_T}\,\overline{\theta_{VT}} + \overline{W_T}\,\overline{\theta_{VT}}\right], \tag{4}$$

$$D(z,t) = -\frac{\partial}{\partial z}\left[\frac{1}{1 - S_T/S}\overline{W_T}\,\overline{q_T} + \overline{W_T}\,\overline{q_T}\right], \tag{5}$$

and

$$\overline{W_T} = \sum_R \pi R^2 W_T(R,z,t) f(R,z,t),$$

$$\overline{\theta_{VT}} = \sum_R \pi R^2 \theta_{VT}(R,z,t) f(R,z,t),$$

$$\overline{q_T} = \sum_R \pi R^2 q_T(R,z,t) f(R,z,t),$$

$$\overline{W_T q_T} = \sum_R \pi R^2 W_T(R,z,t)\, q_T(R,z,t) f(R,z,t).$$

Here $f(R,z,t)$, $W_T(R,z,t)$, $\theta_{VT}(R,z,t)$ and $q_T(R,z,t)$ are size distribution function, vertical velocity, VPT and SH for thermal with radii R at level z and moment t, respectively. The individual thermals' characteristics (W_T, θ_{VT}, q_T) are obtained from Eqs. (6) to (8). The sum $\sum_R$ is over all thermals' radii. The fraction of the area occupied by rising thermals at level z and moment t is calculated by:

$$S_T/S = \sum_R \pi R^2 f(R,z,t).$$

The downdraft characteristics are presented by the mean values dependent on time and height based on the observations showing that the downdraft velocity distribution is rather narrow and has a mode approximately equal to the average downdraft velocity (*Lamb*, 1982).

The thermals are considered as discrete convective elements with various sizes originating near the surface after sunrise (a.s.r.) and lifting in upward direction without interactions with each other, i.e., vertical and horizontal mixing between different thermals are not included in the model. Similar to *Andreev* and *Ganev* (1981) it is assumed that the thermals are spheres with radii R and their characteristics are calculated according to *Andreev* and *Panchev* (1975):

$$\frac{dW_T(R,z,t)}{dt} = -\alpha\, W_T^2(R,z,t) + g\left[\frac{\theta_{VT}(R,z,t) - \overline{\theta_V}}{\overline{\theta_V}}\right], \tag{6}$$

$$\frac{d\theta_{VT}(R,z,t)}{dt} = -\,\alpha\left[\theta_{VT}(R,z,t) - \overline{\theta_V}\right] W_T(R,z,t), \tag{7}$$

$$\frac{dq_T(R,z,t)}{dt} = -\,\alpha\left[q_T(R,z,t) - \overline{q}\,\right] W_T(R,z,t) \tag{8}$$

and

$$\frac{dz}{dt} = W_T,$$

where g is acceleration of gravity and α is entrainment parameter. In this study the simple parametrization for α (see *Andreev* and *Panchev*, 1975) was used, based on the assumption for the inverse relationship between entrainment rate and thermal radius, i.e., α=0.6/R.

The calculations of terms $B(z,t)$, $C(z,t)$ and $D(z,t)$ require information about the size distribution function $f(R,z,t)$ at any level and moment. In order to determine $f(R,z,t)$, the thermals are transformed into cylinders with the same radius R and volume as the spherical ones, and with heights H=4/3R. In this manner the spherical thermals are modified to columns of rising air, that is close to the observations showing that the idealized thermal shape is like that of a sausage (*Stull*, 1988).

It is useful to be mentioned that Eq. (1) in this paper is the same as Eq. (11) in *Mitzeva et al.* (1997), however the potential temperature is replaced here by the virtual potential temperature. Eq. (2) and Eq. (8) are added giving opportunity to study the moisture transport in the CBL.

3. Numerical scheme, initial and boundary conditions

Eqs. (1) and (2) are solved numerically by the Lax scheme (*Roache*,1976) with time step $\Delta t = 1$ s and grid length $\Delta z = 10$ m. The scheme has second-order time and space accuracy and is recommended to be used for preliminary model tests.

For numerical integration of Eqs. (6) to (8) the Runge-Kutta method is run with time step $\Delta t = 1$ s.

The initial level in the model, $z=0$, is set to be the level of the thermals starting. Although this level is in the upper boundary of the surface layer, for simplicity, we assume that $z=0$ coincides with the earth surface.

For numerical simulations the time evolution of VPT, $\overline{\theta_V}(0,t)$ and SH, $\bar{q}(0,t)$ at the initial level has to be given. The temperature at the earth surface follows the changes of the solar radiation. The lower boundary condition for the temperature is:

$$\overline{\theta_V}(0,t) = \overline{\theta_V}(0,0) + k \sin(2\pi t/24)\,(1 + 0.611\,\bar{q}(0,t)), \tag{9}$$

where $\overline{\theta_V}(0,0)$ is the VPT at the earth surface at the moment of sunrise, and k gives the increase of the earth's surface temperature for six hours. The time variations of $\overline{\theta_V}(0,t)$ for different values of the parameter k, following Eq. (9) are shown in *Fig. 2a*.

The evolution of SH near the ground $\bar{q}(0,t)$, typical for the continental area is shown by a bold line in *Fig. 2b* (*Hrgian*, 1969). It is seen that the SH increases during the first two hours and decreases in the next four hours. This evolution at the bottom boundary can be given by:

$$\bar{q}(0,t) = \bar{q}(0,0) + m \sin(2\pi t/d) \qquad \begin{Bmatrix} d = 8 \text{ hours} & 0 < t \le 2 \text{ hours} \\ d = 12 \text{ hours} & 0 < t \le 6 \text{ hours} \end{Bmatrix}, \tag{10}$$

where $\bar{q}(0,0)$ is the SH at the earth surface in the moment of sunrise. For the case presented by a bold line in Fig. 2b, $m = 1.6$ g kg^{-1}.

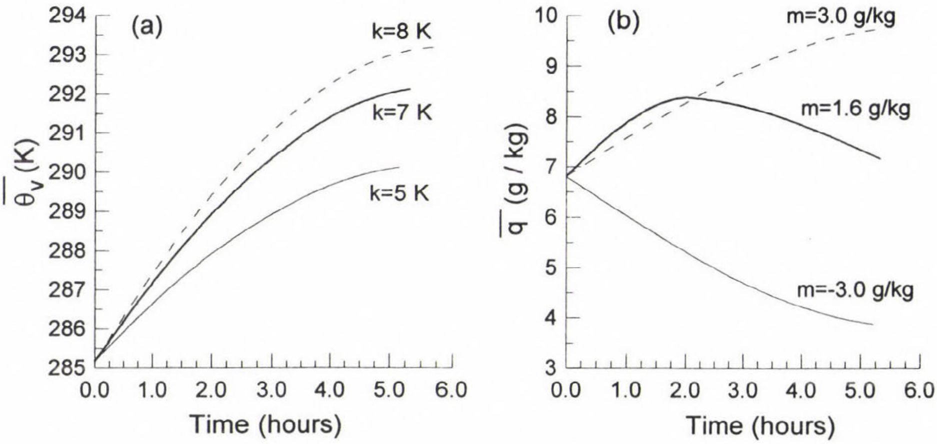

Fig. 2a. Time variations of virtual potential temperature $\overline{\theta_V}$ at the earth surface for different magnitudes of the solar heating: $k=5$ K (thin line), $k=7$ K (bold line) and $k=8$ K (dashed line).

Fig. 2b. Time variations of specific humidity $\overline{q}$ at the earth surface. The typical evolution for the continental area ($m=1.6$ g kg^{-1}) is plotted by bold line, $m=-3.0$ g kg^{-1} by thin line and $m=3.0$ g kg^{-1} by dashed line.

The model requires an initial sounding: thermal size distribution, vertical velocities, temperature and moisture excess of thermals at the earth surface to be set in. For all model calculations the starting velocities of the rising thermals are fixed to be 1 m s^{-1} and the temperature excess is set to be 1 K based on the measurements of *Telford* (1966). The calculations are carried out with $q_T(R,0,t) = \overline{q}(0,t)$, which means that the thermals at the earth surface are warmer but not moister than the environment, which is typical over the continents.

To investigate the impact of the initial thermal size distribution on heat and moisture transport, similar to *Mitzeva et al.* (1997), two types of size distribution (the number of thermals with a given diameter per km^2 at the earth's surface) were used. The first type is presented in *Table 1* and will be refer as ST1. It is extracted by *Andreev* and *Ganev* (1981) from *Vulfson*'s (1961) data. According to ST1, 22% of the earth surface area is covered with thermals for the first three hours a.s.r. and 42% for the second three hours a.s.r. This is in agreement with the results from aircraft measurements showing that updrafts cover 15–43% of the horizontal area (*Stull,* 1988). The second distribution function (ST2) presented in *Table 2* differs from ST1 in thermal diameters, while the fraction of area occupied by thermals at the earth surface is the same as for ST1. ST2 type distribution is uniform and it is taken in some extend arbitrary in the range of thermal sizes quoted in *Warner* and *Telford* (1967).

Table 1. Size distribution of the thermals (ST1) at the earth surface. The statistics is extracted from *Vulfson's* (1961) data by *Andreev* and *Ganev* (1981)

Diameter of the thermals (m)	Number of the thermals per km^2	
	Hours after sunrise 0-3	Hours after sunrise 3-6
5	0.6	1.4
15	4.5	11.2
25	4.9	14.0
35	6.2	14.8
45	6.4	15.5
55	6.2	15.5
65	6.1	14.8
75	4.9	13.5
85	5.7	12.1
95	5.1	10.1
105	4.5	7.7
128	2.3	1.7

Table 2. Size distribution of the thermals (ST2) at the earth surface

Diameter of the thermals (m)	Number of the thermals per km^2	
	Hours after sunrise 0-3	Hours after sunrise 3-6
50	2.2	4.0
100	2.2	4.0
150	2.2	4.0
200	2.2	4.0
250	2.2	4.0

The initial VPT, $\overline{\theta_V}(z,0)$ and SH, $\bar{q}(z,0)$ profiles are linearly interpolated in order to determine the vertical grid values of VPT and SH.

The evolution of VPT and SH profiles for a time step $t+\Delta t$ are obtained following the next sub-steps:

- The Eqs. (6) to (8) are numerically integrated by the Runge-Kutta method using $\overline{\theta_V}(z,t)$ and $\bar{q}(z,t)$. Thus $W_T(R,t+\Delta t)$, $\theta_{VT}(R,t+\Delta t)$, $q_T(R,t+\Delta t)$ and $z(R,t+\Delta t)$ are calculated for the moment $t+\Delta t$.
- The discrete size distribution function $f(R,z,t)$ is determined as the sum of the thermals with radii R which at a given moment t affect the levels z situated between $z-H/2$ (bottom of the cylindrical thermal) and $z+H/2$ (top of the cylindrical thermal).
- The terms $B(z,t)$, $C(z,t)$ and $D(z,t)$ are calculated from Eqs. (3) to (5).
- $\overline{\theta_V}(z,t+\Delta t)$ and $\bar{q}(z,t+\Delta t)$ are obtained from Eqs. (1) and (2) by the Lax scheme.
- For the levels not affected by rising thermals at a given moment t, $f(R,z,t)=0$, $\overline{\theta_V}(z,t+\Delta t)=\overline{\theta_V}(z,t)$ and $\bar{q}(z,t+\Delta t)=\bar{q}(z,t)$.

These calculations are repeated until all the thermals reach the levels at which their velocity $W_T(R,z,t)=0$, i.e., at these levels the thermals lose their individuality and no longer differ from the environmental air.

In the model it is accepted that a new thermal group with a given distribution function starts at initial level when all previous thermals have stopped, but not more frequently than in every 15 minutes.

4. Numerical simulations and results

The aim of the paper is to study the possibilities of the model to simulate the vertical transport of heat and moisture after sunrise in the absence of clouds and wind. The impact of the parameters used in the model on the formation and development of the CBL is also tested.

In all numerical tests the initial temperature profile (bold line in *Figs. 3a, 4a, 5a, 6a*) corresponds to ground inversion with temperature lapse rate $\partial T/\partial z=$ 0.1 K/100 m for the layers between 0 and 600 m, and $\partial T/\partial z=-$ 0.5 K/100 m above 600 m. The initial profile of SH (bold line in *Figs. 3b, 4b, 5b, 6b*) is typical for the morning hours at sunrise.

The evolution of the horizontal-mean VPT and SH profiles during the first five hours a.s.r. are given in Fig. 3a and Fig. 3b, respectively. The calculations are carried out with $k=7$ K (bold line in Fig. 2a). The earth surface SH changes are plotted by a bold line in Fig. 2b; they correspond to an increase of SH during the first two hours (a.s.r.) followed by a decrease in the second three hours.

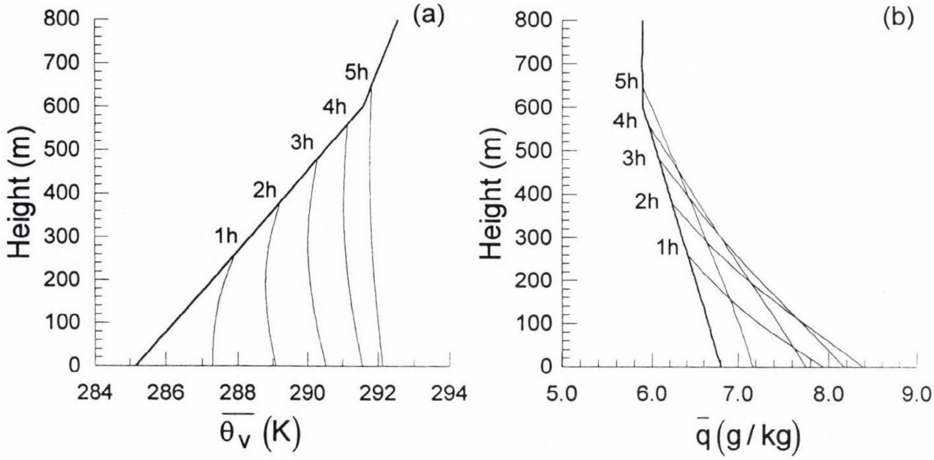

Fig. 3. Hourly vertical profiles (*a*) of the horizontal mean virtual potential temperature $\overline{\theta_V}$ (thin lines); (*b*) of the specific humidity $\bar{q}$ (thin lines). The numbers indicate the hours after sunrise. The initial profile is plotted by bold line. The magnitude of radiation heating corresponds to k = 7 K. The case m=1.6 g kg^{-1} for the earth's surface $\bar{q}$ is used.

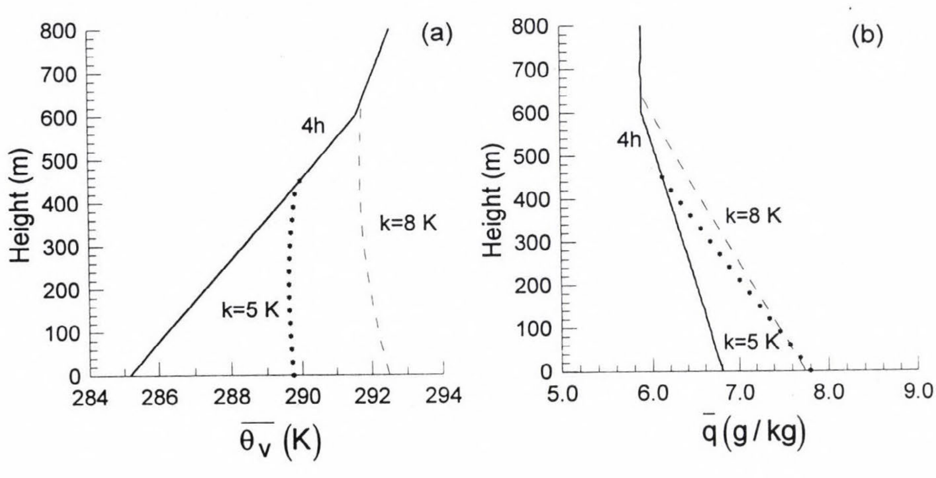

Fig. 4. Vertical profiles (*a*) of the virtual potential temperature $\overline{\theta_V}$; (*b*) of the specific humidity $\bar{q}$ for different magnitudes of radiation heating k=5 K (stars) and k=8 K (dashed line) four hours after sunrise. The initial $\overline{\theta_V}$ and $\bar{q}$ profiles are plotted by bold line.

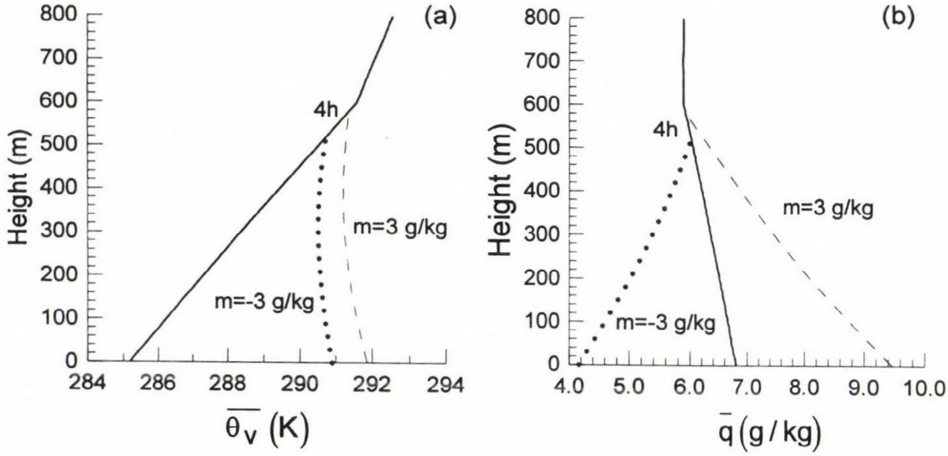

Fig. 5. Vertical profiles (*a*) of virtual potential temperature $\overline{\theta_V}$; (*b*) of specific humidity $\bar{q}$ four hours after sunrise for different values of the earth's surface specific humidity: m=-3.0 g kg^{-1} (stars) and m=3.0 g kg^{-1} (dashed line). The initial $\overline{\theta_V}$ and $\bar{q}$ profiles are plotted by bold line.

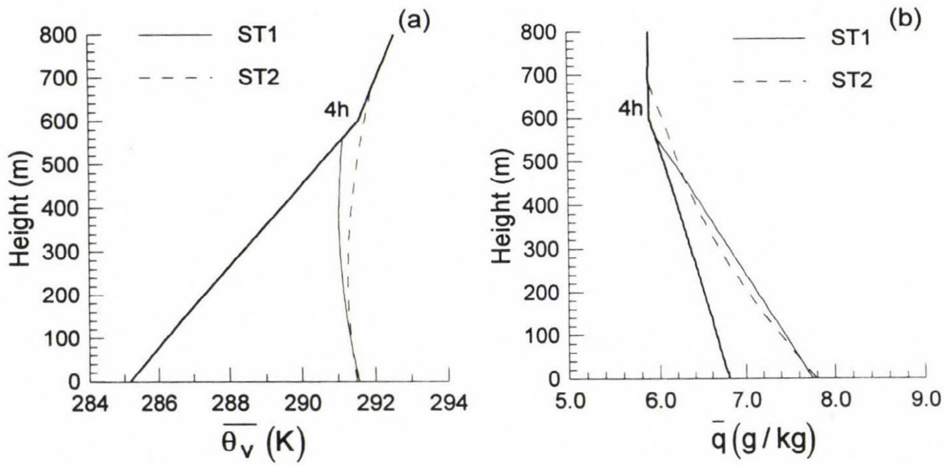

Fig. 6. Vertical profiles (*a*) of virtual potential temperature $\overline{\theta_V}$; (*b*) of specific humidity $\bar{q}$ four hours after sunrise: thin line — ST1 distribution, dashed line — ST2 distribution. The initial $\overline{\theta_V}$ and $\bar{q}$ profiles are given by bold line.

Fig. 3a shows that according to the model calculations, CBL depth grows with time and five hours a.s.r. the CBL height is approximately 650 m. It is seen also that VPT has a minimum near the middle of the CBL, because heating from below (by rising thermals) and entrainment of warm air from above (by downdrafts) lead to slightly warmer VPT in those regions. This result is in agreement with the mean VPT profile in the CBL (*Stull*, 1988). The moisture, presented in Fig. 3b, is redistributed to the same level as VPT. In this particular case the moisture at the earth surface is always greater than the moisture on the upper levels, i.e., a negative gradient in the ML is obtained. This result can be related to the fact that the updrafts transport moist air from the earth surface, while the downdrafts bring drier air from above. Based on the above, one can conclude that the model simulates the evolution of VPT and SH profiles in the morning boundary layer in agreement with generally accepted assumptions for the phenomena under study (*Stull,* 1994).

To study the model reaction to the rate of surface heating, the calculations are carried out with $k=5$ K and $k=8$ K. Fig. 4a shows that the magnitude of solar heating influences strongly the depth of CBL—the greater the heating, the higher the mixed layer is. Four hours a.s.r. the ML developed up to 450 m in the case of $k=5$ K (stars) and up to 640 m at $k=8$ K (dashed line). Fig. 4b shows that SH close to the ground is bigger at a greater solar heating. The comparison of SH at level $z=400$ m gives $q=6.3$ g kg^{-1} in the case of $k=5$ K and $q=6.6$ g kg^{-1} in the case of $k=8$ K, i.e., the difference is about 0.3 g kg^{-1}. This is due to the fact that greater number of thermals have reached height $z=400$ m when the heating is stronger.

The impact of the SH changes at the earth surface on the CBL depth is tested using two different values of the parameter m in Eq. (10) ($d=12$ hours for $0<t<6$ hours). Model outputs with $k=7$ K are shown in Fig. 5a (VPT profile) and Fig. 5b (SH profiles). Results corresponding to an increase of the earth surface SH ($m=3$ g kg^{-1}) are given by dashed lines; stars show the results with $m=-3$ g kg^{-1}, i.e., a decrease of the earth surface SH. It is clear from Fig. 5a that a significant increase in SH at the earth surface leads to slight increase in the CBL height. Four hours a.s.r. the difference in the CBL height is less than 60 m for 4.3 g kg^{-1} difference in the earth surface SH. The changes of SH at the earth surface however are of great importance for the moist quantity reaching the upper levels. The greater the SH at the earth surface, the greater the moisture in the ML is—four hours a.s.r. the SH at 300 m is 7.5 g kg^{-1} in the case of $m=3.0$ g kg^{-1} and 5.4 g kg^{-1} in the case of $m=-3.0$ g kg^{-1}. In comparison with the ground SH, the moisture decreases with height in the case of $m=3.0$ g kg^{-1}, due to the transport of drier air by downdrafts. An increase of the SH with height is observed at $m=-3.0$ g kg^{-1} explained with the fact that downdrafts contain more humid air than updrafts. In conclusion it can be said that the ground moisture influences significantly the SH profile, and its effect on the VPT redistribution and the ML depth is not well pronounced.

The sensitivity of the model to the size distribution of thermals at the earth is visible from Figs. 6a and 6b, where the calculated VPT and SH profiles by two types of size distribution ST1 (thin line) and ST2 (dashed line) are presented four hours a.s.r. The results show that when heat and moisture are transported by larger thermals (ST2 type distribution), the changes in VPT and SH profiles extend for approximately 100 m higher than the corresponding extend for changes caused by smaller thermals (ST1 type distribution). Although the thermals occupied one and the same fraction of area at the earth surface, the larger thermals (ST2) can ascend higher than smaller ones, (ST1), due to the smaller entrainment of the environmental air, hence the higher levels are affected.

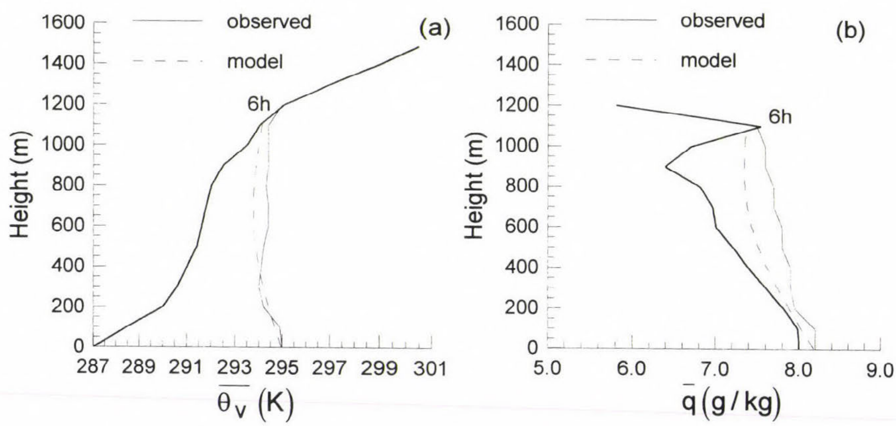

Fig. 7. Vertical profiles (*a*) of virtual potential temperature $\overline{\theta_V}$; (*b*) of specific humidity $\bar{q}$ six hours after sunrise: thin line – observation data, dashed line – model output. The initial profiles of measured $\overline{\theta_V}$ and $\bar{q}$ is given by bold line.

To check the capacity of the presented model to reproduce the evolution of the ML characteristics, the early morning sounding (05:21 LST on July 8, 1986) of the field experiment HAPEX-MOBILHY is chosen. This day is reported as a purely convective case. The initial VPT and SH profiles are taken from Figs. 1a and 2a in *Cuxart et al.* (1994) and plotted by bold lines in *Fig. 7a* and *Fig. 7b*, respectively. The values for k and m for the calculations of $\overline{\theta_V}(0,t)$ and $\bar{q}(0,t)$ are chosen to fit the observed evolution of VPT and SH at the earth surface. Due to the lack of information about size distribution of thermals at the earth surface, the model was run by ST1 and ST2. The results shows that six hours a.s.r. the calculated by ST1 height of CBL is about 950 m, which is 200 m lower than the measured one. Using ST2 distribution function, six hours a.s.r. the modeled ML depth is close to the observed value at 11:14 LST. On account of this, model results using ST2 thermal size distribution six hours a.s.r. (dashed lines on Fig. 7a and Fig. 7b) are compared with corresponding observations (thin lines on Fig. 7a and Fig. 7b). The comparison shows that the model does not reproduce perfectly well the VPT values. However the difference between modeled and observed VPT is less than 0.6°C. The observed VPT profile supports the small stable gradient predicted by the model. Six hours a.s.r. the predicted SH profile in the CBL (dashed line in Fig. 7b) is also quite similar to the observed one (thin line in Fig. 7b), but the calculated vertical gradient is greater than the observed one. The difference between modeled and measured SH is the greatest at z=500 m and it is about 0.4 g kg^{-1} there. It is worthwhile to mention that the observed case is an interesting example for moisture redistribution—the moisture in the ML is transported by the moist updrafts and downdrafts. To summarize the results from comparison between model calculations and field measurements it can be said that the main features of VPT and SH profiles are well simulated.

5. Summary and conclusion

A one-dimensional numerical model of the evolution of the morning convective boundary layer is developed. The basic idea of the model is that the heat and moisture in the convective mixed layer are transported by isolated turbulent eddies (thermals). The model is applicable to the clear-sky days with light mean winds when the dominant mechanism driving the turbulence is the buoyancy. The partition of the CBL into updrafts and compensating downdrafts domains as in *Mitzeva et al.* (1997) leads to the equations for the evolution of horizontal-mean virtual potential temperature and specific humidity. The problem is closed by assuming that thermals ascend as individual ones entraining the environmental air. For the numerical study of the vertical profiles of the horizontal-mean VPT and SH, the vertical velocities, the temperature excesses and size distribution function of thermals at the earth surface are preassigned in accordance to the observations.

The results of the calculations with simulated and observed initial temperature and humidity profiles show that the model reproduces satisfactory well the main features of VPT and SH evolution in the CBL. The model output for VPT shows a slightly unstable lapse rate in the lower part of the CBL and a slightly stable lapse rate in the upper part of the CBL, which is consistent with the observations. The negative gradient in SH is obtained by the model at variations of the earth's surface SH typical for the morning hours. This result is in agreement with the field measurements.

The numerical test indicates the importance of the magnitude of solar heating for the depth of CBL—the greater the heating, the higher the developed mixed layer is. The simulations with the model show that the earth surface SH influences significantly the moisture gradient in the ML and its effect on the CBL height and on the VPT profile is less significant than the magnitude of solar heating.

The numerical experiments and the comparison between model simulations and observations reveal the sensitivity of the model to the distribution of thermals at the starting level, which implies that the determination of these quantities from field measurements would be useful for this type of model.

The parametrization of the thermals' merger during their ascend and the sink of thermals back into the ML after penetrating the temperature inversion will bring the model closer to the physical nature of the phenomenon.

Acknowledgements—This work is partly supported by the Bulgarian Science Foundation grand NZ–610/96. We would like to thank *Dr. K. Ganev* for the useful comments concerning the numerical scheme and *Dr. St. Evtimov* for remarks and discussions.

References

Andreev, V. and *Panchev, S.*, 1975: *Dynamics of Atmospheric Termals* (in Russian). Gidrometeoizdat, Leningrad.

Andreev, V. and *Ganev, K.*, 1981: Model of convective heat exchange due to isolated thermals in the atmospheric boundary layer. *Boundary-Layer Meteorol. 20*, 331-339.

Chatfield, R.B. and *Brost, R.A.*, 1987: A two-stream model of the vertical transport of trace species in the convective boundary layer. *J. Geophys. Res. 92*, 13263-13276.

Cushman-Roisin, B., 1982: A theory of convection. Modeling by two buoyant interacting fluids. *Geophys. Astrophys. Fluid Dynamics 19*, 35-59.

Cuxart, J., Bougeault, P., Lacarrere, P., Noilhan, J. and *Soler, M.R.*, 1994: A comparison between transilient turbulence theory and the exchange coefficient model approaches. *Boundary-Layer Meteorol. 67*, 251-276.

Hrgian, A.X., 1969: *Physics of the Atmosphere* (in Russian). Gidrometeoizdat, Leningrad.

Lamb, R.G., 1982: Diffusion in the convective boundary layer. In *Atmospheric Turbulence and Air Pollution Modeling* (eds: *F.T.M. Nieuwstadt* and *H. van Dop*). D. Reidel Hingham, Mass.

Manton, M.J., 1975: Penetrative convection due to a field of thermals. *J. Atmos. Sci. 32*, 2272-2277.

Mitzeva, R., Evtimov, St. and *Doychinska, S.*, 1997: A one-dimensional thermal model of morning convective boundary layer development. *Időjárás 101*, 1-15.

Roache, P., 1976: *Computational Fluid Dynamics*. Hermosa Publisher, Albuquerque.

Stull, R. B., 1988: *An Introduction to Boundary Layer Meteorology*. Kluwer Academic Publisher, Dordrecht, Boston, London.

Stull, R.B., 1994: Fundamental processes in boundary layers. In *Proc. of a WCRP Workshop on the Parameterization of Sub-grid Scale Tracer Transport* (Virginia Beach, USA, 30 Nov–3 Dec 1993), WMO/TD- No. 823, 5-13.

Telford, J.W., 1966: The convective mechanism in clear air. *J. Atmos. Sci. 23*, 652-666.

Vulfson, N.T., 1961: *Convective Motion in a Free Atmosphere* (in Russian). Publ. Akad. Nauk, Moscow.

Warner, J. and *Telford, J.*, 1967: Convection below cloud base. *J. Atmos. Sci. 24*, 374-382.

IDŐJÁRÁS
Quarterly Journal of the Hungarian Meteorological Service
Vol. 104, No. 2, April–June 2000, pp. 123–136

Reconstruction of the spring temperatures in the 18th century based on the measured lengths of grapevine sprouts

Jaroslav Střeštík[1] and **József Verő**[2]

[1]*Geophysical Institute of the Academy of Sciences of the Czech Republic, Prague, Czech Republic*

[2]*Geodetical and Geophysical Research Institute of the Hungarian Academy of Sciences, H-9401 Sopron, P.O. Box 5, Hungary*

(Manuscript submitted for publication 26 October 1999; in final form 4 May 2000)

Abstract—Lengths of new grapevine sprouts, measured systematically in Kőszeg, Hungary, since 1740 on the same day of each year (24 April) exhibit a good correlation with the average air temperatures in April and in some extent in March. Weighted average (March + 2 × April)/3 shows the best correlation, where the correlation coefficient reaches 0.6. Climatological data taken from Budapest, Vienna and Prague show that the correlation decreases with the increasing distance. Values higher by about 0.05 were obtained with square roots of the lengths instead of the proper lengths for all stations. All correlations between derivatives of the lengths and temperatures instead of original data are higher by 0.1. There is a negative correlation between these lengths and the relative air humidity or cloudiness. The correlation with precipitation, sunspot numbers and geomagnetic activity index is poor and not significant. These results confirm the relatively lower temperatures in the 19th century and the warm decades till the end of the 18th century, moreover, they suggest that the warm period continued back to the past at least till 1740; this statement is valid only for spring temperatures.

Key-words: temperature reconstruction, grapevine sprouts.

1. Introduction

Instrumental air temperature data series at individual stations are relatively short. Observations started at the most central European stations in the second half of the 18th century, e.g., at Prague-Klementinum in 1775, Vienna 1775, Budapest 1780, Munich 1781; longer series are available at Geneva from 1753, Basle 1755, DeBilt in The Netherlands 1716. At some stations the registration started earlier but it was later interrupted, e.g., at Berlin from 1706, but an uninterrupted series is available from 1756 only. All observed data used in this paper originate from the database of *Bradley* (1992). Series with the length of 200 years or a little more render only few possibilities to determine and prove long-term trends or correlations with other sufficiently long observed series. Therefore respective conclusions concerning the possible climate development in future would not be sufficiently supported.

From this point of view it is very desirable to gain any guess of air temperature further to the past using various different observations or natural archives (e.g., *Jacoby* and *D'Arrigo*, 1989). Each of these reconstructions are, however, limited in some extent to the region where the data were taken from or the season connected with these data, and the accuracy is often different. One can claim that independent reconstructions of climate for the period before the instrumental observation are always desirable.

2. Measurements

In this paper we shall use the measured lengths of new grapevine sprouts. These lengths have been systematically measured since 1740 in Kőszeg for different grapevine varieties and in different localities in the vicinity of the town, on the same day of each year (24 April). Kőszeg is situated in West Hungary near the boundary with Austria, where the long Pannonian basin changes into low mountains (last parts of the Alps). Though this is not as famous wine region as other Hungarian ones, inhabitants keep an interesting tradition: every year on St. George's day (24 April) a procession in folk costumes moves through the town bringing new grapevine sprouts from vineyards in the vicinity of the town to the town hall. These sprouts are then drawn on paper as documentation, keeping carefully their size and form. These pictures have been saved in the town museum since 1740 till now.

Till 1868 all drawings were prepared by Indian ink, later completed by colours, and by coloured photos in real size from 1962. Together with them, some information are saved about the wine production. They have not a big meaning because there are not always the data of the vineyard area. Moreover, there are some comments concerning the weather, especially unusual meteorological occasions. E.g., in 1929 it was mentioned that a severe winter occurred in February (on February 11, 1929 the lowest temperature in the Czech Republic was recorded) when many grapevine varieties were destroyed by frost causing significantly lower production. All these comments are written in Hungarian by hand, some older ones are not well legible.

The lengths of the mentioned grapevine sprouts are very different. In some years only not yet opened blossoms could be found on the branches, whereas in other years new branches could grow more than 30 cm till the 24th of April. The paintings have been saved for two centuries in the museum and perhaps nobody, not living in the town, knew about them. At the end of the thirties of the 20th century *Aladár Visnya*, the director of the museum, measured all these painted sprouts and offered them to the Meteorological Institute in Budapest. *Zoltán Berkes*, a meteorologist, compared these lengths to the observed air temperatures in Budapest and Vienna. Results were published in Hungarian and German (*Berkes*, 1942). *Péczely* (1982) carried out a correlation analysis with average temperatures and sunshine duration in March and April, and obtained a rather close quadratic connection with spring temperatures. The results of Berkes and Péczely showed some interesting correlations. The data are by 60 years longer now and represent a very valuable material for further investigations.

3. *Results*

Lengths of grapevine sprouts for 1740–1939 are published in *Berkes* (1942). Lengths for 1900–1998 were measured in the original paintings in the Kőszeg museum (years 1900–1939 for comparison with Berkes' measurements). Visitors can see some of them. All the lengths for 259 years are given in *Table 1*. Besides the original paintings there are copies of smaller size (1:4) available, these are too small and were not used. The lengths in the individual years are graphically represented in *Fig. 1*. Striking low values after 1900 can be distinguished at the first view, it will be explained later.

In his paper *Berkes* gives attention to some inhomogeneities, which could decrease the accuracy of the results found. The measurements have been done on the same day of each year, in this point no objection can be risen. But there are different grapevine varieties, some of them grow earlier and the others later. The sprouts were taken from different localities in the vicinity of the town with possible different microclimate. Fortunately, more sprouts have been documented each year (at least five or often more) and the grapevine variety and locality have always been assigned. The most frequently planted and in museum documented ones are Burgund and Blue Frankos. Their sprouts have usually equal length. *Berkes* used only these varieties. If in some (not numerous) years these varieties were not documented, *Berkes* used other varieties (e.g., the third most frequently used Riesling) and comparing its length with the lengths of other varieties in other years he guessed the corresponding length of Burgund. The most serious inhomogeneity occurred in 1900. In this year the vineyards were attacked by Phyloxera, therefore it was necessary to cut old plants and to introduce new variants. They grow slower than the older ones and this is the explanation of systematically shorter branches in the 20th century.

Berkes compared the measured grapevine sprout lengths with the observed air temperatures in Budapest and Vienna. Temperatures measured directly in Kőszeg are available only for a short recent period. For all variants of temperatures (described later) the correlation with the data of Budapest was higher than with Vienna data. Vienna is nearer, but climatologically it is a bit different from Budapest or Kőszeg. *Berkes* also used data from Prague (Klementinum). He considers them of high quality. Of course, due to the longer distance the correlation with Prague data is worse but still significant.

Table 1. Lengths of grapevine sprouts in centimetres measured in Kőszeg on April 24, each year. The table continues with the corrected data since 1900. A – multiplied by two, B – multiplied by three. Data till 1940 are taken from *Berkes* (1942)

	Year	0	1	2	3	4	5	6	7	8	9
	1740	0	1	0	1	7	21	0	4	1	4
	1750	27	3	11	12	4	28	6	31	1	6
	1760	8	28	12	5	3	5	20	0	6	14
	1770	0	0	0	0	20	21	9	5	9	48
	1780	4	20	0	13	3	0	0	0	5	0
	1790	0	0	2	0	8	0	2	17	33	0
	1800	2	6	5	0	3	0	5	0	2	0
	1810	0	13	0	7	25	9	7	0	5	20
	1820	10	6	11	10	0	3	18	12	17	9
	1830	17	14	8	0	4	5	8	0	0	0
	1840	5	13	3	14	14	0	13	0	20	1
	1850	8	15	1	0	15	4	12	9	0	9
	1860	0	3	20	12	1	7	18	1	4	13
	1870	1	7	7	12	8	1	18	1	10	5
	1880	6	1	9	0	6	9	1	2	3	3
	1890	11	1	6	15	26	2	2	11	8	4
	1900	1	3	1	1	11	4	12	1	1	3
	1910	3	5	1	1	5	5	2	1	5	2
	1920	2	6	2	2	4	2	2	2	3	0
	1930	2	1	1	1	10	2	3	1	4	2
	1940	2	1	1	4	1	10	2	3	4	3
	1950	3	1	4	6	0	1	1	3	0	7
	1960	3	10	1	3	2	1	4	3	3	1
	1970	1	2	2	1	8	2	4	1	1	2
	1980	1	3	1	2	1	2	1	2	1	9
	1990	5	1	2	1	6	3	0	0	2	
(A)	1900	2	6	2	2	22	8	24	2	2	6
	1910	6	10	2	2	10	0	4	2	10	4
	1920	4	11	4	3	8	3	4	3	4	0
	1930	2	1	1	1	23	3	5	2	8	4
	1940	2	2	1	8	2	19	4	5	8	6
	1950	6	2	8	11	0	1	1	5	0	14
	1960	6	20	2	5	4	2	7	5	5	1
	1970	1	4	4	2	15	3	8	2	2	4
	1980	1	5	2	4	2	4	2	3	2	18
	1990	9	2	3	2	11	5	0	0	4	
(B)	1900	3	9	3	3	33	12	36	3	3	9
	1910	9	15	3	3	15	15	6	3	15	6
	1920	7	16	6	4	12	5	6	5	6	0
	1930	4	2	2	2	34	4	7	2	11	6
	1940	4	3	2	12	3	28	7	8	12	9
	1950	8	3	12	16	0	2	2	8	0	21
	1960	9	30	3	8	6	3	10	8	8	2
	1970	2	6	7	3	22	4	12	3	3	5
	1980	3	8	3	7	3	5	3	4	4	27
	1990	14	3	4	4	16	8	0	0	7	

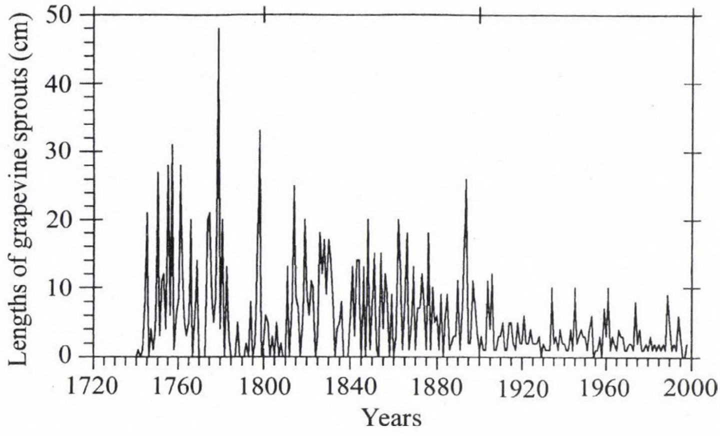

Fig. 1. Lengths of grapevine sprouts in the individual years in centimetres.

The highest correlation appeared for average temperatures in March + April of the current year: for Budapest it is 0.70 and for Vienna 0.58. With respect to the possible inhomogeneity around 1900 he calculated the correlations separately till 1899. In this case the coefficients were even higher: 0.77 for Budapest and 0.63 for Vienna. Using monthly averages only for April he arrived to little lower values: only 0.62 for Budapest. The level of the 99% significance is 0.20 for his 160 year series (i.e., 1740–1899). The correlation with temperatures in other months (February, etc.) were insignificant. Correlation with the precipitation (data series from Budapest were only 80 years long) was on the significance level (–0.21). The more rainy weather is usually colder. *Berkes* found a possible correlation with solar activity; the coefficient is about 0.26.

Series longer by 60 years can bring more accurate results. We shall use some extended combination of climatological data. The purpose is to find how the different kinds of weather influence the growth of grapevine sprouts in spring. In other words, we want to know precisely what the results tell us and what we have reconstructed from the measured lengths. The most important correlation coefficients are summarised in *Table 2*. With respect to a possible inhomogeneity around 1900 first we calculated the correlation with Budapest temperature separately for periods till 1900 and from 1901, and then for the whole period and other stations. Levels for the 99% significance of correlation coefficients are 0.20 for the first part, 0.26 for the second part and 0.16 for the whole period. In columns we found correlations with average temperatures in March (III), April (IV), March + April (A) and with weighted average where temperatures in April were taken with double weight than in March (WA). For the latter combination the highest values were obtained. Temperatures in April influence the growth surely more than in March. As a whole, all correlations are lower than those mentioned by *Berkes*, including periods used by him. *Berkes* probably used average April temperatures only till 24 April instead of the whole month. This calculation is methodically better. However, we are able to repeat this calculation for data of Prague only. These results are written in the last row of Table 2 and marked by Prague G (the same notation is used in other tables). Correlation coefficients calculated for these means are really higher than for the whole month. Correlations with average temperatures in February move between 0.10 and 0.15 being under the 95% significance level. Other combinations of months also result in somewhat lower values than those in the last column of Table 2. Further, in contrary to *Berkes*, there are relatively small differences between coefficients for Budapest and Vienna, and even for Prague we have obtained high values. Correlations were calculated for some other stations, e.g., for Klagenfurt or Geneva. They decrease with the increasing distance, however, for stations mentioned they are still significant.

Table 2. Correlation of lengths of grapevine sprouts with mean air temperatures—original data. Lower part of the table expresses the correlations between derivatives of the data

Station	Period	III	IV	A	WA
Budapest	1780–1900	0.395	0.516	0.598	0.613
Budapest	1901–1998	0.347	0.425	0.508	0.529
Budapest	1780–1998	0.178	0.447	0.405	0.466
Wien	1775–1998	0.186	0.393	0.378	0.422
Prague	1775–1998	0.221	0.371	0.367	0.394
Prague G	1775–1998		0.422	0.403	0.437
Budapest	1780–1900	0.441	0.552	0.615	0.625
Budapest	1901–1998	0.395	0.516	0.597	0.613
Budapest	1780–1998	0.347	0.422	0.499	0.522
Wien	1775–1998	0.390	0.528	0.587	0.608
Prague	1775–1998	0.335	0.473	0.518	0.539
Prague G	1775–1998		0.520	0.552	0.578

Lower lengths after 1900, well observed in Fig. 1, offer a possibility to introduce some corrections and homogenization of the data. We tried to multiply all values after 1900 by two or three. For this purpose we used values directly measured with the accuracy of 0.2 cm, not the published ones (also in Table 1) in cm, so the corrected values are not always simple multiples of the original values. These corrected lengths are given in the lower part of Table 1 (multiplication by 2 is marked by A, by 3 is marked by B. The same notation is used in the other tables.). Correlation coefficients for both corrections and the temperatures in different months are given in *Table 3*. It seems that multiplication by three results in higher coefficients as a whole and seems therefore more suitable. The corrected data are represented in *Fig. 2* together with the smoothed course.

Table 3. Correlation of lengths of grapevine sprouts with mean air temperatures—corrected data. Lower part of the table expresses the correlations between derivatives of the data

Station	Kőszeg data	III	IV	A	WA
Budapest	corr. A	0.283	0.468	0.501	0.543
Budapest	corr. B	0.338	0.441	0.528	0.551
Wien	corr. A	0.279	0.427	0.469	0.500
Wien	corr. B	0.333	0.423	0.508	0.525
Prague	corr. A	0.302	0.422	0.454	0.478
Prague	corr. B	0.350	0.440	0.510	0.494
Prague G	corr. A		0.478	0.492	0.519
Prague G	corr. B		0.494	0.534	0.554
Budapest	corr. A	0.452	0.545	0.635	0.649
Budapest	corr. B	0.435	0.540	0.620	0.638
Wien	corr. A	0.415	0.551	0.618	0.638
Wien	corr. B	0.414	0.546	0.615	0.635
Prague	corr. A	0.356	0.503	0.551	0.572
Prague	corr. B	0.358	0.511	0.557	0.579
Prague G	corr. A		0.520	0.552	0.578
Prague G	corr. B		0.540	0.583	0.611

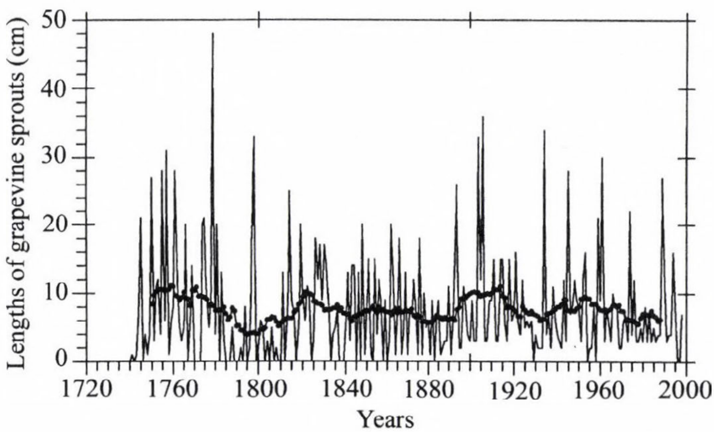

Fig. 2. Lengths of grapevine sprouts in the individual years in centimetres with correction B. Smoothed data—running averages in the 21 year interval— are drawn by thick line.

Introducing a correction for the data after 1900 improves the correlations. Nevertheless, the correlations in the 20th century are always lower than those before 1900. This is caused by the fact that the rapid increase in temperatures during the last decade does not have a corresponding response in the lengths of grapevine sprouts. Using an interval, e.g., 1901–1990 instead of 1901–1998, one arrives to little higher values. It seems therefore that the grapevine sprout lengths reflect the short-time fluctuations more than the long-term trend. Any attempt to separate these two factors (even drawing the long-term trend by hand!) brings higher correlations for the data where the long-term trend was removed, and poor correlations for the long-term trends themselves as well. This regularity is better seen using the derivatives of all data series instead of the original data (i.e., the increase of temperatures and grapevine sprouts lengths with respect to the previous year). All these correlations are given in the second part of Table 2 and the same will be done in all following tables. It is clear that the correlation is higher by about 0.1. Correlations of derivatives of lengths with temperatures (and vice versa) are significantly lower.

Using correlation coefficients one silently supposes that the relation between correlated quantities is linear. In this case this point is not quite satisfied. It is clear that the growth is very slow at the beginning and the spouts only later grow more rapidly. So the difference at the lengths 0 or 1 cm corresponds to a relatively serious difference in temperature whereas there is no such a difference between the lengths 30 or 35 cm. Therefore it is better to correlate the temperature not with the length of sprouts but, e.g., with its logarithm or square root, etc. This transformation decreases the differences between long sprouts (20, 30, 40 cm). We decided for square roots rather than logarithms because of difficulties with zero lengths. The second reason to introduce this transformation was that the grapevine sprout lengths do not exhibit normal distribution (for the temperatures the situation is better). After the transformation the distribution is nearer to the normal one. Correlation coefficients between square roots of grapevine sprout lengths and the same temperatures as in Tables 2 and 3 are given in *Table 4*. In *Fig. 3* a correlation between these square roots for data with correction B and the weighted average of March and April temperature in Budapest are shown. It is clear that with this transformation the relation is nearly linear. Using logarithm instead of square root brings the same result (one must define a value for the zero length). Correlation between derivatives is higher than that for original data also in the case of square roots.

In Fig. 3, on its left side, a small separate group of points can be distinguished. They correspond to the zero sprout length and usually to low temperatures. In these years one may hardly discuss the correlation between sprout lengths and anything else. The same figure prepared without this group shows clearer dependence. The coefficient does not increase significantly but the regression line is steeper. It seems that it has a meaning to exclude years with zero sprout lengths. The regression line in Fig. 3 can be expressed by the formula $T=0.630\ d^{-2}+6.08$, where T is the temperature used in Fig. 2 and d is the length of grapevine sprouts. Without the group with zero lengths the relation is $T=0.650\ d^{-2}+5.96$.

Table 4. Correlation of square roots of lengths of grapevine sprouts with mean air temperatures—original and corrected data B.
Lower part of the table expresses the correlations between derivatives of the data

Station	Kőszeg data	III	IV	A	WA
Budapest	no corr.	0.204	0.491	0.452	0.517
Budapest	corr. B	0.376	0.498	0.592	0.619
Wien	no corr.	0.217	0.429	0.422	0.468
Wien	corr. B	0.375	0.467	0.566	0.584
Prague	no corr.	0.303	0.439	0.464	0.486
Prague	corr. B	0.411	0.490	0.569	0.577
Prague G	no corr.		0.483	0.495	0.524
Prague G	corr. B		0.539	0.601	0.617
Budapest	no corr.	0.460	0.572	0.656	0.674
Budapest	corr. B	0.468	0.591	0.672	0.694
Wien	no corr.	0.452	0.596	0.670	0.692
Wien	corr. B	0.465	0.606	0.686	0.708
Prague	no corr.	0.426	0.551	0.630	0.645
Prague	corr. B	0.438	0.575	0.653	0.669
Prague G	no corr.		0.584	0.655	0.673
Prague G	corr. B		0.603	0.674	0.693

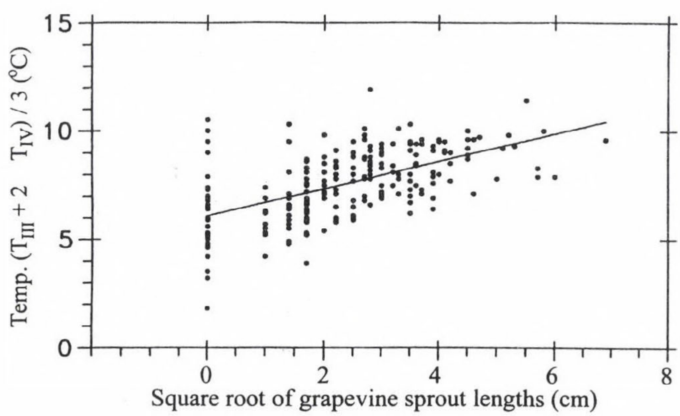

Fig. 3. Correlation of the square roots of lengths of grapevine sprouts with weighted averages of March and April temperatures in Budapest.

Till now only the monthly mean temperatures were used. In the Prague Klementinum series the daily maxima and morning minima have been available since 1775. Their monthly means were calculated and these means were used for correlation with the measured sprout lengths. All combinations of temperatures including April means till April 24 (marked with Prague G) were used. All correlation coefficients are also given in *Tables 5* and *6* for corrected lengths marked with "corr. B". Correlations are also given for square roots (marked with "sq"). When compared with monthly means for Prague corr. B in Tables 3 and 4 it is seen that the correlations are a bit higher for maximal temperatures than for daily means and especially for morning minimal temperatures. It is very probable that also for Budapest and Vienna the correlation with maximal temperatures would be a bit higher than for daily means.

Table 5. Correlation of lengths of grapevine sprouts and their square roots with maximal air temperatures—original and corrected data B.
Lower part of the table expresses the correlations between derivatives of the data

Station	Kőszeg data	III	IV	A	WA
Prague	no corr.	0.203	0.344	0.343	0.369
Prague	corr. B	0.353	0.443	0.446	0.515
Prague	no corr. sq.	0.286	0.416	0.443	0.464
Prague	corr. B sq.	0.413	0.495	0.578	0.585
Prague G	no corr.		0.391	0.376	0.405
Prague G	corr. B		0.495	0.540	0.555
Prague G	no corr. sq.		0.458	0.473	0.497
Prague G	corr. B sq.		0.545	0.610	0.623
Prague	no corr.	0.348	0.486	0.542	0.559
Prague	corr. B	0.374	0.531	0.587	0.607
Prague	no corr. sq.	0.442	0.557	0.651	0.660
Prague	corr. B sq.	0.454	0.585	0.677	0.689
Prague G	no corr.		0.543	0.581	0.605
Prague G	corr. B		0.577	0.621	0.645
Prague G	no corr. sq.		0.599	0.680	0.694
Prague G	corr. B sq.		0.623	0.704	0.718

For comparison of the grapevine sprout lengths with precipitation data in March and April not sufficiently long series are available from stations near Kőszeg. The nearest station with longer series is Klagenfurt (starting in 1813), Kremsmünster (1820), Prague (1805), Geneva (1826), and perhaps Budapest

(1841). Calculating the same correlations as for temperatures we have found no correlation better than 0.1, and this value is much under the significance level.

Table 6. Correlation of lengths of grapevine sprouts and their square roots with minimal air temperatures—corrected data B.
Lower part of the table expresses the correlations between derivatives of the data

Station	Kőszeg data	III	IV	A	WA
Prague	no corr.	0.308	0.354	0.417	0.425
Prague	corr. B sq.	0.374	0.413	0.497	0.506
Prague G	corr. B		0.397	0.441	0.455
Prague G	corr. B sq.		0.457	0.522	0.534
Prague	corr. B	0.297	0.416	0.452	0.476
Prague	corr. B sq.	0.307	0.442	0.475	0.500
Prague G	corr. B		0.456	0.475	0.501
Prague G	corr. B sq.		0.471	0.492	0.519

Comparison with the mean cloudiness or the relative air humidity gives more chance. Cloudiness data from Prague are available from 1775, humidity data only from 1845. Correlation coefficients between sprout lengths and monthly means of cloudiness and relative humidity are given in *Table 7*, arranged in the same way as in Table 6. Values in some columns exceed the 99% significance level, in other at least the 95% level. Nearly zero values for March reflect themselves in lower values for periods that include March (columns A and WA), while the correlation with April data alone is higher than in columns A and WA. Here we can observe a bit higher correlation for square roots again, showing that also in this case the dependence is not linear. Correlation coefficients are negative. The cause is that higher cloudiness and relative humidity in these months are connected with colder weather. The 99% significance level is 0.16 for the cloudiness results and 0.21 for the humidity results. It should be stressed that in the case of cloudiness and relative humidity no increase in correlation coefficients has been found using correction of the lengths after 1900, the values are nearly the same.

As to solar activity, monthly means of sunspot numbers are available for the whole period, but their correlation with the measured lengths is very low. For any combination of months as used for temperatures, for all corrections and using square roots all values are not higher than 0.1, more often only about 0.05, being very much under the 95% significance limit. For geomagnetic activity, where the index aa is available from 1868, the coefficients do not exceed 0.13, however, in this case the 99% significance limit is 0.25.

Table 7. Correlation of lengths of grapevine sprouts with some other quantities—corrected data B. Lower part of the table expresses the correlations between derivatives of the data

Quantity	III	IV	A	WA
Prague, rel. humidity	-0.003	-0.242	-0.073	-0.114
Prague G, rel. humidity		-0.160	-0.091	-0.129
Prague, cloudiness	-0.120	-0.338	-0.275	-0.312
Prague, G. cloudiness		-0.351	-0.292	-0.327
Klagenfurt, precipit.	-0.050	-0.111	.0.108	-0.115
Wolf sunspot number	-0.049	-0.030	-0.040	-0.037
Geomagnetic aa index	-0.124	-0.113	-0.129	-0.126
Prague, rel. humidity	-0.211	-0.206	-0.229	-0.228
Prague G, rel. humidity		-0.209	-0.258	-0.246
Prague, cloudiness	-0.260	-0.291	-0.315	-0.348
Prague, G. cloudiness		-0.363	-0.371	-0.377
Klagenfurt, precipit.	-0.013	-0.026	-0.026	-0.027
Wolf sunspot number	-0.007	0.057	0.027	0.039
Geomagnetic aa index	-0.084	-0.036	-0.071	-0.060

4. Conclusion

To conclusion we shall represent graphically the course of the air temperature in Budapest (weighted averages for March+April=WA used in tables) together with the square roots of the lengths of grapevine sprouts (this combination exhibits the best correlation), both smoothed by running averages in 21 year interval (*Fig. 4*). The picture shows good agreement between the curves. Both curves display similar periods with higher or lower values lasting for several decades, with the exception of the last decades (after 1960). This point confirms other observed and indirect data. The sprouts were relatively long even in decades before 1780 (see Figs. 1 and 4), where no instrumental observation in the region in question was available. We may judge that spring temperatures between 1740–1780 were approximately on the same level as between 1780–1790, whilst they were surely higher than those in the middle of the 19th century.

This result agrees well with the reconstructed course of temperatures received by *Jacoby* and *D'Arrigo* (1989) and based on the tree-rings from the arctic regions. They also found a clear maximum at the end of the 18th and the beginning of the 19th century, which continues with some fluctuations more to the past, with some short-time maxima during 1720–1780. A deeper minimum appears between 1700–1720 but not so deep as that in the 19th century. The correlation coefficient is very low between the temperatures given by *Jacoby* and *D'Arrigo* and the sprout lengths. This is probably due to the relatively stable sprout lengths in the 20th century, when the temperature permanently increases, and due to the big year-to-year fluctuation of the lengths compared with a smooth course of reconstructed temperatures. For corrected data (corr.

B) one arrives to higher correlations, nevertheless, they are still under the significance level. Better results can be obtained for smoothed data (running averages in 21 year interval). For corrected data of sprouts the correlation coefficient reaches 0.15.

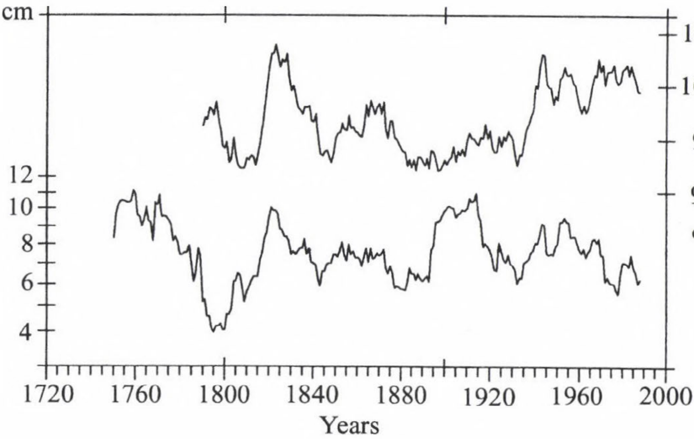

Fig. 4. Course of spring temperatures in Budapest (weighted average March+2 × April) —shown by the upper curve and the right-hand scale. Lengths of grapevine sprouts in Kőszeg—shown by the lower curve and the left-hand scale. Both courses are smoothed using running averages in the 21 year interval.

Low correlation with the data from *Jacoby* and *D'Arrigo* does not mean that the results from grapevine sprout lengths are wrong. Data used for comparison originate from quite different regions and because they are based on tree-rings they include the whole period of vegetation. Grapevine sprouts data, on the other hand, originate from Hungary and are influenced only by the spring temperatures till 24 April, they cannot be influenced by summer temperatures. So we have reconstructed a different kind of data, for a special month. We confirmed high spring temperatures at the end of the 18th century continuing at least till 1740, speaking nothing of summer or winter temperatures in the years in question. The approximately 200 year wave, apparent in the 1780–1980 data, is not so obvious before 1740, at least for spring temperatures, and the natural climate fluctuations are more complicated than it was thought earlier.

Acknowledgements—The authors wish to express their thanks to *Dr. Kornél Bakay*, Director of the Kőszeg Museum who kindly enabled us to provide measurements of the original pictures of grapevine sprouts saved in the museum.

References

Berkes, Z., 1942: Reflection of climate variability in the length of Kőszeg grapevine sprouts (in Hungarian and German). *A Magyar Királyi Földmivelésügyi Minisztériumfennhatósága alatt álló Magyar Kir. Orsz. Meteorológiai és Földmágnességi Intézet kisebb kiadványai, új sorozat 15. szám,* S. 3-17.

Bradley, R., 1992: Climate since AD 1500 Database. IGBP PAGES/World Data Center–A for Paleoclimatology Data Contribution Series # 92-015.

Jacoby, G. C. and *D'Arrigo, R.*, 1989: Reconstructed Northern Hemisphere annual temperature since 1671 based on a high-latitude tree-ring data from North America. *Climatic Change 14*, 39-45 (available also on Internet).

Péczely Gy., 1982: The "Kőszeg Book of grapevine sprouts" (in Hungarian). *Légkör 27*, No. 3, 24-27.

BOOK REVIEWS

Henning Rodhe and Robert Charlson (editors): **The Legacy of Svante Arrhenius Understanding the Greenhouse Effect**. Royal Swedish Academy of Sciences & Stockholm University, 1998. 212 pages.

In April 1896, the Swedish scientist Svante Arrhenius, who was later awarded the Nobel Prize for his outstanding work in the field of chemistry, published a paper in *The Philosophical Magazine* which is still frequently cited in the scientific literature. His work entitled "On the Influence of Carbonic Acid in the Air upon the Temperature of the Ground" made the first attempt to quantify the greenhouse effect caused by atmospheric carbon dioxide of anthropogenic origin. It is not an overstatement to say that the contemporary climate change research is based on this paper. He assumed, a 50% increase in the atmospheric mixing ratio of carbon dioxide would take about 3000 years, but now we know, if the present tendency will not change significantly, that level will be reached before the middle of the new century.

In order to commemorate the centenary of the publication of Arrhenius' paper, the Royal Swedish Academy of Sciences and the International Meteorological Institute in Stockholm organised a workshop on 9–10 April 1996. The book contains the presentations of the workshop. Each chapter/presentation is followed by a remarkable list of references.

The authors of the first chapters of the book review the state-of-the-art of science in the era of Arrhenius and the scientific context of his work. Originally, he intended to explain the formation of the Ice Ages, but nowadays his work is mostly cited in papers covering the global warming issue.

Several further papers discuss the historical development in certain fields of the atmospheric greenhouse effect. Thus, among others, the reader can learn how our knowledge got richer on the global carbon cycle, on the climate forcing of the aerosol particle, and on the greenhouse effect itself. We can get acquainted with the development of the climate models and with the numerical simulations of anthropogenic climate change. In addition to the historical reviews of the topics, the newest results illustrated by impressive colour figures can also be found in the chapters.

The last two presentations lead us on to the field of social sciences. How can the climate affect the human civilisation and what do people know about the climate change issue? What was the relation between Science and Policy 100 years ago and what is it like today?

And, as the last chapter of the book, one can find the facsimile copy of the famous paper of Svante Arrhenius.

The book reviewing the research of the atmospheric greenhouse effect from the beginning to our day can be recommended for both graduate students and research workers in geosciences. It can also be recommended to all educated persons interested in the history of science or in the global climate change issue. The book is available from the publisher.

László Haszpra

L. Göőz: **On the natural resources. Natural resources of Szabolcs-Szatmár-Bereg county** (in Hungarian with English and German summaries). Grafit Press Ltd, Nyíregyháza, 1999, pp. 374, 112 figures, several colour photos, 86 tables.

This book provides a comprehensive survey of the complexity of various resources as well as a summary of the author's scientific activity during the recent three decades. The book consists of ten chapters.

The first chapter deals with the principles of research of natural resources including the definition of the natural resource, the use of the geographic information system (GIS), the aim and methods of regional investigations in Szabolcs-Szatmár-Bereg (Sz-Sz-B) county (the north-east part of Hungary).

In the second chapter the author summarizes the geological structure and mineral possessions of Sz-Sz-B county, emphasizing the stores of oil, coal and natural gas, while the third chapter describes the energy production on the base of sustainable development. In this chapter he gives precious data on energy consumption with different sources of power in Sz-Sz-B county.

The fourth chapter gives characterization on water stores and water management of the county, while the fifth chapter deals with the agricultural potentiality in the region of Sz-Sz-B county.

The sixth chapter provides a summary of the geothermal resources of the county, and gives most recent data on output of thermal water from 27 springs, besides on chemical constituents of the mineral waters in several wells as well as utilization of the thermal water in heating of households.

The seventh chapter is dedicated to the problems of the possible utilization of the atmospheric resources, like solar and wind energy ; the author gives a good survey on radiation and wind climate of the county.

The last three chapters deal with biomass as natural resource, the relationship between the environment and the use of the natural resources and the decision strategy in the exploitation of different renewable resources.

About 360 books and papers are cited.

Finally, the author attaches appendix with data on stores of important minerals, ores, water chemistry, etc.

György Koppány

ATMOSPHERIC ENVIRONMENT

an international journal

To promote the distribution of Atmospheric Environment *Időjárás* publishes regularly the contents of this important journal. For further information the interested reader is asked to contact *Prof. P. Brimblecombe*, School for Environmental Sciences, University of East Anglia, Norwich NR4 7TJ, U.K.; E-mail: atmos_env@uea.ac.uk

Volume 34 Number 2 2000

Volume 34 Number 3 2000

Volume 34 Number 4 2000

Australasias

Antarctica

Volume 34 Number 5 2000

NOTES TO CONTRIBUTORS OF *IDŐJÁRÁS*

The purpose of the journal is to publish papers in any field of meteorology and atmosphere related scientific areas. These may be

- reports on new results of scientific investigations,
- critical review articles summarizing current state of art of a certain topic,
- shorter contributions dealing with a particular question.

Each issue contains "News" and "Book review" sections.

Authors may be of any nationality, but the official language of the journal is English. Papers will be reviewed by unidentified referees.

Manuscripts should be sent to
Editor-in-Chief of IDŐJÁRÁS
P.O. Box 39
H-1675 Budapest, Hungary

in three copies including all illustrations. One set of illustrations has to be of camera ready quality, the other two might be lower quality.

Title part of the paper should contain the concise title, the name(s) of the author(s), the affiliation(s) including postal and E-mail address(es). In case of multiple authors, the cover letter should indicate the corresponding author.

Abstract should follow the title, it contains the purpose, the data and methods as well as the basic conclusion.

Key-words are necessary to help to classify the topic.

The text has to be typed in double spacing with wide margins. Word-processor printing is preferred. The use of SI units are expected. The negative exponent is preferred to solidus. Figures and tables should be consecutively numbered and referred to in the text.

Mathematical formulas are expected to be as simple as possible and numbered in parentheses at the right margin. Non-Latin letters and hand-written symbols should be indicated and explained by making marginal notes in pencil.

Tables should be marked by Arabic numbers and printed in separate sheets together with their captions. Avoid too lengthy or complicated tables.

Figures should be drawn or printed in black and white, without legends, on separate sheets. The legends of figures should be printed as separate list. Good quality laser printings are preferred as master copies.

References: The text citation should contain the name(s) of the author(s) in Italic letter and the year of publication. In case of one author: *Miller* (1989), or if the name of the author cannot be fitted into the text: *(Miller,* 1989); in the case of two authors: *Gamov* and *Cleveland* (1973); if there are more than two authors: *Smith et al.* (1990). When referring to several papers published in the same year by the same author, the year of publication should be followed by letters a,b etc. At the end of the paper the list of references should be arranged alphabetically. For an article: the name(s) of author(s) in Italics, year, title of article, name of journal, volume number (the latter two in Italics) and pages. E.g. *Nathan, K.K.,* 1986: A note on the relationship between photosynthetically active radiation and cloud amount. *Időjárás 90,* 10-13. For a book: the name(s) of author(s), year, title of the book (all in Italics except the year), publisher and place of publication. E.g. *Junge, C. E.,* 1963: *Air Chemistry and Radioactivity*. Academic Press, New York and London.

The final version should be submitted on diskette altogether with one hard copy. Use standard 3.5" or 5.25" DOS formatted diskettes. The preferred word-processors are WordPerfect 5.1 and MS Word 6.0.

Reprints: authors receive 30 reprints free of charge. Additional reprints may be ordered at the authors' expense when sending back the proofs to the Editorial Office.

More information: gmajor@met.hu
Information on the last issues:
http://www.met.hu/firat/ido-e.html

Published by the Hungarian Meteorological Service

Budapest, Hungary

INDEX: 26 361

HU ISSN 0324-6329

IDŐJÁRÁS

QUARTERLY JOURNAL
OF THE HUNGARIAN METEOROLOGICAL SERVICE

CONTENTS

****

http://www.met.hu/firat/ido-e.html

VOL. 104 * NO. 3 * JULY–SEPTEMBER 2000

IDŐJÁRÁS

Quarterly Journal of the Hungarian Meteorological Service

Editor-in-Chief
T. PRÁGER

Executive Editor
M. ANTAL

EDITORIAL BOARD

AMBRÓZY, P. (Budapest, Hungary)
ANTAL, E. (Budapest, Hungary)
BARTHOLY, J. (Budapest, Hungary)
BOZÓ, L. (Budapest, Hungary)
BRIMBLECOMBE, P. (Norwich, U.K.)
CZELNAI, R. (Budapest, Hungary)
DÉVÉNYI, D. (Budapest, Hungary)
DUNKEL, Z. (Brussels, Belgium)
FISHER, B. (Chatham, U.K.)
GELEYN, J.-Fr. (Toulouse, France)
GERESDI, I. (Pécs, Hungary)
GÖTZ, G. (Budapest, Hungary)
HANTEL, M. (Vienna, Austria)
HASZPRA, L. (Budapest, Hungary)
HORÁNYI, A. (Budapest, Hungary)
HORVÁTH, Á. (Siófok, Hungary)
IVÁNYI, Z. (Budapest, Hungary)
KONDRATYEV, K.Ya. (St. Petersburg, Russia)
MAJOR, G. (Budapest, Hungary)
MÉSZÁROS, E. (Veszprém, Hungary)
MIKA, J. (Budapest, Hungary)
MARACCHI, G. (Firenze, Italy)
MERSICH, I. (Budapest, Hungary)
MÖLLER, D. (Berlin, Germany)
NEUWIRTH, F. (Vienna, Austria)
PINTO, J. (R. Triangle Park, NC, U.S.A)
PROBÁLD, F. (Budapest, Hungary)
RENOUX, A. (Paris-Créteil, France)
ROCHARD, G. (Lannion, France)
S. BURÁNSZKY, M. (Budapest, Hungary)
SPÄNKUCH, D. (Potsdam, Germany)
STAROSOLSZKY, Ö. (Budapest, Hungary)
SZALAI, S. (Budapest, Hungary)
SZEPESI, D. (Budapest, Hungary)
TAR, K. (Debrecen, Hungary)
TÄNCZER, T. (Budapest, Hungary)
VALI, G. (Laramie, WY, U.S.A.)
VARGA-HASZONITS, Z. (Mosonmagyaróvár, Hungary)

Editorial Office: P.O. Box 39, H-1675 Budapest, Hungary or
Gilice tér 39, H-1181 Budapest, Hungary
E-mail: prager@met.hu or *antal@met.hu*
Fax: (36-1) 290-7387

Subscription by

mail: IDŐJÁRÁS, P.O. Box 39, H-1675 Budapest, Hungary;
E-mail: prager@met.hu or *antal@met.hu*; *Fax: (36-1) 290-7387*

IDŐJÁRÁS
Quarterly Journal of the Hungarian Meteorological Service
Vol. 104, No. 3, July–September 2000, pp. 143–159

Microscale bare soil evaporation characteristics: A numerical study

Ferenc Ács[1], **István Molnár**[2] and **Gábor Szász**[3]

[1]*Department of Meteorology, Eötvös Loránd University, H-1518 Budapest, P.O. Box 32, Hungary; E-mail: acs@caesar.elte.hu*

[2]*Hungarian Meteorological Service, Kitaibel Pál utca 1, H-1024 Budapest, Hungary*

[3]*University of Debrecen, Böszörményi út 138, H-4032 Debrecen, Hungary*

(Manuscript submitted for publication 17 January 2000; in final form 11 May 2000)

Abstract—Soil evaporation characteristics on spot (few hundred meters × few hundred meters) and patch scale (few kilometers × few kilometers) are analysed comparing a *deterministic* and a *statistical - deterministic* model. Soil evaporation characteristics are considered in terms of analysing evaporation curve (evaporation/soil moisture content dependence), areal distribution characteristics of soil evaporation and the aggregation algorithms for their estimation. The analyses are performed for different soil surface resistance parameterizations and atmospheric forcing conditions. The main results obtained can be summarized as follows: (1) The scale-invariance of soil evaporation depends upon both the parameterization of soil surface resistance and the soil surface wetness regime. (2) The relative frequency distribution of soil evaporation depends upon both the parameterization of soil surface resistance and the areal mean soil moisture content θ_m. Finally, the relationship between the aggregated soil moisture content θ_{ag} and the θ_m is linear and it does not depend upon atmospheric forcing conditions. This latter result plus the *deterministic* model can be applied for estimating patch scale soil evaporation.

Key-words: soil evaporation characteristics, spot scale, deterministic model, patch scale, statistical-deterministic model, areal evaporation.

1. Inroduction

Areal evapotranspiration is one of the most relevant factors in hydrology and meteorology. Its basic features are as follows: it shows high spatial and time variability at all scales and it is non-linearly related to environmental conditions. Concerning these features the basic questions are: Is evapotranspiration a scale-invariant quantity? Under which conditions is it scale-invariant? To study these questions it necessary to analyse all basic aspects of areal evapotranspiration among other things like:

(1) the course of $E(\theta)$ curve which expresses the dependence of evapotranspiration upon soil moisture content,

(2) the areal distribution characteristics of $E(\theta)$, e.g., the relative frequency of $E(\theta)$ and

(3) proposing aggregation algorithms for its estimation.

Such and similar aspects are investigated mainly by modeling, performing comparative numerical studies (e.g., *Rodriguez-Camino* and *Avissar*, 1999; *Li* and *Avissar*, 1994; *Mölders* and *Raabe*, 1996; *Kabat et al.* 1997; *Ács*, 1996; *Ács* and *Hantel* 1997). Many studies (e.g., *Rodriguez-Camino* and *Avissar*, 1999; *Sellers et al.*, 1997; *Wood*, 1997) refer to the landscape scale (about 10 km × 10 km). The attention is payed mainly to the aggregation algorithm problems. Two aggregation algorithm types are used: the so called "deterministic" one (e.g., *Lhomme*, 1992; *Lhomme et al.*, 1994; *Chehbounni et al.*, 1995; *Shuttleworth,* 1997) where the surface heterogeneity is considered via interpatch variability using weighting rules and the so called "statistical" one (e.g., *Famiglietti* and *Wood,* 1991, 1994; *Entekhabi* and *Eagleson,* 1989, 1991) where the surface heterogeneity is considered via intrapatch variability. In these approaches patch is not homogeneous; the patterns of variability are represented statistically via *probability density functions*. In some studies it is also noted (e.g., *Wood*, 1997) that the scale invariance of $E(\theta)$ depends upon the "state of the system". Further, the analyses refer mainly to the surface covered by vegetation.

The quantification of fine scale heterogeneity remains a clear and high priority (*Shuttleworth,* 1996). In spite of this, there are only a few studies dealing with small-scale heterogeneity (e.g., *Wood*, 1997). They use "statistical" approach applying either time-consuming numerical integrations (*Famiglietti* and *Wood*, 1994) or more analytical solutions (*Wood*, 1997). It is also recognized that the scale invariance problem is closely related to both the parameterizations used and the environmental conditions. Nevertheless, there is no any study with a detailed analysis of such type especially for bare soil surface.

The objective of this study is to analyse the scale invariance issues of bare soil evaporation at patch scale in terms of $E(\theta)$, relative frequency of $E(\theta)$ and the aggregation algorithm for $E(\theta)$. In the study we assumed that there are no advective effects accompanied by occasionally observed internal boundary layers (e.g., *Garratt,* 1992; *Hupfer* and *Raabe*, 1994) and there are also no mesoscale circulation patterns induced by surface discontinuities. Then the atmosphere can be assumed to be horizontally homogeneous with constant meteorological boundary conditions above a certain level (*Shuttleworth,* 1988).

2. Models

Two model types are used: on the spot scale a *deterministic* model (DM) characterizing the soil evaporation $E(\theta)$, and on the patch scale a *statistical - deterministic* model (SDM) coupling the deterministic model with a statistical one for generating θ as a random variable. The $E(\theta)$ relationship is simulated using two different parameterizations for bare soil surface resistance.

2.1 Deterministic model

The instantaneous value of $E(\theta)$ on spot can be determined by a deterministic model using atmospheric forcing data (net radiation, air temperature and humidity and wind speed) and surface parameters (roughness length, soil texture or soil hydrophysical parameters). The core of model is the Penman-Monteith's concept.

2.1.1 Turbulent fluxes

The latent heat flux is parameterized using *Penman-Monteith's* equation (*Monteith*, 1965) as follows:

$$L \cdot E = \frac{\Delta \cdot A + \rho \cdot c_p [e_s(T_r) - e_r] / r_a}{\Delta + \gamma \cdot (1 + r_b / r_a)} , \tag{1}$$

where L is the latent heat of vaporization, ρ is the air density, c_p is the specific heat of air at constant pressure, $\Delta(T_r)=L\cdot e_s(T_r)/R_{vap}\cdot T_r^2$ is the slope of saturated vapor pressure curve at reference temperature T_r, R_{vap} is the gas constant for water vapor, $e_s(T_r)$ is the saturation vapor pressure at T_r and e_r is the vapor pressure at reference level z_r. r_b is the bare soil surface resistance, r_a is the aerodynamic resistance and A is the available energy of bare soil surface. A is parameterized as

$$A=R - G, \tag{2}$$

where R is the net radiation and G is the ground heat flux at the surface of bare soil. G is parameterized after *Nickerson* and *Smiley* (1975):

$$G=0.15 \cdot R . \tag{3}$$

The sensible heat flux is estimated as residual,

$$H = R - G - L \cdot E \,. \tag{4}$$

2.1.2 *Surface resistance*

The non-linear relationship between E and θ is expressed using resistance concept. The soil surface resistance r_b is estimated by *Sun*'s (1982) and *Dolman*'s (1993) empirical formulae:

$$\text{Sun:} \qquad r_b^{\text{Sun}} = c_1 + c_2 \left(\frac{\theta_s}{\theta} \right)^{c_3} , \tag{5}$$

$$\text{Dolman:} \qquad r_b^{\text{Dol}} = c_4 \cdot \theta^{c_5} , \tag{6}$$

where θ and θ_s is the actual and saturated soil moisture content. The empirical constants: $c_1=30$ s m^{-1}, $c_2=3.5$ s m^{-1}, $c_3=2.3$, $c_4=3.5$ s m^{-1}, and $c_5=-2.3$. Both parameterizations are known and commonly used in the scientific literature (see *Bastiaanssen,* 1995). They refer to all soil textures. Sun's parameterization uses both θ and θ_s parameters while Dolman's parameterization only one, the θ. Note that there is a direct relationship between the θ_s and the soil texture.

2.1.3 *Aerodynamic transfer*

The aerodynamic transfer is parameterized via resistance concept using Monin-Obukov's similarity theory taking into account the atmospheric stability conditions. We assume that there is no difference between the transfer mechanisms of heat, water vapor and momentum. The set of equations used is as follows:

- *Basic equations*

The aerodynamic resistance can be calculated from wind velocity at reference level U_r and friction velocity u_* by

$$r_a = \frac{U_r}{u_*^2} \,. \tag{7}$$

The friction velocity is calculated by

$$u_* = \frac{k \cdot U_r}{\log(z_r / z_0) - \Psi_m}, \tag{8}$$

where k is the von Kármán constant, z_r and z_0 is the height of reference level and the roughness length, respectively, and Ψ_m is the stability function. Stability function depends upon the stratification of atmospheric surface layer. In neutral stratification

$$\Psi_m = 0. \tag{9}$$

In stable stratification we use two different entries for the argument of Ψ_m. When $z_r/L_{mon} \leq 0.5$ we enter the empirical expression of *Dyer* (1974):

$$\Psi_m = -4.7 \cdot \frac{z_r}{L_{mon}}. \tag{10}$$

For $z_r/L_{mon} > 0.5$ we use formula of *Holtslag* and *de Bruin* (1988):

$$\Psi_m = -A \cdot \frac{z_r}{L_{mon}} - B \cdot \left(\frac{z_r}{L_{mon}} - \frac{C}{D} \right) \cdot e^{-(D \cdot z_r)/L_{mon}} - \frac{B \cdot C}{D}, \tag{11}$$

with A=0.7, B=0.75, C=5 and D=0.35.

For unstable stratification

$$\Psi_m = 2 \log \frac{1+\mathrm{x}}{2} + \ln \frac{1+\mathrm{x}^2}{2} - 2 \,\mathrm{arc\,tg}(\mathrm{x}) + \frac{\pi}{2}, \tag{12}$$

with the function

$$x = \left(1 - 16 \frac{z_r}{L_{mon}} \right)^{1/4}. \tag{13}$$

The Monin-Obukhov length L_{mon} reflects the stability conditions. It is defined by

$$L_{mon} = -\frac{\rho \cdot T_r \cdot u_*^3}{g \cdot k \cdot \left(H/c_p + 0.61 \cdot T_r \cdot E\right)}, \tag{14}$$

where g is the acceleration of gravity (m s^{-2}), and E is the vapor flux (kg m^{-2} s^{-1}). Neutral stratification is supposed for $|L_{mon}| > 800$ m. If the stratification is not neutral, it is stable ($L_{mon} > 0$) or unstable ($L_{mon} < 0$).

- *Calculation procedure*

The turbulent flux/atmospheric stability relationship is implicitly defined, that is H and $L \cdot E$ depend upon L_{mon} and vice versa. To solve L_{mon}, u_*, r_a, and the turbulent fluxes H and $L \cdot E$ we applied the iterative procedure to their implicitly coupled equation system. For given soil moisture content value the computation starts from neutral stratification where $|L_{mon}| > 800$ m and $\Psi_m = 0$. Then via calculating u_* and r_a an estimate of H and $L \cdot E$ is obtained. This estimate of friction velocity and turbulent fluxes is used again to improve the estimate for L_{mon}, and so on. It appears that not more than five iterations are needed to achieve a deviation of 5 per cent in successive values of L_{mon}. In moderately unstable or stable stratification the convergence is quicker; it is usually achieved after three or four iterations. The iteration procedure does not converge in some physically unreal situations (for instance for strong radiation and weak wind; for details see *Czúcz* and *Ács* (1999) and in extremely strong unstable stratification close to free convection conditions (L_{mon} is negative and close to 0).

2.2 Statistical - deterministic model

The *statistical - deterministic* model estimates soil evaporation at patch scale (few kilometers × few kilometers). It consist of a *deterministic* submodel for estimating soil evaporation (see section 2.1), a *statistical* submodel for generating θ as a random variable (*Wetzel* and *Chang*, 1987) and a submodel for calculating the areal of $E(\theta)$. In the following the two latter submodels will be briefly considered.

2.2.1 Modeling soil moisture variability

According to observations of *Bell et al.* (1980) and *Hawley et al.* (1983), areal variations of θ on patch scale can be characterized by a normal distribution. According to *Wetzel* and *Chang* (1987), the corresponding standard deviation

$$\sigma_\theta = \min\left(0.08,\ \theta_m/2\right), \tag{16}$$

where θ_m is the areal mean value of θ. The areal variations of θ on patch scale are generated with Monte-Carlo runs applying a standard random number generation algorithm (see *Dévényi* and *Gulyás,* 1988) and using θ_m and σ_θ as input.

2.2.2 Calculation of areally averaged soil evaporation

Since θ is statistical variable, the turbulent heat fluxes H and $L \cdot E$ are also those. The statistical distribution of $L \cdot E$ or E is analyzed via their relative frequency distribution. The areal mean of E is estimated by numerical integration of its relative frequency distribution function $RF(E_j)$ as follows:

$$\langle E \rangle = \sum_{j=1}^{n} RF\,(E_j) \cdot E_j\,, \tag{16}$$

where $\langle E \rangle$ is the areal mean of E, j is the interval number and E_j is the corresponding E-value for the jth interval. The length of E-interval is choosen as 25 W m^{-2}. The submodel is applied in each step for $0 < \theta_m < \theta_s$ cycle to obtain the $E(\theta_m, \sigma_\theta)$ curve. Note that there is no lower boundary condition for θ_m.

3. Numerical experiments

The numerical experiments are performed by comparing the *deterministic* and the *statistical – deterministic* models. The simulations are made for different soil textures, atmospheric conditions and bare soil surface resistance parameterizations.

- *Soil texture*

The simulations are performed for sand, loam and clay. In this paper only the loam-referred results are presented. The results referring to sand and clay are presented in *Molnár* (1998).

- *Atmospheric forcing*

Atmospheric forcing is considered as the sum of all state and flux variables which determine the evaporation flux. In this study we distinguished strong and weak atmospheric forcing.

Strong atmospheric forcing
The strong atmospheric forcing is characterized by great net radiation flux, wind velocity and humidity deficit. We defined it by

Net radiaton flux, $R_n = 700$ W m^{-2},
Air temperature at reference level, $T_r = 25.8$°C,
Vapor pressure at reference level, $e_r = 18.0$ hPa, and
Wind velocity at reference level $U_r = 6.0$ m s^{-1}.

Weak atmospheric forcing
In weak atmospheric forcing conditions the net radiation flux, wind velocity and humidity deficit are small or moderate. We used

$R_n = 300$ W m^{-2},
$T_r = 25.8$°C,
$e_r = 32.0$ hPa, and
$U_r = 2.0$ m s^{-1}.

- *Parameterization of soil surface resistance*

Soil surface resistance is parameterized by Sun's and Dolman's formulae. They are introduced in section 2.1.2.

During numerical experiments $3 \times 2 \times 2$ runnings have been performed by both the *deterministic* and the *statistical - deterministic* models. Of course the computation time of the latter model is much longer with respect to the former one because of the generation of statistical variables.

3.1 Analysis of soil evaporation

Soil evaporation is analysed calculating evaporation curves $E(\theta)$ for different parameterizations and atmospheric forcing on spot and patch scale. $E(\theta)$ shows the evaporation/soil moisture content dependence. On spot scale θ does not show areal variations; $E(\theta)$ is obtained by running the *deterministic model* so that $E(\theta) \equiv E^{spot}(\theta)$. On patch scale an areal variations of θ is assumed defined via θ_m and $\sigma_\theta \cdot E(\theta)$ is obtained by running the *statistical - deterministic* model so that $\langle E(\theta_m, \sigma_\theta) \rangle \equiv E^{patch}(\theta)$.

$E^{spot}(\theta)$ and $E^{patch}(\theta)$ (including the factor L) obtained by Sun's and Dolman's parameterizations of r_b for strong and weak atmospheric forcing are presented in *Fig. 1* and *2*, respectively. All curves can be separated into three regions. In dry regime (low values of θ) $E(\theta)$ is controlled by soil surface; in wet regime (well-watered surface) $E(\theta)$ is controlled by the atmospheric conditions. Between the two regimes is the transition region where $E(\theta)$ is controlled by both the surface and the atmosphere. The curves can be characterized by two basic parameters: the slope $S=\partial E(\theta)/\partial\theta$ in the transition region and the saturation value $E(\theta_s)$. S is mainly determined by the parameterization of r_b while $E(\theta)$ by the atmospheric conditions, mainly by the radiation.

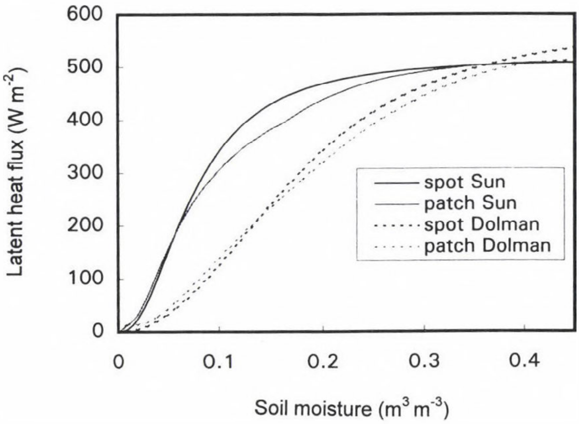

Fig. 1. Bare soil evaporation versus soil moisture changes for Sun and Dolman parameterizations on spot (black solid and dashed lines) and patch (grey solid and dashed lines) scale for strong atmospheric forcing. The curves refer to loam soil texture.

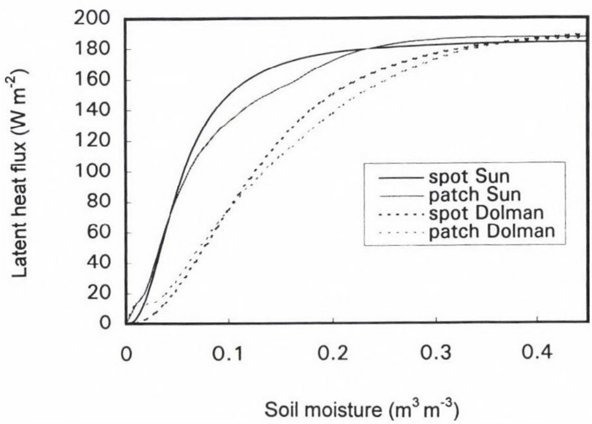

Fig. 2. As in Fig. 1 but for weak atmospheric forcing.

The scale-invariance of $E(\theta)$ depends mainly upon both the parameterization used and the surface wetness regime. In general the $E^{spot}(\theta) - E^{patch}(\theta)$ differences of Dolman's parameterization are smaller than those of Sun's parameterization; the greatest relative difference $E^{spot}(\theta) - E^{patch}(\theta) / E^{spot}(\theta)$ for Sun's parameterization achieves 13 per cent while for Dolman's parameterization between 5 and 8 per cent. These facts show that $E(\theta)$ obtained by Dolman's parameterization is more scale-invariant than the one for Sun's parameterization. Moreover we can say: If we neglect differences under 10 per cent, $E(\theta)$ obtained by Dolman's parameterization can be treated as scale-invariant. In most cases the $E^{spot}(\theta) - E^{patch}(\theta)$ differences are negligible in wet and dry regimes especially for strong atmospheric forcing conditions. This result is in accordance with the statement of *Sellers' et al.* (1997). The greatest differences appear always in the transition zone. It is very interesting to note that the $E^{spot}(\theta) - E^{patch}(\theta) / E^{spot}(\theta)$ relative difference is not negligible in extreme dry regime (θ is about 0.03 m^3 m^{-3}) when the atmospheric forcing is weak. *Sellers et al.* (1997) does not note this interesting behavior.

3.2 Areal variation of soil evaporation

Areal variation of $E(\theta)$ is examined analysing relative frequency RF of $E(\theta)$. Relative frequency of $E(\theta)$ is studied for different soil textures and surface wetness states. The estimates are performed for strong atmospheric forcing conditions. In this study the analyses refer only to loam; the results referring to sand and clay are presented in *Molnár* (1998). The questions we want to consider are as follows:

(1) Does frequency distribution of $E(\theta)$ depend upon the surface wetness state? With which distribution can RF of $E(\theta)$ be approached?
(2) Is RF of $E(\theta)$ determined by the parameterization of r_b?

The relative frequencies of $E(\theta)$ obtained by Sun and Dolman parameterizations for extreme dry (θ=0.03 m^3 m^{-3}), dry (θ=0.07 m^3 m^{-3}), moderate wet (θ=0.13 m^3 m^{-3}) and extreme wet (θ=0.25 m^3 m^{-3}) conditions are presented in *Figs. 3a, 3b, 3c* and *3d*, respectively. Note that the "extreme dry", "dry", "moderate wet" and "extreme wet" descriptions are not exactly defined wetness categories. RF of $E(\theta)$ obtained by Sun's formula is qualitatively in agreement with RF of $E(\theta)$ obtained by Dolman's formula only in extreme dry and extreme wet conditions. In extreme dry conditions the normally distributed soil moisture variations produce an exponential relative frequency distribution of soil evaporation. This is in accordance with simulation results of *Wood*

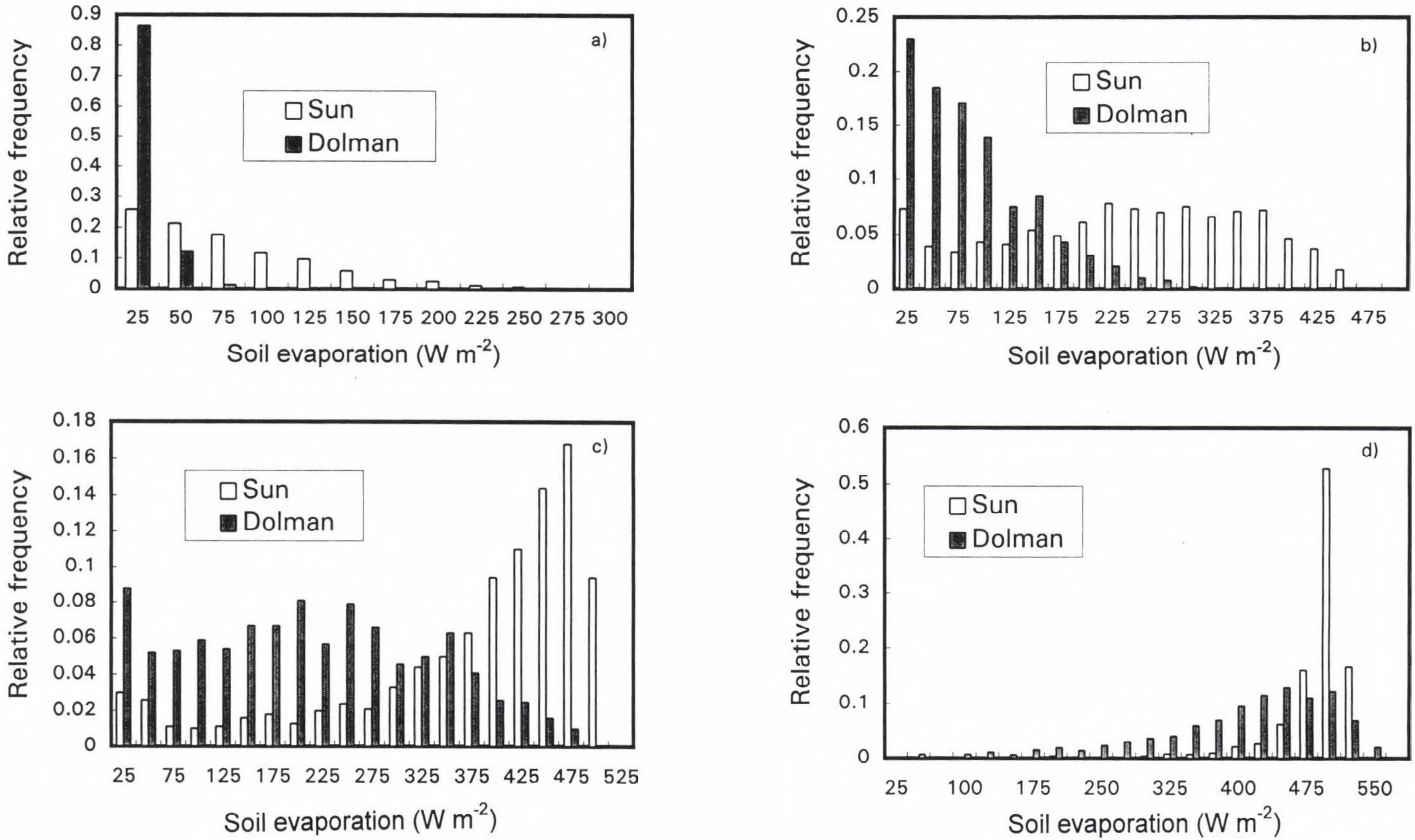

Fig. 3. Histogram of bare soil evaporation for Sun (light columns) and Dolman (dark columns) parameterizations and strong atmospheric forcing conditions in (*a*) extreme dry, (*b*) dry, (*c*) moderate wet and (*d*) extreme wet soil surface wetness conditions.

(1997) and analytical calculations of *Hantel* and *Ács* (1998). In extreme wet conditions the shape of relative frequency distributions is like a lognormal distribution as reflected by mirror. For moisture regimes between the extrem dry and wet regimes the shapes of RF distributions are qualitatively different. Thus for instance in dry conditions (see Fig. 3b) the RF distribution of $E(\theta)$ obtained by Dolman's formula can be characterized by an exponential distribution, while RF distribution of $E(\theta)$ obtained by Sun's formula by a uniform distribution. In moderate wet conditions the deviations between RF distributions are similarly as great as in dry conditions (see Fig. 3b).

3.3 Aggregated soil moisture content

The aggregated soil moisture content θ_{ag} is that soil moisture content value by which the deterministic model yields the areal mean patch scale evaporation. So

$$E(\theta_{ag}) = \langle E(\theta_m, \sigma_\theta) \rangle , \tag{17}$$

where $E(\theta_{ag})$ is the areal mean soil evaporation calculated by *deterministic model* using θ_{ag} and $\langle E(\theta_m, \sigma_\theta) \rangle$ is the areal mean soil evaporation calculated by *statistical - deterministic* model using θ_m and σ_θ . θ_{ag}/θ_m relationship is possible to get comparing $E(\theta)$ curves refering to spot and patch scale (see Figs. 1 and 2). Obviously the relationship is well defined in the transition zone of $E(\theta)$ curves. In dry and wet regimes of $E(\theta)$ curves there is no unequivocal relationship between θ_{ag} and θ_m . The θ_{ag}/θ_m relationship for strong and weak atmospheric forcing conditions using Sun's and Dolman's parameterizations is presented in *Figs. 4* and *5*, respectively. According to the plots we can say:

(1) The relationship between θ_{ag} and θ_m extremly weakly depends upon atmospheric forcing conditions. There is practically no difference between the slope and the intercept of regression lines with respect to the forcing conditions (see Eqs. (18) to (21)),

Sun, strong forcing: $\theta_{ag} = 0.811\theta_m - 0.00002,$ (18)
weak forcing: $\theta_{ag} = 0.795\theta_m - 0.0015$ (19)

and

Dolman, strong forcing: $\theta_{ag} = 0.866\theta_m + 0.011,$ (20)
weak forcing: $\theta_{ag} = 0.834\theta_m + 0.0103.$ (21)

Hence this dependence can be neglected for both parameterizations.

(2) The relationship between θ_{ag} and θ_m are linear; the correlation coefficients in all cases are greater than 0.98.

Similar considerations are also valid for sand and clay (*Molnár*, 1998). Finally, it is obvious that neglecting the effect of atmospheric forcing conditions upon θ_{ag}/θ_m relationship (which is a reasonable assumption), it is possible to calculate areal mean soil evaporation on patch scale using the deterministic model in combination with θ_{ag}/θ_m relationship.

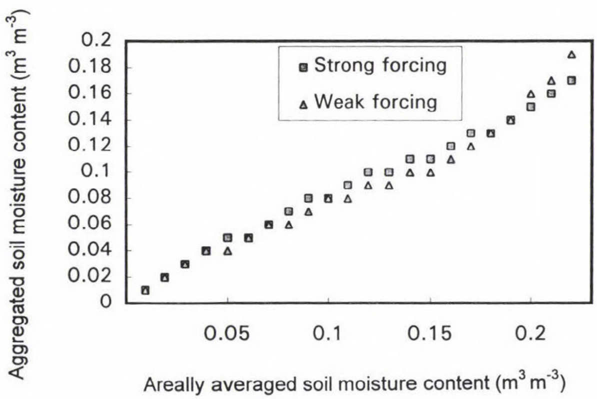

Fig. 4. Aggregated versus areally averaged soil moisture content for Sun parameterization under strong (square) and weak (triangle) atmospheric forcing conditions.

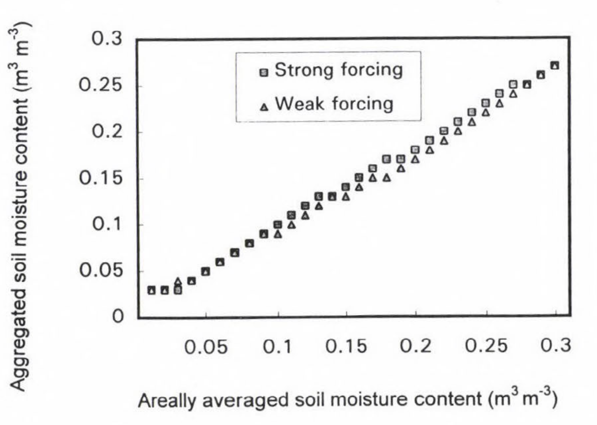

Fig. 5. As in Fig. 4 but for Dolman parameterization.

4. Conclusions

Microscale soil evaporation E characteristics are analysed comparing a *deterministic* and a *statistical – deterministic* evaporation model. Evaporation characteristics are considered in terms of evaporation curves $E(\theta)$, relative frequency distribution of $E^{spot}(\theta)$ and the aggregation algorithms for their estimation. The *deterministic* spot scale E^{spot}-model is based on the *Penman-Monteith* concept (*Ács* and *Hantel,* 1999), that is the evaporation flux is determined by the *Penman-Monteith*'s equation, the ground heat flux at soil surface is parameterized via net radiation and the sensible heat flux is obtained as residual component from the energy balance equation. The *statistical – deterministic* patch scale $E^{patch}(\theta)$ model consist of the $E^{spot}(\theta)$-submodel, a statistical submodel for generating θ as random variable and a submodel for calculating the areal mean $E^{patch}(\theta)$.

The numerical experiments are made for different soil textures, atmospheric conditions and bare soil surface resistance r_b parameterizations. In this study only the loam-referred results are analysed. The results can be briefly summarized as follows:

(1) The scale-invariance of $E(\theta)$ depends upon both the parameterization of r_b and the soil surface wetness regime. In general the normally distributed soil moisture variations on the patch scale moderate the nonlinear relationship between E and θ with respect to that on spot scale. The greatest $E^{spot}(\theta)-E^{patch}(\theta)$ differences appear for Sun's parameterization of r_b in transition region of $E(\theta)$ curves. The $E^{spot}(\theta)-E^{patch}(\theta)$ differences are negligible in wet and dry soil wetness regimes and also in the transition region but for Dolman's parameterization of r_b. Summarizing, if we neglect the differences under 10 per cent, $E(\theta)$ obtained by Dolman's parameterization can be treated as scale-invariant.

(2) The relative frequencies of $E(\theta)$ obtained by Sun's and Dolman's formulae are qualitatively in approximate agreement with each other only in extreme dry and extreme wet conditions. In extreme dry conditions the normally distributed soil moisture variations produce an exponential RF distribution of $E(\theta)$, while extreme wet conditions lead to a distribution like a lognormal distribution as reflected by mirror. For dry and the moderate wet soil moisture regimes the RF distributions obtained by Sun's and Dolman's parameterizations are qualitatively different and they can hardly be described.

(3) For calculating areal mean patch scale evaporation $E^{patch}(\theta)$ it is possible to introduce the aggregated soil moisture content θ_{ag} (see Eq. (17)). The relationship between θ_{ag} and the areal mean soil moisture content θ_m extremly weakly depends upon atmospheric forcing conditions that is the differences between the slope and the intercept of θ_{ag}/θ_m regression lines for both parameterizations are minor with respect to the forcing conditions. Further the relationship between θ_{ag} and θ_m is linear.

The results suggest that $E(\theta)$ characteristics depend strongly upon the parameterization of r_b. In this study we only want to show this fact and not more, that is we do not intend to make a decision which parameterization would be preferred. Furthermore, the θ_{ag}/θ_m relationship can be use for $E(\theta)$'s upscaling from spot to patch scale; that is knowing the relation between θ_{ag} and $\theta_{m,}$ it is possible to calculate $E^{patch}(\theta)$ not only by the *statistical - deterministic* model but also by the *deterministic* one. Of course, these results are valid only —as noticed in introduction—when there are no advective effects and meso-scale circulation patterns. In the latter cases the evaporation characteristics and its upscaling strategy are much more complex.

Acknowledgements—This study is partly financially supported by the *Hungarian Ministry* for *Culture* and *Education* via OTKA Foundation, project number T-02958.

References

Ács, F., 1996: Control of transpiration by soil moisture and atmosphere. *Proc. of the Int. Conf. on Water Resources & Environmental Research: Towards the 21st Century (Vol. I)*, 101-107. Oct 29-31, 1996, Kyoto, Japan.

Ács, F. and *Hantel, M.*, 1997: Upscaling of transpiration from spot to patch scale. *Proc. of the Joint Assemblies of the International Association of Meteorology and Atmospheric Sciences (IAMAS) and the International Association for the Physical Sciences of the Oceans (IAPSO)*, CMH4 Global and Regional Energy and Water Cycles, CMH4PP1-9 July, 1997, Melbourne.

Ács, F. and *Hantel, M.*, 1999: The Penman-Monteith concept based land-surface model PMSURF. *Időjárás 103*, 19-36.

Bastiaanssen, W.G.M., 1995: Regionalization of surface flux densities and moisture indicators in composite terrain. A remote sensing approach under clear skies in Mediterranean climates. *PhD Thesis*, *271* pp. Department of Meteorology, Eötvös Loránd University, Budapest, Hungary.

Bell, K.R., Blanchard, B.J., Schmugge, T.J. and *Witzak, M.W.*, 1980: Analysis of the surface moisture variations within large field sites. *Water Resour. Res. 61*, 796-810.

Chehbouni, A., Njoku, E. G., Lhomme, J.-P. and *Kerr, Y. H.*, 1995: Approaches for averaging surface *parameters* and fluxes over heterogeneous terrain. *J. Climate 8*, 1386-1393.

Czúcz, B. and *Ács, F.*, 1999: Parameterization of unstable stratification in land-surface model PMSURF: An *examination* of the convergence by empirical methods (in Hungarian). *Légkör* Vol. XLIV, No. 2, 2-6.

Dévényi, D. and *Gulyás, O.*, 1988: *Mathematical Statistical Methods in Meteorology* (in *Hungarian*). *Tankönyvkiadó*, Budapest, pp. 443.
Dolman, A. J., 1993: A multiple-source land surface energy balance model for use in general *circulation models*. *Agric. Forest Meteorol.* *65*, 21-45.
Dyer, A. J., 1974: A review of flux-profile Relationships. *Bound. Layer Meteorol.* *7*, 363-372.
Entekhabi, D. and *Eagleson, P. S.*, 1989: Land surface hydrology parameterization for atmospheric *general* circulation *models* including subgrid scale spatial variability. *J. Climate* 2, 816-831.
Entekhabi, D. and *Eaglesson, P. S.*, 1991: Climate and equilibrium state of land surface hydrology *parametrizations*. *Surveys in Geophysics 12*, 205-220.
Famiglietti, J.S. and *Wood, E., F.*, 1991: Evapotranspiration and runoff from large land areas: Land surface hydrology for atmospheric *general* circulation models. *Surveys in Geophysics 12*, 179-204.
Famiglietti,. J. S. and *Wood, E. F.*, 1994: Multi-scale modeling of spatially-variable water and *energy* balance *processes*. *Water Resour. Res.* *30*, 3061-3078.
Garratt, J. R., 1992: The internal boundary layer-A review. *Bound.-Layer Meteorol.* *50*, 171-203.
Hantel, M. and *Ács, F.*, 1998: Physical aspects of the weather generator. *J. Hydrol.* *212-213*, 393-*411*.
Hawley, M. E., *Jackson, T. J.* and *McCuen, R.H.*, 1983: Surface soil moisture variation on small *agricultural* watersheds. *J. Hydrol.* *62*, 170-200.
Holtslag, A. A. M. and *de Bruin, H.A.R.*, 1988: Applied modelling of the nightime surface energy *balance* over land. *J. Appl. Meteor.* *27*, 689-704.
Hupfer, P. and *Raabe, A.*, 1994: Meteorogical transition between land and see in the microscale. *Meteor.* Z. 3, 100-103.
Kabat, P., *Hutjes, R.W.A.* and *Feddes, R.A.*, 1997: The scaling characteristics of soil parameters: From plot scale *heterogeneity* to subgrid parametrization. *J. Hydrol.* *190*, 363-396.
Lhomme, J.-P., 1992: Energy balance of heterogeneous terrain. Averaging the controlling *parameters*. *Agric. Forest Meteorol.* *61*, 11-21.
Lhomme, J.-P., *Chehbouni, A.* and *Monteny, B.*, 1994: Effective parameters of surface energy *balance* in heterogeneous landscape. *Bound.- Layer Meteorol.* *71*, 297-309.
Li, B. and Avissar, R., 1994: The impart of spatial variability of land-surface characteristics on land-surface heat fluxes. *J. Climate 7*, 527-535.
Molnár, I. 1998: Relationship between the bare soil evaporation and the environmental conditions at *microscale*. *Dipl. Thesis*, 37 pp+Appendix. Department of Meteorology, Eötvös Loránd University, Budapest.
Monteith, J., 1965: Evaporation and environment. In *The State and Movement of Water in Living Organism. Proc. of 19th Symp. Soc. Exp. Biol.*, (ed.: *G. Fogg*). Cambride University Press, Cambridge, pp. 105-236.
Mölders, N. and *Raabe, A.*, 1996: Numerical investigations on the influence of subgrid-scale surface *heterogeneity* on *evapotranspiration* and cloud processes. *J. Appl. Meteorol.* *35*, 782-795.
Nickerson, E. and *Smiley, I.* 1975: Surface energy budget parametrizations for urban models. *J. Appl. Meteorol.* *14*, 197-*300*.
Rodriguez-Camino, E. and *Avissar, R.*, 1999: Effective parameters for surface heat fluxes in heterogeneous *terrain*. *Tellus 51A*, 387-399.
Sellers, P.J., *Heiser, M.D.*, *Hall, F.G.*, *Verma, S.B.*, *Desjardins, R.L.*, *Schuepp, P.M.* and *MacPherson, J.I.*, 1997: The *impact* of using area-averaged land surface properties-topography, vegetation condition, soil wetness-in calculations of intermediate scale (approximately 10 km^2) surface-atmosphere heat and moisture fluxes. *J. Hydrol.* *190*, 269-301.
Shuttleworth, J.W., 1988: Macrohydrology-the new challenge for process hydrology. *J. Hydrol.* *100*, 31-56.
Shuttleworth, J.W., 1996: BAHC Focus 2-Future directions in aggregation. In *Bach News*. Edited by BAHC Core Project Office, Potsdam Institute for Climate Impact Research, P.O. Box. 601203, 14412 Potsdam, Germany.

Shuttleworth, J.W., 1997: Hydrological models, regional evaporation, and remote sensing: Let's start simple and maintane perspective. In *Land Surface Process in Hydrology. Trials and Tribulations of Modelling and Measuring* (eds.: *S. Sorooshian, H.V. Gupta* and *S.C. Rodda*). Springer Verlag, Berlin, Heidelberg.

Sun, S.F., 1982: Moisture and heat transport in a soil layer forced by atmosperic conditions. *M.S. Thesis*, Dept. of Civil Engineering, University of Connecticut, 72. pp.

Wetzel, J.P. and *Chang, J.T.*, 1987: Concerning the relationship between evapotranspiration and soil moisture. *J. Climate and Appl. Meteorol. 26*, 18-27.

Wood, E.F., 1997: Effects of soil moisture aggregation on surface evaporative fluxes. *J. Hydrol. 190*, 397-412.

IDŐJÁRÁS

Quarterly Journal of the Hungarian Meteorological Service
Vol. 104, No. 3, July–September 2000, pp. 161–172

Estimation of historical atmospheric lead (Pb) deposition over Hungary

László Bozó

Hungarian Meteorological Service,
H-1675 Budapest, P.O. Box 39, Hungary; E-mail: bozo.l@met.hu

(Manuscript submitted for publication 24 May 2000; in final form 11 August 2000)

Abstract—Lead is one of the most harmful toxic metals in our environment. It is emitted mainly by anthropogenic sources (combustion of gasoline, oil and coal burning, waste incineration etc.) whose source strengths varied significantly during the past several decades in all European countries. Even relatively low fluxes across the Earth's surface can result in accumulation of lead in various soils. From the soils it can be taken up by the plants and maybe leached out into the ground water. This paper presents estimations on the historical lead depositions and the atmospheric lead budgets over Hungary, for the period of 1955–2000. Computations are based on the results of long-range transport model simulations as well as on the regional background air pollution measurements carried out at K-puszta station in Hungary. Besides the estimations of the actual and cumulative atmospheric loads, the geographical origin of lead that is deposited is also calculated.

Key-words: atmospheric deposition, lead, long-range transport.

1. Introduction

Since the middle of this century, energy generation, industrial production and transportation have caused serious environmental contamination by trace elements including lead. The rate of contamination can vary from place to place as a function of source densities and intensities of lead flux as well as meteorological conditions. The pattern of pollution may be characterized not only by local, highly concentrated sites such as densely populated urban areas, but also by lower concentrations of pollution widely dispersed over the landscape including agricultural regions, forests and surface waters. Aerosol particles containing lead and other trace elements can be transported far away from their sources by advection before being deposited on the surface (e.g., *Mészáros*, 1999).

Consumption of leaded gasoline was the major source category in the total lead emission in Europe (*Pacyna*, 1996). Introduction of unleaded gasoline in the mid-80's in western Europe resulted in significant lead emission reduction as well as in re-ranking the relative contributions of source categories. This progress could be detected approximately a decade later in the eastern part of the European continent (*Olendrzynski et al.*, 1995). Long-range transport of atmospheric lead is not simply a clean air protection problem in Europe but a major part of environmental policy as well: considering its characteristic residence time in the atmosphere (a few days) and the sizes of countries in our continent, international co-operation is needed to control the transboundary flux and deposition of atmospheric lead.

2. *Atmospheric long-range transport model applied for the computations*

For the long-range transport computations a continental scale, climatological-type model (TRACE) was used. Input fields of emission inventory, meteorological data and deposition parameters are preprocessed for 150×150 km^2 spatial resolution grid system (EMEP). The concentration of lead at a certain receptor point is given by a simple loss function:

$$c(x_r, y_r; x_e, y_e) = \beta\, E\, (x_e, y_e)\, R^{-1}\, (1-a)\, e^{-(kd+kw)t}\,, \qquad (1)$$

where

- c is lead concentration in the air in a certain receptor point as a result of an individual source point (ng m^{-3});
- (x_r, y_r) and (x_e, y_e) are the spatial co-ordinates of source and receptor points;
- E is the emission at the source point (ng s^{-1});
- β is derived by setting the upward and downward atmospheric fluxes equal assuming mass conservation (s m^{-2})
- R is distance between the source and receptor (m);
- A is local emission coefficient (dimensionless);
- kd, kw are loss parameters for dry and wet depositions (s^{-1});
- t is atmospheric transport time between source and receptor (s);

The total concentration at the receptor point is computed from the sum of contributions coming from each emission source, weighted according to the frequency of 925 hPa backward trajectories, $F(s)$ coming from a particular sector, s:

$$c(x_r, y_r) = \sum_{s=1}^{8} F_{(s)} c_s (x_r, y_r). \tag{2}$$

As indicated in Eq. (2) there are 8 spatial sectors considered during trajectory analyses. In the next step of the calculations, wet and dry deposition of the pollutant at the receptor are computed from the atmospheric lead concentration:

$$d_w = c(x_r, y_r)\ W\,P \tag{3}$$

where

W is the scavenging ratio (dimensionless);
P is the precipitation intensity (m s^{-1}).

Dry deposition is expressed as:

$$d_d = c(x_r, y_r)\ v_d \tag{4}$$

where

d_d is the dry deposition (ng m^{-2} s^{-1});
$c(x_r, y_r)$ is the lead concentration at the receptor point (ng m^{-3});
v_d is the dry deposition velocity (m s^{-1}).

Dry deposition velocities of lead are calculated separately for each grid element, depending on roughness length, friction velocity and size distribution of aerosol particles containing lead. Size distribution of particles were taken from *Mészáros et al.* (1997) whose research group carried out Berner-type cascade impactor sampling and trace metal measurements in Hungary.

For detailed model description, testing and verification see *Alcamo et al.* (1992), *Bozó* (1994) and *Bozó et al.* (1992).

3. *Emission of lead in European countries during the past decades*

The major source of lead during the past several decades was the consumption of leaded gasoline (*Pacyna*, 1996). In addition, coal and oil burning, as well as non-ferrous metal industry contribute to the total anthropogenic emission of lead. Based on a source category ranking study referring to lead in Hungary in the mid-80's, line sources (gasoline) represented approximately 85% of the total emission. Detailed historical (1955–) emission inventories for the European countries were compiled by *Pacyna* (1993, 1996), *Pacyna et al.*

(1991) and *Olendrzynski et al.* (1995). These emission inventories are based on the detailed and country-specific information on the:

- industrial and energy technology used,
- production and consumption rates in industrial, energy and transportation sectors,
- lead content of raw materials and fuels,
- environmental protection installations at the emitters.

During the 50's and 60's the lead content of European gasoline was approximately 0.4 g ℓ^{-1}. It decreased significantly down to 0.15 g ℓ^{-1} in Germany in the mid-70's: similar reductions were achieved in Scandinavia and Benelux countries in early 80's. In Hungary, lead content of gasoline was remarkably reduced in 1985 (< 0.25 g ℓ^{-1}). By that time unleaded gasoline was widely used in western European countries: by the mid-90's it became dominant on the fuel market in those countries. This progress could be detected in Hungary and other central-eastern European countries only approximately 8–10 years later. Temporal variation of lead emission from Hungary is shown in *Fig. 1.* It can be seen that the rate of emission increased rapidly during 1955–1975: highest mass of lead (1150 t a^{-1}) was emitted in the mid-70's. It is expected that by the end of this century the rate of lead emission will have been reduced down to 70-80 t a^{-1}

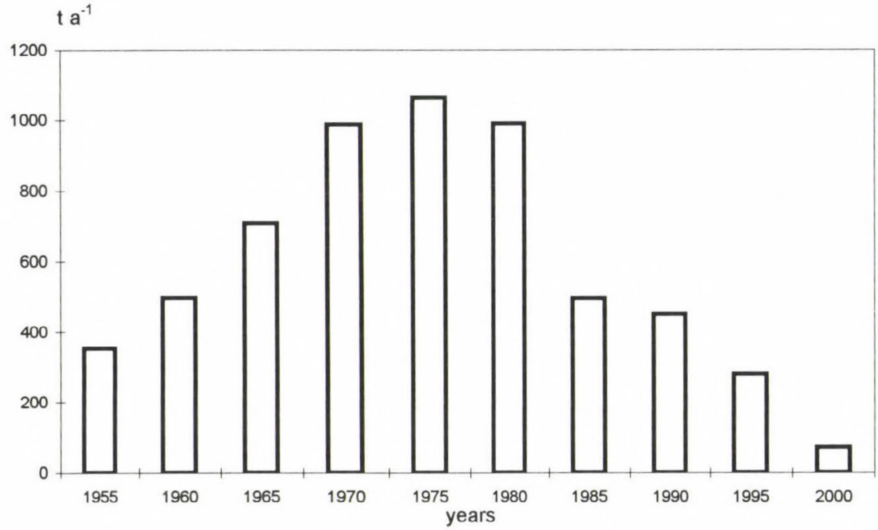

Fig. 1. Emission of lead in Hungary.

4. Origin of lead deposition in Hungary during the period 1955–2000

Model computations have been performed to estimate the temporal variation of the geographical origin of atmospheric lead deposition in Hungary during 1955–2000. Source-receptor relationships of grid elements were first aggregated to country-to-country matrices. Due to the fact that there were significant differences in industrial technologies, environmental installations and lead emission densities in different parts of Europe, for better representation of our results, three main areas, covering the whole European continent, were separated in computations: (i) Hungary; (ii) eastern part of Europe, i.e. the former socialist countries without Hungary and (iii) western part of Europe, i.e. all the remaining European countries. Results are shown in *Fig. 2.* It can be seen that total (wet+dry) lead deposition increased continuously from 510 t a^{-1} up to 1450 t a^{-1} during the period 1955–1975.

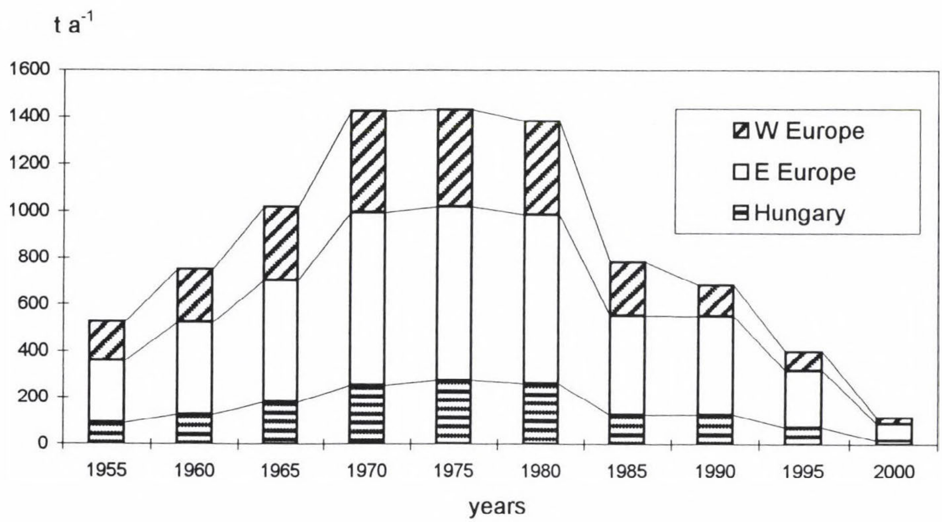

Fig. 2. Origin of total (wet+dry) lead deposition in Hungary.

Total lead deposition in Hungary started to decrease in the mid-80's. It is expected that due to the further reduction of European lead emission (*Berdowski et al.,* 1998), the rate of total lead deposition in Hungary will not exceed 100 t a^{-1} in 2000. Percentage contributions from the different source regions selected are presented in *Fig. 3.* It can be concluded from this figure that the relative share of regions contributing to Hungarian lead deposition were practically unchanged during the period 1955–1980: relative contributions of Hungarian sources, western European sources and eastern European sources were between 18-20%, 29-32% and 48-53%, respectively. Lowest Hungarian contribution to the total lead deposition was estimated for the mid-80's. During the 90's, the relative contribution of the western European sources decreased significantly: it can be explained by the intensive reduction of lead content in gasoline used in western European countries.

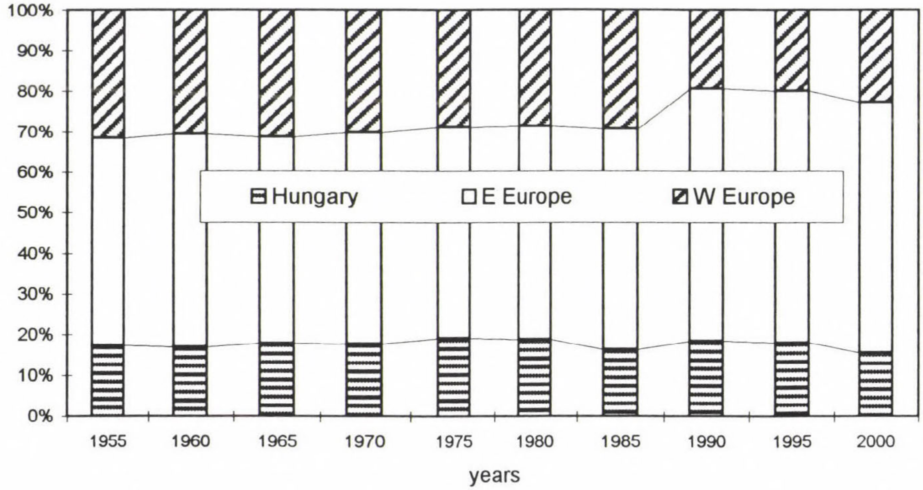

Fig. 3. Origin of total (wet+dry) lead deposition in Hungary (%).

Spatial variabilities of 850 hPa backward trajectories and lead concentrations were estimated at K-puszta station for the ten year period of 1988–1997. It can be seen in *Fig. 4*, that the prevailing backward trajectory directions are NW and W, while highest lead concentrations were observed when air masses came from SE, E and S. It is explained by the fact that lead emission densities were higher over the SE European countries than those of over western and northern part of the European continent during the period investigated.

As it was mentioned in the sections above, atmospheric lead transport and deposition is a long-range environmental problem. It means that Hungary not only "imports" lead through the atmosphere but it is a significant lead "exporter" as well. Based on TRACE model computations it was possible to estimate the quantitative distribution of total lead deposition in Europe, originating from Hungarian sources. Results of computations are plotted in

Fig. 5. It was concluded that 26% of lead emitted in Hungary is deposited in our country, while 57% is deposited in the eastern European region. The remaining 17% is transported and deposited in western Europe. In other words it means that only 260 t of 1063 t lead emitted in 1975 in Hungary was deposited in our country, the majority of lead emitted left Hungary through atmospheric long-range transport processes.

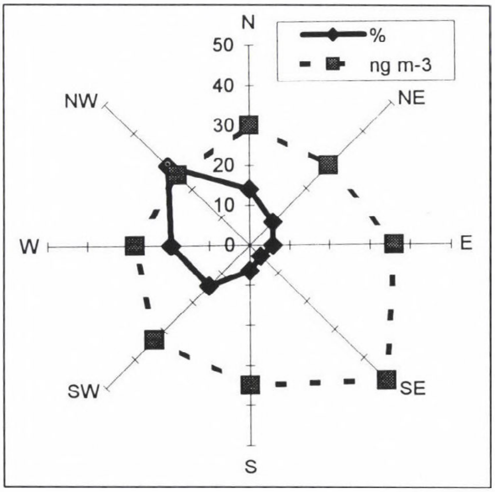

Fig. 4. Distribution of 850 hPa backward trajectories (%) and Pb concentrations (ng m^{-3}) by spatial sectors at K-puszta, during 1988–1997.

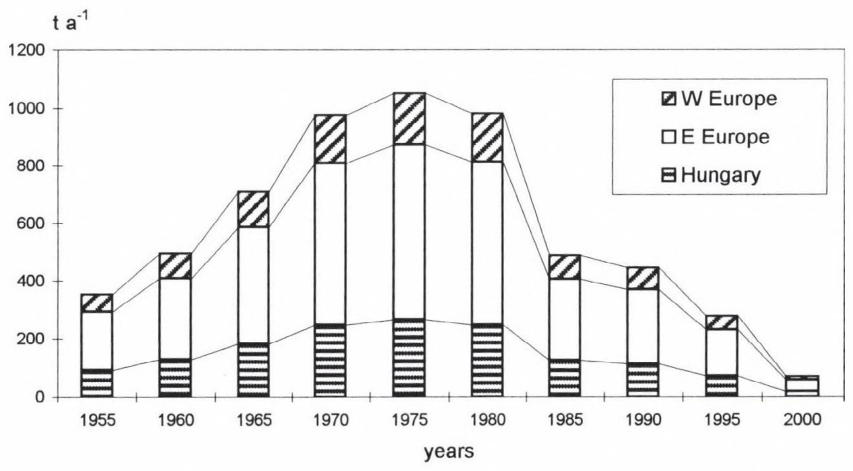

Fig. 5. Total deposition of lead emitted from Hungarian sources.

5. *Comparison of model results with wet deposition measurements in Hungary*

Lead concentration in atmospheric aerosol and precipitation has been monitored since the early-80's in Hungary at the regional background air pollution monitoring station, K-puszta (*Bozó*, 1996). Wet deposition is calculated by multiplying the lead concentration in precipitation water by the precipitation amount. Highest wet deposition rate was detected in 1987 (9.06 mg m^{-2} a^{-1}) while the lowest was detected in 1998 (2.21 mg m^{-2} a^{-1}). Based on historical European emission data model computations were performed for the receptor location of K-puszta, Hungary: their results and the wet deposition rates measured are plotted together in *Fig. 6*. For the period of 1955–1985 only model computations were available: it can be seen that highest wet deposition rates were calculated for the 70's (appr. 11 mg m^{-2} a^{-1}). Since the early 80's there has been a continuous decrease in the wet deposition rate of lead in Hungary: it is reflected both in model computations and regional background measurements. On the basis of model calculations one can expect that wet deposition rate of lead in 2000 could be around 1 mg m^{-2} a^{-1} in Hungary under regional background conditions. It can also be concluded from the figure that results of model simulations underestimate the wet deposition measurements by 10–20%. The reason for that could be the underestimations in lead emission data and the uncertainty in parameterization of wet scavenging processes in the atmosphere.

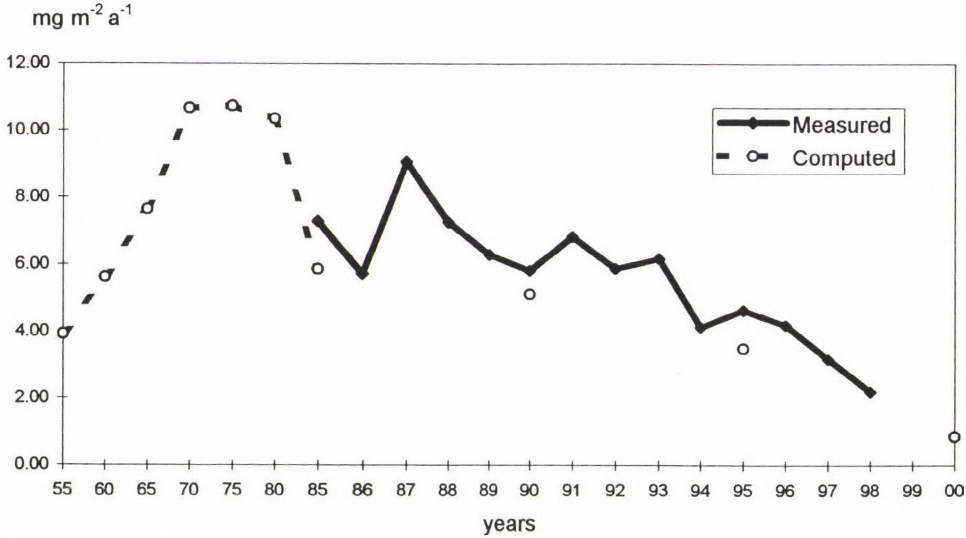

Fig. 6. Computed and measured rates of wet lead depositions.

6. Cumulative lead deposition

The rate of lead deposition varied significantly during the past decades. Due to the cumulative characteristics of lead in our environment, it is advisible to estimate the cumulative lead deposition in Hungary for the past 45 years and to provide some quantitative estimates for the next decade. This type of simulation was also done by means of TRACE model computations. Historical emission data were taken from *Olendrzynski et al.* (1995) while future scenarios are based on the calculations of *Berdowski et al.* (1998). For comparisons, the target of model simulations was not only Hungary but a few other countries in different regions of Europe — United Kingdom, The Netherlands, Spain, Austria, Romania and Poland (*Fig. 7*) It is not surprising that cumulative lead deposition was much higher during the 30 years of the period 1955-1985 than that of 1985–2015. Regarding Hungary, the rate of total lead deposition was 320 mg m^{-2} during 1955–1985, while on the basis of model computations it is expected that it will not exceed 95 mg m^{-2} during the consecutive 30 years period (1985–2015). It can also be stated that in some selected countries (e.g., The Netherlands or Austria) the cumulative lead deposition rate was higher than in Hungary, while in the case of Romania and Spain lower cumulative deposition rates were estimated.

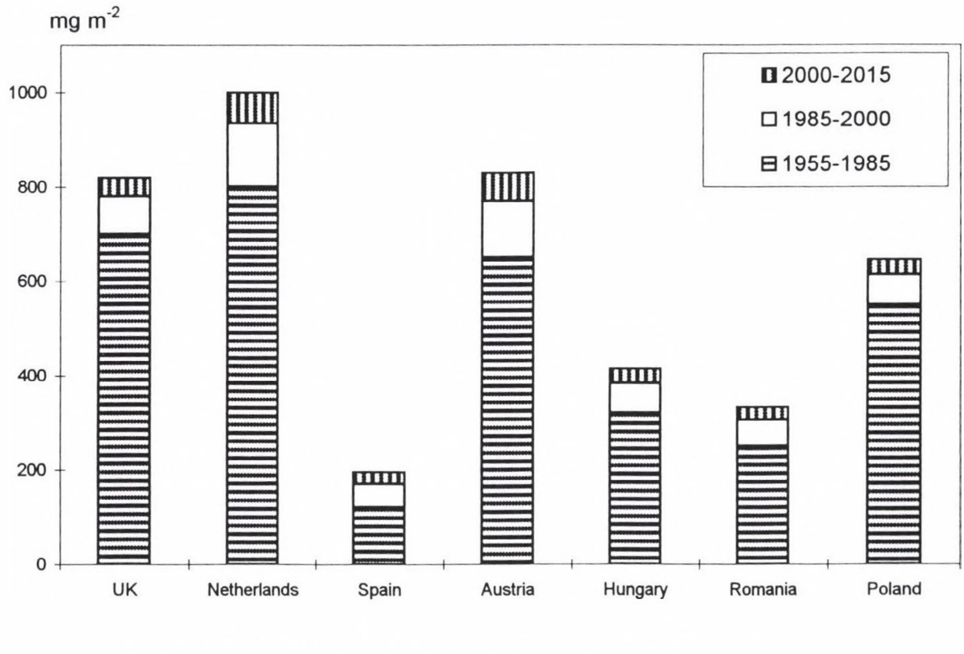

Fig. 7. Cumulative lead depositions in a few European countries.

7. Atmospheric budget of lead over Hungary during 1955–2000

On the basis of model computations performed and the historical lead emission data for Hungary, the atmospheric budget of lead can be estimated as the difference between total deposition and emission. Results are shown in *Fig. 8*. It can be concluded that the budget is positive during the whole period investigated so our country plays a net "importer" role in the European atmospheric lead budget. It was also calculated how the atmospheric budgets relates to the actual emission rates in a few selected European countries. Results for the period 1960–2000 are presented in *Fig. 9*. It was concluded that at the western boundaries of the European continent (UK, The Netherlands) this parameter is negative due to the fact that the relative contribution of the countries' own sources to the total lead deposition in these countries is significant: prevailing atmospheric transport from the Northwest reduces the influence on atmospheric lead transport from other European countries. In Hungary, the value of this ratio varied between 0.32–0.58 between 1960–2000.

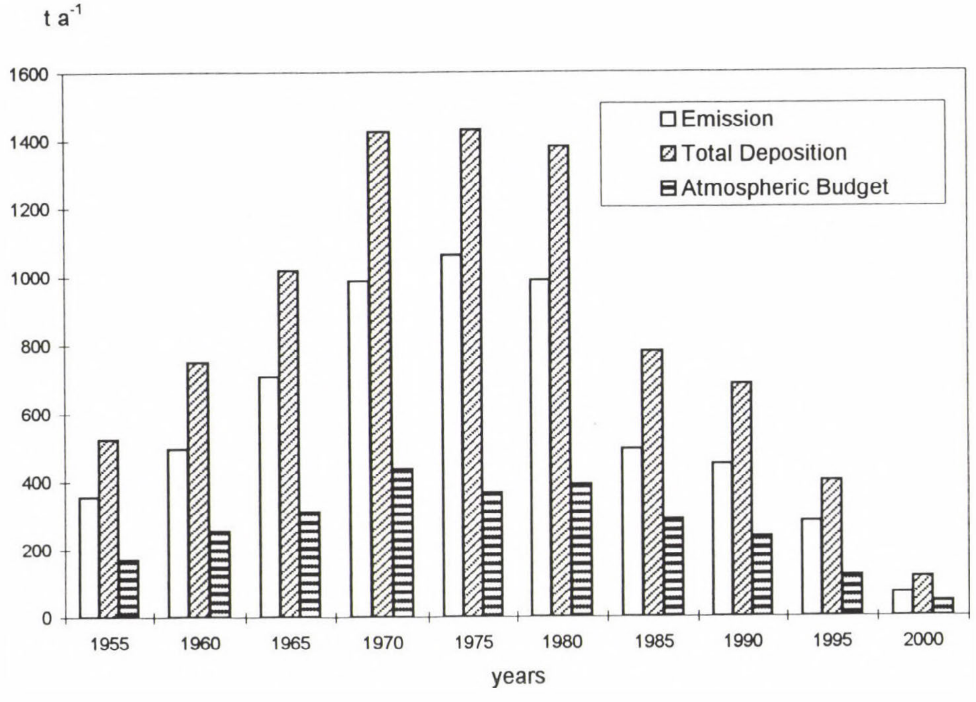

Fig. 8. Atmospheric budget of lead in Hungary.

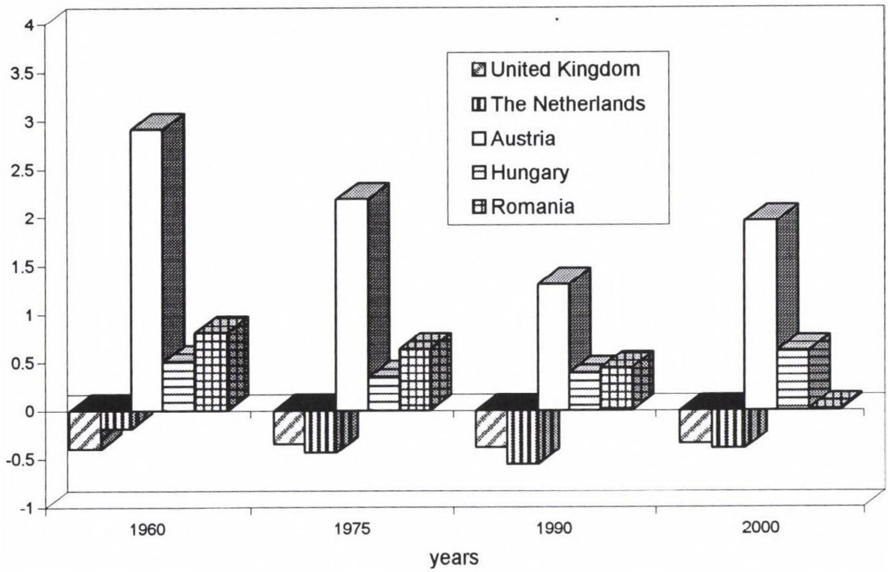

Fig. 9. Ratio of atmospheric lead budget to the lead emission in selected countries.

8. *Conclusions*

Historical lead deposition in Hungary was investigated in this paper by means of long-range transport model computations. To the extent that observations were available, modeling results were compared with the wet deposition rates measured at K-puszta station in Hungary. On the basis of these investigations the following main conclusions can be drawn:

(1) Transboundary sources of lead dominated the total (wet+dry) lead deposition in Hungary during the period 1955–2000: their contribution is estimated to be 81–84% of the total. Highest deposition rates were computed for the 70's (above 1400 t a^{-1} lead deposited);

(2) Cumulative deposition rate of lead in Hungary was computed to be 320 mg m^{-2} for the period 1955–1985, while it is expected not to exceed the rate of 95 mg m^{-2} during the period 1985–2015;

(3) Phasing out leaded gasoline from the market in most of the European countries will eliminate the majority of atmospheric lead pollution and deposition problems during the next decade. Annual emission rates of lead are going to decrease rapidly in SE European countries as well, while the relative contribution of industrial and energy source categories

to the total annual lead emission of countries will reach higher percentage shares than those during the past decades.

(4) Atmospheric budget of lead was positive in Hungary during 1955–2000, that is the rate of total lead deposition in the country exceeded the rate of emission from Hungarian sources: ratio between the atmospheric budget and emission varied in the range of 0.32–0.58.

References

Alcamo, J., Bartnicki, J., Olendrzynski, K. and *Pacyna, J.*, 1992: Computing heavy metals in Europe's atmosphere - I. Model development and testing. *Atmospheric Environment 26A*, 3355-3370.

Berdowski, J.J.M., Pulles, M.P.J. and *Visschedijk, A.J.H.*, 1998: Incremental cost and remaining *emission* in 2010 of Heavy Metals (HM) resulting from the implementation of the draft HM Protocol *under* UN ECE Convention on Long Range Transboundary Air Pollution. *TNO Report* - R 98/020.

Bozó, L., 1996: Long-range transport model estimations on the origin of atmospheric lead and *cadmium* deposition over Hungary. *Időjárás 100*, 43-49.

Bozó, L., Alcamo, J., Bartnicki, J. and *Olendrzynski, K.*, 1992: Total deposition and budgets of heavy metals *over* Eastern Europe. *Időjárás 96*, 61-80.

Mészáros, E., 1999: Fundamentals of Atmospheric Aerosol Chemistry. *Akadémiai Kiadó, Budapest*

Mészáros, E., Barcza, T., Gelencsér, A., Hlavay, J., Kiss, Gy., Krivácsy, Z., Molnár, A. and *Polyák, K.*, 1997: Size distributions of inorganic and organic species in the atmospheric aerosol in Hungary. *J. Aerosol Sci. 28, 1163-1175.*

Olendrzynski, K., Anderberg, S., Bartnicki, J., Pacyna, J.M. and *Stigliani, W.*, 1995: Atmospheric Emissions of Cadmium, Lead and Zink in Europe During the Period 1955-1987. *IIASA Working paper* WP-95-35.

Pacyna, J.M, 1993: Emission inventory for atmospheric lead, cadmium and copper in 1989 in Europe. *A report for the TNO Netherlands Organization for Applied Scientific Research*, the University of Michigan, Ann Arbor, MI.

Pacyna, J.M., 1996: Emission inventories for HMs and POPs in Europe. *WMO GAW Report* No. 117. 4-32.

Pacyna, J.M., Münch, J., Alcamo, J. and *Anderberg, S.*, 1991: Emission trends for heavy metals in Europe. *Proc. Int. Conference on Heavy Metals in the Environment*, Glasgow.

IDŐJÁRÁS

Quarterly Journal of the Hungarian Meteorological Service
Vol. 104, No. 3, July–September 2000, pp. 173–196

Synoptic-climatological investigation of weather systems causing heavy precipitation in winter in Hungary

Tamás Hirsch

Department of Meteorology
Eötvös Loránd University
H-1518 Budapest, P.O. Box 32, Hungary
E-mail: schnee@ludens.elte.hu

Division of Weather Forecasting
Hungarian Meteorological Service
H-1525 Budapest, P.O. Box 38, Hungary
E-mail: hirsch.t@met.hu

(Manuscript submitted for publication 19 January 2000; in final form 20 July 2000)

Abstract–In this paper, winter cases associated with heavy precipitation are examined. The aim of the investigation was to determine as many characteristics of these cases as possible with regard to the geographical and temporal differences. Both the amount and the state of precipitation were considered in order to improve the forecast of winter precipitation. In the first part of the paper the database and methods used, as well as the main features of heavy precipitation events in winter are presented. The most important results connected with these include the quite limited duration and spatial extent of the investigated events, considerable geographical (West vs. East) and seasonal differences, and quite low frequency of the cases with only snow. These results can be considered very useful because a good knowledge of the characteristics of heavy precipitation events is essential to their prediction. The second part of the paper contains the classification of heavy precipitation events (synoptic-climatological examination) and the research called parametrical investigation including the examination of the connection between some meteorological parameters and the state of precipitation. Results have shown that the connections between the macro-synoptic types and winter precipitation are quite strong. Nevertheless, these alone cannot be used for the considerable improvement of precipitation forecasts. Further investigations on smaller scales (sub-synoptic scale, mesoscale, microscale) are needed in order to reveal the important processes determining the development of precipitation. The first step into this direction has already been made in this research. Using a mathematical-statistic method (Bayes-decision) an accurate procedure for the objective forecast of the state of precipitation was developed, which can be successfully used in the operational work, too.

Key-words: winter precipitation, heavy precipitation events, precipitation forecast, synoptic-climatology, state of precipitation, Bayes-decision.

1. Background

Nowadays, numerical models are widely used in many areas of meteorology. They provide valuable information for the operational short-term weather forecast, too. The development of these models has led to a substantial improvement of short-term weather prediction, but there are some meteorological elements, which cannot be forecasted exactly enough using these models. One of them is precipitation.

There are many reasons for the inaccuracy of precipitation forecasts by numerical models. The main problem is associated with the parameterisation of precipitation processes in models with limited resolution in space and time. The only efficient way to improve precipitation forecasts is to examine as many past cases as possible and to try to determine what the dominant processes connected with the development of precipitation are. A proper method is based on synoptic-climatology, which means an investigation of meteorological parameters as a function of the synoptic situation. The rapid development of synoptic-climatology began in the 40-s, when *Baur* (1948) made the first classification of synoptic situations for Europe. Since then many new classifications have been made and much research has been carried out using these weather types.

Many synoptic-climatological studies have been made in connection with precipitation. One of these was performed by *Maddox et al.* (1979). They investigated 151 intense mesoscale weather systems resulting in heavy precipitation between 1973–1977 in the USA. It was found that these systems develop in one of 4 different synoptic situations. Another similar investigation was made by *Bartels* (1989), who studied 82 cases with heavy precipitation between 1931–1980 in Germany. He showed that orografic lifting by the Alps leads to a large difference between the northern and southern parts of Germany in the characteristic weather types related to heavy precipitation.

According to *Lauscher* (1985), Mediterranean cyclones play an important role in the weather of South- and East-Austria. One of his results was that a special kind of Mediterranean cyclone, which passes through the Carpathian Basin and touches the eastern part of Austria (these are also called Vb cyclones; their name created by *Van Bebber* dates back to the end of the 19th century), causes the highest mean daily precipitation amount in Vienna, namely 9.7 mm.

Similar research has been carried out in Hungary, too. *Péczely* (1961), who created the weather types for the Carpathian Basin, investigated some quantities in connection with precipitation. He determined the synoptic situations in which the mean daily precipitation amounts are the largest in Hungary. It was also shown that the situation with Hungary located in the warm sector of a Mediterranean cyclone is very favorable to the development of large precipitation amounts.

Bodolainé (1983) examined the synoptic conditions of floods on the basin of the Danube and the Tisza rivers. She classified the weather types that can lead to flooding using a period of over 100 years. The greatest merit of her classification is that the weather types are defined by relatively stable meteorological fields both on the surface and in the lower Troposphere. These fields always describe a process and not a momentary state of the atmosphere like many other classifications do.

Verifications have shown that the biggest errors of precipitation forecasts occur in case of large amounts of precipitation. Therefore, it is worth performing research in connection with weather systems causing heavy precipitation. Although much research on heavy precipitation during the warm season has occurred, there are only few investigations associated with large precipitation amounts in winter. The main reason for this dearth of research is that such situations are generally not characteristic of this season. But it also must be taken into account that winter precipitation in certain states can cause dangerous situations even if its amount is not too large. Nevertheless, only case studies have mostly been made in this topic. The work of the Spanish researchers *Sellés* and *Franch* (1994) can be considered as an example of the very few exceptions. They investigated the snowfalls in the south-eastern part of the Pyrenees using data from a 30-year period. Among others it was shown that on average 31% of the annual precipitation falls as snow and the biggest daily amounts of snow are caused by Mediterranean cyclones.

In this paper, the gap mentioned above is to be filled. Our aim is to examine winter situations with heavy precipitation in Hungary from as many points of view as possible with regard to the spatial and temporal differences. The biggest part of the research is made up by a synoptic-climatological investigation. The main purpose of this examination was to find out to what extent processes on the synoptic scale determine the amount and state of precipitation. Recent numerical models are able to forecast the macro-synoptic situation quite accurately for a few days. So if there is a very strong connection between the macro-synoptic types and precipitation, the forecast of the latter can be considerably improved. Nevertheless, investigations on smaller scales are absolutely necessary, because many of the important processes determining the development of precipitation are related to these. Accordingly, in the second part of the research, it was tried to carry out investigations on smaller scales. Both the amount and the state of precipitation were involved in this examination, but only the results associated with the latter are presented in the paper.

2. *Database and methods*

The weather systems causing large amounts of precipitation occurring in the winter periods of the years between 1986 and 1997 in Hungary were investigated. The number of the cases in these 11 winter periods was sufficient to carry out statistical investigations. The winter periods consisted of the months November, December, January, February and March. The months November and March were involved because winter precipitation (snow, sleet, freezing rain, etc.) quite often occur in both of these months in Hungary. In order to determine geographical differences, Hungary was divided into six parts each representing a characteristic region of the country: 3 areas in West- and 3 areas in East-Hungary (*Fig. 1*).

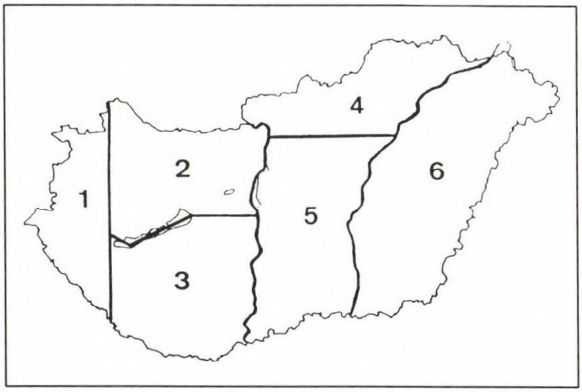

Fig. 1. The six areas of Hungary.

Those days of the mentioned periods were selected when the areal average of the daily precipitation amount was at least 5 mm in at least one of the areas. These cases were regarded as heavy precipitation events. The threshold value of 5 mm can be considered adequate because areal averages of the daily precipitation amount exceeding this value are quite rare in Hungary in winter. The areal average of the precipitation was calculated by the arithmetic mean of the daily precipitation data of the meteorological stations in the area. Data of all meteorological stations were used where precipitation amount is measured, so the calculation can be regarded as quite accurate in spite of using a relatively simple method.

The state of precipitation, the forecast of which is not an easy task during the winter period, was also considered in this research. It is also quite difficult, however, even to determine the state of precipitation occurring earlier because of the large spatial and temporal changes. Relatively detailed data on precipitation type are only available for synoptic stations, but at limited spatial resolution. If all the meteorological stations are considered, then there are sufficient data in space but not in time, because the stations measuring only precipitation report precipitation type just once a day, namely the one with the highest code. Therefore, it has to be accepted that the state of precipitation cannot be determined without errors.

The selected cases were also classified using two different methods, namely Péczely's and Bodolainé's weather types. Péczely's weather types (*Péczely*, 1957, 1983) are defined only by the surface pressure field, but contain all the synoptic situations. Their codes and explanation are shown in the Appendix. Bodolainé's weather types (*Bodolainé*, 1983) are defined by the fields of several meteorological parameters (not just pressure), namely absolute topography of the 500 mb level (AT500), relative topography of the 500/1000 mb level (RT500/1000), surface pressure and precipitable water, but contain only those synoptic situations that can lead to flooding (see the Appendix). In spite of that, they are more suitable for research connected with precipitation than Péczely's weather types.

In the second part of the study the connections between some meteorological parameters and the amount and state of precipitation were examined. In order to carry out these investigations for the weather systems causing heavy precipitation, the fields of the parameters are needed. Because of the sparsity of upper-air data, the data of only one station, Pestlőrinc (Budapest) was used to calculate the parameters for this point only. Those days of the winter periods mentioned earlier were selected when the daily precipitation amount was at least 5 mm at this station. This data is measured from 06 UTC to 06 UTC next day, so this 24-hour period can be divided into the following parts: 06 UTC–18 UTC and 18 UTC–06 UTC. Data from the 12 UTC sounding are taken to refer to the first period and those from the 00 UTC sounding to the second period. Only those 12-hour periods were considered, in which precipitation actually occurred. In this part of our research, emphasis was placed on the state of precipitation. A mathematical-statistic method called Bayes-decision was used to determine the threshold value that separates the values of a certain parameter characteristic for the liquid and the solid state in the most optimal way from a statistical point of view. That makes possible the objective forecast of the state of precipitation, too.

It must be emphasised that—even if it is not always mentioned—everything presented in the paper is relevant only to the cases with heavy precipitation, as defined above.

3. *Characteristics of weather systems causing heavy precipitation in winter*

One of the most important features of heavy precipitation events is their frequency. In *Fig. 2* it is shown how often cases with an areal average of the daily precipitation amount of at least 5, 10 or 20 mm occurred during the investigated period in at least one of the 6 areas. There is a marked seasonal change in the number of the cases. Heavy precipitation events mostly occurred in November and the fewest cases were observed in January. Also, weather systems causing a daily precipitation amount of at least 20 mm on areal average are quite rare in Hungary during winter time. Their mean frequency is smaller than 1 even in November!

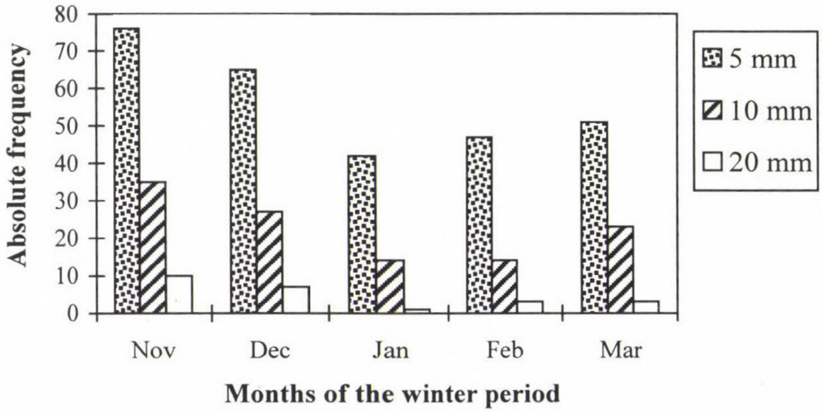

Fig. 2. Frequency of the days with areal average precipitation amount of at least 5, 10 or 20 mm.

The next step was to determine the spatial differences. It was found that in each area the monthly change of the frequency of heavy precipitation events is quite similar to the country-average mentioned earlier, except in East-Hungary, where the majority of the cases occurred in December and not in November as in the other parts of the country. *Fig. 3* compares the number of heavy precipitation events that occurred in the 6 areas during the investigated period. It shows that in Transdanubia (Area 1, 2 and 3) more cases occurred than in the eastern part of the country. It also can be seen that in two of the eastern areas (in the Northern-Mountains area and in East-Hungary) there were no days during the investigated period when the areal average of the precipitation amount was at least 20 mm. Meanwhile, there were days with a precipitation amount of more than 27 mm on areal average in all the three

Transdanubian areas, and the maximum value was 35 mm, which occurred in South-Transdanubia.

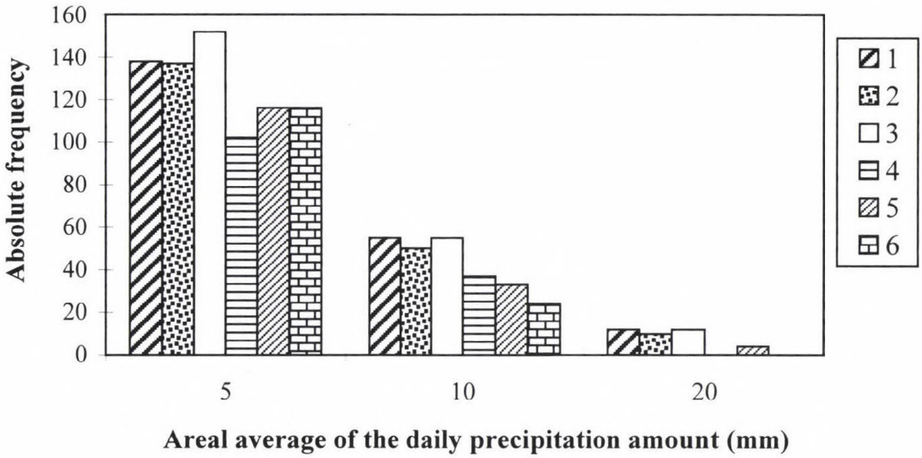

Fig. 3. Frequency of the days with areal average precipitation amount of at least 5, 10 or 20 mm in the six areas.

The maximum daily precipitation amounts were also investigated in our research. It was found that values over 40 mm are quite rare in Hungary during the winter period, but they occurred in the western part of the country much more frequently than in the eastern part. The absolute maximum daily precipitation amount was 75 mm and it was measured in North-Transdanubia. A very close connection was found between the areal average of the daily precipitation amount and the maximum daily precipitation amount measured in the same area. It can be stated that the maximum value is at least 1.5 times higher and on average twice as high as the areal average. Therefore, in case of an areal average precipitation exceeding 20 mm the maximum value must be more than 30 mm and on average more than 40 mm. The possibility that in East-Hungary the lack of cases with a daily precipitation average of at least 20 mm is due to the relatively large extent of the area compared to the other areas can be dismissed, because this was the region where the fewest cases with a maximum value over 40 mm occurred (only 2 cases).

The areal extent of heavy precipitation events was examined as well. Mostly only one or two areas are involved. The cases in which heavy precipitation occurs throughout the country are quite infrequent. It was also shown that heavy precipitation events including at least half of Hungary (3 areas or more) mostly occur in November and their number is decreasing during the winter period, whereas the frequency of the cases when much precipitation occurs in only one or two areas has a minimum in January and maxima in November, December and March.

Following the many spatial characteristics it is worth mentioning some temporal features, too. In *Fig. 4* the distribution of the length of those periods is shown when the areal average of the precipitation amount was at least 5, 10 or 20 mm in at least one of the areas every day of the period. Even in case of 5 mm the heavy precipitation period usually lasts only 1 day. Considering precipitation amounts of at least 20 mm, only one case during the investigated period lasted for 2 days. The maximum length of the period consisting of days with a precipitation average of at least 5 mm is 5 days and for 10 mm is only 3 days. The time intervals between heavy precipitation events vary quite irregularly. There were 3 winter periods without a daily precipitation amount of at least 20 mm on areal average, but there were also periods lasting more than 70 days without a daily precipitation average of at least 5 mm.

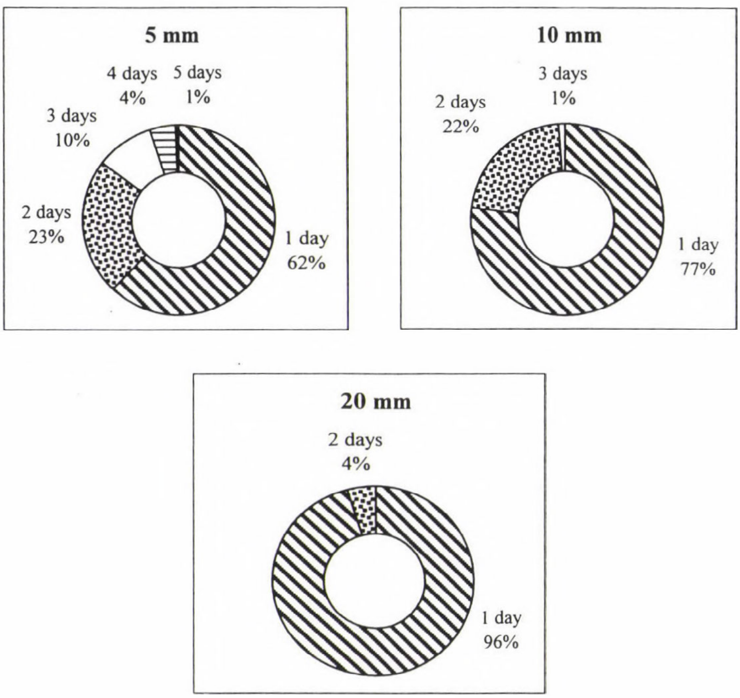

Fig. 4. Distribution of the length of heavy precipitation periods.

Next the state of precipitation was investigated. The type of precipitation was determined in the areas in case of heavy precipitation events. The types used are listed in *Table 1*. The type "only freezing rain" is absent from Table 1 because this case did not occur during the investigated period. Results from the cases with a precipitation amount of at least 10 mm on areal average can be seen in *Fig. 5*. Here the distribution of the precipitation types are shown with those areas where the areal average of the daily precipitation amount was at least 1, 5 or 10 mm. Therefore these results do not refer to one area but to that part of the country where a given amount (1, 5 or 10 mm) of precipitation occurred. In case of the biggest part of heavy precipitation events, only rain occurs. The frequency of cases with snow and rain is also high, but there are not many cases with only snow. Furthermore, if the areas with smaller amounts of precipitation are also considered, their frequency is even lower. Thus, cases with heavy precipitation and only snow in the whole country are very rare in Hungary and they require special conditions. The frequency of freezing rain is also quite low; it occurs more frequently when both rain and snow are falling.

Table 1. Precipitation types used in the research

Precipitation type	**Explanation**
Rain	Only rain in the whole area during the whole 24-hour-period
Snow	Only snow in the whole area during the whole 24-hour-period
Snow, rain	Both snow and rain in the area
Snow, rain, freezing rain	Besides snow and rain, also freezing rain in some parts of the area
Snow, freezing rain	Besides snow only freezing rain in some parts of the area
Rain, freezing rain	Precipitation in fluid state, part of it freezing rain

Spatial differences were also investigated. The relative frequency of cases with only rain is quite similar in the whole country. The same cannot be said for snow, because in the western part of Hungary more cases occurred (the relative frequency is about 25% for precipitation amounts of at least 10 mm occurring in the given area), than in the eastern part of the country. Surprisingly, it was the Northern Mountains area where the relative frequency of the cases with only snow was the lowest during the investigated period for the days with a precipitation amount of at least 10 mm. The most plausible explanation for that will be given in section 4. Finally, it was also found that the frequency of freezing rain during heavy precipitation events is much higher in the eastern areas than in Transdanubia. The change of the characteristic precipitation type during the winter period was investigated very thoroughly as well. It was found among others that freezing rain was the only type that did not occur in each month of the winter period. In March there were no big precipitation events with only snow in any of the eastern areas, but they did occur in all the western areas.

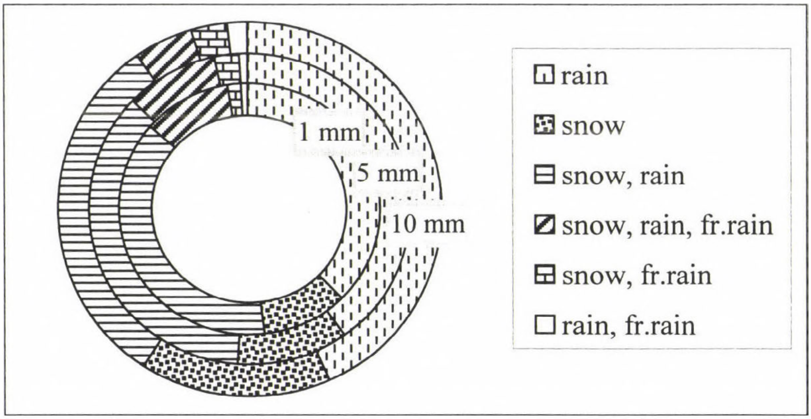

Fig. 5. Distribution of the precipitation types with daily precipitation amount of at least 10 mm considering the areas with a precipitation average of at least 1, 5 or 10 mm.

4. *Classification of heavy precipitation events*

As mentioned in section 2, Péczely's and Bodolainé's weather types were used to classify heavy precipitation events. Péczely's weather types were determined for every day of the investigated period, and since they describe only a momentary state of the atmosphere, it seemed to be expedient to do the classification twice for each day (00 and 12 UTC). It is important to mention that our way of classification does not exactly correspond to that of Péczely's. The main reason for that is that Péczely's method for distinguishing the anti-cyclonic from cyclonic types by determining whether the surface pressure is over or under 1015 hPa in the biggest part of Hungary was not strictly applied in our investigation. The relative value of pressure compared to the surrounding areas was considered to be much more important than its absolute value.

Fig. 6 shows the frequency of Péczely's weather types that occurred in case of large amount of precipitation during the investigated period. More than half of heavy precipitation events were caused by the weather type CMw (Hungary is situated in the warm sector of a Mediterranean cyclone). The frequency of the weather types CMc and C is also quite high, but considerably lower than that of CMw. According to Fig. 6, it is obvious that anticyclonic types do not play an important role in the development of heavy precipitation events in winter. In the following, only cyclonic types will be considered. The types zC and mCw are mostly only the antecedents of heavy precipitation events because their frequency is much higher immediately before the onset of heavy precipitation than during such events.

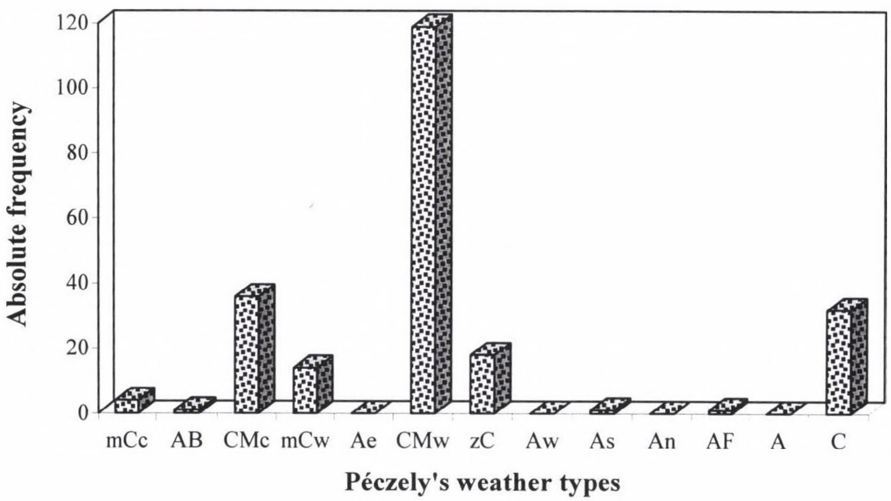

Fig. 6. Frequency of Péczely's weather types with daily precipitation amount of at least 10 mm on areal average.

As for spatial differences, it was found that in all areas of the country the type CMw has the highest relative frequency, but this value becomes gradually lower toward the East. Exactly the opposite can be said for the type CMc, which more often causes heavy precipitation in the eastern areas than in the western ones. The only cyclonic type that did not occur in all the areas in case of heavy precipitation is mCc. Valuable information can be obtained by determining the distribution of the areal average of the precipitation amount for each weather type. The most important result of this examination is that for all weather types the daily precipitation average was less than 5 mm in more than

60% of the cases. This means that even in case of CMw, which most frequently causes heavy precipitation events throughout the country, much precipitation on areal average is not at all guaranteed. That is, it is not enough to know the synoptic situation, it is also necessary to consider other processes and parameters connected with the development of large amounts of precipitation. The results for West-Transdanubia are shown in *Fig. 7*.

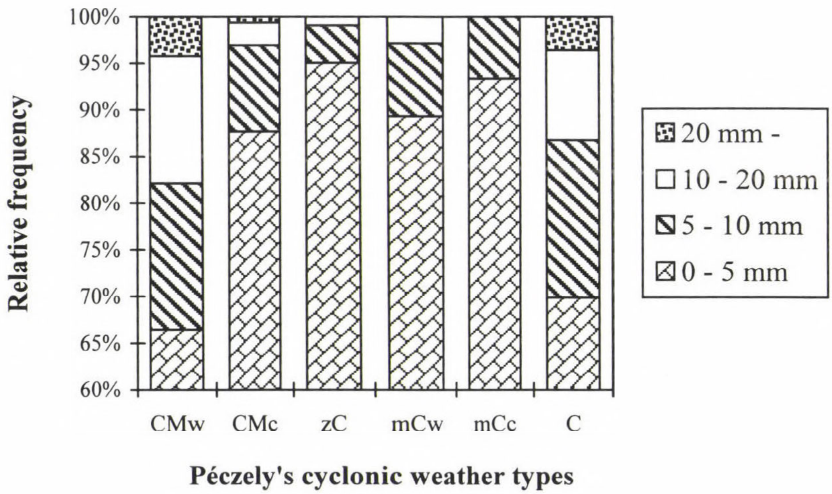

Fig. 7. Distribution of areal average daily precipitation amount in case of Péczely's cyclonic weather types in West-Hungary.

This is the only area where CMw is the weather type with the highest probability of developing daily precipitation averages of at least 5 mm (and also 10 mm). In all the other parts of the country heavy precipitation events are most probable in case of the cyclone centre type (C). The type with the least probability of heavy precipitation is zC in West- and North-Transdanubia, and mCc in the other parts of the country. It was also shown that in the winter period, daily precipitation amounts of at least 20 mm on areal average occur only in case of Mediterranean cyclones and cyclone centres over Hungary. Cases with heavy precipitation in at least half of the country are also mostly caused by these weather types.

One of the problems connected with Péczely's classification is that it is not able to separate the situation with a real cyclone centre from the situation with a temporary cyclone centre connected with the passage of a Mediterranean cyclone through Hungary. This was the primary reason for using

Bodolainé's weather types as well to classify heavy precipitation events. These types were determined only for the days with a precipitation amount of at least 10 mm on areal average in at least one of the areas. The results are shown in *Fig. 8.*

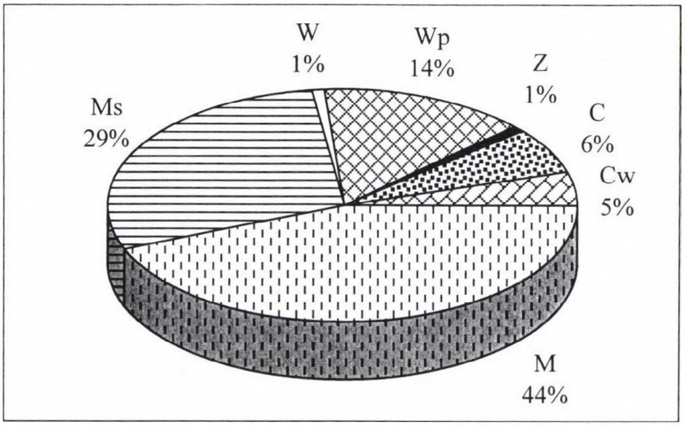

Fig. 8. Relative frequency of Bodolainé's weather types with daily precipitation amount of at least 10 mm on areal average.

A new type with the code Ms can be seen as well, which is not included in Bodolainé's weather types. It was necessary to create it because it quite often caused large amounts of precipitation on areal average, and it could not be classified as any of the Bodolainé's weather types. The type Ms represents a Mediterranean cyclone situated south from Hungary moving very slowly or not at all. This slow motion is caused by a huge blocking anticyclone with centre over Northeast-Europe or by the development of the cyclone also on higher levels of the atmosphere. In this case the deep trough characteristic for Bodolainé's transposing Mediterranean cyclone (type M) is missing. The fast motion of the type M is provided by the very strong south-westerly current in the east side of the trough. Cyclones belonging to the type Ms are mostly much deeper than those belonging to the type M and their genesis is also different in the most cases. Transposing Mediterranean cyclones usually form as frontal waves on cold fronts passing over the Alps. Cyclones belonging to the type Ms can develop directly in the Mediterranean (e.g. as a result of cold surges) or by the movement of cyclones formed over North-Africa or the Atlantic into this region. According to Fig. 8, in 73% of the cases the development of large amount of precipitation was connected with Mediterranean cyclones. From this point of view, Wp is relatively important as well, but the real cyclone centre situations (type C) caused only 6% of all cases. Type W and Z occurred only once and type H did not occur in case of heavy precipitation events during the investigated period.

Seasonal changes were investigated as well. The frequency of the type transposing Mediterranean cyclone (M) is the highest, except for the months January and February, when Ms is the type that most often causes heavy precipitation events. This is due to the higher frequency of blocking anti-cyclones over Northeast-Europe in these months. The real cyclone centre type (C) did not occur in December and January in case of heavy precipitation events, whereas Wp caused about 30% of the cases in these months. As for the spatial differences, the type M turned out to cause the most heavy precipitation events (40–55%) in every area. From this point of view, the type Ms is also very important in most of the areas, especially in West- and North-Transdanubia and in the middle part of Hungary. The relative frequency of the type Ms in case of a daily precipitation amount of at least 10 mm on areal average is lowest in the Northern Mountains area. This is also the area where the role of Mediterranean cyclones (M and Ms) is the least important in the country in the development of heavy precipitation, but their frequency exceeds 60 % even in this part of Hungary. Finally, the relative frequency of types C and Cw in such cases is much higher in the Northern Mountains area and in the middle part of Hungary than in the other regions of the country.

One of the advantages of creating the type Ms can be seen in *Fig. 9*, where some of the results of our investigation concerning the connection between the synoptic situation and the state of precipitation are shown. Only the areas with a precipitation average of at least 5 mm were considered. About 80% of the cases with only snow were caused by the type Ms. The other Mediterranean cyclone type, M turned out to cause only 6–7% of such cases. Type Ms provides favourable conditions for the development of freezing rain as well, whereas the type M mostly causes cases with only rain or both rain and snow. Another important result is that the real cyclone centre type (C) did not cause any cases with only snow or cases with freezing rain during the investigated period.

At the end of this section, we attempt to give an explanation for our most surprising result mentioned in section 3, namely that it is the Northern Mountains area where the cases with only snow make up the smallest part of heavy precipitation events. It has been shown in this section that heavy precipitation events with only snow occurred in about 80% in case of the type Ms. It has also been mentioned that for weather type Ms it is the Northern Mountains area where the probability of heavy precipitation is the smallest in the country. Therefore, it follows that it is the Northern Mountains area where the relative frequency of heavy precipitation events with only snow is the lowest, because the weather type Ms, which is the most favourable for such cases, does not often provide suitable conditions for the development of large amount of precipitation in this area. Here the type M causes heavy precipitation events much more often. For this weather type, higher temperatures are characteristic in the lower Troposphere than for the type Ms, so precipitation mostly falls as rain or both snow and rain even in this mountainous area.

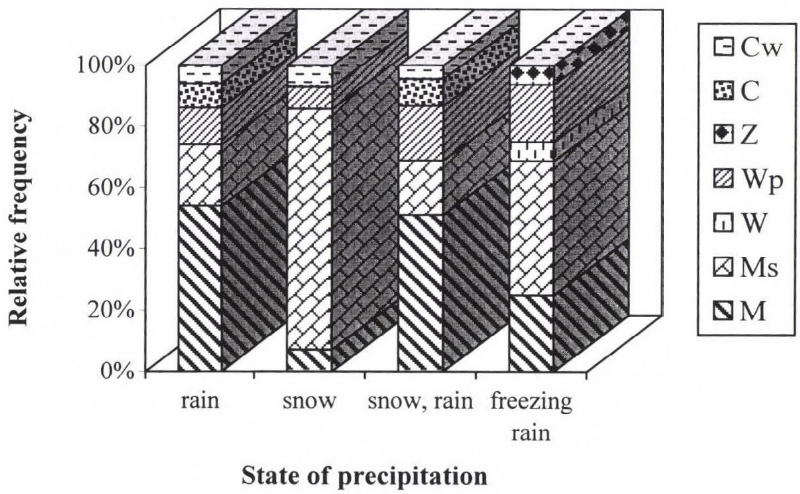

Fig. 9. Relative frequency of Bodolainé's weather types with daily precipitation amount of at least 10 mm on areal average as a function of the state of precipitation.

5. *Parametrical investigations*

In the last part of our research the connections between some meteorological parameters and the amount and state of precipitation were examined. In this section some of our results concerning the state of precipitation will be presented. As mentioned in section 2, the data of the station at Pestlőrinc (Budapest) were used and only those days of the investigated period were considered when the daily precipitation amount was at least 5 mm at this station. Data from the 12 UTC soundings were taken to refer to the first half of these days and those from the 00 UTC soundings to the second half of them.

119 days were found which met the criteria above. They were divided into 238 12-hour periods, but precipitation was observed only in 197 of these cases. First, the distribution of the state of precipitation for these periods was determined. In 65% of the cases only rain occurred and the percentage of the

cases with only snow was merely 20%. Both rain and snow occurred in 11% of the cases and the relative frequency with partly freezing rain made up only 4%. Next, it was examined which surface temperatures (Ts) are characteristic for the different precipitation types (*Fig. 10*). The precipitation types used are shown in *Table 2*. It can be seen that precipitation of liquid and solid state mostly occurred in case of positive and negative surface temperatures, respectively. Between -4°C and +4°C, however, both types were observed and also these are the most characteristic temperature values for the mixed type.

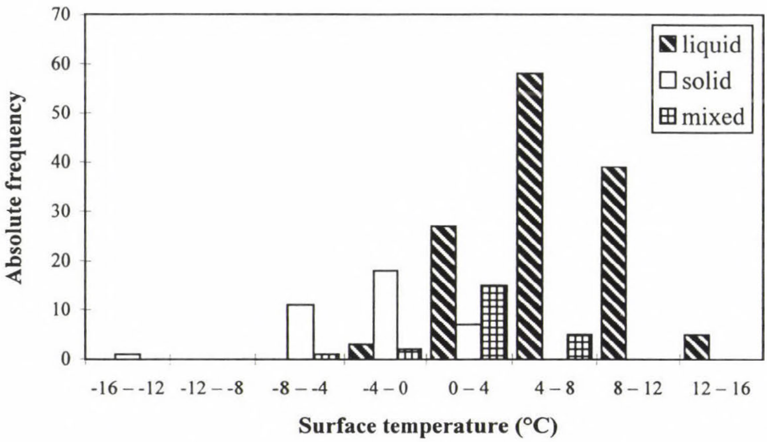

Fig. 10 Distribution of surface temperature for heavy precipitation events in winter as a function of the state of precipitation.

Table 2. Precipitation types used in the research

Precipitation type	Explanation
Liquid type	Only rain or mostly freezing rain during the whole period
Solid type	Only snow during the whole period
Mixed type	Both snow and rain or partly freezing rain

The state of precipitation observed on the surface is influenced by all the layers of the atmosphere that the precipitation elements were falling through. Therefore, the precipitation type reflects the meteorological conditions of the whole lower Troposphere. Although there is connection between the surface temperature and the state of precipitation (as shown in Fig. 10), in most cases the temperature measured near the surface (at a height of 2 m) is obviously not able to influence the precipitation type. The only exception is freezing rain that is caused by negative temperatures near and on the surface. Mostly it is just the other way around, that is the state of precipitation influences the surface temperature. This fact can be illustrated with the following example: if the surface temperature is positive and in spite of that the precipitation elements reach the surface as snow, then after a while the surface temperature is gradually decreased by the thawing of the snow. So other parameters had to be found that really influence the state of precipitation. The parameters chosen can be seen in *Table 3*. The last two parameters provide information about the temperature conditions of atmospheric layers and not only single levels like the other 4 parameters do. After determining the distribution of each parameter in case of the different precipitation types, it was found that there were significant differences in the extent of overlapping the values characteristic for the liquid and the solid state in case of the different parameters. It could be stated that the higher the level, the less the values were separated, resulting in larger overlapping. In case of RT850/1000 the values were quite separated (small overlapping).

Table 3. Meteorological parameters used in the research

Parameter	**Explanation**
T925	Temperature of the 925 hPa level
T850	Temperature of the 850 hPa level
T700	Temperature of the 700 hPa level
T500	Temperature of the 500 hPa level
RT850/1000	Thickness of the layer between 850 and 1000 hPa
RT500/1000	Thickness of the layer between 500 and 1000 hPa

In the following, a mathematical-statistic method based on the Bayes-decision (*Dévényi* and *Gulyás*, 1988) was used to determine the threshold value that separates the values of a certain parameter characteristic for the liquid and the solid state in the most optimal way from a statistical point of view. In this investigation only that part of the cases was considered in which only snow or only rain was observed. Two random variables were used: one of the above-mentioned parameters was regarded as the predictor and the state of precipitation (snow or rain) as the predictand. It is important to emphasise that the value of the predictor was assumed to be known. The function, with the help of which the predictand is estimated from the value of the predictor, is called decision function. The accuracy of the estimation is given by the so-called loss function, which is only a function of the difference between the real and estimated values of the predictand. The loss function is also a random variable and its expected value is called the risk of the estimation.

Our aim was to find the Bayes-decision, that is the decision function with the minimum risk in case of a certain loss function. Since our predictand variable is discrete and it can have only the values "1" and "2" (snow, rain), the decision function is equivalent to dividing the possible values of the predictor variable into two disjoint sets. In this case the decision function operates as follows: if the value of the predictor is in set1, the value of the predictand is "1" (that is the estimation of the state of precipitation is snow) and if the value of the predictor is in set2, the predictand has the value "2" (that is the estimation of the state of precipitation is rain). The predictor variable can be a vector (*Matyasovszky et al.*, 1993), but in our case it was chosen as a scalar, that is it always contains only one of the mentioned parameters. This means that the elements of the two sets are also scalar, so these sets can be simply created by determining the threshold value that separates the values of the predictor belonging to set_1 from those belonging to set2. It can be shown that in this case the sets equivalent to the Bayes-decision are the following:

$$c_1^* = \{x \mid W_{21} \cdot p_2 \cdot f_2(x) \le W_{12} \cdot p_1 \cdot f_1(x)\}, \tag{1}$$

$$c_2^* = \{x \mid W_{21} \cdot p_2 \cdot f_2(x) \ge W_{12} \cdot p_1 \cdot f_1(x)\}. \tag{2}$$

W_{21} and W_{12} are the elements of the loss matrix (equivalent of the loss function in case of a discrete predictand), and both were given the value "1", because both kinds of poor estimations (snow was estimated but rain occurred and the other way around) were regarded as equally important. In the formula above p_1 and p_2 mark the probability of snow and rain, whereas f_1 and f_2 are the conditional density functions of the predictor for snow and rain. Considering the value of W_{21} and W_{12}, it is obvious that the threshold value can be obtained from the following equation:

$$p_1 \cdot f_1(x) = p_2 \cdot f_2(x). \tag{3}$$

The four components of this equation were estimated using the cases that occurred in the investigated period. Probability of snow and rain (p_1 and p_2) were substituted with their relative frequency during the investigated period. The distribution of the predictor variable was assumed to be normal, so the estimation of the expected value by the mean of the sample and that of the variance by the empirical dispersion were sufficient to determine f_1 and f_2. The threshold value could be simply obtained by determining the value that satisfies the equation above. The products on both sides of the equation can also be interpreted as the conditional density functions of the predictor weighted with the probability of the given state of precipitation, and the curves belonging to the two functions intersect at the threshold value.

In order to demonstrate this, *Fig. 11* was made, where the weighted conditional density functions are represented in two cases, namely when RT850/1000 and when T500 was chosen as the predictor variable. These two parameters were selected intentionally, because RT850/1000 is the parameter with the smallest and T500 is the parameter with the largest overlapping the two density functions among the investigated parameters. It also can be seen that in case of T500 the value belonging to the intersection of the two curves (threshold value) is smaller than the expected value of T500 in case of snow, that is the probability of rain is higher than that of snow even if the predictor has the value, in case of which snow most often occurs. A similar statement can be made only in case of T700 (*Table 4*). Obviously, it is worth using only those parameters for estimating the state of precipitation, for which the threshold value is between the two expected values. In order to find out how exact the estimations are in case of the mentioned parameters, the risk of the estimation was determined in each case.

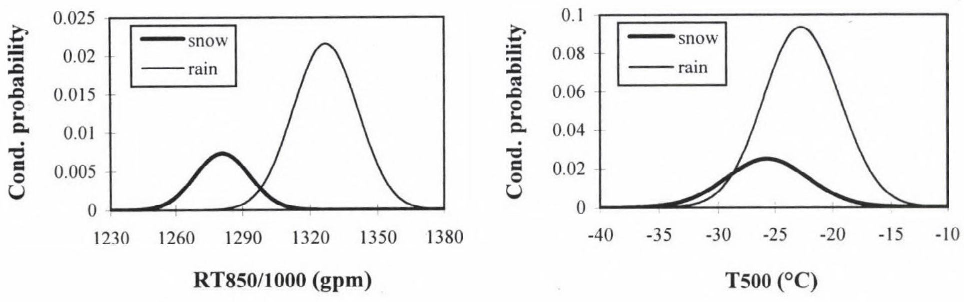

Fig. 11. Weighted conditional density functions of two meteorological parameters for heavy precipitation events in winter.

According to its definition, the risk corresponds to the area situated under the intersection of the two density functions bordered by the curves belonging to these functions (this area has been called overlapping so far). Using an approximation the risk was determined for all parameters investigated. It is made up of two parts, one contains the probability of estimating snow in case of rain (Error1) and the other is the probability of the reversed situation (Error2). In *Table 5* all the three values are given as a percentage. It is important to emphasise that these values are only valid when the value of the predictor is exactly known. In order to forecast the state of precipitation the value of the predictor has to be forecasted as well, with the help of which the estimation is carried out. So the real value of the risk is typically higher than that given by Table 5 depending on how accurate the forecast of the predictor is. Although Ts is the third best predictor among the investigated parameters, there is no value in using it, because its forecast is quite inaccurate as mentioned earlier. The risk is in case of T500 and T700 the largest, which indicates that the temperature conditions over about 3000 m do not influence the state of precipitation too much.

Table 4 Conditional expected values of the investigated parameters and the threshold values

Parameter	**Expected value for snow**	**Expected value for rain**	**Threshold value**
Ts	-2.8°C	6.7°C	0.7°C
T925	-4.5°C	5.1°C	-1.0°C
T850	-5.4°C	2.0°C	-3.1°C
T700	-10.3°C	-6.3°C	-10.7°C
T500	-25.7°C	-22.7°C	-28.7°C
RT850/1000	1281.0 gpm	1326.9 gpm	1298.0 gpm
RT500/1000	5315.6 gpm	5426.3 gpm	5339.8 gpm

Table 5. Mean error of the estimation of the state of precipitation using different parameters as predictor variables

Parameter	**Error1** (%)	**Error2** (%)	**Risk** (%)
Ts	2.05	3.09	5.14
T925	1.90	2.20	4.10
T850	3.45	3.34	6.79
T700	4.49	12.56	7.05
T500	2.67	18.00	20.67
RT850/1000	*1.68*	*1.88*	*3.56*
RT500/1000	4.95	6.75	11.70

Cases with freezing rain were also investigated, but their number was too small to draw conclusions. Another problem was that in most of the cases freezing rain occurred between two soundings, so the data available can not be considered representative. The detailed investigation of freezing rain requires the extension of the examination to the cases with a daily precipitation amount less than 5 mm, because freezing rain very seldom occurs in case of heavy precipitation events investigated in this research.

6. Conclusion

First, it can be stated that many important features of heavy precipitation events in winter were determined. Probably the most important of these was that very special conditions are required for large amounts of precipitation in form of only snow in the whole country. Further results included:

- the marked change in the frequency of the cases and the characteristic precipitation type during the winter period;
- considerable geographical differences (West and East) in the number of the cases, precipitation amounts and the percentage of several precipitation types;
- quite limited duration (usually 1 or 2 days) and spatial extent (mostly only 1 or 2 areas, that is, less than half of the country was involved).

The most important results relevant to the connection of the synoptic situation and heavy precipitation events (HPE) in winter:

- HPEs are mostly caused by Mediterranean cyclones (Péczely's CMw, CMc and Bodolainé's M, "Ms" type), but the cyclone centre type has the highest probability of developing such cases (30–40%) except for West-Hungary.
- The new macro-synoptic type Ms, which was created in order to make Bodolainé's classification complete in terms of this research, caused about 80% of the cases with only snow and nearly 50% of the cases with freezing rain.
- A plausible explanation for the surprising finding about the Northern Mountains area (percentage of the cases with only snow) was given.

Finally, parametrical investigations have led to many valuable results as well including:

- The characteristics of the layer between the surface and about 1500 m are the most important concerning the state of precipitation.

- Using a mathematical-statistic method based on the Bayes-decision a procedure for the objective forecast of the state of precipitation was developed.
- RT850/1000 proved to be the best parameter investigated the mean error of the estimation being only 3.6% in case of using this parameter as the predictand.

To sum up the facts above, it can be stated that synoptic-climatological investigations are able to improve our understanding of the processes connected with the development of precipitation. A considerable improvement of precipitation forecasts, however, cannot be achieved without carrying out comprehensive examinations on smaller scales (sub-synoptic scale, mesoscale, microscale) as well. Nevertheless, our investigation can be considered very useful because it pointed out the utmost importance of the processes on these scales even in winter. Possible further research could include the examination of the applicability of the so-called composite chart method (*Maddox*, 1979; *Bonta*, 1991) to winter cases.

Furthermore, the state of precipitation can be considerably influenced by precipitation intensity as indicated by *Steinacker* (1983), among others. The two main processes connected with that are cooling of the air by the evaporation of precipitation and the melting of snowflakes before reaching the ground. In the future, both of these processes should be taken into account when estimating the state of precipitation. This, however, might only be successful when much better quantitative precipitation forecasts are available.

Acknowledgements–The author would like to thank the Hungarian Meteorological Service (HMS) for providing the data required for this study. Special thanks are due to *Dr. Imre Bonta* (HMS) and *Dr. Zsuzsanna Iványi* (ELTE) for supporting my work.

References

Bartels, H., 1989: *Koordinierte Starkregenregionalisierung, Auswertung.* DeutscherWetterdienst Referat Hydrometeorologie, 04. 1989.

Baur, F., 1948: *Einführung in die Großwetterkunde.* Dieterichsche Verlagsbuchhandlung, Wiesbaden.

Bodolainé, J. E., 1983: *Synoptical Conditions of Floods on the Basin of the Rivers Danube and Tisza* (in Hungarian). OMSZ Hivatalos Kiadványai, LVI. kötet. Országos Meteorológiai Szolgálat, Budapest.

Bonta, I., 1991: *Investigation of weather systems causing heavy precipitation on the basin of the rivers Danube and Tisza* (in Hungarian).*Doctoral Thesis*, ELTE TTK Meteorológiai Tanszék, Budapest.

Dévényi, D. and *Gulyás, O.*, 1988: *Mathematical-statistic Methods in Meteorology* (in Hungarian). Tankönyvkiadó, Budapest.

Lauscher, F., 1985: *Klimatologische Synoptik Österreichs mittels der ostalpinen Wetterlagenklassifikation. Arbeiten aus der Zentralanstalt für Meteorologie und Geodynamik, Heft 64.* Zentralanstalt für Meteorologie und Geodynamik, Wien.

Maddox, R. A., 1979: A methodology for forecasting heavy convective precipitation and flash flooding. *National Weather Digest: Flood 4*, 30-42.

Maddox, R. A., Chappell, C. F. and *Hoxit, L. R.*, 1979: Synoptic and Meso-α scale Aspects of Flash Flood Events. *Bulletin of the American Meteorological Society 60*, 115-123.

Matyasovszky, I., Németh, L., Németh, P. and *Takács, Á.*, 1993: Forecasting the state of winter precipitation (in Hungarian). *Beszámolók az 1990-ben végzett tudományos kutatásokról*, Országos Meteorológiai Szolgálat, Budapest, 46-53.

Péczely, Gy., 1957: *Großwetterlagen in Ungarn. Kleinere Veröffentlichungen der Zentralanstalt für Meteorologie, No.30.* Országos Meteorológiai Szolgálat, Budapest.

Péczely, Gy., 1961: *Climatological Characteristics of the Macrosynoptic Types of Hungary* (in Hungarian). OMSZ Kisebb Kiadványai, No.32. Országos Meteorológiai Szolgálat, Budapest.

Péczely, Gy., 1983: *Catalogue of the macrosynoptic types of Hungary (1881-1983)* (in Hungarian). OMSZ Kisebb Kiadványai, No.53. Országos Meteorológiai Szolgálat, Budapest.

Sellés, C. G. and *Franch, F. S.*, 1994: Snowfall analysis in the Eastern Pyrenees. 23.Internationale Tagung für Alpine Meteorologie. 5-9 September 1994, Lindau. *Annalen der Meteorologie 30*, 303-306.

Steinacker, R., 1983: Diagnose und Prognose der Schneefallgrenze. *Wetter und Leben 35*, 81-90.

APPENDIX

Péczely's weather types

Code	Explanation
mCc	Hungary is located in the rear of an East-European cyclone
AB	Anticyclone over the British Isles
CMc	Hungary is located in the rear of a Mediterranean cyclone
mCw	Hungary is located in the warm sector of a West-European cyclone
Ae	Anticyclone east from Hungary
CMw	Hungary is located in the warm sector of a Mediterranean cyclone
zC	Zonal cyclonic situation
Aw	Anticyclone extending from the west
As	Anticyclone south from Hungary
An	Anticyclone north from Hungary
AF	Anticyclone over the Fennoscandinavian region
A	Anticyclone with centre over the Carpathian-Basin
C	Cyclone with centre over the Carpathian-Basin

Bodolainé's weather types

Code	Explanation
W	West type
Wp	West with secondary disturbation type
Z	Zonal type
M	Transposing Mediterranean cyclone type
C	Cyclone centre type
Cw	West cyclone type

IDŐJÁRÁS

Quarterly Journal of the Hungarian Meteorological Service
Vol. 104, No. 3, July–September 2000, pp. 197–211

Preparation of regional scale wind climatologies

Dezső J. Szepesi[1], **Richárd Büki**[2] and **Katalin E. Fekete**[1]

[1]*Consultants on Air Resources Management Inc., H-1137 Budapest, Katona J. u. 41 V/25, Hungary; E-mail: h12506sze@ella.hu*
[2]*HMMO, H-1885 Budapest, Hungary; E-mail: rbuki@hotmail.com*

(Manuscript submitted for publication 21 December 1999; in final form 11 August 2000)

Abstract—This paper presents newmethod and preliminary regional scale wind patterns for Europe, which fill the gap between the global climatologies and more local scale surface wind climatologies like the European wind atlas. The aim of establishing regional scale wind maps is to provide readily available regionally representative flow statistics. Preliminary maps based on 2 years of measured 850 hPa wind direction and speed data from 120 sounding stations show characteristic patterns (see Figs. 1, 2 and 3). Statistical analysis shows close correlation between short and long series of wind statistics. Such maps could be eventually used for top-down extrapolation of yearly mean surface wind statistics for data sparse areas by considering effects of terrain, surface and obstacles.

Key-words: regionally representative wind, environmental impact assessment, geostrophic wind, harmonization of meteorological data preprocessing, wind atlas.

1. Introduction

The paper describes preparatory work and preliminary results on a new method of wind analysis, which might serve towards the establishment of a regionally representative wind atlas. The research is part of efforts to harmonize meteorological data preprocessing. The atlas—an outcome of such work—might form a useful tool for top-down (considering locally representative surface, topographical and orographical conditions) wind inter- or extrapolation purposes or for checking climatological or territorial representativity of shorter term wind statistics.

In contrast to the wealth of meteorological data pouring from global measuring networks and data assimilation procedures, regionally and temporally representative flow data for environmental applications are, for numerous reasons, in some countries very scarce. In practice, this long standing input-data shortage often led to the situation where even the shortest term measurements of field data were used without their representativity being questioned.

Literature review

Efforts for mapping wind conditions have long history. Vector mean wind direction and speed maps based on 1880–1915 simple surface wind (Wild) observations were analysed for the territory of the former Austrian-Hungarian Monarchy by *Defant* (1920). Global distributions of seasonal standard vector deviations of 700 hPa winds were presented by *Meteorological Office* (1950). *Machta* (1979) presented global analyses of seasonal vector mean wind direction, speed and vector standard deviation at 850 and 700 hPa and presented a graphical methodology to estimate typical concentrations, depositions and flux rates for transport within 100–1000 km-s. *Peixoto and Oort* (1992) and *Landsberg* (1986) also presented global scale wind climatologies. *Jensen* (1984) produced an 850 hPa wind speed map from radiosonde data for a narrow band of the Western Europe coastline for wind energy applications.

Downward interpolation from geostrophic winds to predict surface winds was the original method adopted by the Riso group in producing the Danish Wind Atlas but was dropped in favor of a method based on surface wind data for their European Wind Atlas (*Taylor*, 1997). WAsP (Wind Atlas Analysis and Application Programme; *Troen et al.*, 1988) corrects wind data measured at a specific point and transforms these data into a data set describing the wind climate of a region, called a wind atlas. It utilizes such data sets to estimate the wind conditions at any particular site and height in the region, in principal by applying the same routines.

Szepesi and *Fekete* (1993) and *Szepesi et al.* (1995) reported preparation of regionally representative surface wind maps for Hungary. For the analysis of these maps all available surface wind data series (more than 200 between 1881–1980) and upper air ascents (22 long series between 1929–1989) in Hungary were considered.

Summarizing, it is concluded that while world climate centers are easily able to produce global scale assessments for hemispheric grid points based on stored data from the principal sounding stations, for regional scale assessments there is no substitute for conventional analysis of cleaned long-term data series obtained from national archives (e.g., KLIMA 90).

2. Representativity of flow statistics

One of the most important aspects of pollution transport is representativity of ensemble of flows at the height of the plume. To be representative the ensemble of flows has to meet territorial, temporal and height criteria.

2.1 Regional representativity

Locally measured winds are often biased and not representative of the height of plume. The smoothed out flow pattern is regionally more representative and thus reveals many inconsistencies in siting, measuring and data analysis.

2.2 Temporal representativity

Due to climatic variability of wind conditions temporal representativity is ensured mostly by using long-term (~30-year) historical data. If such data series are not available, short-term (1–5 year) series could be used if they meet temporal representativity criteria i.e., both the short-term and the long-term (10–30 year) periods have similar macrosynoptic weather type (MSWT) frequency distributions.

As far as the presently analysed 1980–81 period is concerned the MSWT analysis shows that cyclonic weather types were 5% more frequent than in the long-term normal period. By using such MSWT analysis and even forecasting, the effect of possible climate modification might also be accounted for by applying similar criteria.

3. Assessment of results

The goal of this research is to establish eventually a design 850 hPa wind concept to promote harmonization of meteorological data preprocessing for dispersion estimates. As a first step upper air wind analyses have to be completed taking into account the following principles: (a) They should be based on all the long-term (10–30 yr) 00 and 12 UTC 850 hPa wind data available, (b) Where only shorter-term (1–5 yr) data series are available they have should be checked against long-term macrosynoptic statistics before inclusion, and (c) Territorial analysis (smoothing) should be used to ensure representative flow data for the region concerned.

The preliminary wind atlas (see *Figs. 1, 2* and *3*) was prepared using 2 year (1980–1981) 850 hPa measured upper air wind direction and speed statistics. This rather old period was selected because the upper air sounding network in Europe was the densest at that time and nothing limited regional scale analyses. The evaluation and analysis was carried out manually in the late 80-ies when the idea of constructing design wind maps emerged. A map showing the station locations (see Fig. 1) allows the reader to make a better judgement of the spatial representativity of data. Sample gradient wind maps were presented at the Ostende Meeting and encountered considerable interest (*Szepesi* and *Fekete*, 1996).

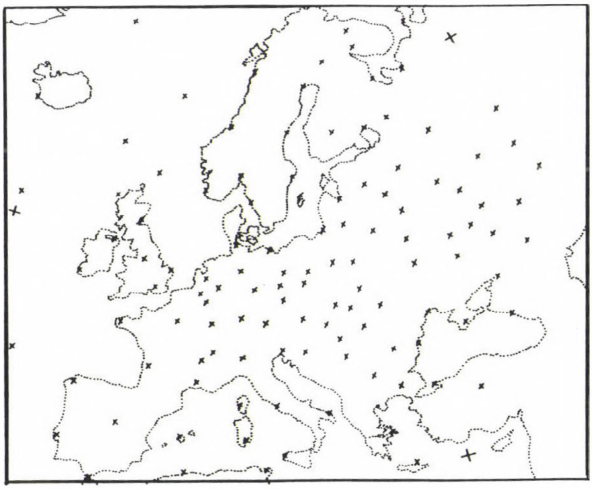

Fig. 1. Upper air station network.

To make these preliminary maps climatologically more representative, the following countries have already provided long-term wind statistics (see *Tables 1–4*). (a) For the UK 12 year (1976–1987) 13 station 850 and 700 hPa 00 and 12 UTC statistics (*D.J. Thomson*), (b) for Germany 30 year (1961–1990) 850 and 700 hPa 00 and 12 UTC statistics (*E. Dittmann*), (c) for Hungary 28 year (1962–1989) 2 sounding and 10 pilot balloon station 850 and 700 hPa 00 and 12 UTC statistics (*D.J. Szepesi*), (d) for Switzerland 32 year (1959–1990) 925, 850 and 700 hPa 00 and 12 UTC wind pattern (*A. Aschwanden*), (e) for Poland 20 year (1971–1990) 4 station statistics (*Z. Litynska*), (f) for Finland 31 year (1965–1995) 3 station statistics (*M. Lahti*). In addition a number of other researchers have indicated their intention to participate in this project.

The comparison of preliminary data from the wind atlas (Figs. 2 and 3) and longer-term data which are yet not to be part of the atlas are shown in *Figs. 4* and *5* and *Tables 5* and *6*. It can be seen in the RMS diagrams (Fig. 4 and 5) that all the data are near to the 45° trendline. It suggests that the data are in strong relationship.

The RMS of data is higher in case of wind directions (Table 5) than in windspeed (Table 6). This means that the windspeed is less changeable than the wind direction. There are only few data, which are relative far from the trendline. This is shown also by the numerical analysis.

The RMS of wind direction data is 3.54 for the long, and 3.98 for the short series. The covariance coefficient between the long, and short series is 11.23, the correlation coefficient is 0.80. The relative high value of the correlation coefficient shows a close relationship.

The RMS of windspeed data is much smaller, the points are very close to the trendline. This is shown by the numerical analysis, too. The RMS of the long series is 2.11, and 1.97 for the short series. The covariance coefficient is 3.62; the correlation coefficient is 0.88, which clearly shows a very close relationship between the two series.

Summarizing we conclude, that the interval of 1980–1981 represents for Europe macrosynoptically quite well the upper air conditions of a long (20 to 35 years) period.

The main results are as follows:

(a) Analyses based on just 2 years of measured upper air wind data show clearly the new method's ability for regional scale analysis of characteristic wind patterns. Even with 2 year long records of wind data, the statistics obtained already approximate long-term patterns provided the years are climatologically normal.

(b) Short series wind speed averages approximate long series averages even better than the wind direction data do.

(c) Sharp chanelling caused by the mountain ranges of e.g., the Alps and the Jura was detected in the short as well as in the long-term wind direction statistics. Inside the dominant wind sectors, however, considerable variation in directional frequencies occurred due to the different MSWT characteristics of the respective periods.

(d) Details of the finer scale structure of e.g. the E and NE wind speeds over level terrain west of Urals should not be considered artifacts. They are mostly due to regional differences in climate. It is expected, however, that 30-year data statistics will show less fine structure in the upper air windspeed pattern.

(e) For the preparation of wind statistics, the application of the conventional 16 meteorological sector distribution is recommended instead of the often used 12 sector standard.

(f) Based on these preliminary results, which were obtained after collecting 30 year wind statistics, finer areal as well as temporal analyses are justified. The final analysis might show new features, which are not apparent from this preliminary assessment.

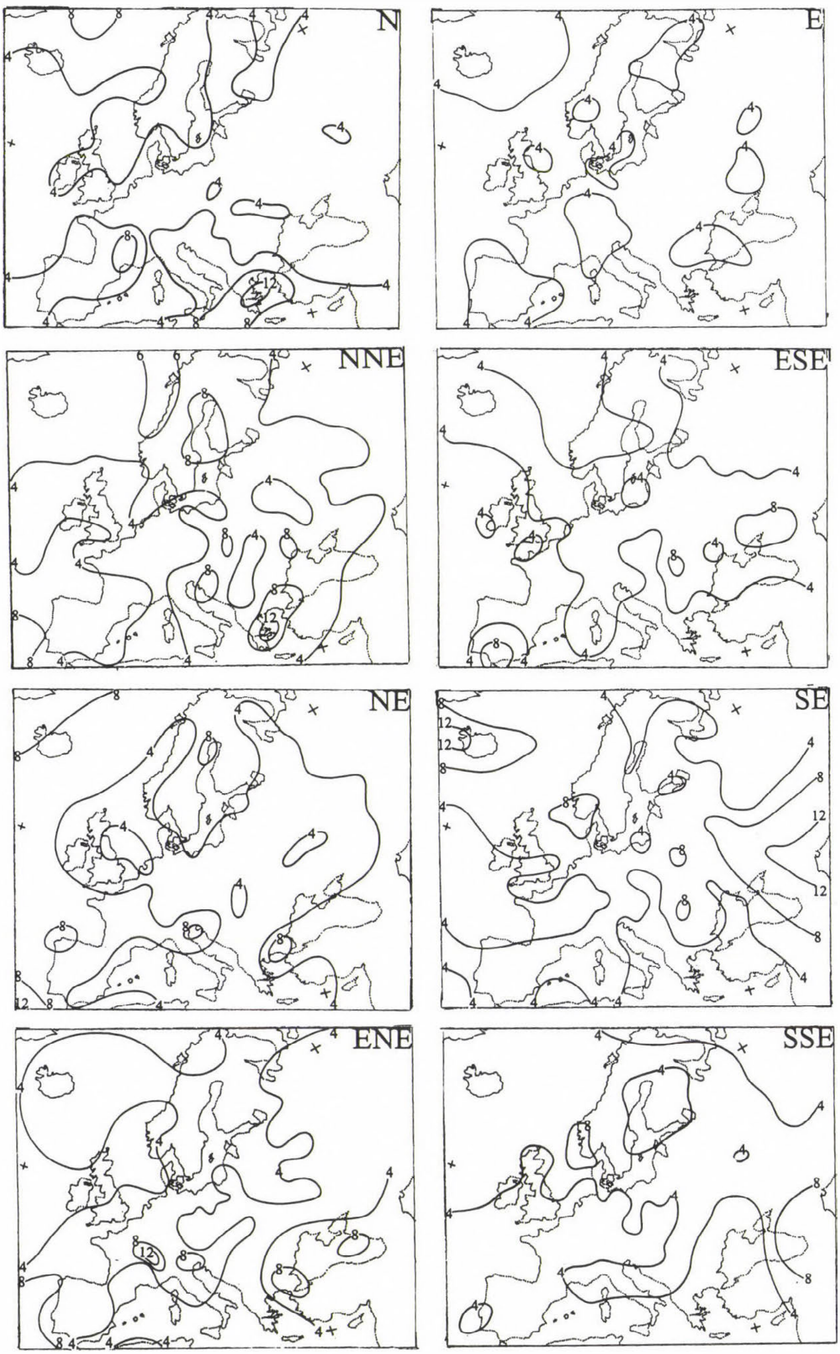

Fig. 2a. Realtive frequency of 850 hPa wind direction (N–SSE) in percent (1980–1981).

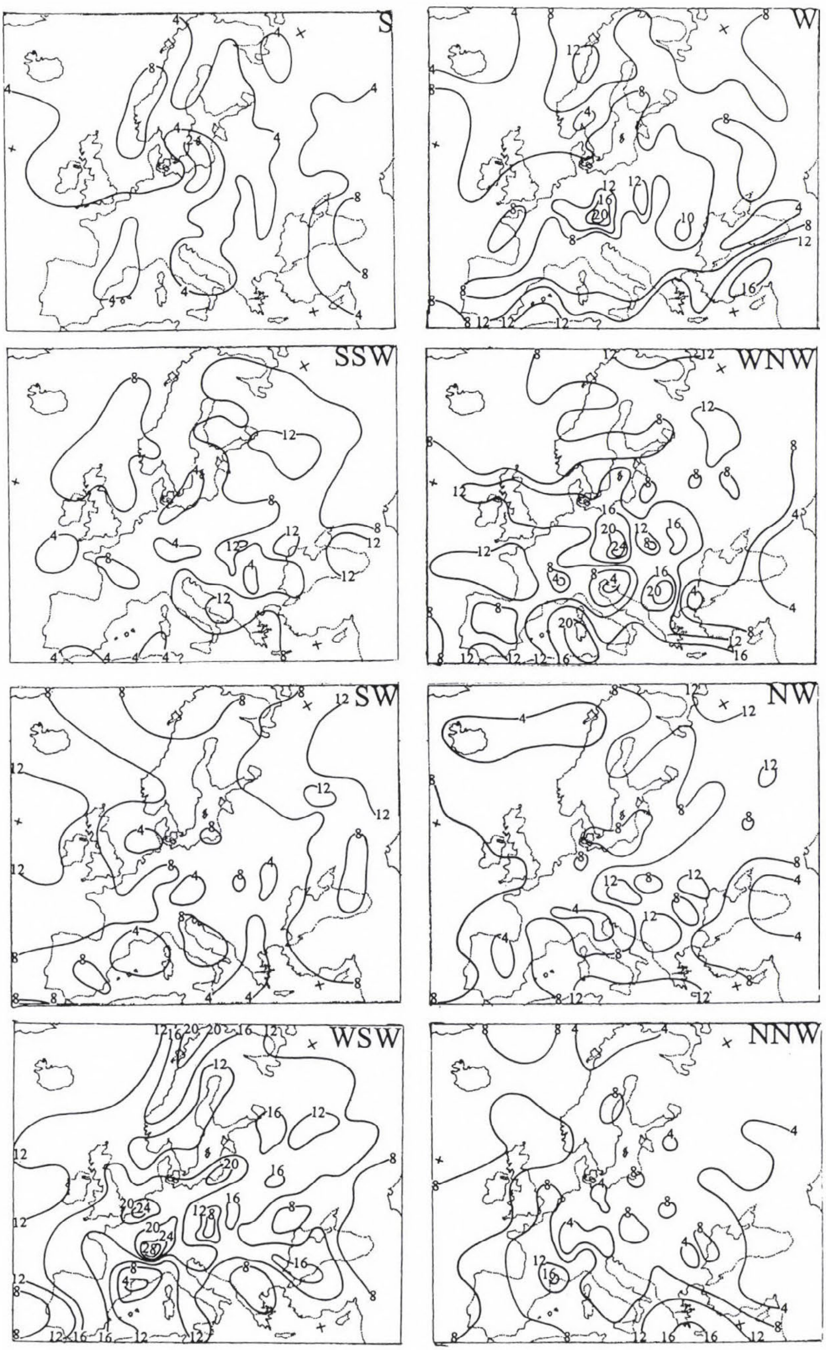

Fig. 2b. Relative frequency of 850 hPa wind direction (S–NNW) in percent (1980–1981).

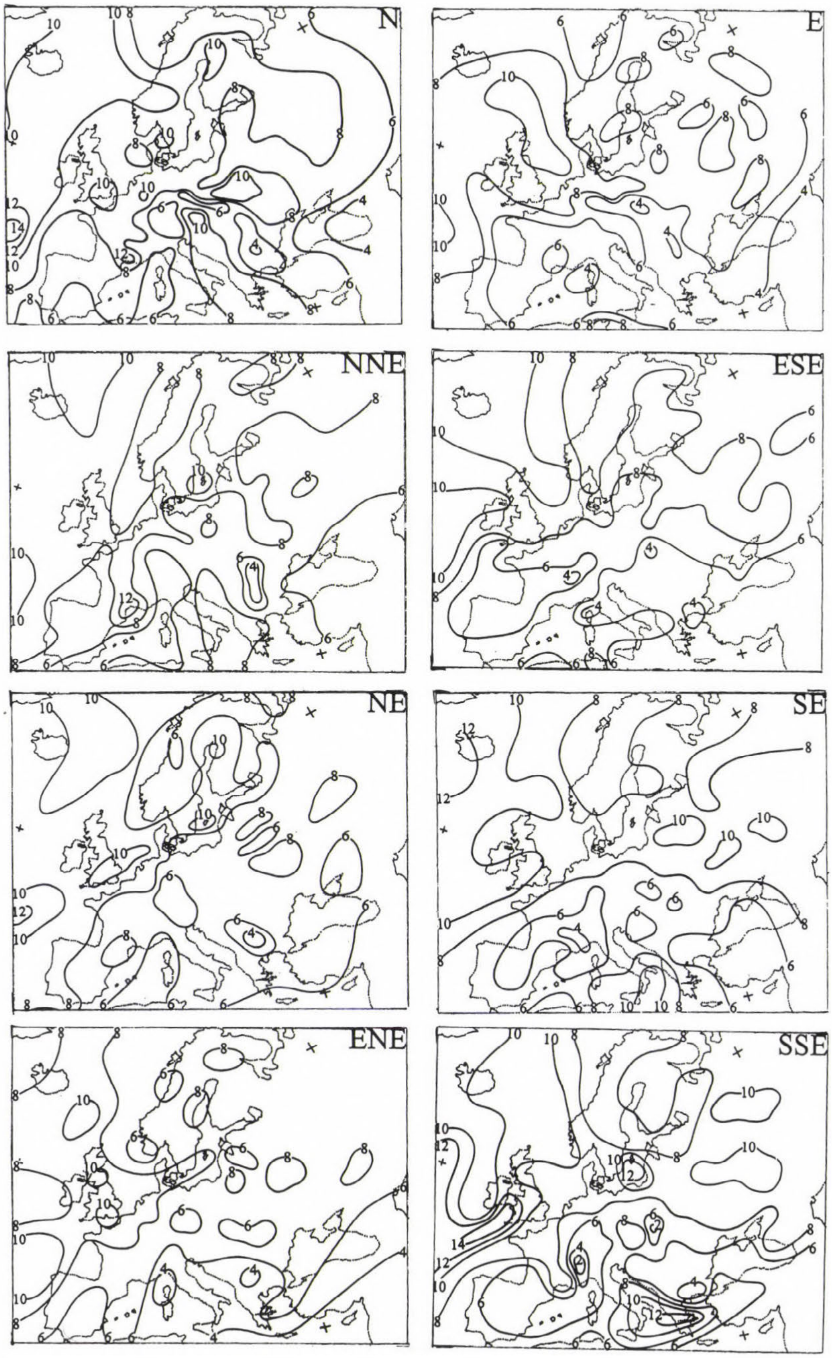

Fig. 3a. Yearly mean 850 hPa wind speed for directions N–SSE, in m sec^{-1}, (1980–1981).

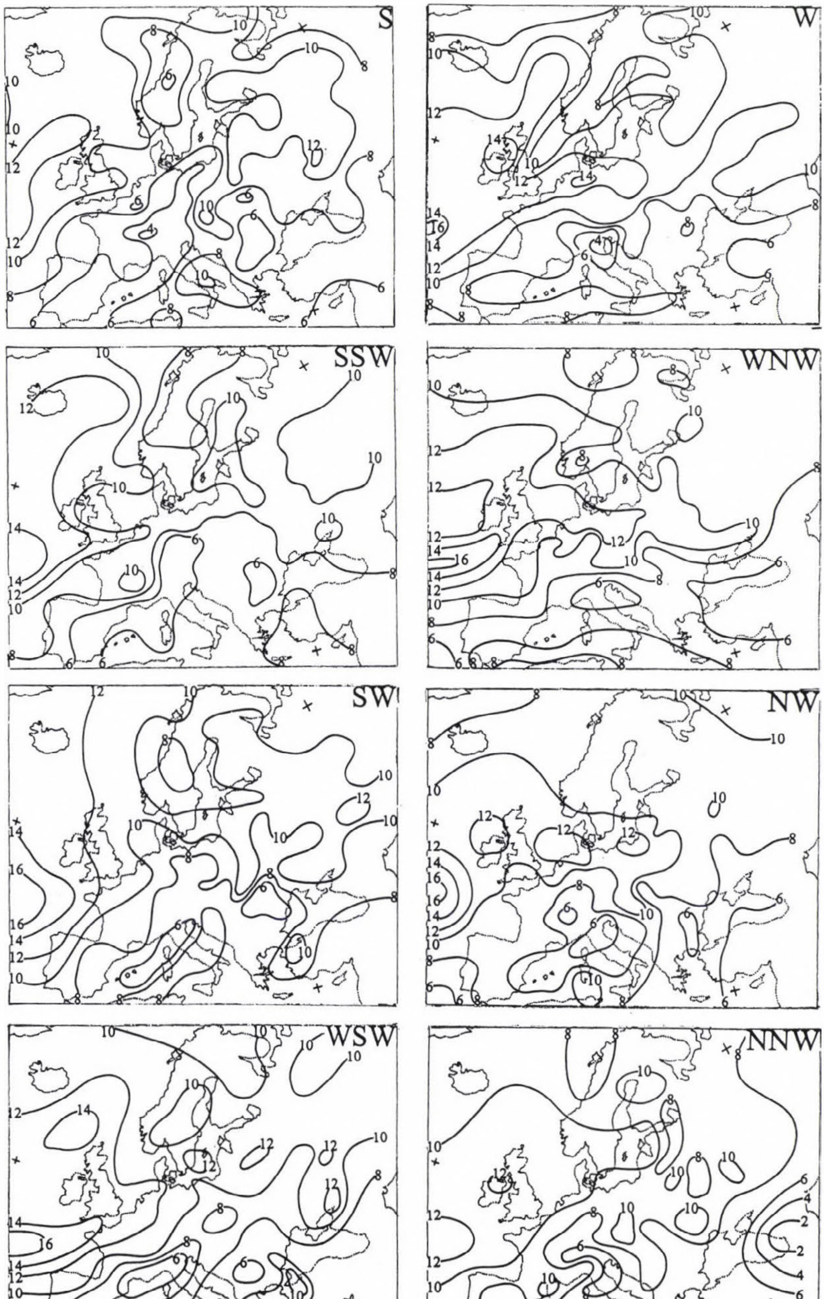

Fig. 3b. Yearly mean 850 hPa wind speed for directions S-NNW, in m sec^{-1}, (1980–1981).

Table 1. Relative frequency of wind direction at 850 hPa, in percent (available long series data)

Station	N	NNE	NE	ENE	E	ESE	SE	SSE	S	SSW	SW	WSW	W	WNW	NW	NNW
1	6.6	5.0	4.2	3.1	3.1	2.7	3.3	4.0	5.3	9.1	11.3	10.2	9.4	7.6	7.9	7.2
2	5.3	4.6	3.7	3.1	3.1	3.0	3.4	4.4	6.6	8.0	10.1	10.1	9.4	8.3	9.8	7.1
3	6.3	4.7	3.8	3.0	3.2	3.0	3.4	4.0	6.4	8.0	10.0	9.8	10.0	9.2	8.3	6.9
4	5.7	3.9	3.2	2.5	2.3	3.1	4.3	5.4	8.3	8.6	10.1	10.6	10.5	7.8	7.3	6.4
5	4.1	3.3	3.1	2.8	3.0	3.1	3.6	4.2	7.3	10.2	12.5	12.9	11.9	7.2	6.0	4.8
6	5.1	3.9	3.3	2.7	3.4	3.2	3.6	3.9	4.8	6.8	10.0	12.1	13.5	9.7	8.0	6 0
7	4.5	3.1	3.1	3.3	3.9	2.6	3.3	4.1	5.5	8.3	9.7	10.1	12.5	10.7	9.0	6.3
8	3.8	3.0	3.2	3.4	3.5	3.5	4.0	4.3	5.6	7.6	10.0	11.4	13.8	10.0	7.8	5.1
9	5.2	3.7	3.7	3.6	3.6	3.2	3.3	3.6	5.5	7.3	9.8	11.3	12.8	9.4	7.9	6.1
10	4.7	3.7	3.7	3.4	2.6	2.7	3.2	3.7	5.7	8.0	10.8	11.9	11.7	8.8	8.3	7.1
11	4.1	4.8	5.1	4.5	3.7	3.1	2.8	2.8	5.1	7.4	9.9	11.4	13.5	9.8	7.3	4.7
12	4.4	4.3	4.5	4.3	4.2	3.4	3.4	3.4	4.9	7.2	9.6	10.9	12.8	9.6	7.7	5.4
13	4.7	4.5	4.8	4.5	4.3	3.1	3.0	3.0	3.7	6.3	9.8	12.2	13.4	9.3	7.7	5.7
14	5.4	3.9	3.8	3.6	3.5	2.9	3.3	3.7	5.5	7.2	9.8	11.2	11.9	9.9	8.3	6.1
15	4.7	3.0	2.8	2.7	3.3	3.3	3.8	4.2	6.2	7.3	9.7	11.3	13.4	10.1	8.3	5.9
16	5.2	3.5	3.1	2.7	3.2	3.1	3.8	4.4	6.6	8.5	10.3	10.7	11 0	9.4	8.2	6.3
17	3.2	2.9	9.6	14.6	3.8	1.3	1.2	1.1	2.1	5.4	22.6	17.2	7.8	3.1	2.2	1.9
18	2.7	1.9	2.1	2.7	5.4	6.2	5.1	3.4	3.3	3.3	4.4	7.2	20.4	16.3	10.9	4.7
19	4.7	3.8	3.7	2.1	3.1	2.8	4.1	4.1	5.5	5.6	9.5	10.8	16.9	10.7	8.2	4.4
20	4.7	3.1	3.2	2.4	3.5	3.0	4.9	4.4	5.5	4.5	7.8	10.0	15.7	12.8	9.6	4.9
21	4.9	3.1	3.1	2.4	3.3	3.2	5.0	4.4	6.1	5.6	8.1	9.2	14.7	11.8	9.7	5.4
22	5.2	3.0	3.3	2.4	3.0	3.2	4.2	3.7	5.6	5.2	6.9	7.1	13.9	14.3	13.0	6 0
23	5.8	4.2	4.2	3.4	3.2	3.0	3.8	5.3	6.1	7.3	8.7	7.3	6.3	9.7	12.3	9.4
24	6.1	5.6	4.0	2.8	2.8	3.1	4.8	6.2	6.1	6.5	7.9	8.7	7.6	7.6	11.5	8.7

Table 2. Mean wind speed at 850 hPa, in m s^{-1} (available long series data)

Station	N	NNE	NE	ENE	E	ESE	SE	SSE	S	SSW	SW	WSW	W	WNW	NW	NNW
1	9.6	8.7	8.4	7.7	6.9	7.3	7.8	8.2	9.0	10.5	11.3	10.5	9.4	9.2	9.3	9.8
2	9.2	8.5	7.8	7.8	7.4	7.8	8.1	9.0	10.0	11.0	11.2	11.1	10.4	10.4	10.5	9.7
3	9.0	8.3	8.0	7.6	7.3	7.7	8.1	8.8	10.1	11.0	11.5	11.3	10.3	10.3	9.9	9.7
17	2.6	4.1	6.1	7.4	4.0	3.0	2.9	2.9	3.8	6.6	10.1	9.0	6.6	4.7	4.1	4.0
18	7.7	7.2	6.9	7.3	7.9	5.6	5.7	6.0	6.3	7.4	8.2	9.0	13.4	12.4	11.1	9.7
19	8.8	8.7	8.2	7.7	7.7	7.9	8.3	8.2	8.4	8.8	10.2	12.0	13.1	12.6	10.2	8.6
20	8.0	7.3	6.9	6.8	7.4	8.2	8.1	8.7	8.2	7.6	8.4	10.5	11.8	12.7	11.0	9.0
21	7.9	7.1	6.6	6.4	6.7	8.1	8.7	8.1	8.1	8.3	9.2	10.1	10.4	11.7	10.5	8.7
22	7.8	6.8	7.0	6.8	6.9	7.4	7.3	8.1	8.8	9.2	8.1	8.9	11.0	13.1	12.4	9.4
23	7.3	5.7	6.0	5.9	5.6	5.5	5.8	7.4	7.2	7.8	9.1	8.6	7.7	9.8	10.6	9.1
24	6.7	7.0	5.6	5.1	4.8	5.1	6.1	7.6	7.2	7.2	7.8	8.4	7.8	7.8	9.0	8.1

Table 3. Sources of data in Tables 1, 2 and 4

Station(s)	Source
1., 2. 3.	M. Lahti. Helsinki. Finland. 1996 COST 710 WG4
4. -16.	D. Thomson. Met.Office. 1996 COST 710 WG4
17.	Aschwanden A. et al.. 1996. Bereinigte Zeitreihen. Die Ergebnisse des Projekts KLIMA90. Band 1. Auswerungen. Klimatologie
18.	E. Dittman. 1996. DWD COST 710 WG4
19.-22.	Z. Lityinska. Legionowo. Poland. 1996 COST 710 WG4
23., 24.	D. Szepesi. 1996 COST 710 WG4

Table 4. Station numbers and WMO-codes with names of the upper air stations

Station number	WMO code	Country	Station name	φ-Coordinate	λ- Coordinate	Interval
1*	2836	Finland	Sodankyla	N 67°21'	E 26°39'	1961–1995
2*	2935	Finland	Jokioinen	N 60°48'	E 23°30'	1961–1995
3	2963	Finland	Jyvaskyla	N 62°23'	E 25°40'	1961–1995
4*	3005	UK	Lerwick**	N 60°06'	W 1°12'	1976–1993
5*	3026	UK	Stornowa**y	N 58°12'	W 6°18'	1976–1993
6*	3170	UK	Leuchars**	N 56°24'	W 2°54'	1976–1993
7	3213	UK	-**	N 54°18'	W 3°24'	1976–1984
8	3322	UK	Aughton**	N 53°36'	W 2°54'	1976–1987
9*	3496	UK	Hemsby**	N 52°42'	E 1°42'	1976–1987
10	3502	UK	Aberporth**	N 52°06'	W 4°36'	1976–1987
11	3693	UK	Shoeburyness**	N 51°36'	E 0°48'	1976–1987
12	3743	UK	Larkhill**	N 51°12'	W 1°48'	1976–1987
13*	3774	UK	Crawley**	N 51°06'	W 0°12'	1984–1992
14	3808	UK	Camborne**	N 50°12'	W 5°18'	1976–1987
15*	3920	UK	Hillsborough**	N 54°30'	W 6°06'	1976–1992
16*	3953	Ireland	Valentia**	N 51°54'	W 10°18'	1976–1987
17*	6610	Switzerland	Payern	N 46°48'	E 6°57'	1961–1990
18*	10866	Germany	München-Riem	N 48°07'	E 11°33'	1961–1990
19	12120	Poland	Leba	N 54°45'	E 17°31'	1971–1990
20*	12330	Poland	Poznan	N 52°24'	E 16°49'	1971–1990
21*	12374	Poland	Legionowo	N 52°09'	E 20°57'	1971–1990
22*	12425	Poland	Wroclaw	N 51°06'	E 16°52'	1971–1990
23*	12843	Hungary	Budapest	N 47°21'	E 19°11'	1962–1989
24*	12982	Hungary	Szeged	N 46°15'	E 20°06'	1962–1989

Note: * Station which appears in the analysis of both series
** Originally 12 directions transformed to 16 directions

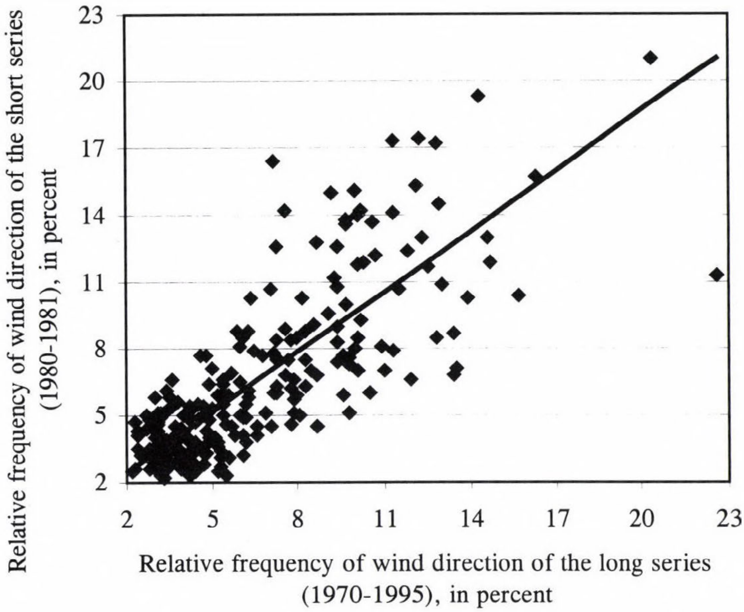

Fig. 4. Scatter diagram of wind direction.

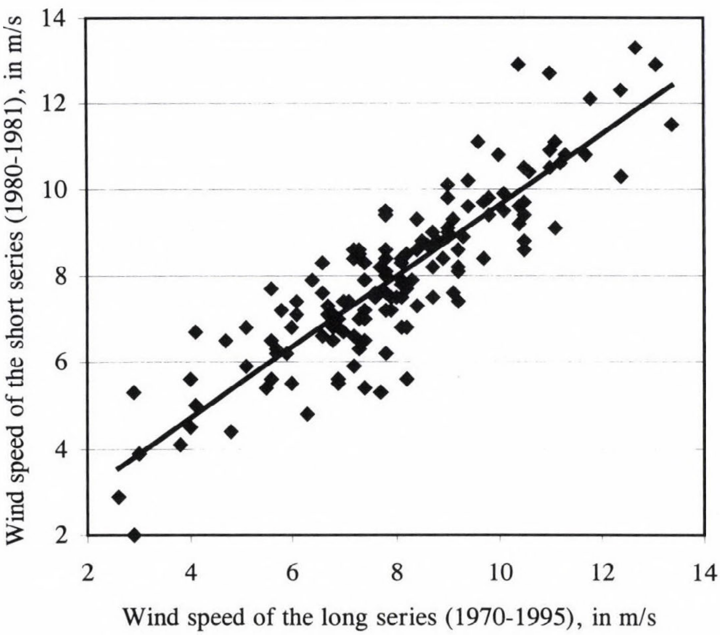

Fig. 5. Scatter diagram of wind speed.

Table 5. Statistics of wind direction

<table>
<tr><th>Statistics</th><th>Long series</th><th>Short series</th></tr>
<tr><td>RMS of the frequency of wind direction</td><td>3.54</td><td>3.98</td></tr>
<tr><td>Correlation</td><td colspan="2">0.80</td></tr>
<tr><td>Average</td><td>6.08</td><td>6.12</td></tr>
<tr><td>Covariance</td><td colspan="2">11.23</td></tr>
</table>

Table 6. Statistics of wind speed

<table>
<tr><th>Statistics</th><th>Long series</th><th>Short series</th></tr>
<tr><td>RMS of wind speed</td><td>2.11</td><td>1.97</td></tr>
<tr><td>Correlation</td><td colspan="2">0.88</td></tr>
<tr><td>Average</td><td>8.01</td><td>8.00</td></tr>
<tr><td>Covariance</td><td colspan="2">3.62</td></tr>
</table>

4. Follow-up work

To finalize this work it is necessary to involve the rest of the European countries in providing 10–30-year upper wind statistics. This program can be realized only after appearance of this paper and has to be based on the joint effort of more contributors. Recent experience in collecting data shows that 30-year series actually were cleaned and processed only after personal contact and request. This also reveals some of the benefits of such conventional approaches.

It is conceivable that authors in their analyses will be able to cope with orographic effects, in say, the Alps region, better than global climatological analyses do. This kind of regional scale wind atlas could be used as a starting point for further surface wind surveys. After completion of the geostrophic wind atlas, countries might construct regionally representative design surface wind charts for their territory (see *Szepesi et al.*, 1995 for Hungary). For environmental applications, the surface wind statistics at any site can be determined from these wind maps using a model correction (e.g., according to WAsP) for the effects of terrain, surface roughness and obstacles.

Acknowledgement—Critical remarks and careful editing of this paper by *David J. Thomson* of UK Meteorological Office, the former chairman of COST 710 project of the EC is gratefully appreciated.

References

Defant, A., 1920: *Windverhältnisse in Gebiete der ehemaligen Österr.-Ungar. Monarchie.* Anhang zum Jahrbuch der ZMG, Wien, *Neue Folge 57.*

Jensen, N.O, 1984: *Extrapolation of Mean Wind Statistics with Special Regards to Wind Energy Applications.* WCP-86, World Meteorological Organization, Geneva.

Landsberg, H.E., 1986: *World Surveys of Climatology.* Elsevier, Amsterdam.

Machta, L., 1979: *A Handbook to Estimate Climatological Concentration, Deposition and Horizontal Fluxes of Pollutants on a Regional Scale.* MARC Tech. Report 11, UNEP, Chelsea College, Univ. of London.

Meteorological Office, 1950: *Upper Winds over the World.* Geophysical Memoirs 85, London.

Peixoto, J.P. and *Oort, A.H.*, 1992: *Physics of Climate.* American Inst. of Physics.

Szepesi, D.J. and *Fekete, K.E*, 1993: *Design Wind Maps for Hungary* (in Hungarian), *Meteorológiai Tudományos Napok,* MTA Budapest.

Szepesi, D.J. and *Fekete, K.E.*, 1996: Inquiry on meteorological data pre-processing for complex terrain dispersion modelling: A european reference Benchmark exercise. *4th Workshop on Harmonization within Atm. Disp. Modelling for Regulatory Purposes.* May 1996, Ostende. Preprint.

Szepesi, D.J., *Fekete, K.E.* and *Gyenes, L.*, 1995: Regulatory models for environmental impact assessment *in* Hungary. *Int. J. Environment and Pollution* 5, 497-507.

Taylor, P., 1997: Personal communication.

Troen, I., *Mortensen, N.G.* and *Petersen E.L.*, 1988: *Wind Atlas Analysis and Application Program.* National *Laboratory* Riso, Denmark.

Wilfried Schröder (editor): **Long and Short Term Variability in Sun's History and Global Change**. Science Edition, D-28777 Bremen-Roennebeck, 2000, 63 pages. Price: $20.

This book is the printed version of the 26 lectures presented during the IUGG (International Union of Geodesy and Geophysics) last General Assembly Meeting (1999, Birmingham, UK) by the members of the Interdivisional Commission on History (IDCH) of IAGA. Like such collections, the papers cover very different topics. However, most of them deal with the connection of solar phaenomenae and the Earth's climate. The investigation of this connection has long history. The recent results suggest a connection of about 20 years cycle, that is the magnetism might have some role. It is also interesting, that the terrestrial and solar atmospheres have some common features.

I think this book is very useful for those scientists and students who are interested in history of solar physics, geophysics and meteorology.

G. Major

Wilfried Schröder (editor): **Geschichte und Philosophie der Geophysik (History and Philosophy of Geophysics)** Science Edition, D-28777 Bremen-Roennebeck, 2000, 219 pages. Price: $30.

The material found in this book has already been published in *Beträge zur Geschichte der Geophysik und Kosmische Physik,* Band 2/2000 and at the same time in *IAGA IDC History Newsletter* No. 42. Most of it is written in German, the rest in English.

The title suggests that this is a complex study of every aspects of the geophysics, but the reader founds that it is wider, it relates to all geosciences. For example on page 40 the list contains the scientific journals founded before 1896 (the first year is 1665). From the 24 items exactly the half belongs to the discipline nowadays called meteorology. It has to be noted that IDŐJÁRÁS was founded in 1897 and since then it has been published continuously.

After the introduction and preface, the next 100 pages have bee written jointly by *Wilfried Schröder* and *Herbert Hörz*. Their work is a systematic study of all scientific aspects of geophysics/geosciences. The main value of this part is the opinion and evaluation of the authors expressed on the history, the methods and data of geophysics. The last 100 pages contain 9 papers from different authors mostly on special partial historical events. There are two exceptions: the first one deals with the scientific and practical use of history of geophysics in general, the last one is "an approximately complete list" of geophysical teaching books appeared between 1912 and 1998, it contains nearly 400 items.

It is suggested to all geoscientists stop for a small time in their rush and read this book and think on our loved disciplines.

G. Major

ATMOSPHERIC ENVIRONMENT

an international journal

To promote the distribution of Atmospheric Environment *Időjárás* publishes regularly the contents of this important journal. For further information the interested reader is asked to contact *Prof. P. Brimblecombe*, School for Environmental Sciences, University of East Anglia,
Norwich NR4 7TJ, U.K.; E-mail: atmos_env@uea.ac.uk

Volume 34 Number 6 2000

Volume 34 Number 7 2000

Volume 34 Number 8 2000

Volume 34 Number 9 2000

Volume 34 Number 10 2000

NOTES TO CONTRIBUTORS OF *IDŐJÁRÁS*

The purpose of the journal is to publish papers in any field of meteorology and atmosphere related scientific areas. These may be

- reports on new results of scientific investigations,
- critical review articles summarizing current state of art of a certain topic,
- shorter contributions dealing with a particular question.

Each issue contains "News" and "Book review" sections.

Authors may be of any nationality, but the official language of the journal is English. Papers will be reviewed by unidentified referees.

Manuscripts should be sent to
Editor-in-Chief of IDŐJÁRÁS
P.O. Box 39
H-1675 Budapest, Hungary

in three copies including all illustrations. One set of illustrations has to be of camera ready quality, the other two might be lower quality.

Title part of the paper should contain the concise title, the name(s) of the author(s), the affiliation(s) including postal and E-mail address(es). In case of multiple authors, the cover letter should indicate the corresponding author.

Abstract should follow the title, it contains the purpose, the data and methods as well as the basic conclusion.

Key-words are necessary to help to classify the topic.

The text has to be typed in double spacing with wide margins. Word-processor printing is preferred. The use of SI units are expected. The negative exponent is preferred to solidus. Figures and tables should be consecutively numbered and referred to in the text.

Mathematical formulas are expected to be as simple as possible and numbered in parentheses at the right margin. Non-Latin letters and hand-written symbols should be indicated and explained by making marginal notes in pencil.

Tables should be marked by Arabic numbers and printed in separate sheets together with their captions. Avoid too lengthy or complicated tables.

Figures should be drawn or printed in black and white, without legends, on separate sheets. The legends of figures should be printed as separate list. Good quality laser printings are preferred as master copies.

References: The text citation should contain the name(s) of the author(s) in Italic letter and the year of publication. In case of one author: *Miller* (1989), or if the name of the author cannot be fitted into the text: *(Miller,* 1989); in the case of two authors: *Gamov* and *Cleveland* (1973); if there are more than two authors: *Smith et al.* (1990). When referring to several papers published in the same year by the same author, the year of publication should be followed by letters a,b etc. At the end of the paper the list of references should be arranged alphabetically. For an article: the name(s) of author(s) in Italics, year, title of article, name of journal, volume number (the latter two in Italics) and pages. E.g. *Nathan, K.K.,* 1986: A note on the relationship between photosynthetically active radiation and cloud amount. *Időjárás 90*, 10-13. For a book: the name(s) of author(s), year, title of the book (all in Italics except the year), publisher and place of publication. E.g. *Junge, C. E.,* 1963: *Air Chemistry and Radioactivity*. Academic Press, New York and London.

The final version should be submitted on diskette altogether with one hard copy. Use standard 3.5" or 5.25" DOS formatted diskettes. The preferred word-processors are WordPerfect 5.1 and MS Word 6.0.

Reprints: authors receive 30 reprints free of charge. Additional reprints may be ordered at the authors' expense when sending back the proofs to the Editorial Office.

More information: gmajor@met.hu
Information on the last issues:
http://www.met.hu/firat/ido-e.html

Published by the Hungarian Meteorological Service

Budapest, Hungary

INDEX: 26 361

HU ISSN 0324-6329

IDŐJÁRÁS

QUARTERLY JOURNAL
OF THE HUNGARIAN METEOROLOGICAL SERVICE

CONTENTS

****

http://www.met.hu/firat/ido-e.html

VOL. 104 * NO. 4 * OCTOBER–DECEMBER 2000

IDŐJÁRÁS

Quarterly Journal of the Hungarian Meteorological Service

Editor-in-Chief
T. PRÁGER

Executive Editor
M. ANTAL

EDITORIAL BOARD

AMBRÓZY, P. (Budapest, Hungary)
ANTAL, E. (Budapest, Hungary)
BARTHOLY, J. (Budapest, Hungary)
BOZÓ, L. (Budapest, Hungary)
BRIMBLECOMBE, P. (Norwich, U.K.)
CZELNAI, R. (Budapest, Hungary)
DÉVÉNYI, D. (Budapest, Hungary)
DUNKEL, Z. (Brussels, Belgium)
FISHER, B. (Chatham, U.K.)
GELEYN, J.-Fr. (Toulouse, France)
GERESDI, I. (Pécs, Hungary)
GÖTZ, G. (Budapest, Hungary)
HANTEL, M. (Vienna, Austria)
HASZPRA, L. (Budapest, Hungary)
HORÁNYI, A. (Budapest, Hungary)
HORVÁTH, Á. (Siófok, Hungary)
IVÁNYI, Z. (Budapest, Hungary)
KONDRATYEV, K.Ya. (St. Petersburg, Russia)
MAJOR, G. (Budapest, Hungary)
MÉSZÁROS, E. (Veszprém, Hungary)
MIKA, J. (Budapest, Hungary)
MARACCHI, G. (Firenze, Italy)
MERSICH, I. (Budapest, Hungary)
MÖLLER, D. (Berlin, Germany)
NEUWIRTH, F. (Vienna, Austria)
PINTO, J. (R. Triangle Park, NC, U.S.A)
PROBÁLD, F. (Budapest, Hungary)
RENOUX, A. (Paris-Créteil, France)
ROCHARD, G. (Lannion, France)
S. BURÁNSZKY, M. (Budapest, Hungary)
SPÄNKUCH, D. (Potsdam, Germany)
STAROSOLSZKY, Ö. (Budapest, Hungary)
SZALAI, S. (Budapest, Hungary)
SZEPESI, D. (Budapest, Hungary)
TAR, K. (Debrecen, Hungary)
TÄNCZER, T. (Budapest, Hungary)
VALI, G. (Laramie, WY, U.S.A.)
VARGA-HASZONITS, Z. (Mosonmagyaróvár, Hungary)

Editorial Office: *P.O. Box 39, H-1675 Budapest, Hungary* or
Gilice tér 39, H-1181 Budapest, Hungary
E-mail: prager@met.hu or *antal@met.hu*
Fax: (36-1) 290-7387

Subscription by

mail: IDŐJÁRÁS, P.O. Box 39, H-1675 Budapest, Hungary;
E-mail: prager@met.hu or *antal@met.hu*; *Fax: (36-1) 290-7387*

IDŐJÁRÁS

Quarterly Journal of the Hungarian Meteorological Service
Vol. 104, No.4, October–December 2000, pp. 219–239

The application of ALADIN model for storm warning purposes at Lake Balaton

Imre Bartha[1], **András Horányi**[2] and **István Ihász**[2]

[1]*Hungarian Meteorological Service, Storm Warning Observatory, Vitorlás u. 17, H-8600 Siófok, Hungary; E-mail: bartha.i@met.hu*

[2]*Hungarian Meteorological Service, P.O. Box 38, H-1525 Budapest, Hungary; E-mail: horanyi.a@met.hu; ihasz.i@met.hu*

(Manuscript submitted for publication 20 January 2000; in final form 8 May 2000)

Abstract—Strong and stormy winds are the most dangerous weather phenomena in the resort region of Lake Balaton, and that is why the weather warnings are of great importance for the protection of life and property. In summer the wind storms breaking out suddenly in the area of Lake Balaton are generally associated with thunderstorms.

In wind forecasting, one of the most difficult tasks is to predict the degree of wind strengthening associated with thunderstorms, as it may vary according to the synoptic situation. This paper studies how correct and useful information is available in the products of the limited area numerical weather prediction model ALADIN for forecasting the spatial and temporal intensity of organised convection using an interactive nowcasting decision-making procedure. The procedure provides a more objective foundation for storm warnings at Lake Balaton. The obtained results are completed by the statistical investigation for the application of meteograms to the storm warning practice.

Key-words: very short range forecast, nowcasting, storm warning, decision-making procedure, limited area numerical weather prediction model, parameterization of organised convection, meteogram.

1. Introduction

Strong and stormy winds are the most dangerous weather phenomena in the resort region of Lake Balaton. In summer the wind storms breaking out suddenly in the area of the lake are generally associated with thunderstorms, that is why the weather warnings are of great importance for the protection of life and property. The Storm Warning Observatory (SWO) at Lake Balaton of the Hungarian Meteorological Service (HMS) was founded with the aim of providing such warnings. In the high season the holidaymakers, sailors and surf-riders require

(1) information on the present weather situation,
(2) a very short range forecast valid for max. 12 hours and
(3) warnings with the help of the National Directorate General for Disaster Management of Ministry of the Interior 1–2 hours ahead of expected wind gusts [V(max)] exceeding 12 or 17 m s^{-1}.

In order to solve the 2nd and the 3rd tasks complying with the requirements, we need a correct very short range forecasting model. On the basis of our experiences, the limited area model (LAM) ALADIN is a good candidate for the precise forecasting of the intensity and period of instability connected to convective activity.

2. *Application of ALADIN products at SWO of HMS*

The HMS has been taking part in the ALADIN international collaboration initiated by Météo France since 1991. The result of this collaboration is the limited area spectral hydrostatic numerical weather prediction model ARPEGE/ALADIN (*Horányi et al.,* 1996), which is used operationally at the Hungarian Meteorological Service. The ALADIN/LACE version of the model is operationally exploited in Prague (for a domain over continental Europe) providing not only forecasting products but also initial and lateral boundary conditions for the workstation version of ALADIN (called ALADIN/HU, which covers a domain over the Carpathian Basin). At the time of the experiments the resolution of the ALADIN/LACE and ALADIN/HU models were 14.7 km and 11 km, respectively. The products of the ALADIN/LACE regional and ALADIN/HU local models are available for the forecasters through the HAWK (Hungarian Advanced WorKstation) visualization system developed by US–Hungarian co-operation (*Horváth et al.,* 1998).

The storm forecast obviously utilizes shorter range forecast (valid for max. 12 hours) due to its nowcasting character. In this field, the possible further application of ALADIN products opened a new perspective with respect to the dangerous quickly evolving small scale weather systems (*Banciu* and *Geleyn,* 1998).

In wind forecasting, one of the most difficult tasks is to predict the degree of wind strengthening associated with thunderstorm, as it may vary according to the synoptic situation. It is known by storm forecasting experience that the summer wind storms breaking out suddenly in the region of Lake Balaton are generally associated with thunderstorms. That is why during the 1980s (*Bartha,* 1987) and later in the 1990s (*Bartha et al.,* 1998) an interactive decision-making procedure *(Fig. 1)* was developed in order to estimate which wind category the maximum wind gusts [V(max) in units of m s^{-1}] belong to. The categories are the following: no warning [D(0): V(max) <12 m s^{-1}], alert [D(1) a: 12 m $s^{-1} \leq$ V(max) $\leq$ 17 m s^{-1}] and storm warning [D(2): V(max)$>$ 17 m s^{-1}].

In Fig. 1 it can be seen that the very short range forecast for the region of Lake Balaton serves as a basis for decision-making on storm warning. The method combines the conventional data with the approach of using radar information. During the decision-making procedure as a monitoring, we use a simple parameter, the so-called cooling rate (ΔT). This monitoring procedure is based on the idea that there is a close relationship between the temperature decrease (ΔT) induced by downdraft and the maximum wind velocity at the surface in non-frontal thunderstorms (*Fawbush* and *Miller,* 1954). We have used the recent improvements of the convection parameterization scheme of ARPEGE/ALADIN in order to investigate the capability of the model for describing the spatial and temporal intensity of convective activity. This evaluation helps to decide how the results of the ALADIN model can be used as input data for the nowcasting decision-making procedure (*Bartha,* 1998).

3. Experiments and data sets

3.1. Experiments

The most important parts of our present investigations are

(1) to asses the impact of the most recent modifications of the convection parameterization scheme for ALADIN based on *Bougeault* (1985), i.e.,

- introduction of downdraft parameterization, based on *Ducrocq* and *Bougeault* (1995) — see *Banciu* and *Geleyn* (1998),
- momentum parameterization, based on *Kershaw* and *Gregory* (1997) as well as *Gregory et al.* (1997) implemented by *Gerard* (1998),
- limitation of humidity convergence by subtracting stratiform precipitation for the available humidity of convection scheme,
- tuning of some free parameters of the convection scheme,

in order to obtain a realistic description for the intensity of organised convection in space and time;

(2) to study how correct information is available in ALADIN/HU meteograms for two local points of Lake Balaton in comparison to the real data during the selected unstable weather conditions.

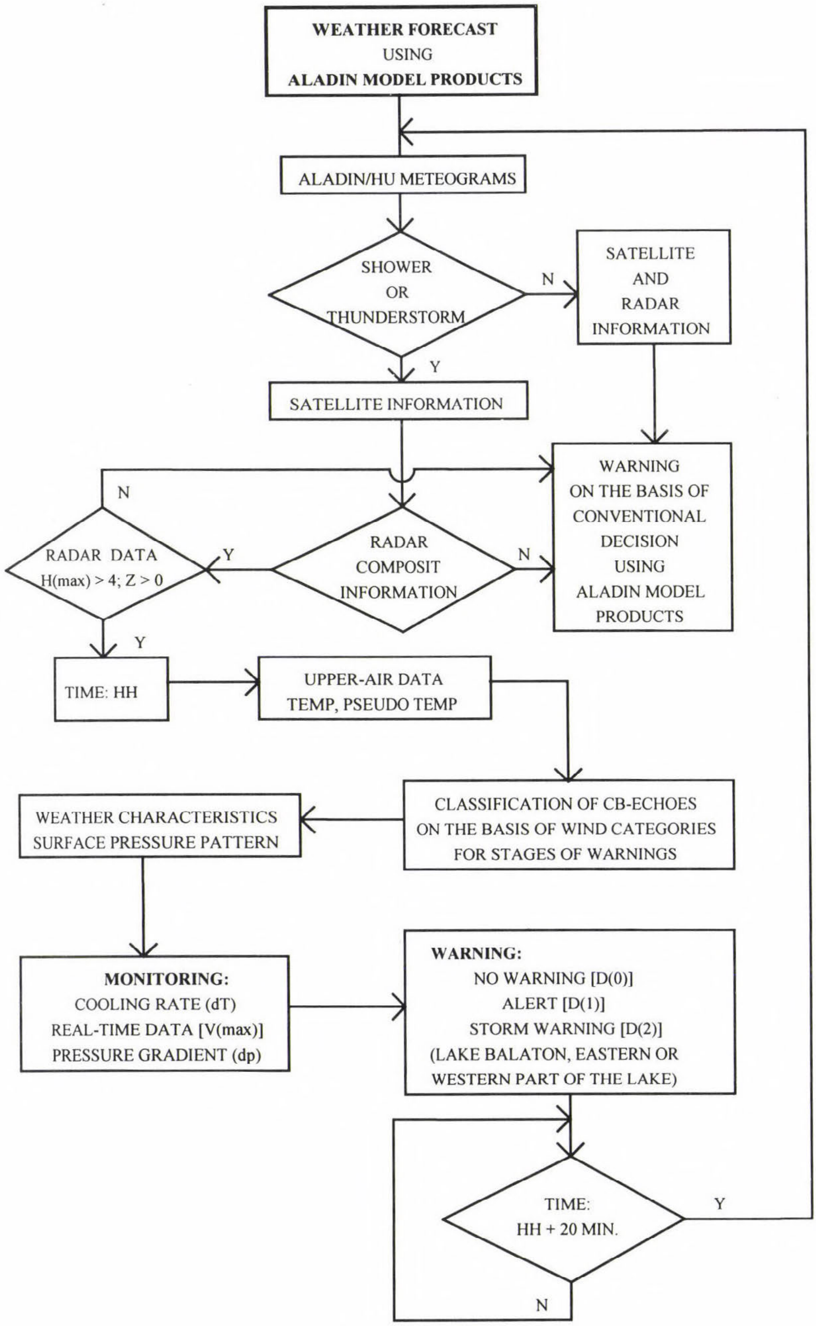

Fig. 1. Nowcasting decision-making procedure using ALADIN products for forecasting the maximum wind gusts associated with thunderstorms.

3.2. Data sets

In order to solve the above mentioned tasks, some active cold fronts associated with thunderstorms (6 cases) and convective systems [local thunderstorm situations (2 cases), convergence zones (5 cases), squall lines (2 cases)] were studied over the western part of Hungary (*Table 1*). These wind–hazardous weather situations were collected in 1998 during the period from May to August.

Table 1. Thunderstorm-hazardous weather situations in the western part of Hungary collected in 1998 during the period from May to August (the squall line cases studied are in bold face)

Date	Period (UTC)	Phenomenon
May 13	12 – 15	convergence zone
May 21	12 – 18	convergence zone
May 29	12 – 18	local thunderstorms
June 01	09 – 15	weak cold front associated with thunderstorms
June 03	15 – 21	convergence zone
June 08	12 – 21	cold front associated with thunderstorms
June 22	**09 – 18**	**squall line and cold front**
June 28	12 – 21	cold front associated with thunderstorms
June 30	15 – 21	convergence zone
July 27-28	**21 – 03**	**squall line and cold front**
July 28	06 – 15	cold front associated with thunderstorms
July 31–August 01	21 – 01	convergence zone
August 05	00 – 09	cold front associated with thunderstorms
August 19	06 – 12	local thunderstorms
August 19	15 – 21	cold front associated with thunderstorms

The following data were used for the investigations:

- hourly (in some cases every quarter of an hour) composite radar pictures from the detection region of Hungary, where the radar is of MRL–5 type and worked on the wavelength of 10 or 3 cm producing information for square elements of 2×2 km^2;
- observed data for Cu- or Cb-clouds (SYNOP code: C_L=2, 3 or 9) and some significant convective weather phenomena (shower, thunderstorm, hailstorm, wind gust connected with Cb-clouds of 7 m s^{-1} or stronger) of 3 principal synoptic stations and 8 automatic meteorological stations transmitting real-time wind information around Lake Balaton;
- three hourly surface meso-synoptic and twelve hourly high level (850, 700 and 500 hPa) operational charts analysing the development and movement of frontal and convective systems over the region of West Hungary;

- vertical profiles in traditional emagram form for the two selected squall line cases;
- ALADIN/LACE pseudo–TEMP messages visualised in time cross-sections for two stations (Siófok and Keszthely) of local interest;
- ALADIN/HU meteograms for two stations (Siófok, Keszthely) of local interest;
- output results (e.g., forecasting charts on various pressure levels with hourly frequency, like vertical velocity at 700 hPa level, 10m wind velocity, 2m temperature, the amount of precipitation, etc.) of the experimental version of the ALADIN model.

4. Results and discussion

We used the above described modifications of the convection scheme (see paragraph 3.1) trying to tune the free parameters of the scheme in order to obtain a better agreement with the observed evolution (in space and time) of the squall lines. For the experimental version of ALADIN/HU, we adopted a bit finer resolution than the operational resolution ($\Delta x = 11$ km) of ALADIN/HU model having 10 km horizontal resolution with 27 vertical levels. The domain (*Fig. 2*) remained, as it is for the operational version and some results were visualized for a zoomed area over Hungary. The forecast base was 00 UTC in the first case and it was 12 UTC in the second case. The maximum forecasting time was +18 hours and the post-processing step was 1 hour.

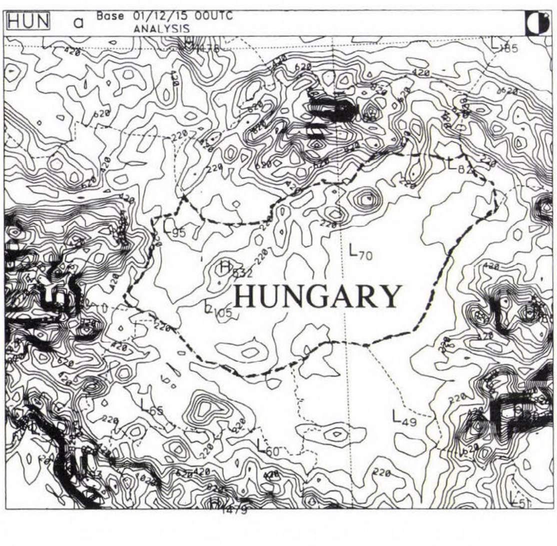

Fig. 2. ALADIN/HU operational domain over the Carpathian Basin with the model orography (unit in meter).

4.1.1 The first case—synoptic situation and associated weather feature

For the purpose of this experiment a rather strong squall line case was selected which developed ahead of a cold front on June 22, 1998. We intentionally chose this interesting case as a first one because it developed very suddenly within one hour and it was limited to a small territory. Sharp squall lines can be forecasted by the other models (e.g., DWD or ECMWF models), too.

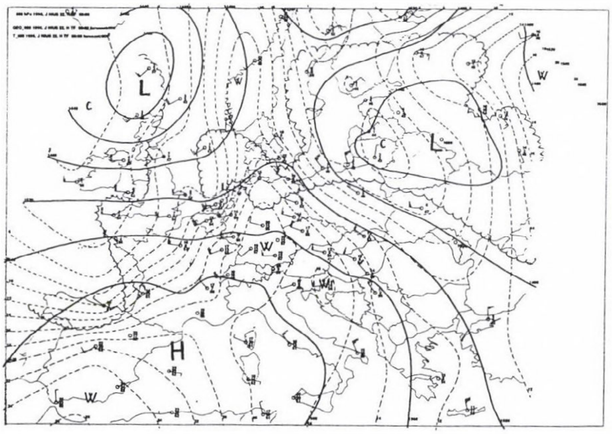

Fig. 3a. HMS analyses of geopotential (solid lines in gpdam) and temperature (dashed lines in °C) at 850 hPa for 00 UTC June 22, 1998 (Legends: L=low, H=high, w=warm, c=cold).

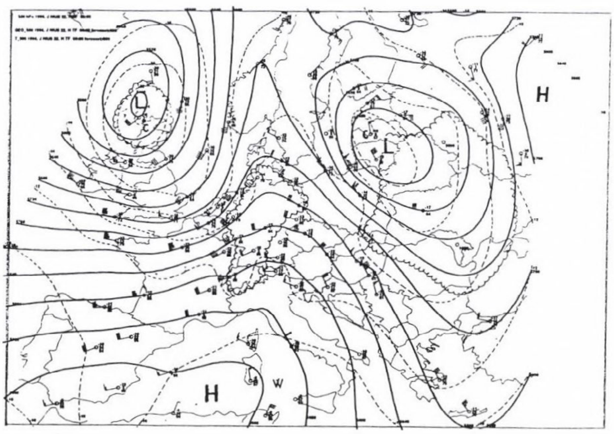

Fig. 3b. HMS analyses of geopotential (solid lines in gpdam) and temperature (dashed lines in °C) at 500 hPa for 00 UTC June 22, 1998 (Legends: L=low, H=high, w=warm, c=cold).

According to the large scale synoptic situation, a cold front reached the line of Hamburg–Frankfurt–Marseille by 00 UTC and ahead of it on the higher levels (*Fig. 3a,b*) very warm, relatively humid and unstable air accumulated over Central and Southern Europe. A radiosonde ascent from Vienna also verified this fact at 00 UTC. Later, on the basis of surface meso-analyses (*Fig. 4a)*, this cold front stopped in Austria near the western border of Hungary. At 12 UTC, a squall line erupting very intensive thunderstorms could be analysed (Fig. 4a). In this situation identifying the first weak radar echoes at 10:30 UTC, the storm warning service ordered warnings [in Fig. 1: D(2)] around Lake Balaton. One hour later severe thunderstorms occurred with hailstones in the western part of the lake and the maximum wind gusts exceeded 22 m s^{-1}. In the mean time, the squall line moved southward at a speed of about 35 km h^{-1} and therefore became more dangerous. According to the radar measurements, the maximum reflectivity factor changed from 20–30 dBZ to maximum 62,5 dBZ and the top of radar echoes reached 11–13 km within half an hour (*Fig. 4b*). Later the cold front system accelerated and merged into the squall line at about 15 UTC.

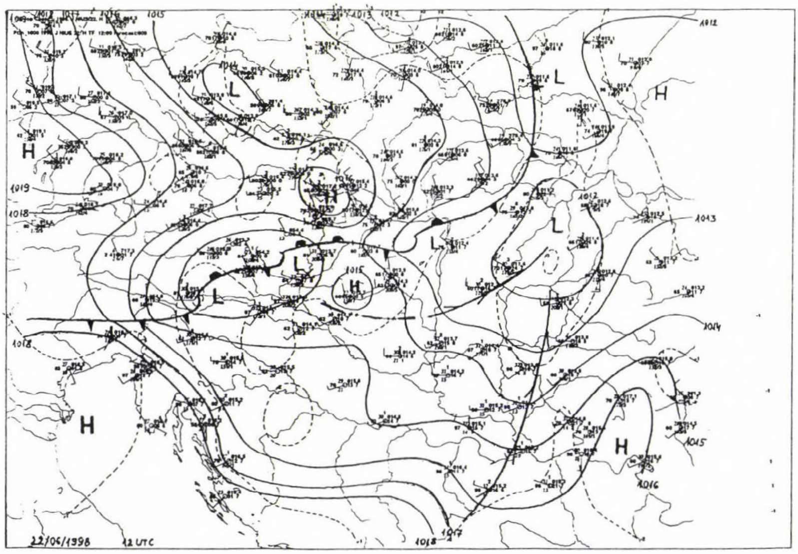

Fig. 4a. HMS meso-analyses for the msl-pressure (hPa) at 12 UTC on June 22, 1998
(Legends: H = High, L = Low)

The squall line caused huge damages in buildings, trees, etc., on the lake-shore and on the lake. Far from the lake, to S-SW of it, about 4–5 villages were flooded with muddy water causing damages in the buildings, gardens and the roads. In these areas, the maximum amount of precipitation was 82 mm, whilst the average monthly amount is 75 mm.

On the basis of the above-mentioned traditional synoptic data sources at 00 UTC, we managed to forecast the maximum air temperature, the thunderstorms, the wind strengthening and the change of wind direction by afternoon in the region of Lake Balaton, but naturally we could not forecast the exact time and place of thunderstorm eruptions.

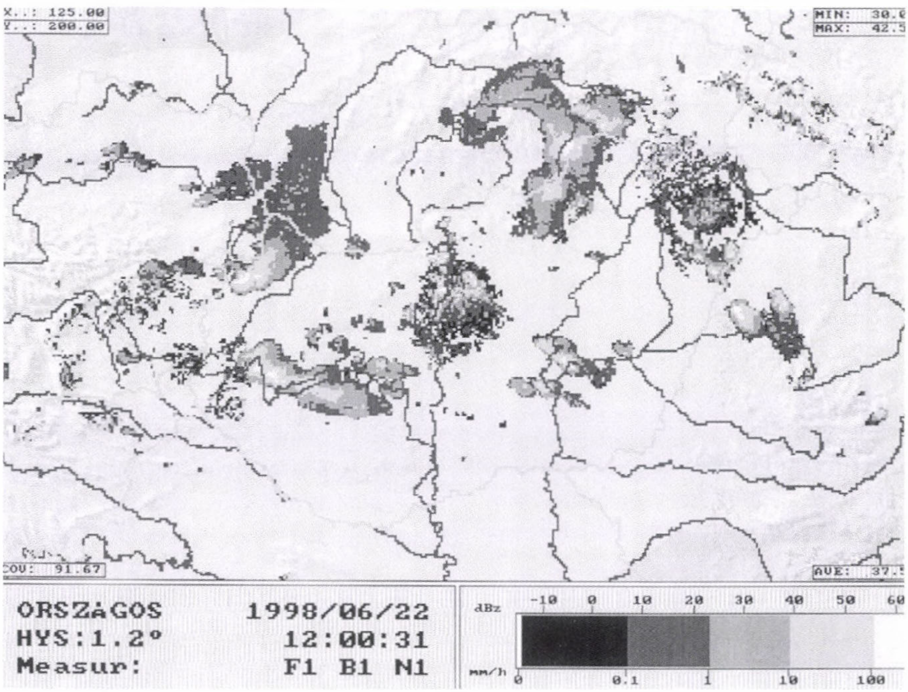

Fig. 4b. HMS composite weather radar image (reflectivity in dBZ) at 12 UTC on June 22, 1998 over the Carpathian Basin.

4.1.2 The first case—impact of the modification of parameterization for convection

This section reports on the results of the simulation for the first selected squall line case. Six experiments (identified as SH10, SH11, SH12, SH13, SH14 and SH15) were carried out to test the ALADIN model's sensitivity regarding the parameterization among the six ones. Only the best version is shown. The results were compared to the observations considering the intensity and position of the squall line.

Parameters used for experiments as it appeared in the ALADIN model:

❶ The threshold level (in Pa), above it the horizontal diffusion was enhanced.
❷ Logical switch to activate the subtraction of large scale precipitation from the humidity convergence available for the convection scheme.
❸ Logical parameter to switch on the parameterization of downdraft.
❹ Logical parameter for evaporation convection under the cloud basis.
❺ Coefficient of pressure gradient for *Kershaw* and *Gregory* parameterization—the reasonable thresholds for this coefficient were still not finally defined at the time of the experiments.
❻ Entrainment rate at the cloud basis.
❼ Downdraft parameter—the fraction of precipitation evaporated to produce the downdraft.

The best experiment with parameter tuning:

Experiment	❶	❷	❸	❹	❺	❻	❼
SH15	0.0	NO	NO	YES	< 1	0.4E-4	0.25

Experiment SH15 (which is basically the operational version, except the value of the first parameter) without downdraft, was proved to be the best. The development of the convergence zone and later gust front is simulated well enough by 10m wind (m s^{-1}) distribution (*Fig. 5a*) in comparison to the real radar measurements (Fig. 4b) and surface meso analyses (Fig. 4a). In Fig. 5a it can be seen that the wind changed from SW to NW behind the line and increased in a small degree. The gust front separates from the cold front system and progresses parallel with the cold front. The distribution of vertical velocity (Pa s^{-1}) also shows the two systems but the core of upward motions are stronger along the cold front than along the convergence line (*Fig. 5b*).

The cooling (not shown) behind the squall line is also simulated but there was an unrealistically big difference between the 2m air temperature and the surface water temperature of Lake Balaton. At that time (at 12 UTC on the June 22) the real water temperature was 23°C (at 1 m depth below the water surface) vs. the simulated surface water temperature value of 17°C.

On the basis of the six experiments it seems that the model is not very sensitive to the tuning of the free parameters of the scheme in this selected squall line case. It was also noticed that the modifications of the convection scheme led to a noisy vertical velocity field in the northern part of the ALADIN/HU operational domain.

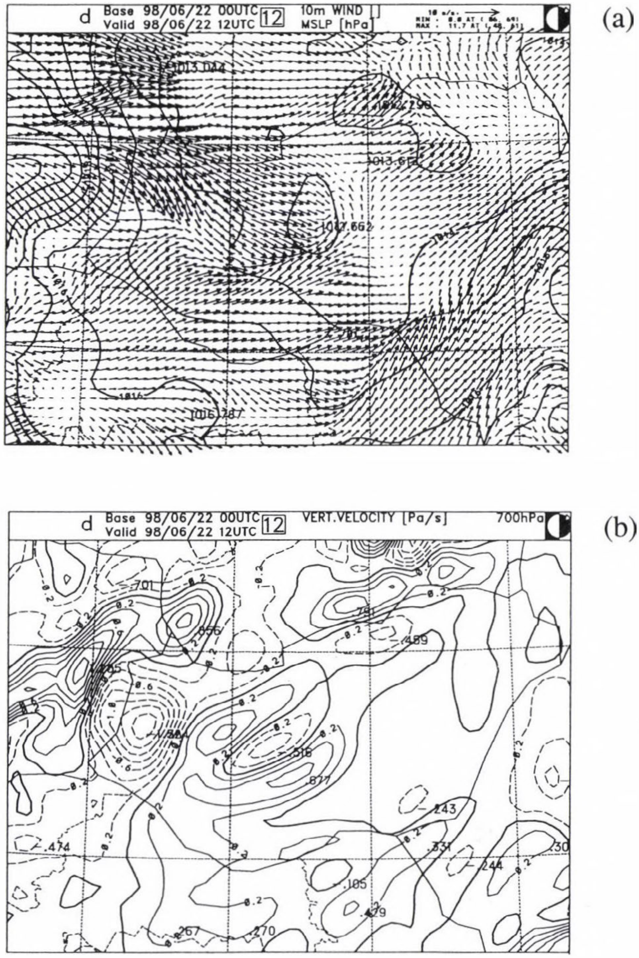

Fig. 5. Distribution in space and time (at 12 UTC) for 10m wind (m s^{-1}) together with the msl-pressure field (*a*) and for vertical velocity (Pa s^{-1}) at 700 hPa (*b*), simulated by ALADIN model experiments SH15 for June 22, 1998.

4.2.1 The second case – synoptic situation and associated weather feature

A shallow cyclone weather situation took place over West Europe between 0 and 10 degrees of longitude at 00 UTC on the operational surface chart (not shown) in the line of Edinburgh–London–Nantes–La Coruna. 12 hours later a fairly warm, relatively humid and unstable air-mass reached the western part of the Alps on the higher levels (*Fig. 6a,b*) ahead of the cold front. A radiosonde ascent from Zagreb also verified this unstable stratification near

Hungary at 12 UTC. In the mean time, the cold front moved towards east and reached the line of Wroclaw–Vienna–Klagenfurt at 21 UTC. Later the cold front reached the eastern part of the Alps where it stopped, and a warm wave occurred along the northern part of the frontal zone *(Fig. 7a)*. Ahead of this zone, a quick squall line began to evolve near the western border of Hungary along the line of Szentgotthárd–Nagykanizsa and moved from SW to NE direction nearly parallel with the stopping cold front. The amount of precipitation was between 1 and 7 mm in the region of Lake Balaton. Large amount of precipitation was measured along the frontal zone in the northern part of Hungary. The maximum wind gust associated with thunderstorms was only 15 m s^{-1} around Lake Balaton. The cold front zone merging in the squall line left the western part of Hungary after 03 UTC.

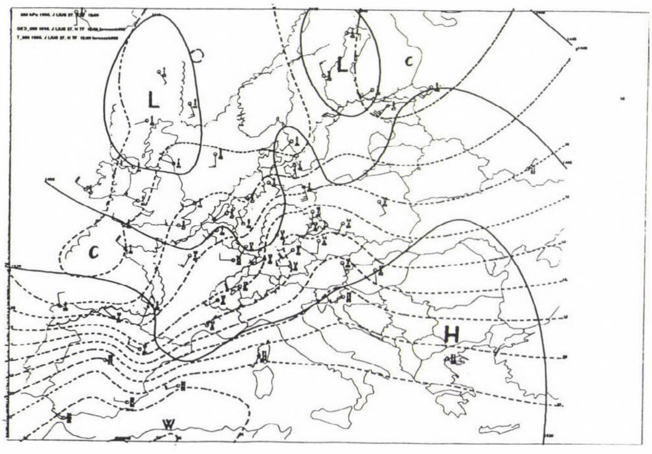

Fig. 6a. HMS analyses of geopotential (solid lines in gpdam) and temperature (dashed lines in °C) at 850 hPa for 12 UTC on July 27, 1998 (Legends: L=low, H=high, w=warm, c=cold).

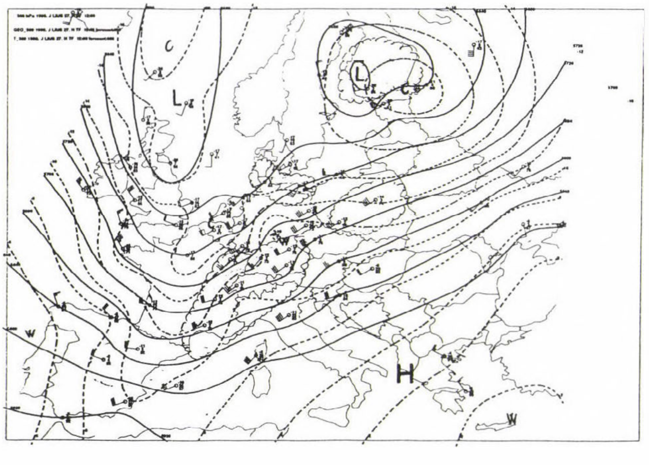

Fig. 6b. HMS analyses of geopotential (solid lines in gpdam) and temperature (dashed lines in °C) at 500 hPa for 12 UTC on July 27, 1998 (Legends: L=low, H=high, w=warm, c=cold).

On the basis of the synoptic data sources at 12 UTC, we managed to forecast the thunderstorms by night and the change of wind direction by the second part of the night in the region of Lake Balaton. Of course, we were not able to forecast the exact time and place of thunderstorm eruptions from these data sources. The ALADIN/HU meteograms for two local points (Siófok, Keszthely) of Lake Balaton were able to forecast the period of maximum intensity of lability very well. For the first time, the developing squall line was detected to SW of the lake by radar at 23:15 UTC. 15 minutes later *(Fig. 7b)*, the squall line reached the western part of Lake Balaton. This sharp and narrow instability line left the eastern part of the lake at 00:45 UTC. The length of the line varied between 150 and 200 km, its width varied between 20 and 40 km.

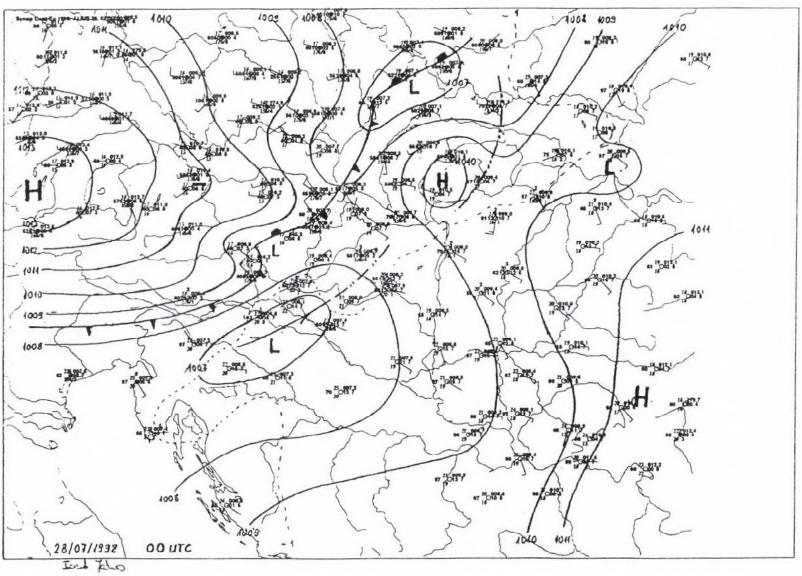

Fig. 7a. HMS meso-analyses at 00 UTC on July 28, 1998 (Legends: H=high, L=low).

4.2.2 The second case—the results by physical coefficient tuning in comparison to real data

The physical parameters used for the experiments were the same as in 4.1.2. Seven experiments (identified as TH00, TH01, TH02, TH03, TH04, TH05 and TH06) were carried out to test the ALADIN model's sensitivity regarding the parameterization among the seven ones. Only the best version is shown.

The best experiment with parameter tuning:

Experiment	❶	❷	❸	❹	❺	❻	❼
TH03	50000	YES	YES	NO	< 1	0.6E–4	0.25

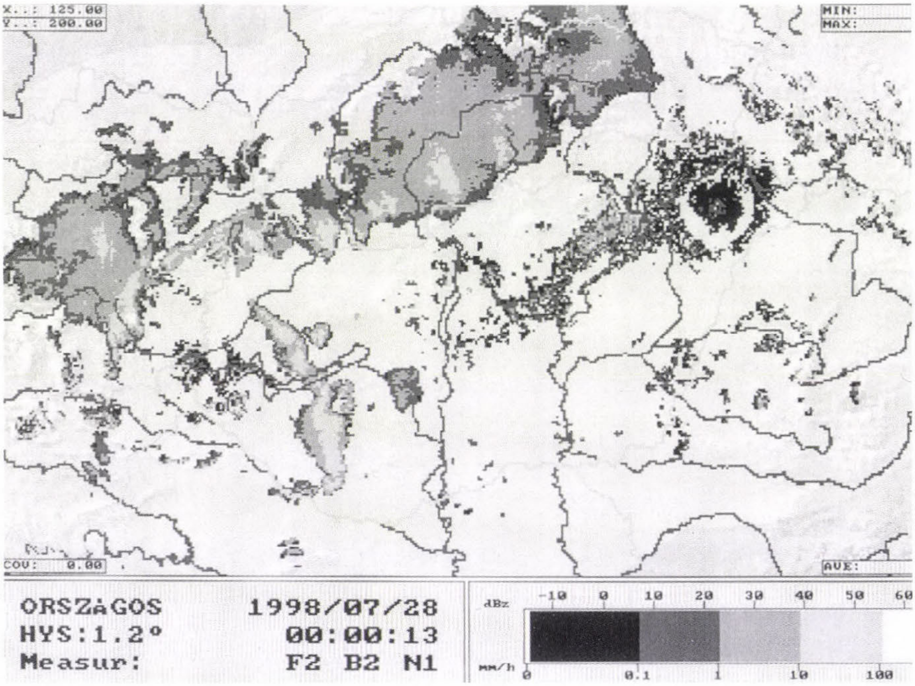

Fig. 7b. HMS composite weather radar image (reflectivity in dBZ) at 00 UTC on July 28, 1998 over the Carpathian Basin.

Experiment TH03 proved to be the best one with downdraft parameterization. The development of the gust front was simulated well enough by the 10m wind distribution with the mean sea level pressure structure (*Fig. 8a*). The results were compared to the suitable surface meso-analyses (Fig. 7a) and radar image (Fig. 7b). It can be seen that the position of the squall line at 00 UTC is nearly the same. Fig. 8a demonstrates very well that the wind direction changed from SW to NW behind the line and increased in larger degree. The gust front separates from the cold front system well enough and progresses parallel with the cold front. The pattern of vertical velocity also shows the two systems (*Fig. 8b*), but the cores of upward motions are stronger along the cold front than the squall line.

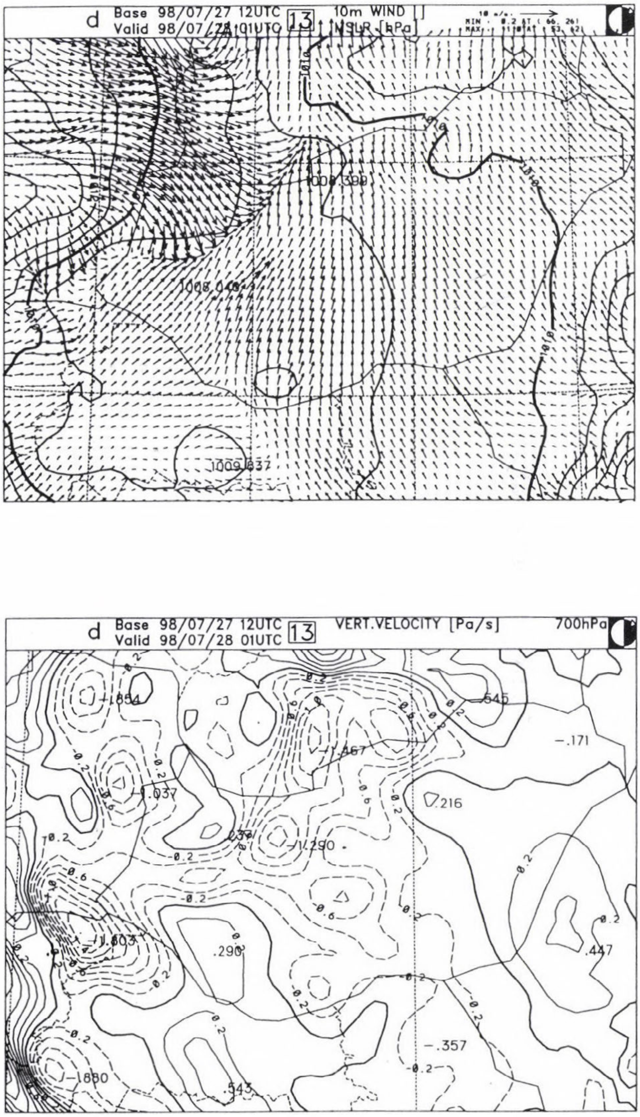

Fig. 8. Distribution in space and time (at 01 UTC) for 10m wind (m s^{-1}) together with the msl-pressure field (*a*) and for vertical velocity (Pa s^{-1}) at 700 hPa (*b*) simulated by ALADIN model experiments TH03 for July 28, 1998.

4.3 Studying how correct information is available according to ALADIN/HU meteograms for two local points of Lake Balaton in comparison to real data

We compared in space (Siófok, Keszthely) and time (every 3 hours) the forecasts according to ALADIN/HU meteograms of total cloud cover [N(F)], convective cloud cover [NL(F)], 10m wind velocity [V(F)], 2m temperature [T(F)] to the real synoptic observations [N(O), NL(O), V(O), T(O), respectively] for the thunderstorm-hazardous weather situations (Table 1) — see *Fig. 9.*

4.3.1 Forecast of total cloud cover [N(F)]

On the basis of this investigation, it was clear that there was no statistical difference between the forecasts of total cloud cover [N(F)] for two local points (Siófok and Keszthely) in the region of Lake Balaton. The mean error [ME/N(F)/] for the forecast of total cloud cover was one octant as an underestimation with standard deviation of two octants *(Fig. 9a)*.

4.3.2 Forecast of convective cloud cover [NL(F)]

Statistically we did not find any difference between the results as for the two local points (Siófok, Keszthely) in the region of Lake Balaton. The mean error [ME/NL(F)/] for the forecast of convective cloud cover was near to zero with relatively big standard deviation (3 octants, *Fig. 9b*). This fact is remarkable for forecasting the convective periods.

4.3.3 Forecast of 10m wind velocity [V(F)]

On the basis of this statistical evaluation investigation, there were significant differences in wind forecasts belonging to the two local points (Siófok, Keszthely). The 10m wind velocity forecasts for Siófok [VS(F)] were underestimated by ALADIN/HU meteograms (*Fig. 9c*). The mean error [ME/VS(F)/] was -1.25 m s^{-1} with standard deviation of 3.10 m s^{-1}. One of the possible explanations for the underestimation of wind velocity may be that the grid point (in ALADIN model) is not in suitable agreement with the real climatic characteristics of Siófok. The fact is that the meteorological station in Siófok stands close to the lake (10 meters from the lake) and that is why the influence of the water surface is significant particularly during no (pressure) gradient weather situations. This influence depends on the direction of air circulation between lake and land. Namely, in day-time the wind usually blows from the lake and in this way, if thunderstorms are able to break out north of Siófok, the wind gusts induced by cold air spreading out at the surface under a thundercloud could become stronger and stronger over the relatively smooth water surface. At the same time the forecasts [VK(F)] for Keszthely were overestimated. The mean forecast error [ME/VK(F)/] was +0.59 m s^{-1} with standard deviation of 1.78 m s^{-1} (*Fig. 9d*).

The forecast in space (Siófok, Keszthely) and time (every 3 hours) for the change of wind direction and the course of wind strengthening are equivalent of the real observations in quality. Unfortunately the degree of wind strengthening is significantly underestimated in Siófok, and at the same time it is overestimated in Keszthely.

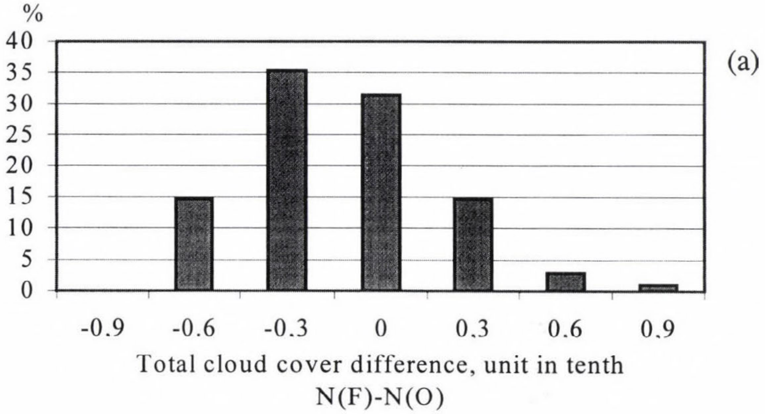

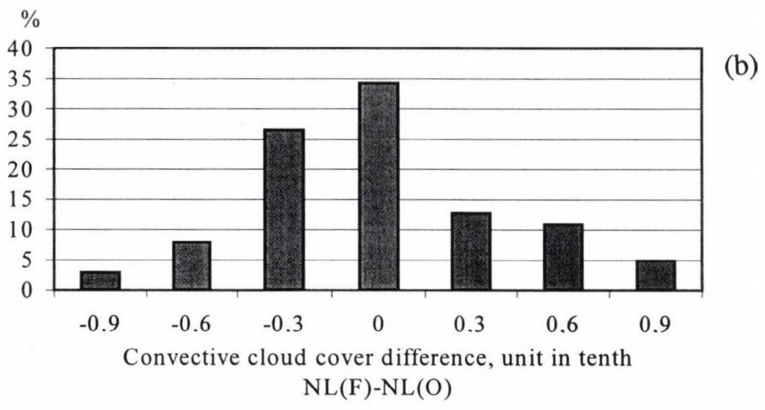

Fig. 9. Differences between the forecasts given by ALADIN/HU meteograms and observations (for all the cases in Table 1) as a function of percentage of cases for (*a*) total cloud cover (N(F), unit in tenth), (*b*) convective cloud cover (NL(F), unit in tenth), (*c*) 10m wind velocity in Siófok (VS(F), unit in m s^{-1}), (*d*) 10m wind velocity in Keszthely (VK(F), unit in m s^{-1}) and (*e*) 2m temperature (T(F), unit in °C). (*f*) Mean error [ME/T(F)] for the forecast by ALADIN/HU meteograms) of 2m temperature (°C) with respect to observations as a function of forecast range.→ →

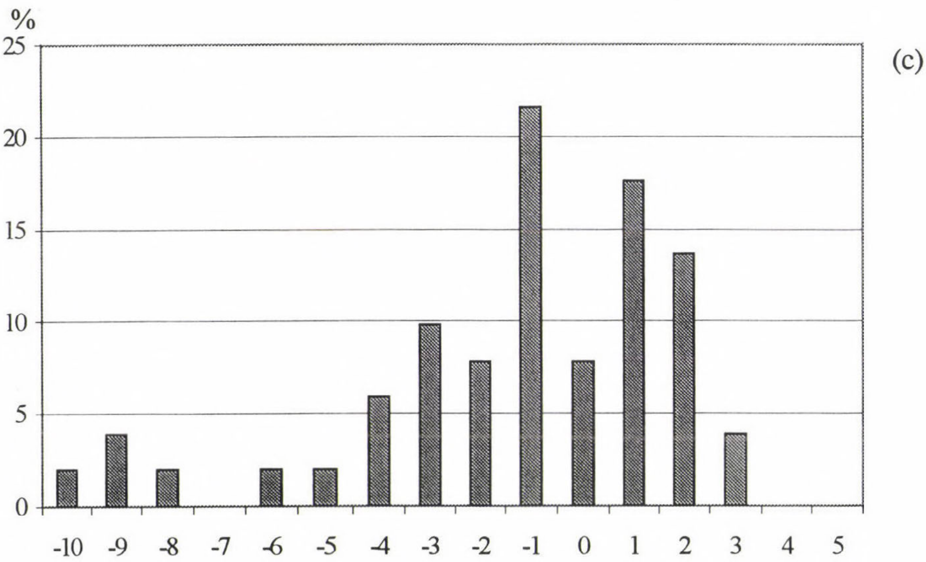

10m wind velocity difference (m s^{-1}) in Siófok
VS(F) – VS(O)

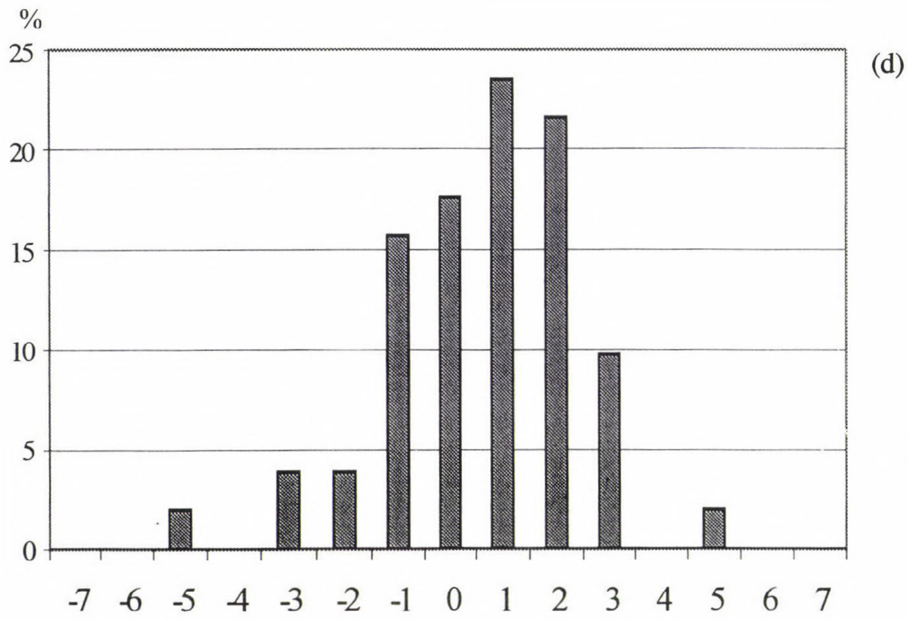

10m wind velocity difference (m s^{-1}) in Keszthely
VK(F) – VK(O)

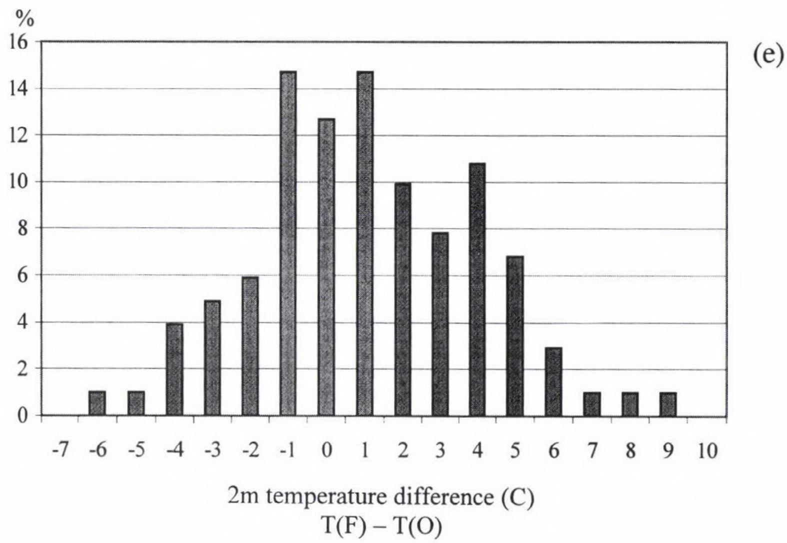

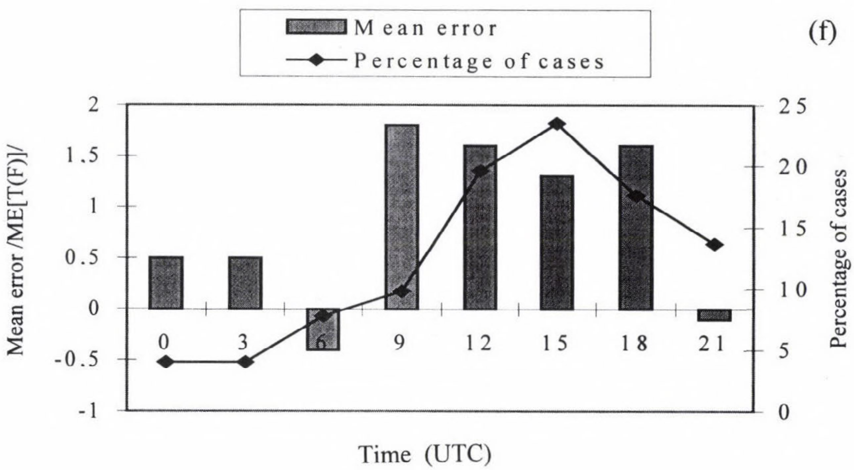

4.3.4 Forecast of 2m temperature [T(F)]

It is well known in the practice of making very short range forecasts for the region of Lake Balaton that the forecasts according to ALADIN/HU meteograms of 2m temperature are significantly overestimated. That is why it was necessary to use some correction for these data. Statistically we did not find any difference between the results belonging to the two local points (Siófok, Keszthely). The mean forecast error [ME/T(F)/] was +1.09°C with standard deviation of 2.93°C. The results are shown in *Fig. 9e*. It is worth considering the distribution in time (every 3 hours) of mean forecast errors according to ALADIN/HU for 2m temperature. As it can be seen on *Fig. 9f*, the significant overestimation appears between 09 and 18 UTC, which period is most important for the holiday-makers near Lake Balaton.

5. Concluding remarks

On the basis of the simulation experiments of the two selected squall lines, it can be underlined that the ALADIN model is able (even in operational version) to simulate a squall line although with deficiencies. It seems that the modification of available humidity for convection and the introduction of downdraft brings some benefits for the forecasting practice. So the ALADIN model is a useful tool for the storm forecasters at Lake Balaton. Since the quality of the forecast depends on the weather situation, we can use the following procedure:

The unstable periods are marked out monitoring continuously the forecasts made in 1- or 3-hour steps according to the ALADIN/HU meteograms for the two local points of Lake Balaton on the basis of data sources at 00 and 12 UTC. When the reality of ALADIN/HU forecasts is supported by the actual meso-analyses on the surface and the relevant analyses on the higher pressure levels, we can use the convection parameter tuning similar to our experiments for forecasting the development in space and time of organised convection considering the unstable period marked out.

Nevertheless, more experiments are necessary to evaluate the impact of the new modifications regarding the convection parameterization.

The values of accuracy for the forecasts of ALADIN model can be corrected by considering the quicker (e.g., daily or weekly) change of water temperature at Lake Balaton than it appears in the monthly climatic averages. The systematic errors of 2m temperature and 10m wind velocity forecasts according to ALADIN/HU meteograms can be corrected by filtering (e.g., Kalman-filter) procedure.

The model output data can be used for the nowcasting decision-making procedure (Fig. 1) of storm warning at Lake Balaton as input data, after correcting the forecasts for temperature and wind velocity of ALADIN/HU meteograms. This procedure provides a more objective foundation for storm warnings at Lake Balaton.

Acknowledgements—The authors are grateful to all the members of the ALADIN project, especially to *Jean-François Geleyn* as the project leader, and to *Doina Banciu* for their personal guidance and comments provided in Toulouse.

References

Banciu, D. and *Geleyn, J.-F.*, 1998: Les effets l'introduction de la parametrization des courants descendants convectifs dans le modele atmospherique ALADIN. *Atelier de Modélisation de l'Atmosphere,* 8-9 decembre 1998, Toulouse, 70-73.

Bartha, I., 1987: An objective decision procedure for prediction of maximum wind gusts associated with Cumulonimbus clouds. *Időjárás 91,* 330-346.

Bartha, I., 1998: ALADIN model from the storm forecaster point of view. *Internal Report on the experiments made in Toulouse during 19/10/1998 - 19/12/1998.* Manuscript.

Bartha, I., Gyarmati, Gy., Horváth, Á., Lénárt, L. and *Nagy, J.*, 1998: Prediction of wind storms associated convective activity using radar data (in Hungarian). *Meteorological Notes of Universities 11,* 89-93, Budapest.

Bougeault, Ph., 1985: A simple parameterization of the large-scale effects of Cumulus convection. *Mon. Wea. Rev. 113,* 2108-2121.

Ducrocq, V. and *Bougeault, P.*, 1995: Simulation of an observed squall line with a meso-beta scale hydrostatic model. *Weather and Forecasting,* 380-399.

Fawbush, E. J. and *Miller, R. C.*, 1954: A basis for forecasting peak wind gusts in non-frontal thunderstorms. *Bull. Amer. Meteorol. Soc. 5,* 1.

Gerard, L., 1998: Paramétrisation du profil de quantité de mouvement horizontale dans le nuage convectif. *Atelier de Modélisation de l'Atmosphére,* 8-9 decembre 1998, Toulouse, 74-77.

Gregory, D., Kershaw, R. and *Innes, P. M.*, 1997: Parameterization of momentum transport by convection. II: Tests in single-column and general circulation models. *Quart. J. Roy. Meteorol. Soc. 123,* 1153-1183.

Horányi, A., Ihász, I. and *Radnóti, G.*, 1996: ARPEGE/ALADIN: A numerical weather prediction model for Central-Europe with the participation of the Hungarian Meteorological Service. *Időjárás 100,* 277-301.

Horváth, Á., Duska, G., Kertész, S. and *Lénárt, L.*, 1998: The HAWK meteorological workstation (in Hungarian). *Légkör XLIII,* 18-23.

Kershaw, R. and *Gregory, D.*, 1997: Parameterization of momentum transport by convection. I: Theory and cloud modelling results. *Quart. J. Roy. Meteorol. Soc. 123,* 1133-1150.

IDŐJÁRÁS

Quarterly Journal of the Hungarian Meteorological Service
Vol. 104, No. 4, October–December 2000, pp. 241–252

Nowcasting of precipitation type Part I: Winter precipitation

István Geresdi[1] and **Ákos Horváth**[2]

[1]*University of Pécs, Institute of Geography, H-7624 Pécs, Ifjúság u. 6, Hugary; E-mail: geresdi@ttk.pte.hu*

[2]*Hungarian Meteorological Service, Storm Warning Observatory, H-8600 Siófok, Vitorlás u. 17, Hungary; E-mail: horvath.a@met.hu*

(Manuscript submitted for publication 2 June 2000; in final form 10 October 2000)

Abstract—The purpose of this research was to develop a numerical model to give the type and phase of winter precipitation in real time with high horizontal resolution. This model is a part of the nowcasting system developed by the Hungarian Meteorological Service (HMS). The input data are temperature and water vapor profile with horizontal resolution of 3 km. Melting and refreezing rate of precipitation particles are calculated by a microphysical model. The possible outputs are snow, snow and rain, rain, freezing drizzle and rain, freezing rain, ice pellet. The microphysical model was tested by comparison of the simulated precipitation events with the precipitation types observed at a meteorological station. The input data used for the test were from sounding taken at the same station. Although in some cases the calculation misses the precipitation type and/or phase, generally the categories provided by the simulation agree well with the surface observations. An output given by the nowcasting system and its comparison with ground base observation is also presented.

Key-words: nowcasting, winter precipitation, freezing rain, microphysics, numerical simulation.

1. Introduction

The HMS runs a project to develop a nowcasting system. One of the purposes of this project is to improve the nowcast of form and phase of precipitation. In this paper the method applied for winter cases is presented, and in the second part of this series the technique for estimation of the maximum hail size is intended to publish. Nowcasting of precipitation type during winter in the Carpatian Basin is a very important problem, because of the peculiar geographical conditions, the appearance of dangerous precipitation type like freezing rain has a relatively high frequency.

Numerous papers have been presented discussing the formation of winter precipitation (e.g., *Rauber et al.*, 1994; *Stweart* and *King*, 1987a, b; *Zerr*, 1995, 1997). These researches have investigated the environmental condition necessary for the formation of freezing rain or melting of snow flakes. Zerr made microphysical calculation to trace the phase change of the falling hydrometeor (*Zerr*, 1997). Our microphysics is very similar to that of presented by *Zerr* (1997), but the effect of evaporation cooling was also taken into consideration. According to *Mitra et al.* (1990) subsaturated conditions can significantly increase the distance needed for completely melting of the ice particles. Correct simulation of the phase change needs detailed microphysical description and good time and spatial resolution of the environmental parameters (temperature and vapor content) in the boundary layer. This could be the reason that — to knowledge of the authors — only case studies were made in this field. This is the first effort which tries to give the phase and type of the precipitation on the ground in real time and with high horizontal resolution. Winter precipitation is divided into six categories: (i) snow, (ii) snow and rain, (iii) rain, (iv) freezing drizzle and rain, (v) freezing rain and (vi) ice pellet.

2. *Description of the model*

Input data of the model are coming from of the nowcasting system developed at the Hungarian Meteorological Service. This system uses real time data of surface observations (SYNOP), forecasted fields of a limited area model ALADIN (*Horányi et al.*, 1996) and calculates the objective analysis using optimal interpolation for data assimilation. Procedure for analysis of relative humidity using radar reflectivity data is also involved. The MEANDER (Mesoscale Analysis Nowcasting and Decision Routines) system produces high resolution (dx, dy ~ 3 km, dz ~ 200 m) 3D fields of basic parameters: pressure, height, temperature, relative humidity and wind.

A low density particle starts to fall with its terminal velocity at the highest 0°C level (denoted by h_0 in *Fig. 1*). Density and type of the particle are very uncertain. They strongly depend on the microphysical processes taken place in the cloud. In this research the particles were supposed to be graupel ones with initial density of 400 kg m^{-3}. Previous laboratory results show that the meltwater does not shed and remains attached to the ice core if the diameter of the graupel particle is less than 9 mm (*Rasmussen et al.,* 1984). These observations support the assumption that the mass of the falling hydrometeor changes only due to the diffusional transport of water vapor. The equations suggested by *Rasmussen* and *Heymsfield* (1987) were used to calculate the terminal velocity

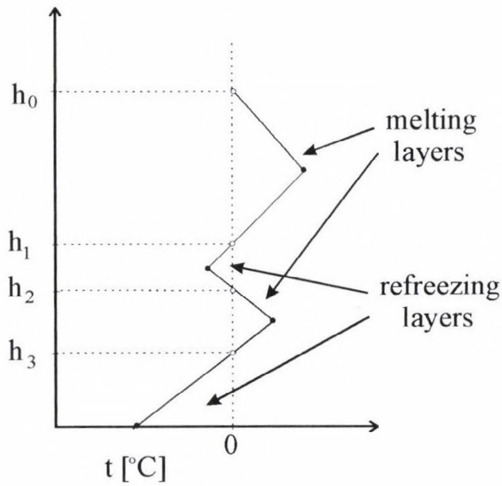

Fig. 1. Main characteristics of a temperature profile used as the model input. While the values at the significant levels (black dots) are given by another subprogram, the height of 0°C levels are calculated in the model.

of the falling particle. It is supposed that the falling particle does not collect either liquid or solid hydrometeors. So the heat transfer from the collected particles could be neglected, and the melting rate depends only on the heat transfer from the ambient air and the heat released due to the diffusion of water vapor from the surface of the particle:

$$\frac{dm_i}{dt} = \frac{1}{L_f} \cdot \frac{dq}{dt}, \tag{1}$$

where m_i and L_f are the mass of the ice core and the latent heat of fusion, respectively. The heating rate is given by the next equation:

$$\frac{dq}{dt} = C \cdot \left\{ -4\pi \cdot r_g \cdot k_a \cdot (T_\infty - T_s) \cdot f_h - 4\pi \cdot r_g \cdot L \cdot D_v \cdot (\rho_{v,\infty} - \rho_{v,s}) \cdot f_v \right\}, \tag{2}$$

where C depends on the Reynolds number (*Rasmussen* and *Heymsfield,* 1987). If $N_{Re} < 250$ C is equal to 2, otherwise C is unit. r_g is the radius of the particle, k_a and D_v are heat conductivity of air and vapor diffusion coefficient in air, respectively (*Pruppacher* and *Klett*, 1997). T_∞ and T_s are the temperature in the environment and on the surface of the graupel, $\rho_{v,\infty}$ and $\rho_{v,s}$ are the vapor density far from the graupel and on its surface. L is the latent heat of condensation if the graupel is completely or partly melted, otherwise it means the latent heat of deposition. f_v and f_h are ventilation coefficients for vapor and heat transfer (*Pruppacher* and *Klett*, 1997), respectively:

$$f_v = 0.78 + 0.308 \cdot N_{Sc}^{1/3} \cdot N_{Re}^{1/2},$$

$$f_h = 0.78 + 0.308 \cdot N_{Pr}^{1/3} \cdot N_{Re}^{1/2},$$

where N_{Sc} and N_{Pr} are the Schmidt and Prandtl numbers. The first term between the brackets in Eq. (2) is the heat transfer due to the conduction, the second term is the releasing latent heat due to vapor diffusion.

When an incompletely melted particle falls into the refreezing layer (Fig. 1), the ice core starts to increase. The rate of the increase is given by the following equations (*Johnson* and *Hallett*, 1968):

$$\frac{dy}{dt} = -\frac{1}{3 \cdot y^2 \cdot t_0}, \tag{3}$$

where

$$t_0 = \frac{\rho_w \cdot L_f \cdot r_g^2}{3 \cdot f_h \cdot k_a \cdot \Delta T}\left(1 - \frac{\Delta T \cdot c_w}{L_f}\right),$$

and

$$y = \frac{a}{r_g},$$

where r_g is the radius of the melted particle and a is the radius of the ice core. ρ_w, L_f , and c_w are the density of water, the latent heat of fusion and the specific heat of water, respectively. ΔT is the supercooling of the water (ΔT= 273.15 - T_s). Relatively small time step of 1 s was used during the calculation to avoid overestimation heat transfer.

To give the type of the particles on the ground, the critical radius (R_{crit}) is calculated at every grid point where existence of precipitation was detected by radar. The meaning of the critical size is that the particles are completely melted if their initial size is smaller than the critical size. Graupel particles with larger size remain frozen or have an ice core when they reach the ground. The initial radius is calculated by the following recursive formulas:

$$R_n = 0.5 \cdot R_{n-1}$$

if the particle with initial radius of R_{n-1} did not melt completely, and

$$R_n = 0.5 \cdot (R_{n-2} + R_{n-1})$$

if the particle with initial radius of R_{n-1} completely melted, but the one with that of R_{n-2} did not. R_0 was chosen to be 3 mm. The calculation was ceased when $|R_n - R_{n-1}| < 0.1$ mm and $R_{crit}=R_n$. One of the six categories for the precipitation type was chosen depending on the value of R_{crit}, surface temperature and number of the melting layer (*Fig. 2*). Specification of precipitation type was based on the relation between R_{crit} and a given radius (R^*). R^* was related to the size distribution of the graupel particles in the cloud. It was supposed that the concentration of the particles larger than R^* is negligible. In this research R^* was chosen to be a constant value of 1.0 mm. In most cases this value is acceptable, concentration of the garupel particles larger than 2.0 mm is very low in layer clouds (solid line in *Fig. 3*). If R_{crit} is larger than R^* most of the precipitable particles melt, and depending on the surface temperature the precipitation on the ground is freezing rain or rain. If R_{crit} is less than 0.1 mm, only few liquid particles can fall on the ground, because water drops smaller than 0.1 mm generally evaporate before reaching the ground. In this case the precipitation is ice pellet or snow. If R_{crit} is between R^* and 0.1 mm the precipitation is mixed type: snow and rain if the ground temperature is over 0°C, and ice pellet and freezing drizzle otherwise.

Of course R_{crit} is not calculated when the maximum temperature is below the melting temperature in the air mass above the grid point. In this case the model output is snowfall.

3. *Evaluation of the microphysical model*

The model was tested by comparison of calculated and observed data. The test focused mainly on the formation of the freezing rain. Freezing rain or drizzle can produce extremely dangerous conditions for almost every kind of traffic by coating the surface with continuous ice layer. Precipitation type reported from synoptic station located in Budapest was compared with calculated data (*Table 1*). The temperature profiles were given from data measured by rawinsondes taken two times a day (12:00 UTC and 00:00 UTC) from this station. Sounding data, nearer to the beginning of precipitation events were used to give ambient conditions for the falling particles. The observed precipitation type is given in the second column, the value of the critical radius and the simulated precipitation type are written in the third and fourth column, respec-

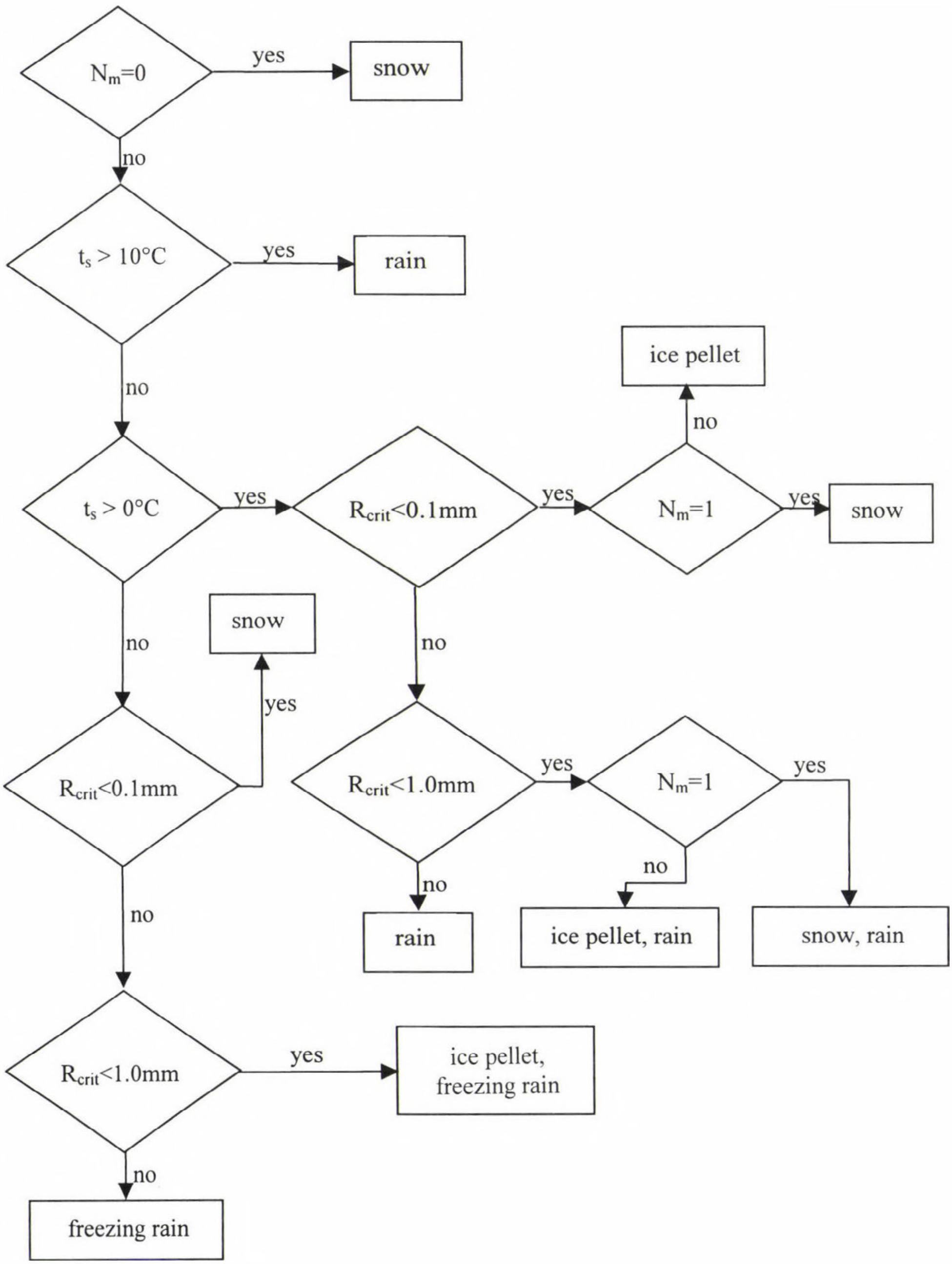

Fig. 2. Flow chart used to separate the different precipitation types. The decision depends on the number of the melting level (N_m), the surface temperature (t_s) and the value of the critical radius (R_{crit}). More details about R_{crit} are in the text.

tively. Between 1991 and 1997 one or more melting layers were observed on 41 days. In this period freezing rain was reported on 21 days. Six other days — when other precipitation types were also observed — were also involved into the dataset. Because the calculation confined to the lowest, 2–3 km thick air layer, sounding data describe well the environmental condition for the falling particles, if short time passes between the sounding and the precipitation fall out. Fortunately the time gap between the sounding and the report of the precipitation was longer than 4 h only in few cases.

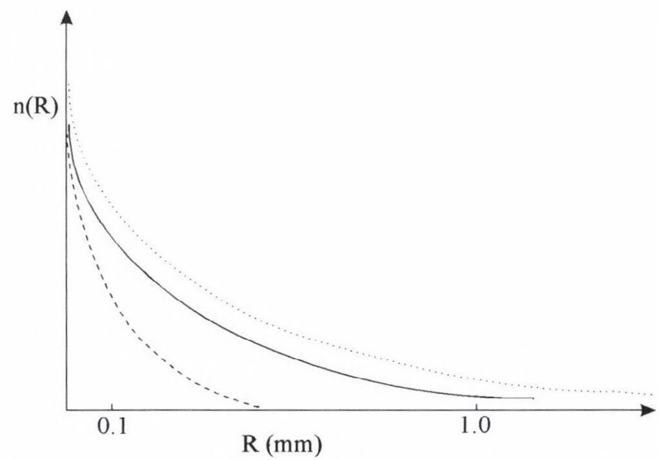

Fig. 3. Dependence of the size distribution on the precipitation intensity. At present calculation it was supposed that the size distribution of the garupel particles is given by thick solid line. If the precipitation intensity increases number concentration of particles larger than 1 mm increases (dotted line). If the precipitation intensity decreases the maximum particle radii is smaller than 1 mm (dashed line).

Comparison of data in the third and fourth column shows that the observed and the simulated precipitation types agree well. However, the model was not able to describe the change of the precipitation type between two soundings. This is not necessarily caused by change of the temperature profile. The fluctuation in precipitation intensity can result in similar effect. If the intensity decreases, the number concentration of the larger particles also decreases (dashed line in Fig. 3). In this case $R_{crit} < 1.0$ mm does not mean that some of the particles will have an ice core on the ground, but all of them will completely melt. Because $R^{*} = 1.0$ mm is used to separate the different precipitation types, the model prefers the formation of ice pellet and freezing rain to the freezing rain, furthermore it overestimates the occurrence of snow and

Table 1. Comparison of the observed and calculated precipitation type. Observation times are given in UTC. Rows shaded by gray show the days when the difference between the observation and simulation were significant

Date	Duration	Observed precip.	R_{crit} (mm)	Simulated precipitation
12. 20. 1991	10:25 - 11:00	ice pellet	0.21	ice pellet, snow
	11:00 - 11:10	ice pellet	0.21	ice pellet, snow
12. 29. 1991	21:15 - 21:50	ice pellet	0.25	ice pellet, snow
01. 05. 1992	08:30 - 09:00	freezing rain	1.5	freezing rain
01.28. 1992	01:00 - 04:00	freezing drizzle	-	snow
12. 21. 1992	08:05 - 10:10	freezing rain	0.70	ice pellet, freezing rain
	10:10 - 10:50	ice pellet	0.70	ice pellet, freezing rain
	10:50 - 12:20	freezing rain	0.70	ice pellet, freezing rain
	20:20 - 20:50	ice pellet	0.70	ice pellet, freezing rain
	20:50 - 21:00	freezing rain	0.70	ice pellet, freezing rain
01. 06. 1993	20:30 - 21:00	ice pellet	0.66	ice pellet, freezing rain
01. 07. 1993	09:30 - 10:20	freezing rain	1.38	freezing rain
	11:20 - 15:00	freezing rain	1.38	freezing rain
01. 08. 1993	16:40 - 17:30	freezing rain	1.75	freezing rain
	17:30 - 19:10	freezing drizzle	1.75	freezing rain
02. 06. 1993	11:35 - 14:00	freezing rain	0.88	ice pellet, freezing rain
	14:30 - 15:00	freezing rain	0.88	ice pellet, freezing rain
	18:30 - 19:00	ice pellet	0.88	ice pellet, freezing rain
12. 28. 1993	07:15 - 08:00	ice pellet	0.87	ice pellet, rain
01. 23. 1994	21:35 - 23:40	freezing rain	1.48	freezing rain
12. 05. 1994	01:20 - 04:00	freezing drizzle	2.00	freezing rain
12. 28. 1994	05:00 - 09:00	freezing rain	1.85	freezing rain
01. 22. 1995	evening	freezing rain	2.23	freezing rain
11. 24. 1995	05:20 - 06:30	snow	-	snow
	06:30 - 09:00	freezing drizzle	0.47	ice pellet, freezing rain
	09:00 - 24:00	snow	0.47	ice pellet , freezing rain
11. 25. 1995	00:00 - 06:30	snow	0.93	ice pellet, freezing rain
12. 18. 1995	01:25 - 04:55	freezing rain	1.2	freezing rain
	04:55 - 08:00	freezing drizzle	1.2	freezing rain
12. 20. 1995	20:15 - 21:20	snow and rain	0.83	snow and rain
	21:20 - 23:00	rain	0.83	snow and rain
12. 31. 1995	20:10 - 22:55	freezing rain	-	snow
01. 07. 1996	13:40 -14:10	freezing rain	0.34	ice pellet, freezing rain
	14:10 -15:10	ice pellet	0.34	ice pellet, freezing rain
	16:40 -20:20	freezing rain	0.34	ice pellet, freezing rain
01. 08. 1996	01:10 -02:15	freezing rain	1.00	freezing rain
01. 26. 1996	03:00 - 05:30	freezing drizzle		snow
	09:10 - 09:30	ice pellet		snow
	11:30 - 12:00	ice pellet		snow
	17:20 - 20:00	freezing drizzle		snow
	23:35 - 02:15	freezing rain	0.64	ice pellet, freezing rain
01. 27. 1996	07:15 - 09:00	freezing rain	0.64	ice pellet, freezing rain
02. 03. 1996	05:40 - 08:10	freezing rain	0.28	ice pellet, freezing rain
01. 03. 1997	08:45 - 11:40	freezing rain	0.12	ice pellet, freezing rain
	11:40 - 12:40	ice pellet	0.12	ice pellet, freezing rain
	12:40 - 13:00	freezing rain	0.12	ice pellet, freezing rain
	13:00 - 14:00	ice pellet	0.12	ice pellet, freezing rain
	14:00- 23:20	freezing rain	0.89	ice pellet, freezing rain
01. 04. 1997	05:09 -05:40	freezing rain	0.89	ice pellet, freezing rain
12. 19. 1997	11:06 - 12:00	ice pellet	0.85	ice pellet, freezing rain
	12:00 - 12:20	freezing rain	0.85	ice pellet, freezing rain

rain against only rain. When the precipitation intensity increases, the number concentration of the particles at the tail of the size distribution also increases (dotted line in Fig. 3). More graupel particles can survive the fall through the melting layer than it could be expected from the model results. The appearance of larger particles increases the possibility of the ice pellet events against the freezing rain ones. The problem caused by the fluctuation of precipitation intensity could be solved by linking the value of R^* to the radar reflectivity, instead of using fixed value.

Within the investigated period the model was not able to predict correctly the precipitation types on five days.

(a) On January 28, 1992, although freezing drizzle was reported between 01:00 and 04:00 UTC, the model output was snow. Analysis of the sounding data shows that just before the precipitation started to fall, temperature was below 0°C (the maximum temperature was equal to −3°C and measured on the surface), and the presence of the melting layer was indicated only 24 hours later by next midnight sounding. It is assumed that this freezing drizzle event did not originate from ice clouds. If the cloud top temperature is larger than −10°C, only few ice crystals can form and the collision-coalescence of the supercooled droplets results in drizzle size drops (>50μm). If the cloud base is near to the ground, these small drops can reach the ground.

Freezing drizzle event occurred also on December 31, 1995, and it could be the consequence of similar microphysical processes, because no melting layer was observed this day as well.

(b) On November 24, 1995, snowfall started early in the morning at 5:20 UTC and it ended only in the next morning. This continuous snowfall was interrupted by freezing drizzle events occurred between 6:30 UTC and 9:00 UTC. The model simulated well the precipitation types until 9:00. While the surface observer reported snow from 9:00, the model output did not change, it remained ice pellet and freezing rain. The sounding taken at 12:00 UTC and 00:00 UTC on November 25 indicated a melting layer. The characteristic parameters of the melting layer — depth and the maximum temperature — increased form 600 m to 800 m and from 0.8°C to 2.0°C, respectively. This strong warming resulted in favorable condition for freezing rain formation and some of the particles should have melted. It is assumed that observation error caused the discrepancy in this case.

(c) The differences between observed and simulated precipitation types on January 26, 1996, were caused by different reasons. The freezing drizzle events at dawn (3:00–5:30 UTC) could be the consequence of the formation of supercooled drops, because melting layer was not observed neither at 00:00 UTC nor at 12:00 UTC soundings (see point (a)). Unfortunately the model is not able to simulate the formation of large supercooled drops via collision–coalescence processes of small water drops. This is the reason of that the model gave snow instead of freezing drizzle. After 9:00 the observed precipitation type was ice pellet and the model output was snow. Due to the absence of melting layer, melting and subsequent refreezing could not occur. It is assumed that this discrepancy was caused by observational uncertainty. The midnight sounding indicated melting layer and the model results agrees well with the observation after 23:15 UTC. The difference noticed in the time interval of 17:20–20:00 UTC could be caused by change of the ambient conditions. The model used the environmental parameters given by 12:00 UTC sounding, which were not consistent with environmental condition at late afternoon. Although the time difference between the precipitation events and the 00:00 UTC sounding (on 27 January) was large, it might have been more suitable to use.

4. Application

The above described microphysical model is in operative usage at the Hungarian Meteorological Service as a part of the MEANDER system. In every grid point a radar reflectivity value is provided, which represents the radar measured precipitation intensity of the given area. The precipitation type decision model runs only in grid points where radar echoes indicate precipitation, saving considerable run time. Distribution of precipitation phase can be displayed on the operative meteorological workstation among other derived meteorological image type information.

Fig. 4 shows the output of the system on 24 November, 1999. Early in the morning of this day precipitation types were freezing rain and snow. Cloud formation was initiated by a warm advection at the middle tropospheric level in the warm sector of a Mediterranean cyclone. Since temperature remained below 0°C on the surface, conditions were favorable for freezing rain formation. On areas where the warm advection had resulted in melting layer, freezing rain event occurred, elsewhere the form of precipitation was snow. Dark gray regions denote freezing rain events and white regions denote the snowfall. For comparison with surface observation, the observed precipitation types reported by the meteorological stations are also given in the figure. The calculated precipitation type agrees well with the observation in Transdanubia region, but there are some discrepancies in the southeastern and the northeastern part of the country. The limited area model might have overestimated the warm advection over the northeastern region and might have underestimated the increase of temperature over the southeastern region.

Although the model simulates well the precipitation types in most cases, improvements are planned. To take into account the possible effect of change of precipitation intensity, the value of R^* will be calculated on the base of radar reflectivity data.

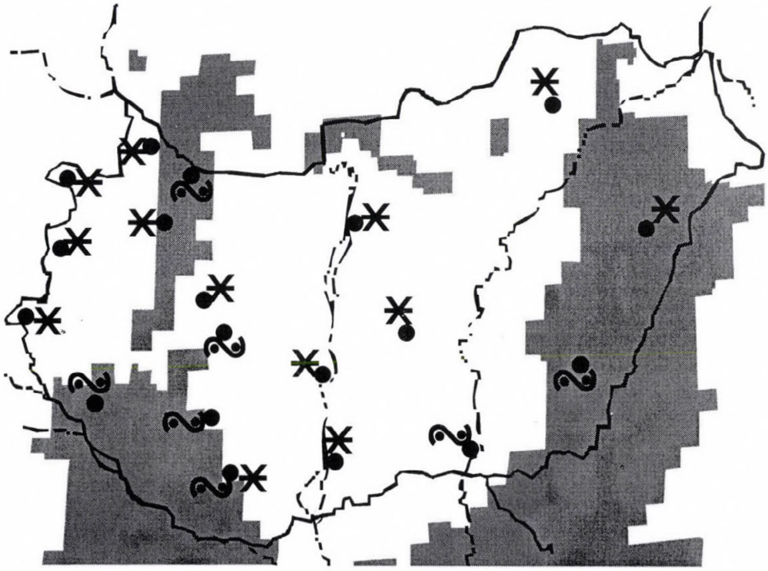

Fig. 4. Nowcasting system output for winter precipitation type at 9:00 UTC on November 24, 1999. The dark gray and white regions denote the freezing rain events and snow fall, respectively. Also the precipitation types reported between 6:00 and 9:00 UTC by meteorological stations (black dots) are shown. Symbol ⌒∪ and ∗ denote freezing rain and snowfall, respectively.

Test data suggest that a few percent of freezing drizzle events occurred without melting layer. Unfortunately the model with simple microphysics is not able to describe the formation of large supercooled drops. The uncertainty both in form and value of initial density of the falling particles can effect the final result. The authors think that the application of the polarized radar data can help to solve these problems and the data given by this type of radar are intended to use in future.

Acknowledgement—The research was supported by the Hungarian Scientific Research Fund (Number: T030857).

References

Horányi, A., Ihász, I. and *Radnóti, G.*, 1996: ARPAGE/ALADIN: A numerical weather prediction model for Central-Europe with the participation of the Hungarian Meteorological Service. *Időjárás 100,* 277-301.

Johnson, D. A. and *Hallett, J.*, 1968: Freezing and shattering of the supercooled water drops. *Quart. J. Roy. Meteorol. Soc. 94,* 468-482.

Mitra, S. K., Vohl, O., Ahr, M. and *Pruppacher, H. R.*, 1990: A wind tunnel and theoretical study of the melting behavior of atmospheric ice particles. IV: Experiment and theory for snow flakes. *J. Atmos. Sci. 47,* 584-591.

Pruppacher, H. R. and *Klett, J. D.*, 1997: *Microphysics of Clouds and Precipitation.* Kluwer Academic Publisher, p. 954.

Rasmussen, R. M. and *Heymsfield, A. J.*, 1987: Melting and shedding of graupel and hail. Part I: Model physics. *J. Atmos. Sci. 44,* 2754-2763.

Rasmussen, R. M., Levizzani, V. and *Pruppacher, H. R.*, 1984: A Wind Tunnel and Theoretical Study on the Melting Behavior of Atmospheric Ice Particles: III. Experiment and Theory for-Spherical Ice Particles of Radius <500 μm. *J. Atmos. Sci. 41,* 381-388.

Rauber R. M., Ramamurthy, M. K. and *Tokay, A.*, 1994: Synoptic and mesoscale structure of a severe freezing rain event: The St. Valentine's Day ice storm. *Wea. Forecasting 9,* 183-208.

Stewart, R. E. and *King, P.*, 1987a: Freezing precipitation in winter storms. *Mon. Wea. Rev. 115,* 1270-1279.

Stewart, R. E. and *King, P.*, 1987b:Rain-snow boundaries over southern Ontario. *Mon. Wea. Rev., 115,* 1894-1907.

Zerr, R. J., 1995: Wind and reflectivity signatures as obtained by a Doppler radar for a freezing-rain episode. *Preprints, 27th Conf. On Radar Meteorology,* Vail, Co. *Amer. Meteorol. Soc.,* 414-415.

Zerr, R. J., 1997*: Freezing rain: An observational and theoretical study. J. Appl. Meteorol. 36,* 1647-1661.

IDŐJÁRÁS

Quarterly Journal of the Hungarian Meteorological Service
Vol. 104, No. 4, October–December 2000, pp. 253–268

Urban heat island development affected by urban surface factors

János Unger[1], Zsolt Bottyán[2], Zoltán Sümeghy[1] and Ágnes Gulyás[1]

[1]Department of Climatology and Landscape Ecology, University of Szeged, P.O. Box 653, H-6701 Szeged, Hungary; E-mail: unger@geo.u-szeged.hu, sumeghy@geo.u-szeged.hu, agulyas@geo.u-szeged.hu
[2]Department of Natural Sciences, Zrínyi University, P.O. Box 1, H-5008 Szolnok, Hungary; E-mail: zbottyan@solyom.szrfk.hu

(Manuscript submitted for publication 8 May 2000; in final form 11 September 2000)

Abstract—This study examines the spatial and quantitative influence of urban factors on the surface air temperature field of the medium-sized city of Szeged, Hungary, using of mobile measurements under different weather conditions between March 1999 and February 2000. This city with a population of about 160,000 is situated on a low, flat flood plain. The efforts have been concentrated on investigating the development of the urban heat island (UHI) in its peak development during the diurnal cycle. Tasks include determination of spatial distribution of mean maximum UHI intensity, using of standard kriging procedure and determination of statistical model equations in the one-year study period, as well as in the heating and non-heating seasons. Multiple correlation and regression analyses are used to examine the effects of urban surface parameters (land-use characteristics and distance from the city centre determined in a grid network) on the UHI. Results indicate isotherms increasing in regular concentric shapes from the suburbs toward the inner urban areas with a seasonal variation in the UHI magnitude. In the city centre the mean maximum UHI intensity reaches more than 2.6°C, 3.1°C and 2.1°C, respectively. As the patterns show, there is a clear connection between urban thermal excess and built-up density. As the model equations show, strong relationships exist between urban thermal excess and distance, as well as built-up ratio, but the role of water surface is negligible.

Key-words: UHI, spatial distribution, grid network, built-up ratio, water surface ratio, distance, statistical analysis, regression equations.

1. Introduction

The temperature-increasing effect of cities caused by urbanization (the so-called urban heat island — UHI) is one of the most deeply examined fields of climatology. Features of the UHI are well documented from different cities mainly from the temperate zone (e.g., *Oke*, 1997; *Kuttler*, 1998) and one of the most difficult aspect of this phenomenon is studying of its peak development during the diurnal cycle.

The detection of real factors and physical processes generating the distinguished urban climate is extremely difficult because of the very complicated urban terrain (as regard surface geometry and materials) as well as artificial production of heat and air pollution. The simulation of these factors and processes demands complex expensive instrumentation and sophisticated numerical and physical models. Despite these difficulties, several models have been developed for studying small-scale climate variations within the city, including the ones based on energy balance (*Tapper et al.*, 1981; *Johnson et al.*, 1991; *Myrup et al.*, 1993), radiation (*Voogt* and *Oke*, 1991), heat storage (*Grimmond et al.*, 1991), water balance (*Grimmond* and *Oke*, 1991) and advective (*Oke*, 1976) approaches.

As an other solution of the above mentioned problems, utilisation of statistical models may provide useful tools, which give us quantitative information about the magnitude as well as spatial and temporal features of the UHI intensity (defined as the temperature difference between urban and rural areas) by employing urban and meteorological parameters. Some examples of the modeled variables (surface and near surface air UHI intensity or even the possible maximum UHI intensity) and the employed variable parameters are gathered in *Table 1*.

Table 1. Survey of some statistical models with modeled UHI variables, employed parameters and authors

Modeled variable	Employed parameters	Author(s)
UHI intensity	wind speed, cloudiness	*Sundborg* (1950)
UHI intensity	population, wind speed	*Oke* (1973)
Max. UHI intensity	population	
UHI intensity	wind speed, wind speed, cloudiness, atmospheric stability, traffic flow, energy consumption, temperature	*Nkemdirim* (1978)
UHI intensity	wind speed, land-use type ratios	*Park* (1986)
Max. UHI intensity	impermeable surface, population	
UHI intensity	cloudiness, wind speed, temperature, humidity mixing ratio	*Goldreich* (1992)
Surface UHI intensity	solar radiation, wind speed, cloudiness	*Chow et al.* (1994)
UHI intensity	built-up area, height, wind speed, time, temperature amplitude	*Kuttler et al.* (1996)

Counting all weather conditions except rain, the main purpose of this study is to investigate the effects and interactions inside the city on the surface air temperature a few hours after sunset, when the UHI effect is most pronounced. To achieve this aim, we construct horizontal isotherm maps to show the average spatial distribution of maximum UHI intensity in the investigated period as a whole and in the distinguished, so-called heating and non-heating, seasons. Then, we intend to reveal some obvious relationships between temperature patterns and urban factors using built-up (covered surface) ratio within the city. Further aim was to determine quantitative influences of the urban surface factors on the patterns of urban-rural temperature.

2. Study area and methods

Szeged is located in the south-eastern part of Hungary on the Great Hungarian Plain (46°N, 20°E) at 79 m above sea level (*Fig. 1*). The city and its countryside situate on is a large flat flood plain. The River Tisza passes through the city, otherwise, there are no large water bodies nearby. This geographical situation (no orographic climate influences) makes Szeged a good case for the study of a relatively undisturbed urban climate. Using Köppen's classification, the area belongs to the climatic region *Cf*, which means a temperate warm climate with a rather uniform annual distribution of precipitation (*Table 2*). The regional climate of Szeged has, however, a certain Mediterranean influence. It appears mainly in the annual variation of precipitation, namely in every 10 years approximately 3 years show some Mediterranean (relatively high autumn-winter rainfall) characteristics (*Unger*, 1999).

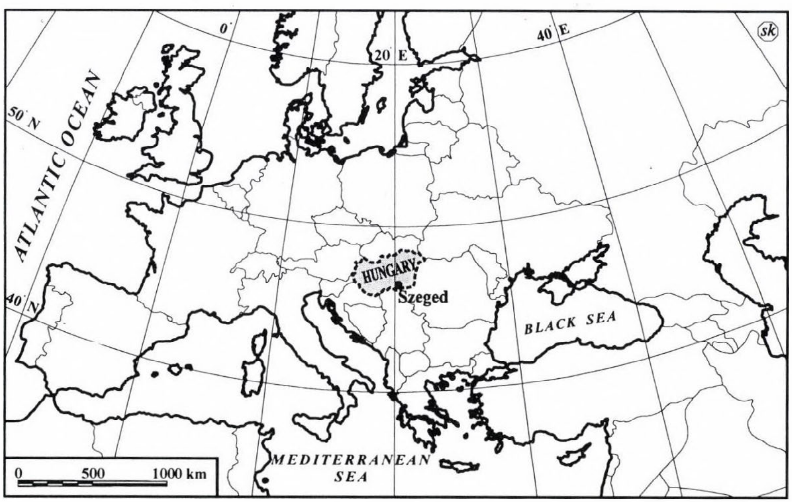

Fig. 1. Location of Hungary and Szeged in Europe.

Table 2. Monthly and annual means or sums of meteorological parameters in the region of Szeged (1961–1990)

Parameter	J	F	M	A	M	J	J	A	S	O	N	D	Year
Temperature (°C)	-1.8	1.0	5.6	11.1	16.2	19.2	20.8	20.2	16.4	11.0	5.1	0.6	10.4
Precipitation (mm)	29	25	29	40	51	72	50	60	34	26	41	40	497
Sunshine duration (h)	62	87	143	181	235	252	288	267	211	170	82	51	2029
Cloudiness (%)	70	68	63	60	58	54	45	42	45	49	69	76	58
Wind speed (ms^{-1})	3.3	3.4	4.0	3.7	3.2	2.9	2.9	2.7	2.6	3.0	3.0	3.7	3.2
Relative humidity (%)	85	82	73	68	66	67	65	67	70	73	83	87	74
Vapor pressure (hPa)	4.9	6.5	6.8	8.9	12.3	15	16	15.8	13.2	9.8	7.6	5.8	10.1

The city's population of 160,000 (1998) lives within an administration district of 281 km^2. As for the city structure, its basis is a boulevard-avenue road system. Numbers of different land-use types are present including a densely built center with medium wide streets and large housing estates of tall concrete blocks of flats set in wide green spaces. Szeged also contains areas used for industry and warehousing, zones occupied by detached houses and considerable open spaces along the banks of the river, in parks and around the city's outskirts (*Fig. 2*).

As the urban and suburban areas occupy only about 25–30 km^2, our investigation focused only on the inner part of the administration district (Fig. 2). This study area was divided into two sectors and subdivided further into 0.5 km × 0.5 km square grid cells (*Fig. 3*). The same grid size was employed, for example, in a human bioclimatological analysis of Freiburg, Germany, a city of similar size to Szeged (*Jendritzky* and *Nübler*, 1981) and in an other investigation of UHI in Seoul, Korea (*Park*, 1986). *Sailor* (1998) chose a 2 km × 2 km network for his hypothetical city, where he simulated the impacts of vegetative augmentation on the annual heating and cooling degree days. Therefore, our grid network can be regarded as a rather dense one. In the study area there are 107 grid cells totaling 26.75 km^2, covering the urban and suburban parts of Szeged (mainly inside of the circle dike that protects the city from floods caused by the Tisza River). Outlying parts of the city, characterized by village and rural features, are not included in the grid except for four cells at the western side of the area. These cells are needed in order to determine the temperature contrast between urban and rural areas. The grid was established by quartering the 1 km × 1 km square network of the Unified

National Mapping System (EOTR), that can be found on topographical maps of Hungary at the scale of 1:10,000.

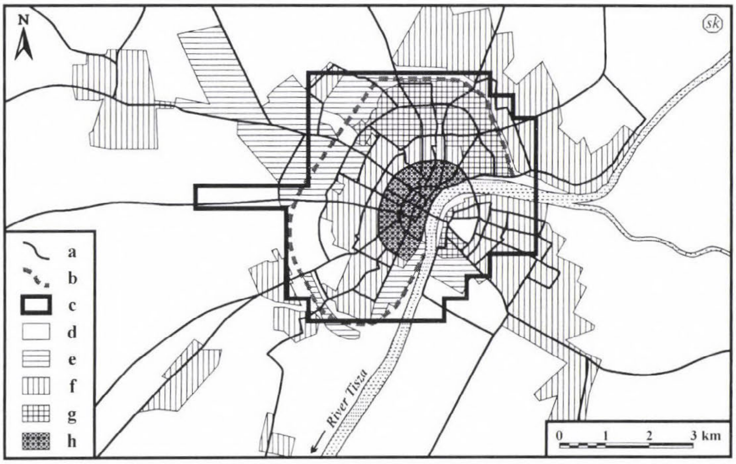

Fig. 2. Characteristic land-use types and road network in Szeged: (**a**) road, (**b**) circle dike, (**c**) border of the study area, (**d**) agricultural and open land, (**e**) industrial area, (**f**) 1–2 storey detached houses, (**g**) 5–11 storey apartment buildings and (**h**) historical city core with 3–5 storey buildings.

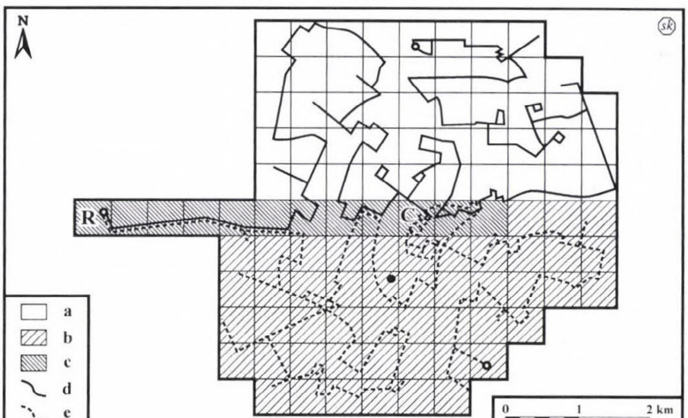

Fig. 3. Division of the study area into 0.5 km × 0.5 km grid cells: (**a**) northern sector, (**b**) southern sector, (**c**) overlap area and (**d, e**) the measurement routes. Rural and central grid cells are indicated by R and C, respectively. The permanent measurement site at the University of Szeged is indicated as •.

The examination of the spatial and temporal distribution of surface air temperature was based on mobile observations during the period of March, 1999–February, 2000. In case of surface UHI and near surface air UHI investigations, the moving observation with different vehicles (car, tram, helicopter, airplane, satellite) is an often used process (e.g., *Johnson*, 1985; *Yamashita*, 1996; *Voogt* and *Oke*, 1997; *Klysik* and *Fortuniak*, 1999; *Tumanov et al.*, 1999).

In order to collect data on maximum UHI intensity (namely the temperature difference between urban and rural areas) at every grid cell, mobile measurements were performed on fixed return routes once a week during the studied period (altogether 48 times) to accomplish an analysis of air temperature over the entire area. This one-week frequency of car traverses secured sufficient information on different weather conditions, except for rain.

Division of the study area into two sectors was needed because of the large number of grid cells. The northern and southern sectors consisted of 59 grid cells (14.75 km^2) and 60 grid cells (15 km^2), respectively, with an overlap of 12 grid cells (3 km^2). The lengths of the fixed return routes were 75 and 68 km in the northern and southern sectors, respectively, and took about 3 hours to traverse (Fig. 3). Such long and return routes were necessary to gather temperature values in every grid cell and to make time-based corrections. Temperature readings were obtained using a radiation-shielded LogIT HiTemp resistance temperature sensor (resolution of 0.01 °C), which was connected to a portable LogIT SL data logger for digital sampling inside the car. Since the data were collected every 16 s at an average car speed of 20–30 km h^{-1} the average distance between measuring points was 89–133 m. The temperature sensor was mounted 0.60 m in front of the car at 1.45 m above ground to avoid engine and exhaust heat. This is similar to the measurement system used by *Ripley et al.* (1996) in Saskatoon, Saskatchewan. The car speed was sufficient to secure adequate ventilation for the sensor to measure the momentary ambient air temperature.

After averaging the measurement values by grid cells, time adjustments to the reference time were applied assuming linear air temperature change with time. This linear change was monitored using the continuous records of the permanent automatic weather station at the University of Szeged (Fig. 3). The linear adjustment appears to be correct for data collected a few hours after sunset in urban areas. However, because of the different time variations of cooling rates, it is only approximately correct for suburban and rural areas (*Oke* and *Maxwell*, 1975). The reference time, namely the likely time of the occurrence of the strongest UHI, was 4 hours after sunset, a value based on earlier measurements in 1998 and 1999 (*Boruzs* and *Nagy*, 1999). Consequently, every grid cell of 59 in the northern sector or every grid cell of 60 in the southern sector can be characterized by one temperature value for every measuring night. These temperature values refer to the center of each cell.

We determined urban-rural air temperature differences (UHI intensity) by cells referring to the temperature value of the grid cell (the most western cell in the investigated area), where the synoptic weather station of the Hungarian Meteorological Service is located. This grid cell (labeled by R) containing this station was regarded as rural (Fig. 3), because the records of this station were used as rural data in the earlier studies on the urban climate of Szeged (e.g., *Unger*, 1996, 1999). The 107 points (the above mentioned grid cell center-points) cover the urban parts of Szeged and they provide an appropriate basis to interpolate isolines. The isolines, therefore, can show detailed descriptions of thermal field within the city at the time of the strongest effects of urban factors. In order to draw the isotherms, a geostatistical gridding method, the standard kriging procedure was used.

Parameters of land-use for the grid cells were determined by GIS (Geographical Information System) methods combined with remote sensing analysis of SPOT XS images (*Mucsi*, 1996). Vector and raster-based GIS databases were produced in the Applied Geoinformatics Laboratory of the University of Szeged. The digital satellite image was rectified to the EOTR using 1:10 000 scale maps. The nearest-neighbour method of resampling was employed, resulting in a root mean square value of less than 1 pixel. Since the geometric resolution of the image was 20 m × 20 m, small urban units could be assessed independently of their official (larger scale) land-use classification. Normalised Vegetation Index (*NDVI*) was calculated from the pixel values, according to the following equation:

$$NDVI = (IR - R) \,/\, (IR + R), \tag{1}$$

where *IR* is the pixel value in the infrared band and *R* is the pixel value in the red band. The range of *NDVI* values is from -1 to +1, indicating the effect of green space in the given spatial unit (*Lillesand* and *Kiefer*, 1987). Built-up, water, vegetated and other surfaces were distinguished according to the *NDVI* value. The spatial distribution of these land-use types of each grid element was calculated using cross-tabulation.

In order to assess the extent of the relationships between the maximum UHI intensity and various urban surface factors, multiple correlation and regression analyses were used. The selection of the parameters was based on their role in determining small-scale climate variations (*Adebayo*, 1987; *Oke*, 1987; *Golany*, 1996).

The selected urban parameters were percentage of built-up area (covered surface-building, street, pavement, parking lot, etc.) and water surface by grid cells, as well as distance to the city centre (grid cell labeled by C, see Fig. 3).

This distance can be considered as an indicator of the location of a cell within the city. These three parameters are constants for the complete (one-year long) measurement period. However, in each cell their values vary from place to place within the city. They are constants temporally but variables spatially. Searching for statistical relationships, we will take into account that our parameters are at once variables and constants.

The ratio of the built-up area to the total area by grid cells in 25% increments is displayed in *Fig. 4*. Fig. 4 shows, that, for example, the location of the River Tisza (low built-up ratio) is clearly recognised with its east-to-south curve in the south-eastern part of the study area (see also Fig. 2).

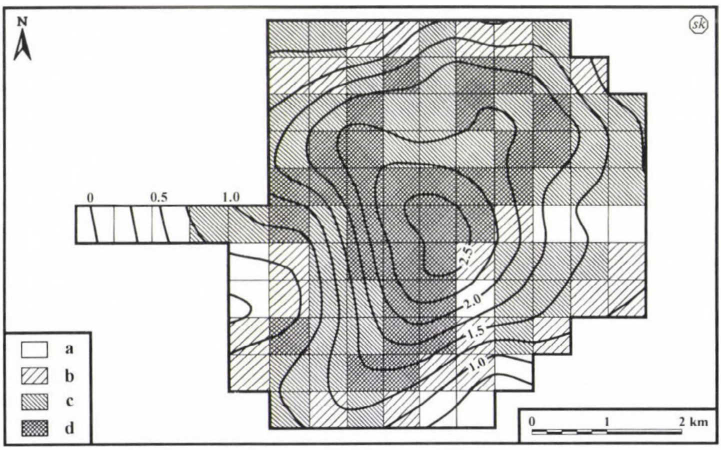

Fig. 4. Spatial distribution of the mean maximum UHI intensity (°C) and the built-up density of the study area by grid cells (ratio of the built-up area to the total cell area) (**a**) 0–25%, (**b**) 25–50%, (**c**) 50–75% and (**d**) 75–100%) during the studied one-year period (March 1999–February 2000) in Szeged.

3. Result and discussion

3.1 Spatial distribution of the maximum UHI

In our investigation not only the one-year period is studied, but within this period we distinguish the so called heating (between October 16 and April 15) and non-heating (between April 16 and October 15) seasons.

It can be seen in *Figs. 4, 5* and *6* that built-up density has a significant influence on the spatial patterns of the mean maximum UHI intensity (4 hours after sunset as supposed). The most obvious common features of these patterns are that the isotherms show almost regular concentric shapes with values increasing from the outskirts toward the inner urban areas. A vigorous deviation from this concentric shape occurs in the north-eastern part of the city, where the isotherms stretch toward the suburbs. This can be explained by the influence of the large housing estates with tall concrete buildings located mainly in the north-eastern part of the city with a built-up ratio higher than 75% (Fig. 2).

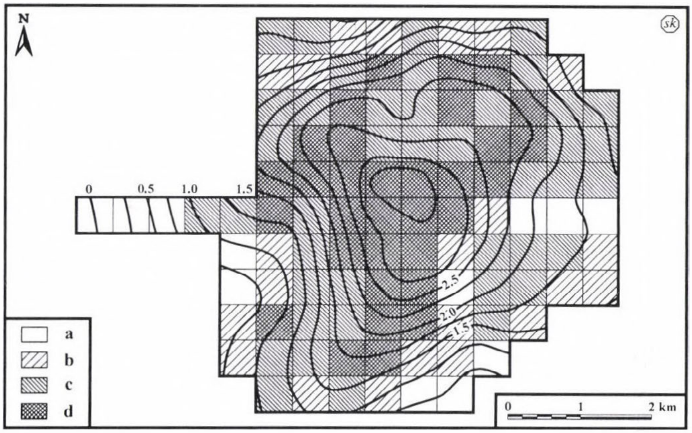

Fig. 5. Spatial distribution of the mean maximum UHI intensity (°C) during the non-heating season (April 16–October 15) in Szeged.

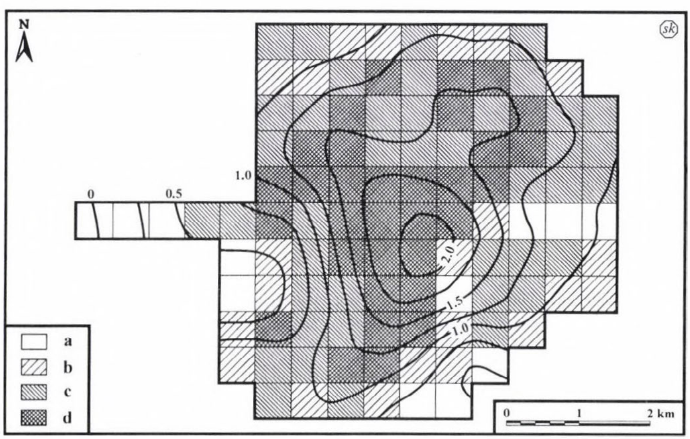

Fig. 6. Spatial distribution of the mean maximum UHI intensity (°C) during the heating season (October 16–April 15) in Szeged.

For the one-year period (Fig. 4), as it was expected, the highest differences (more than 2.5°C) are concentrated mainly in the densely built-up city center (>75%) covered by about 2.5 grid cells (about 0.6 km^2). The strongest intensity (2.60°C) occurs in the central grid cell (C). A mean maximum UHI intensity of higher than 2°C indicates significant thermal modification. In this period in Szeged, the extension of the area, characterized by significant thermal modification, is about 19 grid cells (4.5–5.0 km^2), which is about 18% of the total investigated area.

In the non-heating season, the spreading out of the isolines of 2.25°C and 2.5°C to the north-west of the center, and the isolines of 1.5°C and 1.75°C to the south-west are also caused by the high built-up ratio of more than 75% (Fig. 5). The highest differences (more than 2.75°C) are concentrated in the densely built-up city center (>75%) covered by about 8 grid cells (2 km^2). The greatest intensity (3.18°C) is to the north of the central grid cell (C) in an adjacent cell. The mean maximum UHI intensity of higher than 2°C is relatively large compared to the size of the study area. It covers about 40 grid cells (10 km^2), which is about 37% of the investigated area.

In the heating season, the high built-up ratio of more than 75% also caused the streching out of the isoline of 1.5°C to the north-west, and the isolines of 1°C and 1.25°C to the south-west (Fig. 6). The highest differences (more than 2°C) are concentrated in the city centre (>75%), covered by less than 2 grid cells (0.5 km^2), which is only about 2% of the total area. The strongest intensity (2.12°C) occurs in the central grid cell (C).

The seasonal differences may be formed as a consequence of different weather characteristics in the two seasons rather than as a consequence of heating or non-heating of inhabitants. This explanation is supported by *Klysik* and *Fortuniak* (1999), who found similar differences in the UHI intensities between warm and cold seasons in Łódź, Poland. As in Poland, in Hungary (particularly in the Szeged region) the climate conditions in winter, conducive to the formation of UHI, are less common (Table 1). Thus, in the warmer, therefore non-heating season, the role of appropriate weather conditions (stronger solar radiation income, more frequent clear sky and weak wind) and the reduced latent heat transport because of the more impermeable and guttered urban terrain is more pronounced in the development of UHI than the building heating in urban areas. Consequently, in case of Szeged, the significance of artificial heating in the development of UHI is rather limited.

3.2 Statistical relationships

In order to determine model equations for the maximum value of UHI intensity in the diurnal temperature course (ΔT), we use the earlier mentioned parameters (their labels are in brackets): distance from the central grid cell in km

(D), ratio of built-up surface as a percentage (B) and ratio of water surface as a percentage (W). These parameters are variables spatially, namely by grid cells, but constants temporally.

The bivariate analysis will be accurate if the total period averages of ΔT for each cell are correlated against each of the cell value of D, B and W, thus the time averages of the maximum UHI intensities vary by grid cells (the number of data pairs is $n = 107$).

Table 3 contains the results of the bivariate correlation analyses on ΔT against the urban surface parameters considered in this study. As the table shows, among the examined parameters D has the largest correlation coefficients ($r_{\Delta T,D}$). This fact supports the establisment in Chapter 3.1 on the regular concentric shapes of the UHI isotherms in Szeged. The first two coefficients (D, B) are significant at 0.1% in all the three periods. The strong relationships between ΔT and D as well as B by periods can be seen in the *Figs. 7, 8* and *9.* The ratio of water surface seems not to be important ($r_{\Delta T,W} < 0.06$ always, so it is not significant even at 10% level), for this reason it is not necessary to be used in the multiple regression equations. This statistically insignificant role of water surfaces (mainly connected with the River Tisza) in the development of the maximum heat island in Szeged can be explained by the relatively large size of the grid cells, therefore, water surfaces can be found only in 39 grid cells from the total number of 107 and their ratio is only few percentages in most of the grids.

Table 3. Values of bivariate correlation coefficients between the average of maximum UHI intensity (ΔT) in °C and urban surface parameters (D – distance from the city center in km, B – ratio of built-up area as a percentage and W – ratio of water surface as a percentage) by grid cells in different periods in Szeged ($n = 107$)

Bivariate correlation coefficient (n = 107)	**March 1999–February 2000**		**April 16–October15 (non-heating season)**		**October 16–April 15 (heating season)**	
	Value	**Significance level**	**Value**	**Significance level**	**Value**	**Significance level**
$r_{\Delta T,D}$	-0.837	0.1%	-0.861	0.1%	-0.760	0.1%
$r_{\Delta T,B}$	0.685	0.1%	0.675	0.1%	0.674	0.1%
$r_{\Delta T,W}$	0.044	–	0.056	–	0.020	–

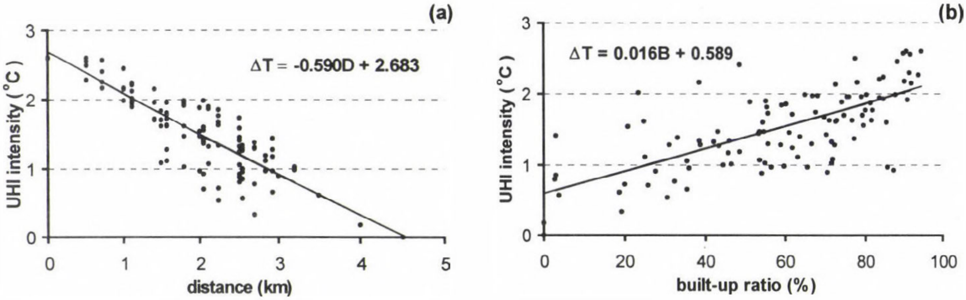

Fig. 7. Maximum UHI intensity (ΔT) as a function of (*a*) the distance from the center (D) and (*b*) built-up ratio (B) with the best fit regression lines in the one-year period (March 1999–February 2000) in Szeged.

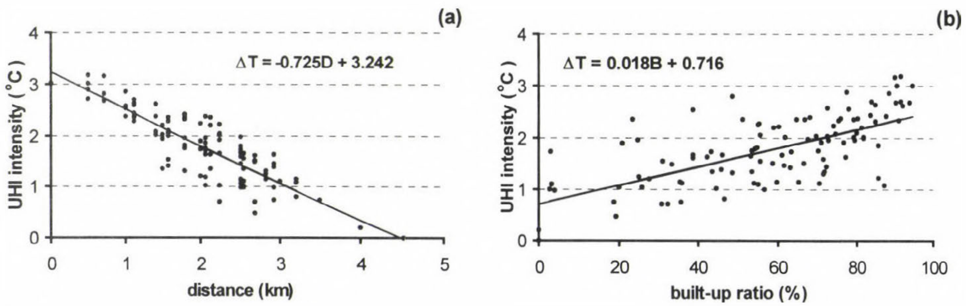

Fig. 8. As *Fig. 7* but in the non-heating season (April 16–October 15).

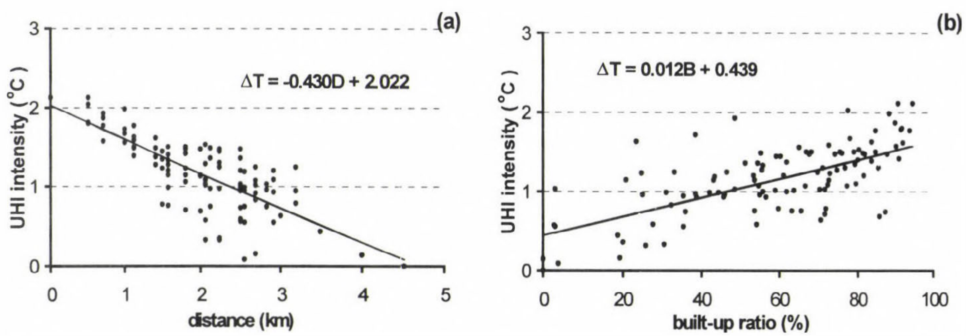

Fig. 9. As *Fig. 7* but in the heating season (October 16–April 15).

The sequence of the parameters, entered in the multiple stepwise regression, was determined with the help of the magnitude of the bivariate correlation coefficients. *Table 4* contains the results of this stepwise regression on ΔT against the urban surface parameters in the three investigated periods. As the results show, the distance from the city center is most pronounced, but the role of the built-up density is also important. The improvements in the explanation caused by entering of B, namely the differences as a percentage in the correlation coefficients in the fourth column of the table (Δr^2) of 6.8%, 5.3% and 15.0% cannot be neglected. The moderate large values of Δr^2 can be explained by the fact that D and B in a city structure are not entirely independent from each other.

Table 4. Values of the stepwise correlation of maximum UHI intensity (ΔT) and urban surface parameters by grid cells in different periods in Szeged (n = 107)

Period	Parameter entered	Multiple $\lvert r \rvert$	Multiple r^2	Δr^2
March 1999–	D	0.837	0.701	0.000
February 2000	B	0.877	0.769	0.068
April 16–October 15	D	0.861	0.742	0.000
(non-heating season)	B	0.892	0.795	0.053
October 16–April 15	D	0.760	0.577	0.000
(heating season)	B	0.816	0.666	0.150

Table 5. Best fit model equations for the average of maximum UHI intensity (ΔT) using urban surface parameters in different periods in Szeged (n = 107)

Period	Parameters	Multiple linear regression equations	Significance level
March 1999–	D	$\Delta T = -0.590D + 2.683$	0.1%
February 2000	D, B	$\Delta T = -0.466D + 0.007B + 2.016$	0.1%
April 16–	D	$\Delta T = -0.725D + 3.242$	0.1%
October 15	D, B	$\Delta T = -0.593D + 0.008B + 2.533$	0.1%
October 16–	D	$\Delta T = -0.430D + 2.022$	0.1%
April 15	D, B	$\Delta T = -0.315D + 0.007B + 1.406$	0.1%

Referring to the investigated periods, *Table 5* contains the model equations which describe ΔT in the best way. The absolute values of the multiple correlation coefficients (r) between the maximum UHI intensity and the parameters are 0.837 and 0.877 for the one-year period, 0.861 and 0.892 for the non-heating season and 0.760 and 0.861 for the heating season (they are all significant at 0.1% level) (*Tables 4* and *5*). The corresponding squares of these multiple correlation coefficients (r^2) provide explanations of 70.1% and 76.9%, of 74.2% and 79.5 and of 57.7% and 66.6% of the variance, respectively.

4. Conclusions

The seasonal spatial distribution of the maximum urban heat island and its quantitative relationships with urban surface parameters are investigated in the present study. The results indicate that:

- The spatial patterns of the maximum UHI intensity have regular concentric shapes and the isotherms increase from the outskirts towards the central urban areas in all the three studied periods.

- The anomalies in the regularity are caused by the alterations in the built-up density.

- There are significant differences in the magnitudes of the seasonal (heating and non-heating) patterns. The area of the mean maximum UHI intensity of higher than 2°C — indicates significant thermal modification caused by urbanisation — is 18 times larger in the non-heating than in the heating season (2% and 37%, respectively).

- As the correlation coefficients of the parameters show, a short distance from the city center and a high built-up ratio, which prevail mostly in the inner parts of the city, play important roles in the increment of the urban temperature.

Consequently, our preliminary results prove that the statistical approach which determines the behaviour of the UHI intensity in Szeged is promising and this fact urges us to make more detailed investigations. We are planning to extend this project by modeling urban thermal patterns as they are affected by weather conditions with a time lag. We intend to employ the same parameters used in this study, as well as additional urban and meteorological parameters, to predict the magnitude and spatial distribution of the maximum UHI intensity on the days characterised by any kind of weather conditions (apart from the ones with precipitation) at any time of the year without recourse to extra mobile measurements. These tasks require longer-term data sets, so we intend to gather data for a period of more than one year.

The results will be of practical use in predicting the pattern of energy consumption inside the city. They can be used to forecast and plan the energy demand, particularly in cold and warm periods of the year, when energy consumption of heating and cooling, respectively, is highest.

Acknowledgements—The research was supported by the grants of the Hungarian Scientific Research Fund (OTKA T/023042) and the Ministry of Education (FKFP-0001/2000.). The authors wish to give special thanks to the students who took part in the measurement campaigns and in data pre-processing.

References

Adebayo, Y.R., 1987: Land-use approach to the spatial analysis of the urban 'heat island' in Ibadan. *Weather 42,* 272-280.

Boruzs, T. and *Nagy, T.*, 1999: *Urban Influence on the Climatological Parameters* (in Hungarian). MSc thesis, University of Szeged, Szeged, 81 pp.

Chow, S.D., Zheng, J. and *Wu, L.*, 1994: Solar radiation and surface temperature in Shangai City and their relation to urban heat island intensity. *Atmos. Environ. 28,* 2119-2127.

Golany, G.S., 1996: Urban design morphology and thermal performance. *Atmos. Environ. 30,* 455-465.

Goldreich, Y., 1992: Urban climate studies in Johannesburg, a sub-tropical city located on a ridge - A review. *Atmos. Environ. 26B,* 407-420.

Grimmond, C.S.B., Cleugh, H.A. and *Oke, T.R.*, 1991: An objective urban heat storage model and its comparison with other schemes. *Atmos. Environ. 25B,* 311-326.

Grimmond, C.S.B. and *Oke, T.R.*, 1991: An evapotranspiration-interception model for urban areas. *Water Resources Res. 27,* 1739-1755.

Jendritzky, G. and *Nübler, W.*, 1981: A model analysing the urban thermal environment in physiologically significant terms. *Arch. Met. Geoph. Biol. Ser.B. 29,* 313-326.

Johnson, D.B., 1985: Urban modification of diurnal temperature cycles in Birmingham. *J. Climatology 5,* 221-225.

Johnson, G.T., Oke, T.R., Lyons, T.J., Steyn, D.G., Watson, I.D. and *Voogt, J.A.*, 1991: Simulation of surface urban heat islands under 'ideal' conditions at night, I: Theory and tests against field data. *Boundary Layer Met. 56,* 275-294.

Klysik, K. and *Fortuniak, K.*, 1999: Temporal and spatial characteristics of the urban heat island of Łódź, Poland. *Atmos. Environ. 33,* 3885-3895.

Kuttler, W., 1998: *Stadtklima*. In *Stadtökologie* (eds.: *Sukopp, H.* und *Wittig, R.*). *Gustav Fischer, Stuttgart-Jena-Lübeck-Ulm,* 125-167.

Kuttler, W., Barlag, A-B. and *Roßmann, F.*, 1996: Study of the thermal structure of a town in a narrow valley. *Atmos. Environ. 30,* 365-378.

Lillesand, T.M. and *Kiefer, R.W.*, 1987: *Remote Sensing and Image Interpretation.* J. Wiley & Sons, New York, 705 pp.

Mucsi, L., 1996: Urban land use investigation with GIS and RS methods. *Acta Geographica Univ. Szeged 25,* 111-119.

Myrup, L.O., McGinn, C.E. and *Flocchini, R.G.*, 1993: An analysis of microclimatic variation in a suburban environment. *Atmos. Environ. 27B,* 129-156.

Nkemdirim, L.C., 1978: Variability of temperature fields in Calgary, Alberta. *Atm. Environment 12,* 809-822.

Oke, T.R., 1973: City size and the urban heat island. *Atmos. Environ. 7,* 769-779.

Oke, T.R., 1976: The distinction between canopy and boundary layer urban heat islands. *Atmosphere 14,* 268-277.

Oke, T.R., 1987: *Boundary Layer Climates.* Routledge, London and New York, 405 pp.

Oke, T.R., 1997: *Urban climates and global environmental change.* In *Applied Climatology* (eds.: *R.D Thompson.* and *A Perry*). Routledge, London-New York, 273-287.

Oke, T.R. and *Maxwell, G.B.*, 1975: Urban heat island dinamics in Montreal and Vancouver. *Atmos. Environ. 9,* 191-200.

Park, H-S., 1986: Features of the heat island in Seoul and its surrounding cities. *Atmos. Environ. 20,* 1859-1866.

Ripley, E.A., Archibold, O.W. and *Bretell, D.L.*, 1996: Temporal and spatial temperature patterns in Saskatoon. *Weather 51*, 398-405.
Sailor, D.J., 1998: Simulations of annual degree day impacts of urban vegetative augmentation. *Atmos. Environ. 32*, 43-52.
Sundborg, A., 1950: Local climatological studies of the temperature conditions in an urban area. *Tellus 2*, 222-232.
Tapper, P.D., Tyson, P.D., Owens, I.F. and *Hastie, W.J.*, 1981: Modeling the winter urban heat island over Christchurch. *J. Appl. Meteorology 20*, 365-367.
Tumanov, S., Stan-Sion, A., Lupu, A., Soci, C. and *Oprea, C.*, 1999: Influences of the city of Bucharest on weather and climate parameters. *Atmos. Environ. 33*, 4173-4183.
Unger, J., 1996: Heat island intensity with different meteorological conditions in a medium-sized town: Szeged, Hungary. *Theor. Applied Climatology 54*, 147-151.
Unger, J., 1999: Urban-rural air humidity diferences in Szeged, Hungary. *Int. J. Climatology 19*, 1509-1515.
Unger, J., Sümeghy, Z., Gulyás, Á., Bottyán, Zs. and *Mucsi, L.*, 1999: Modeling the maximum urban heat island. *Proceed. ICB-ICUC'99*, Sydney, Australia, ICUC10.4.
Voogt, J.A. and *Oke, T.R., 1991*: Validation of an urban canyon radiation model for nocturnal long-wave radiative fluxes. *Boundary Layer Met. 54*, 347-361.
Voogt, J.A. and *Oke, T.R.*, 1997: Complete urban surface temperatures. *J. Appl. Meteorology 36*, 1117-1132.
Yamashita, S., 1996: Detailed structure of heat island phenomena from moving observations from electric tram-cars in metropolitan Tokyo. *Atmos. Environ. 30*, 429-435.

IDŐJÁRÁS

Quarterly Journal of the Hungarian Meteorological Service
Vol. 104, No. 4, October–December 2000, pp. 269–277

The use of biometeorological forecasting to raise sports achievements

Imre Örményi

International Committee for Research and Study of Environmental Factors, Hungarian Section, Király utca 52, H-1061 Budapest, Hungary

(Manuscript submitted for publication 16 March 2000; in final form 26 June 2000)

Abstract—The author furnished sport biometeorological forecasts to a selected team before each of its matches during the indoor handball championship in the men's premier league of Hungary in 1990/1991. The players' individual weather sensitivity was established prior to the championship. Keeping this in mind, the outcome of earlier studies on the interrelationship between sports achievements and various weather phenomena and alterations in solar activity and/or geomagnetism made possible to predict alterations of the players' nervous state and their expected individual performances. Particular attention was paid to the goalkeepers' performances and the expected changes of their reaction time. As a result of the applied procedure the selected handball team won the championship, moving from the fifth place to the first.

Key-words: handball players, sporting activity, biometeorological forecasting.

1. Introduction

Sport specialists are more or less familiar with the investigations of influence of certain climates on sports and their practical use. It is less known, however, that alterations of weather components, especially those with frontal passages have influence on sport performance too. Such investigations were carried out in Hungary on marksmen (*Horváth,* 1960), male handball players (*Örményi* and *Ried,* 1966), on Hungarian sprinters and long-distance runners, discus and hammer throwers and high jumpers (*Miltényi* and *Kereszty,* 1966). Most recently *Örményi* (1991) investigated the physiological reactions and performances of representative ice hockey goalkeepers.

To compensate the players' possible bad performances, benefit of forecasting of sport achievements can be a useful tool. Compensation is possible by substituting some of the players for others and resort new tactics.

Sport meteorological forecast was first tested on an ice hockey goalkeeper of the national team on December 9, 1961 in the Kisstadion of Budapest. The forecast was tested after founding interrelations between weather elements and sport achievements. On that particular occasion, after completing on him the appropriate medical examinations, the goalkeeper's excellent performance was expected, and in fact he reached an extremely good result of 91% as compared to his 63% performance averaged over the entire ice hockey season. (Performance means the scores divided by the number of shots reaching the goal.)

Since that time our intuition concerning reality of raising sports achievements by the use of biometeorological forecasts has been confirmed by the relevant research on the matter. This time we investigated the use of biometeorological forecasts during a complete indoor handball championship. This type of sport had been investigated before, so we could apply the results to test the forecasts serially.

2. *Methods and used material*

Complex effect of meteorological, biological and psychological factors on the performance of indoor handball players was investigated in details by *Örményi* and *Ried* (1966). During the winter championship of the national handball league in 1958/1959, were the three top teams of Hungary, named Honvéd of Budapest, Elektromos of Budapest and Kábelgyár of Budapest, investigated.

The authors considered endogenous and exogenous factors that have influences on sports achievements. Physical state of the contestants, stage fright, circadian rhythm of the organism and the sportsmen's health state were counted among endogenous factors. Exogenous factors were those characterized by changes in the outside world, e.g., referees, spectators, climatic and meteorological factors. Investigations were extended to the physiological functions, psychological state, meteorological conditions, players' sporting achievements.

The following meteorological factors were taken into consideration: dry and wet bulb temperature, relative humidity, vapor pressure of the air, air movements, cooling power[1], the equivalent temperature, the effective temperature, air pressure tendency, various types of frontal passages, air masses near the surface and vertical motions.

Records were made about the successful actions and those with no success, directions and strengths of shots, shortened playing time because of substitution or referees' bad judgements, number of offensive and defensive actions were summed up.

---

[1] Measured by katathermometer providing a value on the complex effect of air temperature, humidity and air flow.

All the data recorded were systematized and analyzed according to Schelling's T-method (*Schelling,* 1940). For better understanding *Table 1* presents the T-values characterising the interrelationships between frontal passages and the playing elements in handball (*Örményi* and *Ried*, 1966). We took into consideration happenings ± 10 hours around the front passage.

Table 1. Interrelationships between frontal passages and the playing elements in handball

Playing elements	**Frontal passages**					
	Warm front		**Cold front**		**Subsidence**	
	before	**after**	**before**	**after**	**before**	**after**
Performance*	-2.2	0.7	2.37	0.19	–	-0.47
Efficiency from the first half to the second one*	-2.31	-0.43	1.67	0.38	–	-1.16
Mishit*	-1.14	-1.84	-0.20	0.03	–	2.15
Goal*	-1.84	2.10	-0.99	-0.96	–	-0.94
Total number of shots	20.6	18.6	18.5	24.3	–	17.9
Number of attacks	18.8	23.1	21.3	21.3	–	21.5

* If $T=1.96$ the probable error is $P=0.05$. In case of $T=3.0$ the probable error level is $P=0.0027$

Table 1 indicates that performances as well as the players' efficiency in the second half of the game significantly decrease *before a warm front passage* and the number of goals is remarkably less due to the increased errors in aiming.

After a warm front passage performance and efficiency for the second half of the game increase in relation to the prefrontal situation. Number of attacks and the number of goals are the highest (probable error level $P<0.05$).

The players' performance and the efficiency are the best ($P<0.05$) *before a cold front passage*, though they are not very active (number of shots and attacks are relatively low), and the goals are below the average level.

After a cold front passage performance and efficiency changes are around the average. Shots are very numerous but the rate of success is not good at all.

Nothing can be said about the figures before a divergence (subsidence), as no such cases were observed during the investigated period.

Performance decreases *after a divergence*. A remarked lack of concentration resulting in high number of mishits ($P<0.05$) can be experienced and the number of shots is the smallest at the same time.

Considering the *air masses on the ground level,* performance significantly increases ($P<0.05$) during *subtropical air masses*. In *maritime Arctic air masses* the performance is negative (T=–1.38) compared to the average level.

If there is a warm advection in the higher levels of the troposphere with a sudden subtropical influx, the achievements seem to be the worst (T=–3.40). Compare this with the figures before warm front passages. If there is no influx of subtropical air masses or warm front or advection in the higher levels of the troposphere, accomplishments seem to be the best (T=2.97).

These results can be applied only to those teams where most of the players are warm front sensitive. These results were applied to the first division of the team Elektromos during a whole handball season from September 29, 1990 to April 28, 1991.

3. Weather sensitivity

It can be determined by various methods such as filling out a questionnaire (*Örményi,* 1972), inhalation of artificial air ions of various polarity (*Örményi, et al.*, 1981) or visual inspection of videoclips based on anthropogenic determination of weather sensitivity types according to *Curry* (1969). Prior to the first match we have determined the type of weather sensitivity by two methods. The first one consisted of filling out a questionnaire based on elaboration of answers of 26,000 Hungarian citizens (*Örményi,* 1972, 1987). The results were published in journal Időjárás (*Örményi*, 1993).

Table 2. Weather sensitivity of Budapest population and numbers of the selected team (in percent)

Sensitivity	Budapest population	Selected team's members
Cold front	29.5	18.8
Mixed front	19.3	18.8
Mixed front	51.2	62.5

The second test was based on inhalation of artificial air ions of various polarity (*Örményi et al.,* 1981). The reason of the ion inhalation was the following. Our former natural atmospheric ion measurements carried out in Budapest at the Danube riverside (opposite to the Margaret Island in Buda), have proved, that the unipolarity coefficient (q = n+/n– where n is the number of ions in 1 ccm) was below 1 during the first day of inflow of Arctic air masses, which means negative ion preponderance against positive one in the medium small ion range. (The limit mobility $K_g = 1.9 \times 10^{-2}$ cm^{-2} Vsec). During an influx of subtropical air masses, the preponderance of positive ions seems to be in excess to negative ones (*Örményi*, 1967).

During the inhalation of artificially generated ions (by a Medicor made bipolar type ionizator), we have measured blood pressure and pulse rate and calculated the vegetative index[2] (V.I.) of *Kérdő* (1966). If V.I. < 0, vegetative reactions tend to orthostatic (vagotonic), if V.I. > 0, then to sympathetic form of reactions. Generally the trend in physical burden is more expressive. The standard error of vegetative index calculated from measurement of 1000 healthy sportsmen was ± 13 units. This index showed differences (5–50 units of vegetative index) during inhalation of ions of different polarity. The type of weather sensitivity can be determined during inhalation of positive or negative ions as follows: Prior to the inhalation of ions[3] (25 cm away from the mouth) p and d values are measured, then 5 minutes after the inhalation of ions another measurement (p and d) follows. This is followed by a 15-minute recovery period (adaptation and normal breathing without artificial ions). Calculus of pulse and measurement of diastolic pressure follow again, so we obtain 3-3 V.I. values.

The type of weather sensitivity gives that type of ion polarity, where the vegetative tone trends to sympathetic tone. *In case of warm front sensitivity, this situation occurs during positive ion preponderance, meanwhile in case of cold front sensitivity, during negative ion preponderance. In case of mixed type weather sensitivity, the burden of both type of ion polarity results in a similar trend in vegetative index.*

The type of weather sensitivity of top players of rival teams had been determined. This was applied before each derby using video records of the mentioned teams such as BRAMAC (Fotex) Veszprém, RÁBA ETO from Győr and Tatabánya. This procedure was based on anthropogenic determination of the types of weather sensitivity according to *Curry* (1969). Having these results there was a possibility to change tactics.

4. *Danger of injury*

Ambulance cases including sports accidents and changes of the 3 Hz ELF sferics level in Budapest were investigated by *Örményi and Majer* (1985) on the basis of a vast amount of data. The outcome of this investigation is of

---

[2] V.I. = $(1 - d/p) \times 100$, where d = the diastolic blood pressure in mmHg, p = the pulse rate during 1 minute.

[3] The ion flux was 50,000 ion/ccm of small ions.

prognostic significance. The mathematical-statistical analysis showed that the number of sports accidents significantly increases if the sferics level decreases by 50% on successive days.

5. *Forecasting*

Prior to each match the first trainer got a forecast for the following factors: (1) Types of expected weather changes, i.e., frontal passage, subsidence, situation without fronts. (2) Types of expected air masses near the ground — according to *Berkes* (1961). It should be noted, that the unipolarity coefficient differs in various biologically active air masses. (3) During disturbed weather conditions, the expected tendency of visual reaction time of each goal keeper (shortened or prolonged). (4) The character of play: quiet, average, tense atmosphere with rudeness or overhastiness with inaccurate ball technique. (5) Bad or good achievements of certain top players, especially before hard games. (6) Possibility of danger of injury during the match. (7) There was also a forecast during a geomagnetic storm referring to the expected general stress condition. This was measured by indirect method, namely with alteration of natural secondary gamma radiation and ELF sferics on 3 Hz range measured in my former institute (National Institute for Rheumatics and Physiotherapy, Budapest).

6. *Philosophy*

The basic idea of this experiment was to provide regular biometeorological forecast for the coach of a selected handball team who showed interest in learning its use and saw the changes in the team's achievements.

7. *Results and discussion*

On the basis of the measurements of weather sensitivity types, it was established, that 10 players belonged to different subtypes of warm front sensitivity, 3 to mixed front sensitive type and 3 to cold front sensitive type. Previous experiences have shown that among top trained contestants, weather sensitivity seems to be rather rare (*Örményi* and *Ried*, 1966). In spite of that, in this study 4 players proved to be strongly labile and other 2 were near to this condition.

It should be noted, that the distribution of weather sensitivity of the questioned 26,000 people was similar to that of the selected team (Table 2).

Since the percentage distribution of warm front sensitive players was

62.5%, there was a positive deviation contrary to the average distribution of our previous elaboration.

The long term biorhythm, according to Fliess was was taken into consideration in the absence of biologically active weather situations. In disturbed weather situations, however, there is no such significance of biorhythm as we could show at ice hockey players (*Örményi*, 1990).

According to the visual reaction time measurements of *Ried* (1971), a good relationship was established during a frontal passage. The reaction time of warm front sensitive people significantly increased at the time of warm front passages ($P<0.01$).

Cold front sensitive people had an increased reaction time during cold front passages ($P<0.05$).

The reaction time of mixed type people (they are sensitive to both types of frontal passage) increased, but not significantly.

This result seems to be of *primer importance* considering the performance of goal keepers. If the reaction time is longer than generally (average level), the goal keeper cannot reach the shot arriving at door.

Sport-biometeorological forecasting was furnished 26 times (*Table 3*). It should be noted, that only the forecast of warm or cold front passages does not furnish any information on expected sporting behaviour and performance. Naturally at the start of the work there was some difficulties in teaching the coaches, who accepted the forecast with scepticism. Later the situation has changed. The trainer got information by phone before matches on strange ground, too.

The championship was won by the team of Elektromos. It should be noted, that a year before the experiment, the mentioned team was on the fifth place at the end of the championship. According to the leaders of the Hungarian Handball Association, the team of Elektromos did not consist of the best players, and in spite of this, *they won the championship*.

In absence of forecast the team of Elektromos finished on the second place in the 1991/1992 and 1992/1993 championships, and finally in the 1993/1994 championship they finished only at *the third place* and remained at the same level. On the other hand there were foreign professional players too, while formerly only Hungarians played in the team.

8. Conclusions

To furnish a sport biometeorological forecast and apply the notices, it is necessary to work with the competitors and *educate the trainers* to the manifestation of influence at the team work. The primary need is to achieve fitness and high level trained conditions of the players.

Table 3. Survey of the matches and the relevant biometeorological forecasts

Date	Match place	Opponent	Scores	Front[a]	Air mass[b]	Reaction time	Game-character	Der-by	In-jury	Geomag-netism
1990										
Sep 29	Dunaújváros	Dunaferr	22-27	W	cA	short	quite	-	-	-
Oct 3	Budapest	Debrecen	20-14	Wu	mC	short	average	-	+	-
Oct 5	Budapest	Szolnok	33-17	C	mW	average	quiet	-	-	-
Oct 12	Várpalota	Várpalota	17-23	-	cT	average	tense	-	+	disturbance
Oct 18	Budapest	Pécs	31-22	C_u	mW	long	tense	-	+	-
Oct 21	Nyíregyháza	Nyíregyháza	24-24	C	cA	long	tense	-	+	-
Nov 2	Budapest	Tatabánya	28-23	C	mM	long	quiet	+	+	disturbance
Nov 11	Szeged	Tisza Volán	23-23	-	cC	long	tense	+	+	storm
Nov 23	Budapest	Bramac	26-23	I	mT	average	tense	+	+	disturbance
Nov 25	Budapest	Rába ETO	25-15	C_u	mT	long	tense	+	+	disturbance
Dec 2	Békéscsaba	Békéscsaba	19-24	Wa	mA	average	quiet	-	-	-
Dec 7	Budapest	Komló	35-27	W	mM	long	quiet	-	-	-
Dec 9	Solymár	Pemű Honv.	17-16	W	mM	short	quiet	-	-	-
1991										
Jan 22	Tatabánya	Tatabánya	27-26	C	cM	long	tense	+	+	-
Jan 27	Budapest	Tisza Volán	33-15	C_u	cC	average	tense	+	-	-
Feb 24	Győr	Rába ETO	20-19	-	cM	average	tense	+	-	-
Feb 28	Veszprém	Bramac	19-19	W_u	cC	short	tense	+	-	disturbance
Mar 3	Budapest	Békéscsaba	37-23	C	mA	long	average	-	-	-
Mar 10	Komló	Komló	20-27	-	mM	average	quiet	-	-	-
Mar 17	Budapest	Pemű Honv.	25-17	-	mT	short	quiet	-	+	disturbance
Mar 22	Debrecen	Debrecen	21-21	W_u	mT	average	tense	-	+	disturbance
Mar 29	Budapest	Dunaferr	33-17	W	mA	short	tense	-	-	-
Apr 6	Szolnok	Szolnok	19-20	I	cT	average	tense	-	+	disturbance
Apr 14	Budapest	Várpalota	22-17	-	mC	short	quiet	-	-	-
Apr 21	Pécs	Pécs	21-21	C	cA	long	tense	-	-	-
Apr 28	Budapest	Nyíregyháza	28-19	-	mC	average	average	-	-	disturbance

a : W=warm front, W_u=upper warm front, C=cold front, C_u=upper cold front, I=instability line

b : mA=maritime Arctic, cA=continental Arctic, mC=maritime cold, cC=continental cold, mM=maritime mild, cM=continental mild, mW=maritime warm, mT=maritime subtropical, cT=continental subtropical

References

Berkes, Z., 1961: Luftmassen und fronttypen in Karpathenbecken (in Hungarian). *Időjárás* 65, 289-293.

Curry, M., 1969: *Schlüssel zum Leben*. Schweiz. Verlaghaus. A.G. Zürich.

Horváth, L. G., 1960: *Some Results of Sportphysiological Investigation During Shotter Racing* (in Hungarian). Scientific Books of Sport Council, Budapest.

Kérdő, I., 1966: Ein aus Daten der Blutzirkulation kalkulierter Index zum Beurteilung der vegetativen Tonuslage. *Acta Nettrovegetativa 29*, 250-268.

Miltényi, M. and *Kereszty, A.*, 1966: Interrelations between meteorological frontal passages and 10 years athletic records (in Hungarian). *Testnevelési Főiskola Közlemények*, 85-96.

Örményi, I., 1967: Investigations of atmospheric ionisation in surroundings of St. Lucas Spa. *Annales of the Hungarian Balneoclimatological Society*, Budapest, 105-129.

Örményi, I., 1972: Questionnairy method for determination of sensitivity for weather (in Hungarian). *Ergonomia* 5 (2), 156-165.

Örményi, I., 1987: Variation of weather sensitivity (Geophysical Biotopology) over 40 years among representative population of Budapest (in Hungarian). *Publ. of the National Institute of Rheumatology and Physiotherapy*. Budapest, 169 p.

Örményi, I., 1990: Alteration in performance and some physiological parameters on ice hockey players due to their biorhythms according to Fliess. *Proc. Symp. of Human Biometeorology*. Strbské Pleso, 1989, 297-304.

Örményi, I., 1991: Biometeorological investigation of representative ice hockey goal keepers (in Hungarian). *Physical Education and Sport Science*. Budapest, 22. 22-27, 35-41.

Örményi, I., 1993: An advanced accidents forecasting technique based on weather sensitivity of drivers. *Időjárás* 97, 187-200.

Örményi, I. and *Majer, J.*, 1985: Ambulance cases and changes of the 3 Hz static levels (ELF sferics) in Budapest (in Hungarian). *Magyar Mentésügy 5,* 165-173.

Örményi, I., Megyer, M. and *Nyíri, L.*, 1981: One possibility of determination of adaptation of man depending on individual geophysical-biotopology useing artificial atmospheric ions. *Abstract. Vol. 9th International Congress of Biometeorology*. 1980. Osnabrück. Swets and Zeitlinger. 70. p.

Örményi, I. and *Ried, J.*, 1966: Complex effect of meteorological, biological and psychological factors on the performance of indoor handball players (in Hungarian). Copies of the Scientific Council of Physical Education. Budapest. 120 p.

Ried, J., 1971: Influence of weather on psychical factors and sporting achievements (in Hungarian). Thesis for Ph.D. Hungarian Academy of Sciences, Budapest.

Schelling,. H., 1940: Arbeiten aus dem Staatlichen Institut für experimentelle *Therapie und dem Forschungsinstitut für Chemotherapie*. No. 39. 35.S.

IDŐJÁRÁS

VOLUME 104 * 2000

EDITORIAL BOARD

AMBRÓZY, P. (Budapest, Hungary)
ANTAL, E. (Budapest, Hungary)
BARTHOLY, J. (Budapest, Hungary)
BOZÓ, L. (Budapest, Hungary)
BRIMBLECOMBE, P. (Norwich, U.K.)
CZELNAI, R. (Budapest, Hungary)
DÉVÉNYI, D. (Budapest, Hungary)
DUNKEL, Z. (Brussels, Belgium)
FISHER, B. (Chatham, U.K.)
GELEYN, J.-Fr. (Toulouse, France)
GERESDI, I. (Pécs, Hungary)
GÖTZ, G. (Budapest, Hungary)
HANTEL, M. (Vienna, Austria)
HASZPRA, L. (Budapest, Hungary)
HORÁNYI, A. (Budapest, Hungary)
HORVÁTH, Á. (Siófok, Hungary)
IVÁNYI, Z. (Budapest, Hungary)
KONDRATYEV, K.Ya. (St. Petersburg, Russia)
MAJOR, G. (Budapest, Hungary)
MÉSZÁROS, E. (Veszprém, Hungary)
MIKA, J. (Budapest, Hungary)
MARACCHI, G. (Firenze, Italy)
MERSICH, I. (Budapest, Hungary)
MÖLLER, D. (Berlin, Germany)
NEUWIRTH, F. (Vienna, Austria)
PINTO, J. (R. Triangle Park, NC, U.S.A.)
PROBÁLD, F. (Budapest, Hungary)
RENOUX, A. (Paris-Créteil, France)
ROCHARD, G. (Lannion, France)
S. BURÁNSZKY, M. (Budapest, Hungary)
SPÄNKUCH, D. (Potsdam, Germany)
STAROSOLSZKY, Ö. (Budapest, Hungary)
SZALAI, S. (Budapest, Hungary)
SZEPESI, D.J. (Budapest, Hungary)
TAR, K. (Debrecen, Hungary)
TÄNCZER, T. (Budapest, Hungary)
VALI, G. (Laramie, WY, U.S.A.)
VARGA-HASZONITS, Z. (Mosonmagyaróvár, Hungary)

Editor-in-Chief
TAMÁS PRÁGER

Executive Editor
MARGIT ANTAL

BUDAPEST, HUNGARY

AUTHOR INDEX

TABLE OF CONTENTS
I. Papers

II. Book review

III. Contents of journal Atmospheric Environment, 2000

IV. SUBJECT INDEX

The asterisk denotes book reviews

A

B

C

D

E

F

G

H

L

M

N

O

P

Q

R

S

T

U

W

Y

NOTES TO CONTRIBUTORS OF *IDŐJÁRÁS*

The purpose of the journal is to publish papers in any field of meteorology and atmosphere related scientific areas. These may be

- reports on new results of scientific investigations,
- critical review articles summarizing current state of art of a certain topic,
- shorter contributions dealing with a particular question.

Each issue contains "News" and "Book review" sections.

Authors may be of any nationality, but the official language of the journal is English. Papers will be reviewed by unidentified referees.

Manuscripts should be sent to
Editor-in-Chief of IDŐJÁRÁS
P.O. Box 39
H-1675 Budapest, Hungary

in three copies including all illustrations. One set of illustrations has to be of camera ready quality, the other two might be lower quality.

Title part of the paper should contain the concise title, the name(s) of the author(s), the affiliation(s) including postal and E-mail address(es). In case of multiple authors, the cover letter should indicate the corresponding author.

Abstract should follow the title, it contains the purpose, the data and methods as well as the basic conclusion.

Key-words are necessary to help to classify the topic.

The text has to be typed in double spacing with wide margins. Word-processor printing is preferred. The use of SI units are expected. The negative exponent is preferred to solidus. Figures and tables should be consecutively numbered and referred to in the text.

Mathematical formulas are expected to be as simple as possible and numbered in parentheses at the right margin. Non-Latin letters and hand-written symbols should be indicated and explained by making marginal notes in pencil.

Tables should be marked by Arabic numbers and printed in separate sheets together with their captions. Avoid too lengthy or complicated tables.

Figures should be drawn or printed in black and white, without legends, on separate sheets. The legends of figures should be printed as separate list. Good quality laser printings are preferred as master copies.

References: The text citation should contain the name(s) of the author(s) in Italic letter and the year of publication. In case of one author: *Miller* (1989), or if the name of the author cannot be fitted into the text: *(Miller,* 1989); in the case of two authors: *Gamov* and *Cleveland* (1973); if there are more than two authors: *Smith et al.* (1990). When referring to several papers published in the same year by the same author, the year of publication should be followed by letters a,b etc. At the end of the paper the list of references should be arranged alphabetically. For an article: the name(s) of author(s) in Italics, year, title of article, name of journal, volume number (the latter two in Italics) and pages. E.g. *Nathan, K.K.,* 1986: A note on the relationship between photosynthetically active radiation and cloud amount. *Időjárás 90,* 10-13. For a book: the name(s) of author(s), year, title of the book (all in Italics except the year), publisher and place of publication. E.g. *Junge, C. E.,* 1963: *Air Chemistry and Radioactivity.* Academic Press, New York and London.

The final version should be submitted on diskette altogether with one hard copy. Use standard 3.5" or 5.25" DOS formatted diskettes. The preferred word-processors are WordPerfect 5.1 and MS Word 6.0.

Reprints: authors receive 30 reprints free of charge. Additional reprints may be ordered at the authors' expense when sending back the proofs to the Editorial Office.

More information: gmajor@met.hu
Information on the last issues:
http://www.met.hu/firat/ido-e.html

Published by the Hungarian Meteorological Service

Budapest, Hungary

INDEX: 26 361

HU ISSN 0324-6329